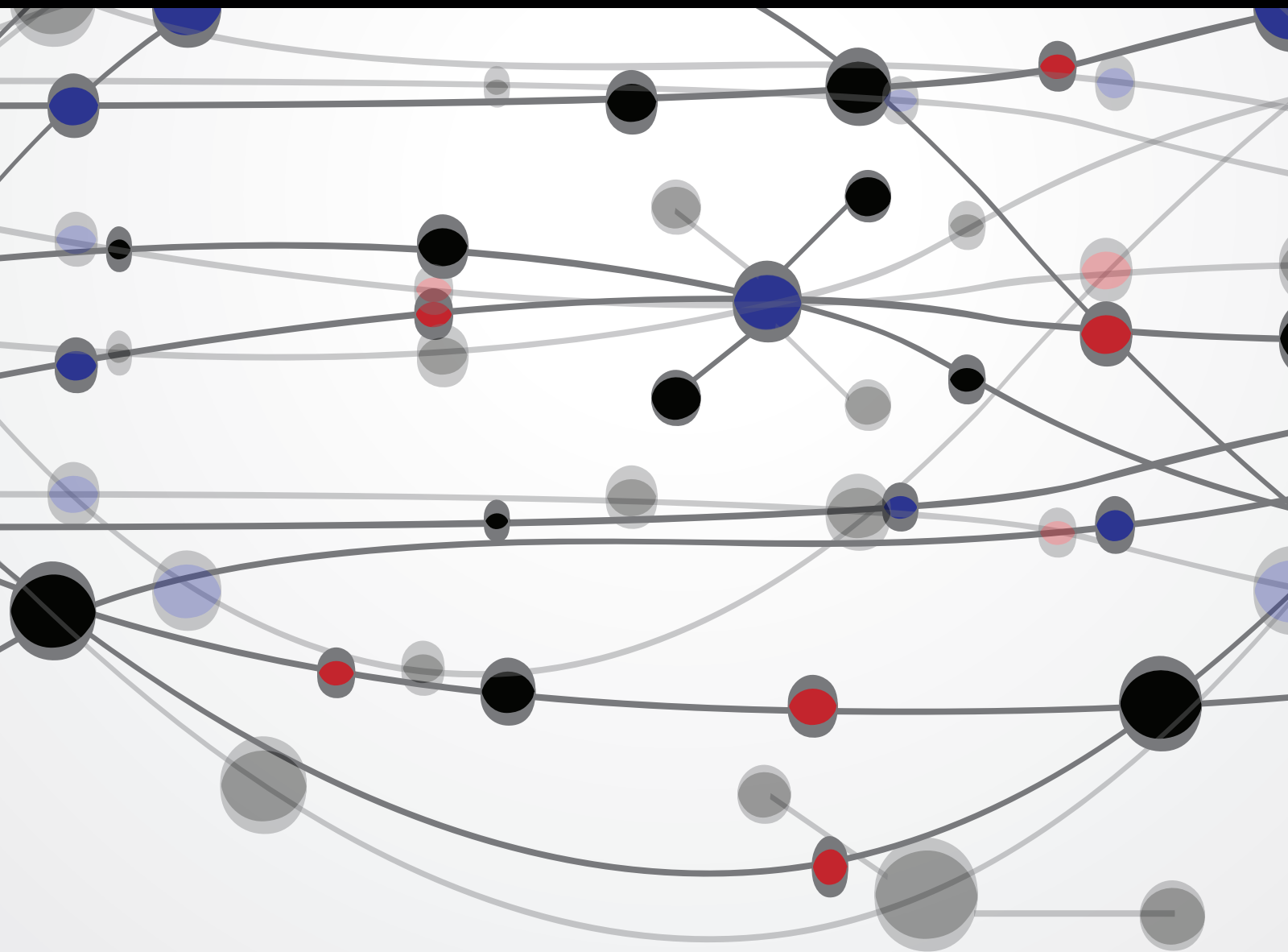


# Optical Metrology under Extreme Conditions

Guest Editors: Xide Li, Giancarlo Pedrini, and Yu Fu





---

# **Optical Metrology under Extreme Conditions**

The Scientific World Journal

---

# **Optical Metrology under Extreme Conditions**

Guest Editors: Xide Li, Giancarlo Pedrini, and Yu Fu



---

Copyright © 2014 Hindawi Publishing Corporation. All rights reserved.

This is a special issue published in "The Scientific World Journal." All articles are open access articles distributed under the Creative Commons Attribution License, which permits unrestricted use, distribution, and reproduction in any medium, provided the original work is properly cited.

# Contents

**Optical Metrology under Extreme Conditions**, Xide Li, Giancarlo Pedrini, and Yu Fu  
Volume 2014, Article ID 263603, 1 page

**Interferometric Dynamic Measurement: Techniques Based on High-Speed Imaging or a Single Photodetector**, Yu Fu, Giancarlo Pedrini, and Xide Li  
Volume 2014, Article ID 232906, 14 pages

**Interfacial Micromechanics in Fibrous Composites: Design, Evaluation, and Models**, Zhenkun Lei, Xuan Li, Fuyong Qin, and Wei Qiu  
Volume 2014, Article ID 282436, 9 pages

**A Real-Time Optical Tracking and Measurement Processing System for Flying Targets**, Pengyu Guo, Shaowen Ding, Hongliang Zhang, and Xiaohu Zhang  
Volume 2014, Article ID 976590, 11 pages

**Nanoscale Strain Fields Research of Boundaries between B2 Matrix and G.P. Zone in Ni-Ti Alloy Thin Films**, Shilei Zhao and Chunwang Zhao  
Volume 2014, Article ID 127032, 5 pages

**3D Online Submicron Scale Observation of Mixed Metal Powder's Microstructure Evolution in High Temperature and Microwave Compound Fields**, Dan Kang, Feng Xu, Xiao-fang Hu, Bo Dong, Yu Xiao, and Ti-qiao Xiao  
Volume 2014, Article ID 684081, 5 pages

**In Situ Investigation of the 3D Mechanical Microstructure at Nanoscale: Nano-CT Imaging Method of Local Small Region in Large Scale Sample**, Bo Dong, Feng Xu, Xiao-fang Hu, Hong-yan Qu, Dan Kang, and Ti-qiao Xiao  
Volume 2014, Article ID 806371, 10 pages

**Automatic Three-Dimensional Measurement of Large-Scale Structure Based on Vision Metrology**, Zhaokun Zhu, Banglei Guan, Xiaohu Zhang, Daokui Li, and Qifeng Yu  
Volume 2014, Article ID 185269, 10 pages

**Formation of Three-Way Scanning Electron Microscope Moiré on Micro/Nanostructures**, Qinghua Wang, Satoshi Kishimoto, and Hiroshi Tsuda  
Volume 2014, Article ID 281954, 8 pages

**Strain Sensor of Carbon Nanotubes in Microscale: From Model to Metrology**, Wei Qiu, Shi-Lei Li, Wei-lin Deng, Di Gao, and Yi-Lan Kang  
Volume 2014, Article ID 406154, 9 pages

**Fiber Optic Projection-Imaging System for Shape Measurement in Confined Space**, Lujie Chen, Viswanath Bavigadda, Theodoros Kofidis, and Robert D. Howe  
Volume 2014, Article ID 206569, 10 pages

## *Editorial*

# **Optical Metrology under Extreme Conditions**

**Xide Li,<sup>1</sup> Giancarlo Pedrini,<sup>2</sup> and Yu Fu<sup>3</sup>**

<sup>1</sup> *Department of Engineering Mechanics, Tsinghua University, Beijing 100084, China*

<sup>2</sup> *Institut für Technische Optik, University of Stuttgart, Pfaffenwaldring 9, 70569 Stuttgart, Germany*

<sup>3</sup> *Temasek Laboratories, Nanyang Technological University, Research Techno Plaza, 50 Nanyang Drive, Singapore 637553*

Correspondence should be addressed to Xide Li; [lixide@mail.tsinghua.edu.cn](mailto:lixide@mail.tsinghua.edu.cn)

Received 11 May 2014; Accepted 11 May 2014; Published 26 May 2014

Copyright © 2014 Xide Li et al. This is an open access article distributed under the Creative Commons Attribution License, which permits unrestricted use, distribution, and reproduction in any medium, provided the original work is properly cited.

Optical metrology provides full field, noncontact, precise measurement of various physical parameters of materials, structures, and devices. These properties include kinematic parameters (displacement, velocity, and acceleration), deformation parameters (strains, curvature, and twist), surface parameters (shape and roughness), and mechanical properties of materials (Young's modulus, Poisson's ratio, etc.). Researchers have developed many delicate optical measurement techniques and methods, such as photoelasticity, holographic interferometry, speckle metrology, Moiré methods, fiber sensing, laser Doppler vibrometry and velocimetry, and computer-vision-based techniques. However, new requirements arise with the recent development in fundamental research and industry applications to fulfill nondestructive and precise measurement under extreme conditions, such as high temperature or pressure, micro/nanoscale samples, large-scale curved structures, and transient events.

It is our pleasure to have this opportunity to present the readers of The Scientific World Journal (SWJ) to some of the current research being performed in optical techniques and image processing under some extreme conditions. There are 10 papers in this special issue, which cover a broad range of topics from microscopic image analysis to nanoscale strain field research, from interfacial mechanical analysis to Raman spectroscopy detection, and from high temperature measurement to large-scale structure optical tracking and dynamical or transient optical metrology. All of the published papers are peer-reviewed.

*Xide Li  
Giancarlo Pedrini  
Yu Fu*

## Review Article

# Interferometric Dynamic Measurement: Techniques Based on High-Speed Imaging or a Single Photodetector

Yu Fu,<sup>1</sup> Giancarlo Pedrini,<sup>2</sup> and Xide Li<sup>3</sup>

<sup>1</sup> Temasek Laboratories & School of Mechanical & Aerospace Engineering, Nanyang Technological University, 50 Nanyang Drive, Singapore 637553

<sup>2</sup> Institut für Technische Optik, Universität Stuttgart, Pfaffenwaldring 9, 70569 Stuttgart, Germany

<sup>3</sup> Department of Engineering Mechanics, AML, CNMM, Tsinghua University, Beijing 100084, China

Correspondence should be addressed to Xide Li; [lixide@tsinghua.edu.cn](mailto:lixide@tsinghua.edu.cn)

Received 4 November 2013; Accepted 15 April 2014; Published 12 May 2014

Academic Editors: S. Grilli, M. Strojnik, and J. Yu

Copyright © 2014 Yu Fu et al. This is an open access article distributed under the Creative Commons Attribution License, which permits unrestricted use, distribution, and reproduction in any medium, provided the original work is properly cited.

In recent years, optical interferometry-based techniques have been widely used to perform noncontact measurement of dynamic deformation in different industrial areas. In these applications, various physical quantities need to be measured in any instant and the Nyquist sampling theorem has to be satisfied along the time axis on each measurement point. Two types of techniques were developed for such measurements: one is based on high-speed cameras and the other uses a single photodetector. The limitation of the measurement range along the time axis in camera-based technology is mainly due to the low capturing rate, while the photodetector-based technology can only do the measurement on a single point. In this paper, several aspects of these two technologies are discussed. For the camera-based interferometry, the discussion includes the introduction of the carrier, the processing of the recorded images, the phase extraction algorithms in various domains, and how to increase the temporal measurement range by using multiwavelength techniques. For the detector-based interferometry, the discussion mainly focuses on the single-point and multipoint laser Doppler vibrometers and their applications for measurement under extreme conditions. The results show the effort done by researchers for the improvement of the measurement capabilities using interferometry-based techniques to cover the requirements needed for the industrial applications.

## 1. Introduction

In the last several decades, the drive for higher performance and reliability of devices, structures, and processes in engineering has placed stringent demands on the methods used in their development and measurement. Optical metrology is a major and indispensable part of the measurement methods. The field of optical metrology is arguably more than one century old. However, major advances have resulted from the invention of laser only about fifty years ago. This new light source opened a realm of new techniques to both the physicist and the engineer. With the advent of the laser, coherent optics has been brought into measurement techniques of various areas. Optical interferometry [1] is a well-known technique to measure the path-length change of laser light caused by deformation, movement, or unevenness of an object. Generally, there are two types of techniques: one is

based on two-dimensional sensor like CCD or CMOS camera and the other is based on single-pixel photodetector.

*1.1. Interferometric Dynamic Measurement (IDM).* The typical camera-based interferometry includes different methods, such as photoelasticity [2], moiré interferometry [3], electronic speckle pattern interferometry (ESPI) [4], shearography [5], digital holography [6], and white-light interferometry [7]. Generally, they are noncontacting and whole-field techniques providing results in the form of fringe patterns that represent different physical quantities, such as distance, in-plane or out-of-plane displacements, strain, stresses, or refractive-index. Although a fringe pattern representing distance, deformation, or distortion is readily obtained, expert interpretation is necessary to convert these fringes into the desired information. For the accurate mapping of these physical quantities various fringe processing

algorithms, notably the Fourier transform [8] and phase shifting [9], have been used. Due to the limited capturing rate of the camera and the long processing time for fringe pattern, initially these interferometers were mainly used for quasi static measurements. For high-frequency periodical vibration measurement, the camera-based interferometry is applied to determine vibration modes of objects. Time-average methods, based on digital holography [10], ESPI [11], DSSI [12], or moiré [13], directly acquire a spatially dense, full-field, real-time image of the mode shape, while other techniques require the reconstruction of the mode shape from single point measurements. Methods using stroboscopic light sources [14] allow “fixing” the steady-state vibration and can be applied in principle for the measurement of nonsinusoidal vibrations, but the movement should be periodical. In addition, if low-speed CCDs are used, the time for acquiring the interferograms may be quite long and this makes the technique poorly suited to be used in an industrial environment.

In many cases, high-resolution three-dimensional (3D) dynamic displacement or surface profiling can give useful information about the dynamic response of a mechanical structure. However, it is difficult to achieve this with the abovementioned techniques. The use of double-pulse laser interferometry [15] has been reported as an alternative to obtain transient deformations. However, this technique has a fatal limitation, since, to obtain the evolution of the transient deformation, an experiment must be repeated many times with a different interval of two pulses. This means that nonrepeatable events cannot be studied in detail. Due to the rapid development of high-speed digital recording devices, it is possible to record interferograms with rates exceeding 100,000 frame/s. In order to measure various physical quantities at any instant, high-speed camera is adopted in various interferometric techniques to satisfy the Nyquist sampling theorem along time axis. This leads to a series of interferometric dynamic measurement techniques based on high-speed imaging.

On the other hand, single-pixel detector-based interferometry has already been successfully applied for dynamic measurement. Laser Doppler vibrometry [16] and laser Doppler velocimetry [17] are two similar techniques. The former is for the measurement of out-of-plane displacement or velocity and the latter is for in-plane displacement or velocity measurement. Compared to a full-field measurement based on high-speed camera, detector based interferometry can only offer a point-wise measurement, but with large measurement velocity range. For the extraction of the Doppler frequency shift, different interferometric solutions can be used. The heterodyne Mach-Zehnder and the homodyne Michelson interferometers are two typical configurations. In order to measure the vibration at different points, laser Doppler vibrometers are equipped with a video camera and a scanning system. These scanning laser Doppler vibrometers (SLDV) give the possibility of moving the measurement point rapidly and precisely on the testing surface, allowing the analysis of large surface with high spatial resolution [18].

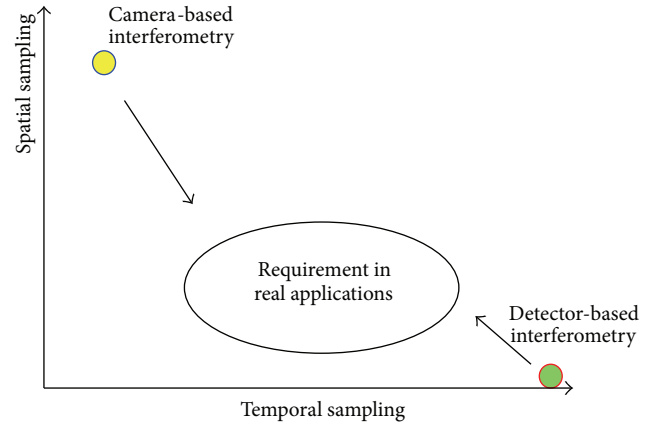


FIGURE 1: The current status of camera-based and detector-based interferometry.

**1.2. Current Status of IDM.** Figure 1 shows that the camera-based technique has very high spatial resolution but its temporal resolution is low compared with the requirement of real applications. Even a 100 k frame/s capturing rate sometimes cannot satisfy the Nyquist sampling theorem; as for every measurement point, the phase change between two consecutive images should be less than  $\pi$ . In addition, a high power laser is needed for the illumination and the cost of high-speed camera also limits the applications in industrial areas. On the contrary, detector-based laser Doppler techniques have enough sampling rate along the time axis, but only one measurement point in spatial domain. A scanning device is usually used to perform 2D measurements. This method assumes that the measurement conditions remain invariant while sequential measurements are performed. Hence, it is only suitable to measure steady-state or well-characterized vibrations. However, most engineering applications do not satisfy these requirements. Transients, including impact or coupled vibrations, are commonly observed in real applications and scanning LDVs impractical to generate a vibration image in these cases.

In this paper, some new measurement and processing technologies based on high-speed imaging and single detector are reviewed. Several issues of the camera-based IDM are discussed; these include the carrier and processing domain, phase extraction technique, and how to increase the measurement range by using the multiwavelength method. A detector-based IDM technique using a multipoint laser Doppler vibrometer (LDV) based on a spatially-encoded technology is described. Some applications under extreme conditions are presented and the results show the trend of IDM to meet the requirements necessary for industrial applications with sufficient temporal and spatial sampling points.

## 2. High-Speed-Imaging-Based IDM

In the high-speed-imaging-based interferometric dynamic measurement technique (IDM), the signal obtained is

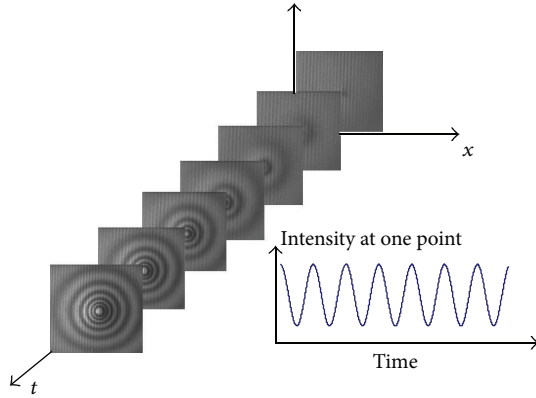


FIGURE 2: Schematic layout of the high-speed-imaging-based IDM.

a sequence of interferograms recorded at time  $t$  (see Figure 2) that can be written as

$$f(x, y; t) = I_b(x, y; t) + A(x, y; t) \cos(\varphi(x, y; t) + \varphi_0(x, y)), \quad (1)$$

where  $I_b(x, y; t)$  and  $A(x, y; t)$  are the intensity bias and the modulation factor, respectively. Both items are slowly time-varying functions.  $\varphi(x, y; t)$  is a phase variation due to a vibration or a continuous displacement.  $\varphi_0(x, y)$  is the initial phase value of each pixel. The purpose of the imaging-based IDM is to extract the phase  $\varphi(x, y; t)$  from a 3D matrix as expressed in (1).

**2.1. Phase Extraction Techniques.** There are quite a lot of phase extraction techniques for interferometric fringe patterns and these are classified into three categories: phase-shifting methods, transform-based methods, and others.

**2.1.1. Phase-Shifting Techniques.** The phase-shifting techniques can be classified into temporal and spatial phase shifting. In the temporal phase shifting technique, at least three phase-shifted fringe patterns or specklegrams are collected. In order to keep the phase nearly unchanged during the phase shifting, a fast phase shifter and a high capturing rate are necessary. In 1996, de Lega and Jacquot [19] proposed the object-induced temporal phase changes where a piezoelectric transducer (PZT) with the driven frequency of 80 Hz was used to produce a phase shift between two consecutive frames. In 1999, Huntley et al. [20] developed a phase shifting speckle interferometer operated at 1 k Hz capturing rate using a high-speed camera. A Pockels cell producing a phase shift of  $\pi/2$  between two consecutive frames was used and the system was synchronized with the camera. In 2003, Kaufmann [21] used a similar system to monitor the out-of-plane deformation of a plate with flaw. In these techniques, temporal phase unwrapping [22] was applied. Hence, the measurement errors were also accumulated. In 2002, Kao et al. [23] applied the phase shifts to the initial status  $t_0$  but not to other instances  $t$ . Phase-shifted speckle-correlation fringe patterns can be formed between  $t_0$  and  $t$ . This method is very simple but

suffers from speckle decorrelation. In 2005, the rereferencing rate, that is, the update rate of the reference frame, was studied [24] to avoid the influence of the speckle decorrelation. Generally, the temporal phase-shifting method is only suitable to measure a slow-varying deformation or profile changing producing a phase variation which is much slower compared with the temporal carrier generating the reference phase shift.

In the spatial phase-shifting techniques, several phase-shifted fringe patterns are captured in one shot at different locations by either different cameras or on different areas of a camera. Several such systems are described in [25–27]. A significant innovation is a camera with a pixelated phase mask that can be combined with different interferometers [28, 29]. This technique converts a  $2 \times 2$  superpixel into four phase-shifted pixels using micropolarizers, avoiding the registration of several phase-shifting fringe patterns. Compared to temporal phase-shifting techniques, the measurement range along the time-axis is increased, with the cost of slightly sacrificing the spatial resolution. Similar technique can be found in fringe projection profilometry [30], although this is not considered as an interferometric technique.

**2.1.2. Transform-Based Techniques.** Transform-based techniques are the predominant phase extraction methods in the imaging-based IDM. These techniques include Fourier transform [8], Hilbert transform [31], windowed Fourier transform [32], wavelet transform [33], and a combination of Fourier and windowed Fourier transform [34]. Like the phase-shifting techniques, the transform-based phase extraction methods can be applied in the spatial domain, temporal domain, or even spatial-temporal domain. The processing can be one-dimensional (1D), 2D, or even 3D. The only requirement is that a carrier has to be introduced along one-axis in the processing domain to avoid the phase ambiguity. Carrier-based 2D spatial Fourier transform [8] was firstly applied in IDM as it allows extracting the phase distribution from a single carrier fringe pattern. It has been applied to measure the transient phenomena by moiré interferometry [35] and speckle interferometry. A spatial carrier leads to a fringe pattern with various fringe densities in one image. However, in the speckle interferogram, the fringe density cannot be too high due to the speckle noise and this limits the measurement. In recent years, other transforms such as windowed Fourier transform [32] and wavelet transform [33] have also been used to process the carrier fringe pattern.

After the introduction of the high-speed camera in IDM, a temporal version of the Fourier analysis and other transform-based methods were applied to extract the phase. In this case, a temporal carrier is required. In 1998, Joenathan et al. performed a series of studies on temporal phase evaluation through speckle interferometry for out-of-plane deformation [36], in-plane deformation [37], the derivative of out-of-plane deformation [38], and the shape measurement [39]. The influence of decorrelation, speckle size, and nonlinearity of the camera were also discussed [40] and

TABLE 1: Comparison of spatial-carrier and temporal-carrier-based techniques in interferometry.

Factors	Spatial-carrier-based technology	Temporal-carrier-based technology
Processing domain	$x$ - and $y$ -axis	$t$ -axis
Dimension	2-D	1-D
Reflectivity	Affected by nonuniform reflectivity	Not affected
Height step	Affected by height step of test objects	Not affected
Shape	Affected by irregular shape of surface	Not affected
Retrieved phase map quality	Poor and affected by speckle noise when laser is used	Much better than spatial carrier as the process is 1-D along time axis.
Measurement range in temporal domain	Determined by Nyquist sampling theorem	Affected by temporal carrier and much less measurement range than spatial carrier

a rotating half-wave plate was proposed to introduce a temporal carrier. In 2002, Kaufmann and Galizzi compared the temporal phase-shifting method with the temporal Fourier transform method [41]. In 1997, de Lega firstly described a temporal wavelet phase extraction algorithm for dynamic measurement [42]. The research was continued by Fu et al. [43, 44] as well as Federico and Kaufmann [45]. The S transform, a similar algorithm to wavelet transform, has also been used for temporal phase evaluation [46]. Another technique is the windowed Fourier transform (WFT). In 2003 Ruiz et al. elegantly linked a temporal phase-shifting algorithm to the temporal windowed Fourier transform and showed that the WFT provided better performance [47]. In 2006, Qian et al. applied a 3D WFT to process a sequence of fringe pattern from speckle interferometry [48]. In 2007, Fu et al. applied the WFT to digital holography for vibration measurement and demonstrated its superior performance over the Fourier transform [49]. In the same year, they proposed a combination of two transforms, namely, the temporal Fourier transform and the spatial windowed Fourier transform, and showed that this combination performed better than either single transform [34].

**2.1.3. Miscellaneous Algorithms.** Another simple but effective temporal phase extraction algorithm, for time sequence analysis, was proposed by Li et al. in 2001–2004 [50–52]. It includes phase scanning method, sequence pulse counting method, and matched correlation sequence analysis. These methods retrieve the phase from the variation of the gray values. The significant advantage of the time sequence analysis algorithm is that it is simple and efficient. The drawback is that it cannot be applied to a very noisy signal as the accuracy of the methods relies on the correct identification of the fluctuations of the interference intensity in each cycle. Li et al. also applied this algorithm to speckle fringe patterns but the method is more suitable for low noise patterns obtained by incoherent methods such as fringe projection and shadow moiré. Furthermore, it needs enough sampling points in one cycle of gray value variation. Li et al. mentioned at least 6 sampling points, but from the experiments it was found that 10 to 16 sampling points per cycle produce the best results.

In recent years, some algorithms for the extraction phase values from one fringe pattern without spatial carrier were reported [53–57]. However, these algorithms are based on

some assumptions and they may be working on some fringe patterns but fail on others. Hence, adding a carrier frequency is still the most reliable and effective method.

**2.2. Carrier and Processing Domain.** For the interferometric dynamic measurement, the carrier can be introduced either in the spatial domain (along  $x$ - or  $y$ -axis) or in the temporal domain (along the  $t$ -axis). Table 1 shows the comparison of spatial and temporal carrier-based techniques. In the spatial-carrier-based technique, the quality of the retrieved phase map is affected by several factors, such as speckle noise, nonuniform reflectivity, and irregular shape of the surface. Figure 3 gives an example of the effect of irregular shape of surface in the fringe projection technique. Although fringe projection is not an interferometric method, the problem involved in the fringe processing is the same as in interferometry. In fringe projection the carrier already exists in the spatial domain. However, the result of the spatial processing will be seriously affected by a nonuniform reflectivity of the surface or a height step on the surface. Zero-padding is also needed for an irregular shape and this will also generate large error at the edge. Figure 3(a) shows a fringe pattern projected on a cantilever beam with irregular shape. Figures 3(b) and 3(c) show a wrapped phase map after 2D Fourier transform and the phase distribution after unwrapping and removal of the carrier. The phase distortion close to the edge is due to the zero-padding. The results obtained by WFT and CWT are worse due to their lower resolutions in the spatial and frequency domains. This example shows that spatial processing may not be a good choice in some cases.

Figure 4 shows a comparison of spatial and temporal carriers in digital shearography [58]. In this technique, the phase change represents the deflection derivative. Figure 4(a) shows a shearographic fringe pattern with spatial carrier on a fully clamped circular plate with central-point loading where the nearly straight parallel carrier modulates the shearography fringes. The density of the carrier fringes should be high enough to enable the unambiguous determination of the fringe orders. A two-dimensional Fourier transform is then applied to extract the phase from one fringe pattern. The quality of the phase map depends on the proper selection of the band-pass filtering window. Figure 4(b) shows the best result obtained. However, the noise effect is still obvious on the phase map. Figure 4(c) shows the unwrapped phase

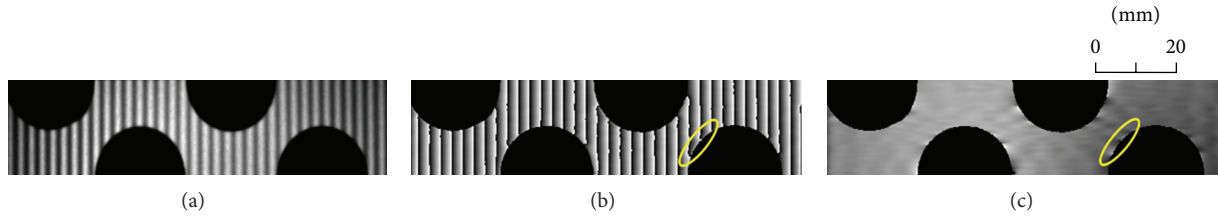


FIGURE 3: (a) Typical fringe pattern on a cantilever beam with irregular shape; (b) wrapped phase obtained by 2D spatial transform; (c) phase distribution after unwrapping and removal of the carrier.

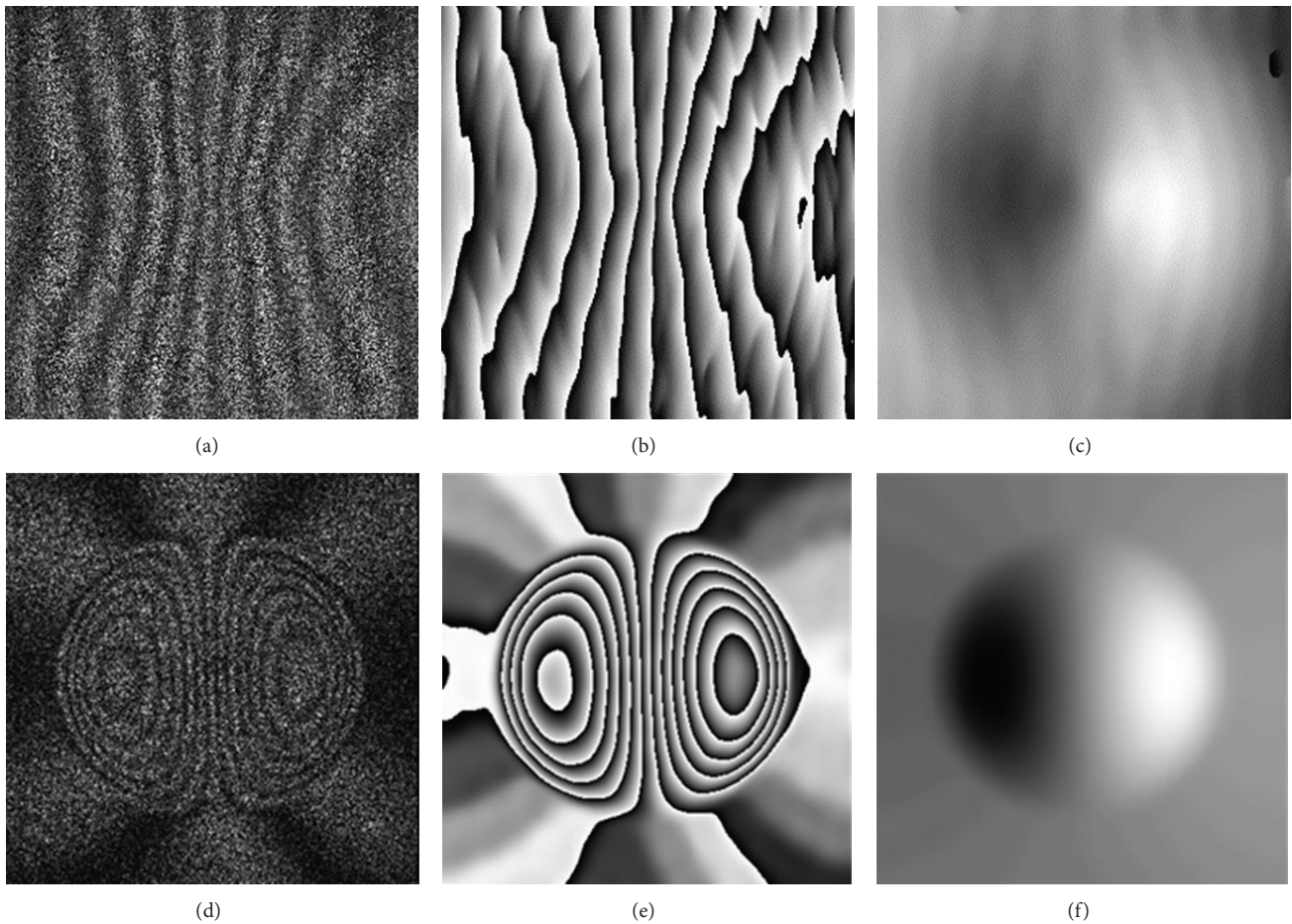


FIGURE 4: (a) Typical shearography fringe pattern, (b) wrapped phase map, and (c) phase after unwrapping and removal of the spatial carrier; (d) shearography fringe pattern, (e) wrapped phase map, and (f) phase after unwrapping when the temporal carrier is applied (reprint from [58]).

map after removal of the carrier. Figure 4(d) shows a typical shearography fringe pattern obtained from a dynamic measurement when a temporal carrier is introduced. The fringe density is much higher in this case. The wrapped phase map after temporal analysis and unwrapping are shown in Figures 4(e) and 4(f), respectively. We may see that good results can be obtained even when the fringes are dense.

This example shows that the processing along the time-axis usually gives better results. However, due the capturing

rate of camera a carrier in the temporal domain will dramatically reduce the measurement range along the time-axis limiting the applications. Hence, a compromise is necessary between these two techniques. This leads to a tradeoff processing in the spatial-temporal domain. The carrier is still in the spatial domain but a 2D algorithm (FFT or WFT) is applied in the spatial-temporal domain [59]. Figure 5 shows an image-plane digital holographic microscopy setup sensitive to out-of-plane displacements. A spatial carrier is

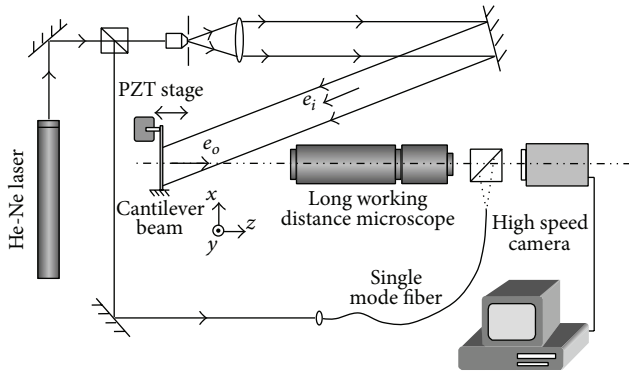


FIGURE 5: Schematic layout of an image-plane digital holographic microscope (reprint from [59]).

introduced by proper positioning of the fiber tip carrying the reference beam. A sequence of digital holograms is captured during the vibration of cantilever beam excited by a PZT.

A 2D Fourier analysis is applied at each interferogram to obtain a series of 2D wrapped phase maps. The temporal phase variations along the central-line of the cantilever beam generate a spatiotemporal distribution as shown in Figure 6(a). Phase unwrapping along the time axis yields a continuous phase map (Figure 6(b)), from which the instantaneous displacement along the central-line can be calculated. Figure 6(c) shows the displacement of the beam at different time  $t_n$ . Figure 6(d) shows the displacement variation of two points located on the central line at the positions  $x_1 = 100 \mu\text{m}$  and  $x_2 = 500 \mu\text{m}$ . The phase values in Figure 6(a) are then converted to the exponential values  $\exp(j \cdot \Delta\phi)$  and processed in the spatial-temporal domain by using the windowed Fourier ridge algorithm to extract the instantaneous velocity and acceleration.

**2.3. Dual-Wavelength Technique.** In many IDM cases, the frequency of the vibrating object is low and the amplitude is large. As the measurement still needs to satisfy the Nyquist theorem, the requirement on capturing rate should still be very high. In this case, a longer wavelength can effectively increase the measurement range. Lasers emitting infrared radiation (e.g.,  $10.6 \mu\text{m}$   $\text{CO}_2$  laser) are available but unfortunately for such wavelengths the detectors are very expensive and have limited resolution. Hence, dual and multiwavelength techniques were introduced to generate a longer synthetic wavelength. Different types of dual-wavelength interferometers have been reported during the past several decades. A typical application of dual-wavelength is the measurement of a surface profile with height steps [60]. The method can also be used with digital holography for surface profiling where the phase at single wavelength can be reconstructed from separately recorded digital holograms [6, 61]. However, it is not suitable for dynamic measurement since two holograms need to be recorded and reconstructed individually. Here a dual-wavelength interferometer combined with image-plane digital holography is presented to achieve a dynamic measurement on a vibrating object. The

object was simultaneously illuminated by two lasers with different wavelengths, and a sequence of digital holograms was captured by a CCD camera [62].

A schematic layout of a dual-wavelength image-plane digital holography configuration, sensitive to out-of-plane displacement, is shown in Figure 7. Two lasers with different wavelengths are used. Light from the first laser is split into an object beam and a reference beam. This object beam illuminates a vibrating specimen with a diffuse surface along a direction  $\mathbf{e}_{i1}$ . Some light is scattered in the observation direction  $\mathbf{e}_o$  where an image-plane hologram is formed on the CCD sensor, as a result of the interference between the reference beam and the object beam. An aperture is put immediately behind the imaging lens to limit the spatial frequencies of the interference pattern. Similarly a second different laser wavelength is used to generate a second interferogram on the CCD sensor. When these two lasers simultaneously illuminate the object and the detector, the two interferograms will be superimposed on the CCD sensor and one digital hologram containing information about these two interferograms will be obtained.

Figure 8(a) shows a typical digital hologram captured by the CCD camera. With a proper selection of the aperture size and a careful adjustment of the two fiber-end positions, it is possible to separate the spectra of two superimposed holograms in the frequency domain. In our experiment, one hundred and twenty holograms are captured during an eight-second period. Figure 8(b) shows a typical Fourier spectrum of digital holograms captured by the CCD camera. The shadow of the fiber ends can be observed on the spectra of both digital holograms. When *filtering window A* is selected, the reconstructed phase difference between the two instants represents the out-of-plane displacement for the wavelength  $632.8 \text{ nm}$  (Figure 8(c)). When *filtering window B* is selected, the reconstructed phase between the two instants is the result with wavelength of  $532 \text{ nm}$  (Figure 8(d)). A slight difference can be observed between these two wrapped phase maps. At each instant  $t_m$ , a new phase distribution is calculated directly by the subtraction of these two wrapped phases:

$$\Phi = \begin{cases} \Delta\phi_1 - \Delta\phi_2 & \text{if } \Delta\phi_1 \geq \Delta\phi_2, \\ \Delta\phi_1 - \Delta\phi_2 + 2\pi & \text{if } \Delta\phi_1 < \Delta\phi_2, \end{cases} \quad (2)$$

where  $0 \leq \Phi < 2\pi$ . This phase map is equivalent to a phase distribution of an out-of-plane displacement measurement with a synthetic wavelength  $\Lambda$ , where

$$\Lambda = \frac{\lambda_{\text{eq1}}\lambda_{\text{eq2}}}{|\lambda_{\text{eq1}} - \lambda_{\text{eq2}}|}. \quad (3)$$

Figure 9 shows the phase variation of point C (indicated in Figure 8(d)) after 1D temporal phase unwrapping. In our experiment, the synthetic wavelength equals  $3342 \text{ nm}$ . In this case, the measurement range in the temporal domain has been increased by 5 times. This is a typical technique to increase the temporal measurement range with the cost of sacrificing some resolution in the spatial domain, which shows the efforts to balance the temporal and spatial resolutions in IDM.

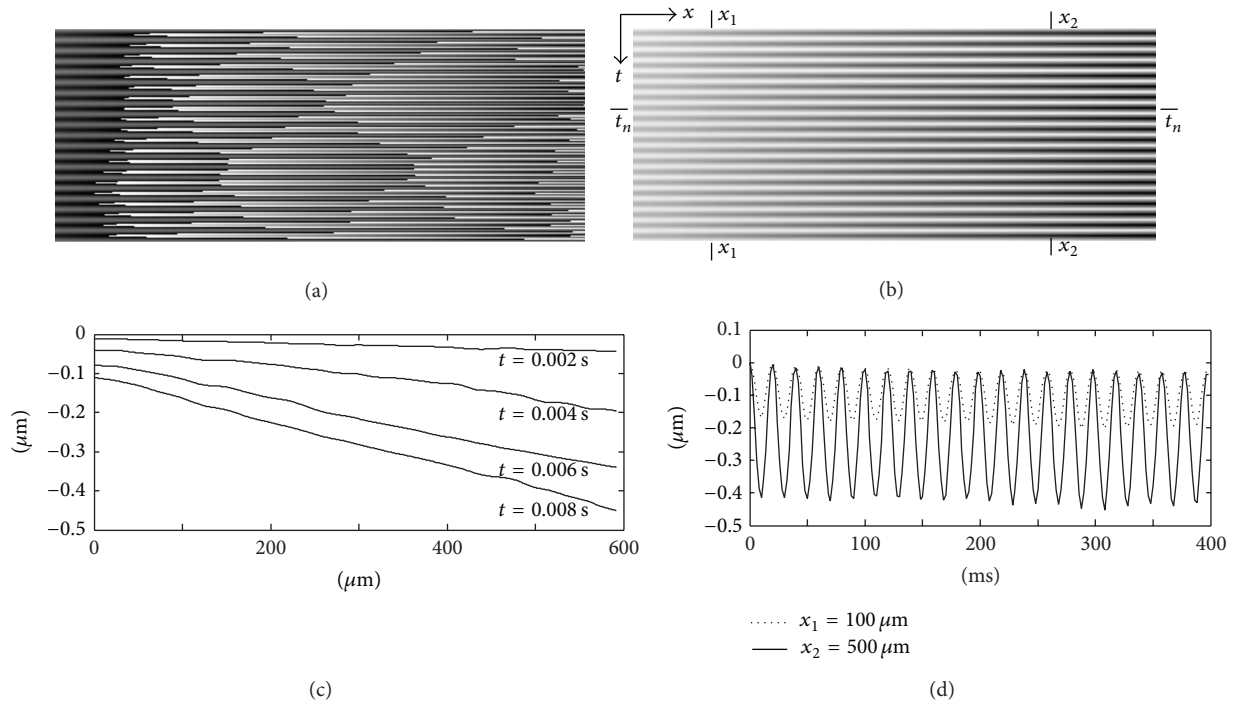


FIGURE 6: (a) Wrapped phase map in the spatiotemporal plane; (b) unwrapped phase map shows the displacement variation in the spatiotemporal plane; (c) displacement distributions of the cantilever beam at different instants; (d) Displacements of two points on the cantilever beam (reprint from [59]).

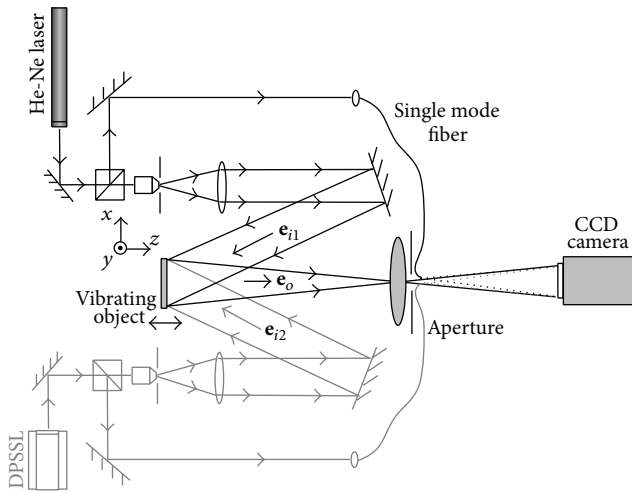


FIGURE 7: Schematic layout of dual-wavelength image-plane digital holography for dynamic measurement (reprint from [62]).

### 3. Detector-Based IDM

Detector-based interferometry is usually used for high temporal resolution point-wise measurements and allows measuring large vibrations amplitudes and frequencies. Two specifications of various single-pixel detectors make the detector-based IDM an effective method for industrial applications: (1) large pixel area and (2) wide frequency response. The detectors size is more than several tens of micrometer;

many of them are  $>0.5\text{ mm}$  with an output bandwidth of  $1\text{ GHz}$ . Compared to CCD or CMOS cameras, they are more sensitive to low-power laser light. Typical detector-based interferometry includes two similar technologies: laser Doppler vibrometer for out-of-plane displacement or vibration measurement [16] and laser Doppler velocimeter for in-plane velocity measurement [17]. Here we will focus on the laser Doppler vibrometer (LDV) and its applications.

**3.1. Conventional Single-Point Laser Doppler Vibrometer.** The laser Doppler vibrometer is based on the Doppler Effect that occurs when the laser light is scattered from a moving surface. The instantaneous velocity of the surface is converted to the Doppler frequency shift of the laser light which can be extracted by interference between the object and the reference beams. Two configurations have been developed to avoid the directional ambiguity problem: the heterodyne (Mach-Zehnder interferometer including one detector and one acousto-optic modulator) and the homodyne (Michelson interferometer with two detectors and polarization components). Figure 10 shows the schematic layout of a typical heterodyne single-point laser Doppler vibrometer.

In a single-point LDV, a laser beam with wavelength  $\lambda$  is projected on an object moving with velocity  $V$ ; due to the Doppler effect the shifted frequency  $f_D$  of the reflected beam is proportional to the velocity of the object and can be expressed as

$$f_D(t) = \frac{\mathbf{V}(t) \cdot \mathbf{S}}{\lambda}, \quad (4)$$

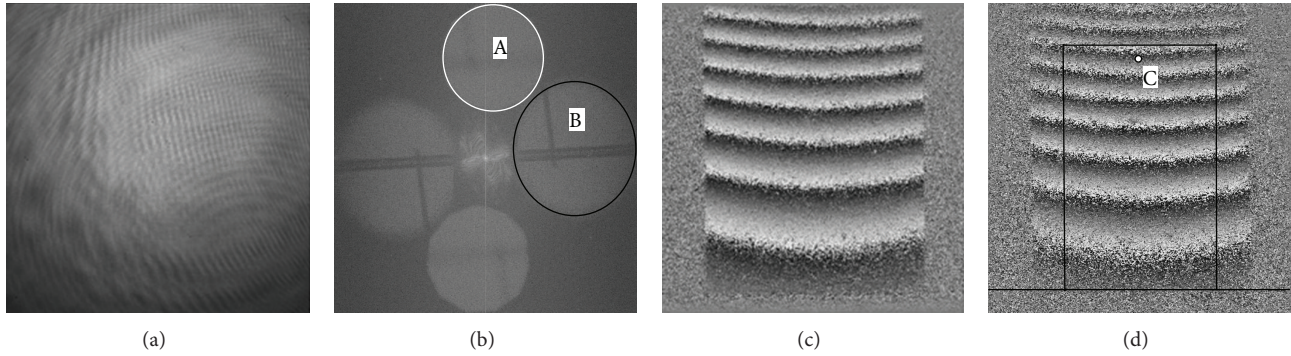


FIGURE 8: (a) Typical digital hologram obtained by illumination from two lasers; (b) spectrum of the digital hologram obtained; (c) typical original wrapped phase map with  $\lambda_1 = 633$  nm; (d) typical original wrapped phase map with  $\lambda_2 = 523$  nm, and the selected area to process (reprint from [62]).

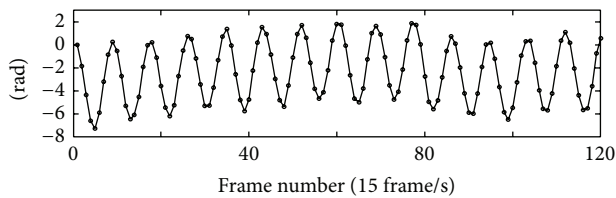


FIGURE 9: Phase variation of the point C with the synthetic wavelength of 3342 nm which is proportional to the displacement of the object (reprint from [62]).

where  $\mathbf{S} = \mathbf{e}_i - \mathbf{e}_o$  is the sensitivity vector given by the geometry of the setup, and  $\mathbf{e}_i$  and  $\mathbf{e}_o$  are the unit vectors of the illumination and observation, respectively. In order to avoid the directional ambiguity in frequency shift, the most common solution is the heterodyne interferometer where an optical frequency shift is introduced into one arm of the interferometer by an acousto-optic modulator (AOM) to obtain a virtual velocity offset. The intensity fluctuation at the detector can be expressed as [63]

$$I = I_{DC} + I_{RO} \cos(2\pi(f_D + f_{AOM})t + \Delta\phi), \quad (5)$$

where  $f_D$  and  $f_{AOM}$  are the Doppler frequency shift and the carrier frequency introduced by the AOM, respectively.  $\Delta\phi$  is the phase difference between the reference and object beams. The modulation factor  $I_{RO}$  is the product of the square root of object and reference beam intensities  $\sqrt{I_R I_O}$ . The photodetector will convert the intensity fluctuation to a current signal for later analog or digital decoding.

Most of the vibrometric systems offer point-wise measurement. And in order to measure vibrations at different points, a scanning system is used to move the measurement point rapidly and precisely on the testing surface [18]. This technique works only when the measurement conditions remain invariant during the sequential detection. Hence, it is only suitable to measure steady-state or well-characterized vibrations. Unfortunately, most engineering applications do not satisfy these requirements. Transients, including impact or coupled vibrations, are commonly observed in real applications.

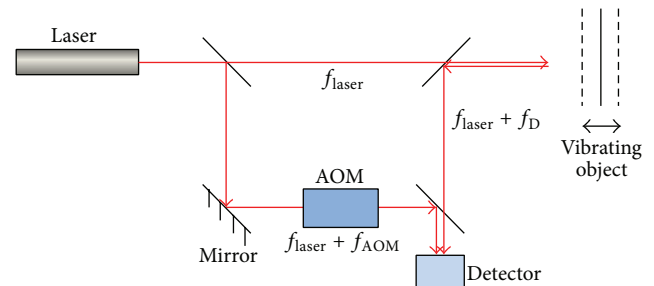


FIGURE 10: Schematic layout of the heterodyne laser Doppler vibrometer.

**3.2. Multipoint Laser Doppler Vibrometer.** In recent years, several types of multichannel and multipoint LDVs have been reported [64, 65]. This novel idea first appeared in a scientific paper where Zheng et al. [66] proposed a multichannel laser vibrometer based on a commercial single-point Polytec vibrometer and an acousto-optic beam multiplexer. It is still a point-wise measurement but with a switch among different channels instead of a scanning mechanism. Now some robust prototypes [67] and even customer-designed commercial products are available [68]. However, these multipoint versions are usually a combination of several sets of single-point vibrometers systems [69], where multiple detectors or detector array is used [70]. Synchronization is still needed among detectors. Recently some simultaneous multipoint measurements [17, 71, 72] using one laser source and one detector have been reported. These techniques use at least two acousto-optic devices to generate various frequency shifts at spatially-separated points and resolve the signals in frequency domain. However, the measurement results only on two or three points were presented, where cross-talk region can be easily identified in the spectrum. When this approach is applied all object beams will interfere with each other and with a common reference beam. Resolving the measurement signals from cross-talk regions is difficult when the number of measurement points is increasing.

A method based on spatial-encoding [73] was presented recently to overcome the abovementioned problems in the

multipoint LDV system and realize a simultaneous vibration measurement on 20 points using one laser source and one single-pixel detector [74]. Twenty laser beams with various frequency shifts were generated by four AOMs at Raman-Nath and Bragg regions. These twenty laser beams were projected onto a vibrating object. The reflected beam array is collected and interferes with a reference beam. The detected interference signal can be expressed by

$$\begin{aligned}
 I = I_{DC} &+ \sum_{i=1}^{20} I_{M(i)} \cos(2\pi(f_{D(i)} + f_{AOM(i)})t + \Delta\phi_{(i)}) \\
 &+ \sum_{m=1}^{19} \sum_{n>m}^{20} I_{mn} \cos(2\pi[(f_{D(m)} - f_{D(n)}) \\
 &\quad + (f_{AOM(m)} - f_{AOM(n)})]t \\
 &\quad + \Delta\phi_{mn}), \tag{6}
 \end{aligned}$$

where  $i$ ,  $m$ , and  $n$  are integers,  $f_{AOM(i)}$  are the central frequencies of twenty object beams. The second term is the interference signal between twenty object beams and reference beam, from which the useful vibration information of twenty points can be extracted. The third term is the sum of the cross-talk between any two object beams, which has to be avoided when the interference signal is decoded. The carrier frequencies of twenty laser beams have to be elaborately designed so that the useful signals can be separated from the cross-talk regions in frequency spectrum or temporal-frequency spectrogram [75]. Several methods were proposed to bypass the effect of cross-talk. Considering the current capability of A-D converter, a half-step frequency shift was proposed. The disadvantage of this technique is that the velocity measurement range is limited due to the cross-talk of the object beams. However, this will not limit the proposed multipoint LDV in normal engineering applications. This method increases the spatial measurement points with the cost of sacrificing the measurement range in the temporal domain.

**3.3. Applications of LDV.** Two applications are presented in this section to show the capability of single-point and multipoint LDV. One is an application of single-point LDV in a scanning near-field optical microscope (SNOM); and the second is a transient event measurement by a four-point LDV.

**3.3.1. Single-Point LDV for Shear-Force Dynamics in the SNOM.** Scanning near-field optical microscopy is a powerful technique having the capability of breaking the diffraction limits by using evanescent waves [76–79]. This is done by conducting a laser beam through a subwavelength fiber probe aperture which is placed in the near-field of the sample surface or conducting a laser beam to illuminate an aperture less probe tip located very close to the sample surface. In a SNOM system, the control of the probe tip at a constant distance away from the sample surface is a critical issue for gaining reliable optical signals. A commonly adopted method

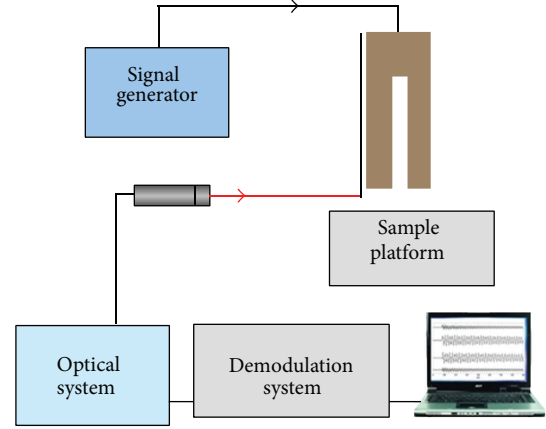


FIGURE 11: Schematic diagram of single-point LDV based tuning fork probe assembled structure.

uses a tuning fork (TF) driven at its resonance, a probe attached to the one prong of the TF, and a lock-in detection synchronized with the excitation frequency to keep the probe tip scanning at a stable height [80, 81]. In our recent work [82], a single-point LDV is introduced to investigate the dynamic mechanical properties of the TF probe assembled structure where the amplitude and the velocity of the probe were measured in real time. Figure 11 is a schematic diagram of our setup. The probe is placed at the focal point of the laser beam. The diameter of the focus spots is small enough ( $8\ \mu\text{m}$ ) compared to the dimension of the probe ( $100\ \mu\text{m}$ ) and therefore ensures the signal strength reflected to the sensing head. Figure 12(a) shows the displacement of the probe tip when excited at 32 kHz and Figure 12(b) shows its frequency spectrum. Figure 12(c) is the frequency-amplitude curve of the probe tip while the TF probe assembled structure is working under sweep operation. The peak at 32.1 kHz is clear which indicates one of the resonance frequencies of the system. Figure 12(d) is the displacement curve while the probe tip approaches a wet surface. When the probe tip touches the water film, the vibration amplitude reduces dramatically.

**3.3.2. Multipoint LDV for Transient Events Measurement.** Based on the spatially encoded technique, a fiber-based prototype of 4-point self-synchronized LDV was developed. The measurement points can be on different surfaces and/or in arbitrary positions. However, the beam array generated by the AOMs is a regular 1D or 2D pattern and this limits the flexibility of the measurement. In this case we can improve the flexibility by using a fiber-based configuration where different frequency shifts are coupled into the fiber. The reflected object beams are combined with one reference beam. Figures 13(a) and 13(b) show the schematic layout of a 4-point LDV system and its optical design. Four sensing heads are connected with the main optical system and focus the laser beams on different points of the object (points A, B, C, and D). A 4-channel demodulation system was connected to the optical system for real-time decoding.

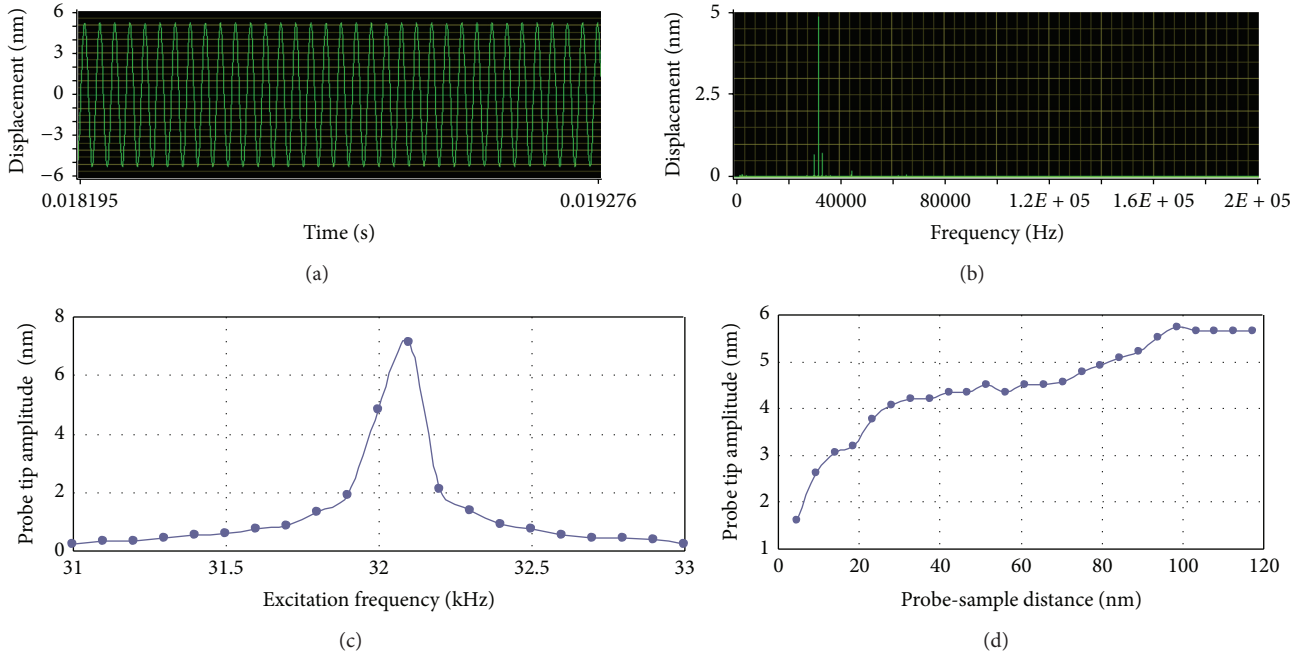


FIGURE 12: (a) Displacement of the probe tip in a few periods when excited at 32 kHz; (b) spectrum of displacement shown in (a); (c) the frequency-amplitude curve of the TF probe assembled structure in the ambient environment; (d) the amplitude of the probe tip approaching a wet sample surface.

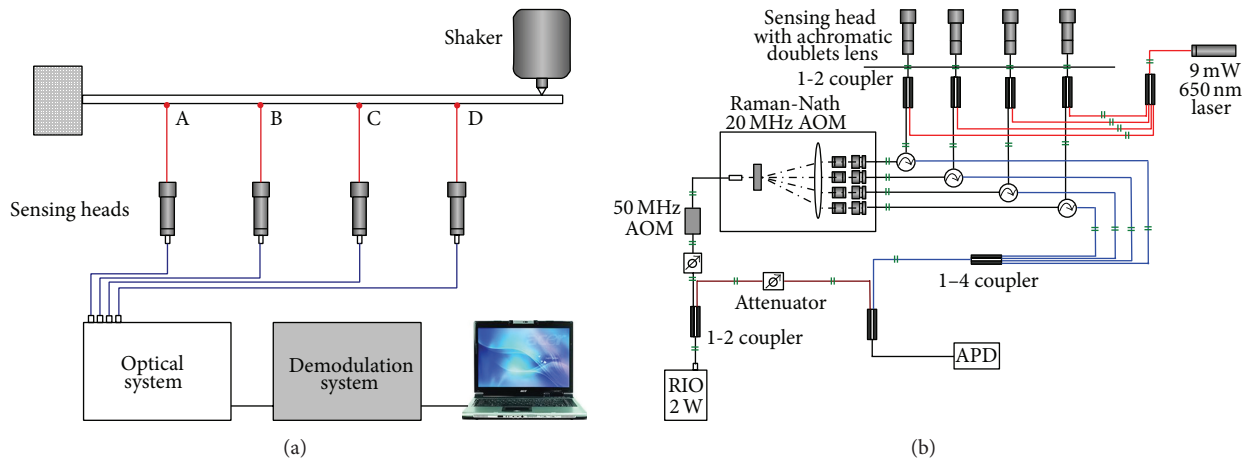


FIGURE 13: Schematic layout of (a) 4-point laser Doppler vibrometer and (b) its optical system.

Figure 14(a) shows the displacement of points A, B, C, and D in the first 0.5 sec after trigger when pendulum hits point E. The absolute values of the displacements are not indicated as the values vary with different hitting forces. Figure 14(b) shows the displacement in the period as indicated in Figure 14(a). The displacements of these four points contain different frequencies. Figure 15 shows the spectrum of the displacement on four measurement points. The spectra are calculated in the range of 0 to 2000 Hz. On points A and D, five peaks at 131.5 Hz, 351.2 Hz, 565.9 Hz, 1253 Hz, and 1813 Hz can be clearly observed, which indicate the first five resonance frequencies of the structure. On points B and C, only two high peaks at 131.5 Hz and 351.2 Hz are observed.

It is worth noting that only one photodetector is used in the prototype and thus synchronization is never an issue; we call it self-synchronizing. This configuration is very useful when the transient response of different points is measured, especially when the propagation of the wave in a structure is studied.

#### 4. Conclusions

Optical dynamic measurement based on interferometry can be classified into camera-based and detector-based techniques. The bottleneck of camera-based methods is in the

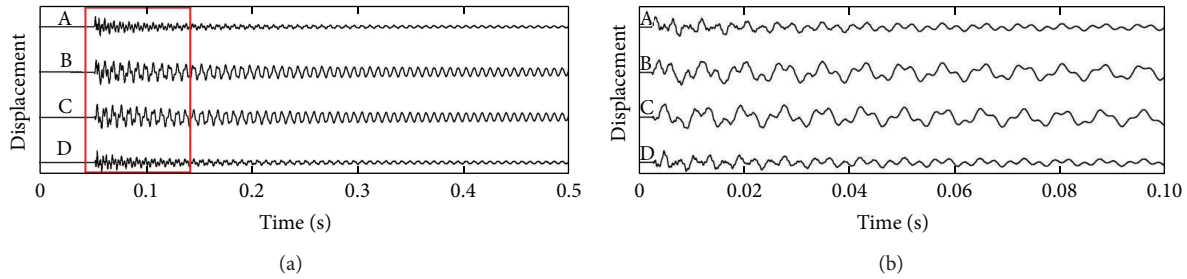


FIGURE 14: (a) Displacement of points A, B, C, and D in the first 0.5 sec after trigger when the excitation is at point E; (b) the displacement of 4 points in period shown in (a).

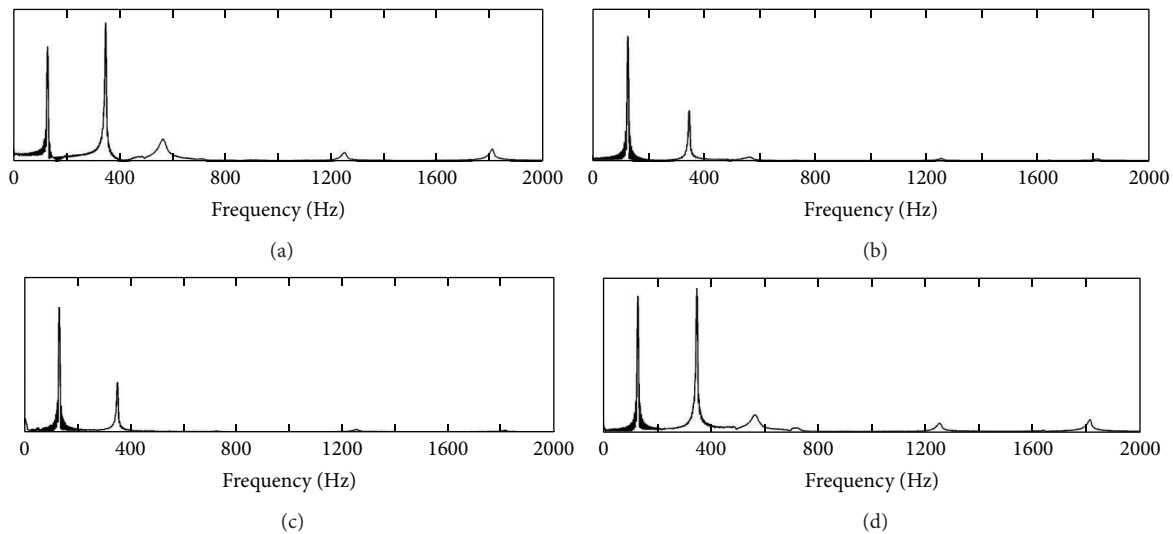


FIGURE 15: Spectrum displacement shown in Figure 14 on points (a) A, (b) B, (c) C, and (d) D.

temporal domain, which is mainly limited by the frame rate of the camera. On the other hand, the limitation of the detector-based techniques is in spatial domain. This paper reviewed the main developments of these two methods in the last ten years. With the current status of the hardware, several technologies were introduced to increase the measurement range and seek the balanced resolution along spatial or temporal axis. The main purpose of the research is to reduce the huge gap in the spatiotemporal domain between these two techniques as shown in Figure 1, so that they can meet the requirements of industrial applications.

### Conflict of Interests

The authors declare that there is no conflict of interests regarding the publication of this paper.

### Acknowledgments

This work is supported by the research Pproject TRF10-MUPLAD, DRTech, MINDEF, Singapore, and by the NSFC (Grant no. 11227202), the National Basic Research Program of China (Grant nos. 2013CB934203 and 2010CB631005), and SRFDP (Grant no. 20130002110043).

### References

- [1] G. L. Cloud, *Optical Methods of Engineering Analysis*, Cambridge University Press, Cambridge, UK, 1995.
- [2] J. W. Dally and W. F. Riley, *Experimental Stress Analysis*, McGraw-Hill, New York, NY, USA, 3rd edition, 1991.
- [3] D. Post, "Moire interferometry," in *Handbook on Experimental Mechanics*, A. Kobayashi, Ed., chapter 7, Prentice Hall, Englewood Cliffs, NJ, USA, 1987.
- [4] R. Jones and C. Wykers, *Holographic and Speckle Interferometry*, Cambridge University Press, Cambridge, UK, 2nd edition, 1989.
- [5] Y. Y. Hung, "Shearography: a new optical method for strain measurement and nondestructive testing," *Optical Engineering*, vol. 21, no. 3, pp. 391–395, 1982.
- [6] U. Schnars and W. Jueptner, *Digital Holography*, Springer, Berlin, Germany, 2005.
- [7] J. C. Wyant, "White Light Interferometry," *Proceedings of SPIE*, vol. 4737, pp. 98–107, 2002.
- [8] M. Takeda, H. Ina, and S. Kobayashi, "Fourier-transform method of fringe-pattern analysis for computer-based topography and interferometry," *Journal of the Optical Society of America*, vol. 72, no. 1, pp. 156–160, 1982.
- [9] K. Creath, "Phase-shifting speckle interferometry," *Applied Optics*, vol. 24, no. 18, pp. 3053–3085, 1985.

- [10] P. Picart, J. Leval, D. Mounier, and S. Gougeon, "Time-averaged digital holography," *Optics Letters*, vol. 28, no. 20, pp. 1900–1902, 2003.
- [11] W. C. Wang, C. H. Hwang, and S. Y. Lin, "Vibration measurement by the time-averaged electronic speckle pattern interferometry methods," *Applied Optics*, vol. 35, no. 22, pp. 4502–4509, 1996.
- [12] S. L. Toh, C. J. Tay, H. M. Shang, and Q. Y. Lin, "Time-average shearography in vibration analysis," *Optics and Laser Technology*, vol. 27, no. 1, pp. 51–55, 1995.
- [13] Y. Y. Hung, C. Y. Liang, J. D. Hovanesian, and A. J. Durelli, "Time-averaged shadow-moiré method for studying vibrations," *Applied Optics*, vol. 16, no. 6, pp. 1717–1719, 1977.
- [14] J. Moore, J. D. Jones, and J. D. Valera, "Dynamic measurements," in *Digital Speckle Pattern Interferometry and Related Techniques*, P. K. Rastogi, Ed., chapter 4, pp. 225–288, Wiley, New York, NY, USA, 2001.
- [15] S. Schedin, G. Pedrini, H. Tizani, A. Aggarwal, and M. Gusev, "Highly sensitive pulsed digital holography for built-in defect analysis with a laser excitation," *Applied Optics*, vol. 40, no. 1, pp. 100–103, 2001, Line 20–22, page 12.
- [16] P. Castellini, M. Martarelli, and E. P. Tomasini, "Laser Doppler Vibrometry: development of advanced solutions answering to technology's needs," *Mechanical Systems and Signal Processing*, vol. 20, no. 6, pp. 1265–1285, 2006.
- [17] E. B. Li, J. Xi, J. F. Chicharo, J. Q. Yao, and D. Y. Yu, "Multi-point laser Doppler velocimeter," *Optics Communications*, vol. 245, no. 1–6, pp. 309–313, 2005.
- [18] J. La, J. Choi, S. Wang, K. Kim, and K. Park, "Continuous scanning laser Doppler vibrometer for mode shape analysis," *Optical Engineering*, vol. 42, no. 3, pp. 730–737, 2003.
- [19] X. C. de Lega and P. Jacquot, "Deformation measurement with object-induced dynamic phase-shifting," *Applied Optics*, vol. 35, no. 25, pp. 5115–5121, 1996.
- [20] J. M. Huntley, G. H. Kaufmann, and D. Kerr, "Phase-shifted dynamic speckle pattern interferometry at 1 KHz," *Applied Optics*, vol. 38, no. 31, pp. 6556–6563, 1999.
- [21] G. H. Kaufmann, "Nondestructive testing with thermal waves using phase-shifted temporal speckle pattern interferometry," *Optical Engineering*, vol. 42, no. 7, pp. 2010–2014, 2003.
- [22] J. M. Huntley and H. Saldner, "Temporal phase-unwrapping algorithm for automated interferogram analysis," *Applied Optics*, vol. 32, no. 17, pp. 3047–3052, 1993.
- [23] C. Kao, G. Yeh, S. Lee, C. Lee, C. Yang, and K. Wu, "Phase-shifting algorithms for electronic speckle pattern interferometry," *Applied Optics*, vol. 41, no. 1, pp. 46–54, 2002.
- [24] A. Davila, J. M. Huntley, G. H. Kaufmann, and D. Kerr, "High-speed dynamic speckle interferometry: phase errors due to intensity, velocity, and speckle decorrelation," *Applied Optics*, vol. 44, no. 19, pp. 3954–3962, 2005.
- [25] M. Kujawinska, "Spatial phase measurement methods," in *Interferogram Analysis*, D. W. Robinson and G. T. Reid, Eds., pp. 141–193, Institute of Physics Publishing, Bristol, UK, 1993.
- [26] A. J. P. van Haasteren and H. J. Frankena, "Real-time displacement measurement using a multicamera phase-stepping speckle interferometer," *Applied Optics*, vol. 33, no. 19, pp. 4137–4142, 1994.
- [27] Q. Kemao, M. Hong, and W. Xiaoping, "Real-time polarization phase shifting technique for dynamic deformation measurement," *Optics and Lasers in Engineering*, vol. 31, no. 4, pp. 289–295, 1999.
- [28] J. Millerd, N. Brock, J. Hayes, M. N. Morris, M. Novak, and J. Wyant, "Pixelated phase-mask dynamic interferometer," *Proceedings of SPIE*, vol. 5531, pp. 304–314, 2004.
- [29] M. N. Morris, J. Millerd, N. Brock, J. Hayes, and B. Saif, "Dynamic phase-shifting electronic speckle pattern interferometry," *Proceedings of SPIE*, vol. 5869, Article ID 58691B, 2005.
- [30] P. S. Huang, Q. Hu, F. Jin, and F. Chiang, "Color-encoded digital fringe projection technique for high-speed three-dimensional surface contouring," *Optical Engineering*, vol. 38, no. 6, pp. 1065–1071, 1999.
- [31] S. L. Hahn, *Hilbert Transforms in Signal Processing*, Artech House, Boston, Mass, USA, 1996.
- [32] Q. Kemao, "Two-dimensional windowed Fourier transform for fringe pattern analysis: principles, applications and implementations," *Optics and Lasers in Engineering*, vol. 45, no. 2, pp. 304–317, 2007.
- [33] J. Zhong and J. Weng, "Spatial carrier-fringe pattern analysis by means of wavelet transform: wavelet transform profilometry," *Applied Optics*, vol. 43, no. 26, pp. 4993–4998, 2004.
- [34] Y. Fu, R. M. Groves, G. Pedrini, and W. Osten, "Kinematic and deformation parameter measurement by spatiotemporal analysis of an interferogram sequence," *Applied Optics*, vol. 46, no. 36, pp. 8645–8655, 2007.
- [35] M. Kujawinska, "Automated moiré interferometry for local and global analysis of transient phenomena," *Advances in Electronic Packaging*, vol. 10-2, pp. 1179–1185, 1995.
- [36] G. Joenathan, B. Franze, P. Haible, and H. J. Tiziani, "Speckle interferometry with temporal phase evaluation for measuring large-object deformation," *Applied Optics*, vol. 37, no. 13, pp. 2608–2614, 1998.
- [37] C. Joenathan, B. Franze, P. Haible, and H. J. Tiziani, "Large in-plane displacement measurement in dual-beam speckle interferometry using temporal phase measurement," *Journal of Modern Optics*, vol. 45, no. 9, pp. 1975–1984, 1998.
- [38] C. Joenathan, B. Franze, P. Haible, and H. J. Tiziani, "Novel temporal Fourier transform speckle pattern shearing interferometer," *Optical Engineering*, vol. 37, no. 6, pp. 1790–1795, 1998.
- [39] C. Joenathan, B. Franze, P. Haible, and H. J. Tiziani, "Shape measurement by use of temporal Fourier transformation in dual-beam illumination speckle interferometry," *Applied Optics*, vol. 37, no. 16, pp. 3385–3390, 1998.
- [40] C. Joenathan, P. Haible, and H. J. Tiziani, "Speckle interferometry with temporal phase evaluation: influence of decorrelation, speckle size, and nonlinearity of the camera," *Applied Optics*, vol. 38, no. 7, pp. 1169–1178, 1999.
- [41] G. H. Kaufmann and G. E. Galizzi, "Phase measurement in temporal speckle pattern interferometry: comparison between the phase-shifting and the Fourier transform methods," *Applied Optics*, vol. 41, no. 34, pp. 7254–7263, 2002.
- [42] X. C. de Lega, *Processing of nonstationary interference patterns: adapted phase-shifting algorithms and wavelet analysis. Application to dynamic deformation measurement by holographic and speckle interferometry [Ph.D. thesis]*, Swiss Federal Institute of Technology of Lausanne, Lausanne, Switzerland, 1997.
- [43] Y. Fu, C. J. Tay, C. Quan, and L. J. Chen, "Temporal wavelet analysis for deformation and velocity measurement in speckle interferometry," *Optical Engineering*, vol. 43, no. 11, pp. 2780–2787, 2004.
- [44] Y. Fu, C. J. Tay, C. Quan, and H. Miao, "Wavelet analysis of speckle patterns with a temporal carrier," *Applied Optics*, vol. 44, no. 6, pp. 959–965, 2005.

- [45] A. Federico and G. H. Kaufmann, "Robust phase recovery in temporal speckle pattern interferometry using a 3D directional wavelet transform," *Optics Letters*, vol. 34, no. 15, pp. 2336–2338, 2009.
- [46] R. G. Stockwell, L. Mansinha, and R. P. Lowe, "Localization of the complex spectrum: the S transform," *IEEE Transactions on Signal Processing*, vol. 44, no. 4, pp. 998–1001, 1996.
- [47] P. D. Ruiz, J. M. Huntley, and G. H. Kaufmann, "Adaptive phase-shifting algorithm for temporal phase evaluation," *Journal of the Optical Society of America A: Optics and Image Science, and Vision*, vol. 20, no. 2, pp. 325–332, 2003.
- [48] K. Qian, Y. Fu, Q. Liu, H. S. Seah, and A. Asundi, "Generalized three-dimensional windowed Fourier transform for fringe analysis," *Optics Letters*, vol. 31, no. 14, pp. 2121–2123, 2006.
- [49] Y. Fu, G. Pedrini, and W. Osten, "Vibration measurement by temporal Fourier analyses of a digital hologram sequence," *Applied Optics*, vol. 46, no. 23, pp. 5719–5727, 2007.
- [50] X. Li, G. Tao, and Y. Yang, "Continual deformation analysis with scanning phase method and time sequence phase method in temporal speckle pattern interferometry," *Optics and Laser Technology*, vol. 33, no. 1, pp. 53–59, 2001.
- [51] X. Li, A. K. Soh, B. Deng, and X. Guo, "High-precision large deflection measurements of thin films using time sequence speckle pattern interferometry," *Measurement Science and Technology*, vol. 13, no. 8, pp. 1304–1310, 2002.
- [52] X. Li, K. Wang, and B. Deng, "Matched correlation sequence analysis in temporal speckle pattern interferometry," *Optics and Laser Technology*, vol. 36, no. 4, pp. 315–322, 2004.
- [53] M. Servin, J. Estrada, and A. Quiroga, "Single-image interferogram demodulation," in *Advanced in Speckle Metrology and Related Techniques*, G. H. Kaufmann, Ed., pp. 105–146, Wiley-VCH, Weinheim, Germany, 2011.
- [54] K. Li and B. Pan, "Frequency-guided windowed fourier ridges technique for automatic demodulation of a single closed fringe pattern," *Applied Optics*, vol. 49, no. 1, pp. 56–60, 2010.
- [55] O. S. Dalmau-Cedeño, M. Rivera, and R. Legarda-Saenz, "Fast phase recovery from a single closed-fringe pattern," *Journal of the Optical Society of America A: Optics and Image Science, and Vision*, vol. 25, no. 6, pp. 1361–1370, 2008.
- [56] H. Wang and Q. Kema, "Frequency guided methods for demodulation of a single fringe pattern," *Optics Express*, vol. 17, no. 17, pp. 15118–15127, 2009.
- [57] Q. Kema and L. Kai, "Fast frequency-guided sequential demodulation of a single fringe pattern," *Optics Letters*, vol. 35, no. 22, pp. 3718–3720, 2010.
- [58] Y. Fu, M. Guo, and H. Liu, "Determination of instantaneous curvature and twist by digital shearography," *Optical Engineering*, vol. 51, no. 8, Article ID 083602, 2012.
- [59] F. Yu, S. Hongjian, and M. Hong, "Vibration measurement of a miniature component by high-speed image-plane digital holographic microscopy," *Applied Optics*, vol. 48, no. 11, pp. 1990–1997, 2009.
- [60] K. Creath, "Step height measurement using two-wavelength phase-shifting interferometry," *Applied Optics*, vol. 26, no. 14, pp. 2810–2816, 1987.
- [61] M. Ohlidal, L. Sir, M. Jakl, and I. Ohlidal, "Digital two-wavelength holographic interference microscopy for surface roughness measurement," *Proceedings of SPIE*, 2005.
- [62] Y. Fu, G. Pedrini, B. M. Hennelly, R. M. Groves, and W. Osten, "Dual-wavelength image-plane digital holography for dynamic measurement," *Optics and Lasers in Engineering*, vol. 47, no. 5, pp. 552–557, 2009.
- [63] G. Cloud, "Optical methods in experimental mechanics: part 17: laser doppler interferometry," *Experimental Techniques*, vol. 29, no. 3, pp. 27–30, 2005.
- [64] J. J. Dirckx, H. J. van Elburg, W. F. Decraemer, J. A. N. Buytaert, and J. A. Melkebeek, "Performance and testing of a four channel high-resolution heterodyne interferometer," *Optics and Lasers in Engineering*, vol. 47, no. 3-4, pp. 488–494, 2009.
- [65] A. Waz, P. R. Kaczmarek, M. P. Nikodem, and K. M. Abramski, "WDM optocommunication technology used for multipoint fibre vibrometry," *Proceedings of SPIE*, vol. 7098, Article ID 70980E, 2008.
- [66] W. Zheng, R. V. Kruzelecky, and R. Changkakoti, "Multi-channel laser vibrometer and its applications," *Proceedings of SPIE*, vol. 3411, pp. 376–384, 1998.
- [67] R. Burgett, V. Aranchuk, J. Sabatier, and S. S. Bishop, "Demultiplexing multiple beam laser Doppler vibrometry for continuous scanning," *Proceedings of SPIE*, vol. 7303, Article ID 730301, 2009.
- [68] J. M. Kilpatrick and V. Markov, "Matrix laser vibrometer for transient modal imaging and rapid non-destructive testing," *Proceedings of SPIE*, vol. 7098, Article ID 709809, 2008.
- [69] R. Di Sante and L. Scalise, "A novel fiber optic sensor for multiple and simultaneous measurement of vibration velocity," *Review of Scientific Instruments*, vol. 75, no. 6, pp. 1952–1958, 2004.
- [70] K. Maru, K. Kobayashi, and Y. Fujii, "Multi-point differential laser doppler velocimeter using arrayed waveguide gratings with small wavelength sensitivity," *Optics Express*, vol. 18, no. 1, pp. 301–308, 2010.
- [71] T. Pfister, L. Büttner, K. Shirai, and J. Czarske, "Monochromatic heterodyne fiber-optic profile sensor for spatially resolved velocity measurements with frequency division multiplexing," *Applied Optics*, vol. 44, no. 13, pp. 2501–2510, 2005.
- [72] D. Garcia-Vizcaino, F. Dios, J. Reolons, A. Rodríguez, and A. Comeron, "One-wavelength two-component laser Doppler velocimeter system for surface displacement monitoring," *Optical Engineering*, vol. 47, no. 12, Article ID 123606, 2008.
- [73] Y. Fu, M. Guo, and P. B. Phua, "Spatially encoded multibeam laser Doppler vibrometry using a single photodetector," *Optics Letters*, vol. 35, no. 9, pp. 1356–1358, 2010.
- [74] Y. Fu, M. Guo, and P. B. Phua, "Multipoint laser Doppler vibrometry with single detector: principles, implementations, and signal analyses," *Applied Optics*, vol. 50, no. 10, pp. 1280–1288, 2011.
- [75] Y. Fu, M. Guo, and P. B. Phua, "Cross-talk prevention in optical dynamic measurement," *Optics and Lasers in Engineering*, vol. 50, no. 4, pp. 547–555, 2012.
- [76] E. H. Synge, "A suggested method for extending microscopic resolution into the ultra-microscopic region," *The London, Edinburgh, and Dublin Philosophical Magazine and Journal of Science*, vol. 6, pp. 356–362, 1928.
- [77] E. A. Ash and G. Nicholls, "Super-resolution aperture scanning microscope," *Nature*, vol. 237, no. 5357, pp. 510–512, 1972.
- [78] D. W. Pohl, W. Denk, and M. Lanz, "Optical stethoscopy: image recording with resolution  $\lambda/20$ ," *Applied Physics Letters*, vol. 44, no. 7, pp. 651–653, 1984.
- [79] A. Lewis, M. Isaacson, A. Harootunian, and A. Muray, "Development of a 500 Å spatial resolution light microscope. I. Light is efficiently transmitted through  $\lambda/16$  diameter apertures," *Ultramicroscopy*, vol. 13, no. 3, pp. 227–231, 1984.

- [80] B. Hecht, B. Sick, U. P. Wild et al., "Scanning near-field optical microscopy with aperture probes: fundamentals and applications," *Journal of Chemical Physics*, vol. 112, no. 18, pp. 7761–7774, 2000.
- [81] K. Karrai and R. D. Grober, "Piezoelectric tip-sample distance control for near field optical microscopes," *Applied Physics Letters*, vol. 66, pp. 1842–1844, 1995.
- [82] F. Gao, X. Li, J. Wang, and Y. Fu, "Dynamic behavior of tuning fork shear-force structures in a SNOM system," *Ultra-microscopy*, vol. 142, pp. 10–23, 2014.

## Research Article

# Interfacial Micromechanics in Fibrous Composites: Design, Evaluation, and Models

Zhenkun Lei,<sup>1</sup> Xuan Li,<sup>1</sup> Fuyong Qin,<sup>1</sup> and Wei Qiu<sup>2</sup>

<sup>1</sup> State Key Laboratory of Structural Analysis for Industrial Equipment, Dalian University of Technology, Dalian 116024, China

<sup>2</sup> Department of Mechanics, Tianjin University, Tianjin 300072, China

Correspondence should be addressed to Zhenkun Lei; [leizk@163.com](mailto:leizk@163.com)

Received 31 October 2013; Accepted 23 January 2014; Published 7 April 2014

Academic Editors: Y. Fu and G. Pedrini

Copyright © 2014 Zhenkun Lei et al. This is an open access article distributed under the Creative Commons Attribution License, which permits unrestricted use, distribution, and reproduction in any medium, provided the original work is properly cited.

Recent advances of interfacial micromechanics in fiber reinforced composites using micro-Raman spectroscopy are given. The faced mechanical problems for interface design in fibrous composites are elaborated from three optimization ways: material, interface, and computation. Some reasons are depicted that the interfacial evaluation methods are difficult to guarantee the integrity, repeatability, and consistency. Micro-Raman study on the fiber interface failure behavior and the main interface mechanical problems in fibrous composites are summarized, including interfacial stress transfer, strength criterion of interface debonding and failure, fiber bridging, frictional slip, slip transition, and friction reloading. The theoretical models of above interface mechanical problems are given.

## 1. Introduction

Polymer-matrix fibrous composites have been widely used in the aerospace and industrial locomotives fields. There exist many interfacial phenomena and all kinds of defects including inclusions, pores, and layer shrink zones in fibrous composites during design and manufacturing processes. Fiber fracture and interface debonding will appear inside the material in service and result in early fatigue, aging, damage, and failure, so it is a hidden danger to risk a major engineering accident. With development of composite material science and aerospace industry applications, the light-weight and high-tough carbon fibers have been widely applied to fibrous composites. Therefore, many researchers coming from physics, chemistry, materials, mechanics, and engineering are attracted by many basic mechanical problems in fibrous composites, such as mechanical properties characterization of high-performance fiber, fiber/matrix interface debonding, fiber bridging, fiber fracture, and matrix cracking [1].

Besides the effects of fiber surface treatments on fibrous composites have been studied; the basic problems of microscopic interfacial stress transfer and failure were focused in decades [2, 3]. Materials' microstructure configuration determines its response to external action. As a connection

between reinforcing fiber and matrix, the interface is an important microstructure of fibrous composites including fiber, fiber transition region, fiber surface coating, matrix transition region, and matrix. The interface is a bridge connecting both reinforced fiber and matrix and a deliverer of mechanics information. Although the interface is much smaller than the size of composite bulk, there are many mechanical problems on the interface, such as load transfer, shear strength, interface debonding, damage, and stress singularity [4, 5]. Interfacial bonding quality directly affects the entire composites on interlaminar shear, fracture, impact, heat aging, wave propagation, and other mechanical properties. Therefore, it is necessary to study on fiber interface mechanics from a microscopic view by examining and analyzing the linkages among microstructure, interfacial mechanics properties, and macrofracture properties. The establishment and improvement of interfacial stress transfer and failure models will help to understand the composite stress transfer, debonding, and failure mechanisms from microscale experiments.

With unique advantages of nondestructive, noncontact, and high spatial resolution ( $1\mu\text{m}$ ), micro-Raman spectroscopy (MRS) is most likely applied to the integrity characterization of interfacial micromechanical properties

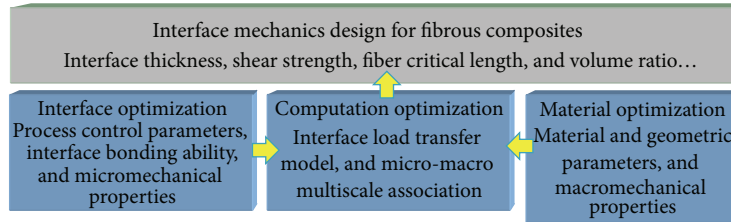


FIGURE 1: Interface design routes for fiber composites.

in fibrous composites [6], porous silicon [7–9], and carbon nanotubes [10, 11]. In the process of interface debonding of fibrous composites, the evolution of interface mechanical parameters including the frictional shear stress, interfacial shear stress, and debonding length happened in real time, while the pulling force and displacement are also changed accordingly. At present, the main mechanical problems on fiber/matrix interface include the stress transfer, interfacial strength criterion, fiber bridging, and other aspects in fibrous composites.

Based on the outline of interface mechanics design, interface evaluation method, and fine characterization techniques of fibrous composites, the research progress on the interface mechanics by MRS is introduced in the paper, including the interfacial stress transfer, interfacial debonding and strength failure criterion, fiber bridging, interface friction, and slip transition. At last, some theoretical models on those interface mechanics problems are summed up.

## 2. Interface Mechanics Design

The mechanical properties of fibrous composites are closely related to the interface control process, material compound, material properties, and interfacial failure modes, so these are very important for the interface mechanics design and optimization of fibrous composites. However, there is no effective criterion yet to optimize the performance of interface mechanics. Based on the existing interface mechanics models and numerical analysis works, it is possible to get the interfacial mechanical parameters and material parameters having no interface failure and to give the reference of the process controls and material options for the optimization of interface mechanical properties [12, 13].

The design of interface mechanics in fibrous composites should consider the process technology, materials and environment, and other complex factors. It mainly consists of three optimization approaches: material optimization, interface optimization, and computation optimization, as shown in Figure 1. The former two approaches control the macro- and micromechanical properties of fibrous composite, respectively. Meanwhile, they are helpful to study the interfacial load transfer and failure models for different scales and to provide the theoretical and experimental basis for the interface mechanics design of fibrous composites. The third approach is utilizing the multiscale computation to associate the macro- and micromechanical models and to predict the ultimate bearing performance of the designed

fibrous composites through optimizing material constituents and fiber laying configurations.

**2.1. Material Optimization.** The selection and optimum combination of materials is the most commonly used method for the interface design of fibrous composites. Through choosing fiber and matrix resin having specific properties, the composite laminates are formed by curing according to a certain volume ratio and fiber laying manner. Thus, the loading capacity of fibrous composites can be improved by means of the excellent mechanical properties of fibers. Typically, the macroscopic mechanical tests are used to characterize the interfacial properties of fibrous composites. There are a lot of works to get the interfacial shear strength and other interface parameters, such as the fiber critical length obtained by single fiber fragmentation test and the relationship between fiber pullout force and displacement by single fiber pullout test [17, 18].

The interface mechanical parameters obtained by the macroscopic mechanical tests are the average results for characterizing the macroscopic performance of interface bonding capability. However, it is difficult to get the fine stress distribution along the fiber/matrix interface and to observe the interfacial debonding and failure processes. Therefore, the development of microscale measurement methods is necessary [19]. In addition, there are still more researches on the mechanical testing of fiber and resin matrix itself, including tensile or compressive stress-strain behaviors of single fiber and fiber bundle, the impact of fiber surface treatment on the interface shear strength, the resin curing behavior, and wetting behavior between fiber and resin. The impact of these factors on the fiber/matrix interface physicochemical properties and geometric characteristics still needs further study.

**2.2. Interface Optimization.** Nowadays, it has been recognized that the way of traditional compound optimization is insufficient to improve the whole mechanical properties of fibrous composites and then the researchers turned to the interface bonding ability to improve the mechanical properties of fibrous composites. Due to different mechanical properties, compound process, and geometric conditions on the fiber/resin interface, there are thermal, mechanical, chemical, and physical coupling effects existing on the interface. Resultantly, different interfacial structures and characteristics appear and affect the fiber/resin interface bonding capacity, and then the fibrous composites exhibit different macrophysicochemical and mechanical properties [20].

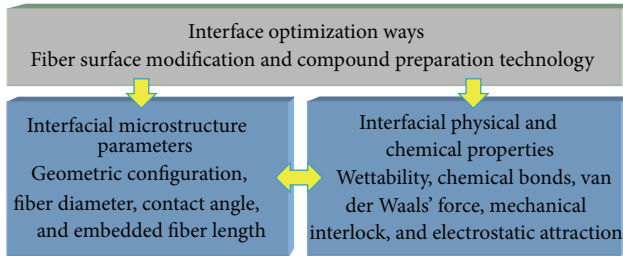


FIGURE 2: Interface optimization ways.

As shown in Figure 2, the interface control means for fibrous composites are mostly through the fiber surface modification and compound process to obtain specific fiber/matrix interface microstructure, such as the geometric configurations, contact angle, and embedded fiber length. The specific interface microstructure will exhibit different physical and chemical properties, such as wettability, chemical bond, and van der Waals force; thus the interface bond strength is changed to improve the performance of interfacial load transfer. At present, the fiber surface modification can be used to get appropriately bonded interface, but the physicochemical mechanisms that are how to affect the interfacial micromechanical properties as well as how to control the interfacial stress transfer have been concerned. Although a variety of interface theories in fibrous composites have been proposed, such as wettability theory, chemical bond theory, and friction theory, there is no perfect theory to explain all phenomena of interface [2].

**2.3. Computation Optimization.** If the interface strength of fibrous composites is too low, the fiber is easy to debond, pullout, break, and fail. On the contrary, if the interface strength is very high, the stress between the fiber and matrix cannot be relaxed and the brittle fracture would occur at the interface. Therefore, the interface design can be optimized by considering the best comprehensive mechanical properties. The interfacial mechanical properties and geometrical parameters are regarded as design variables, and then certain optimization method such as genetic algorithm combines with the finite element analysis to find the best design variables. This is the fast optimization path of interface mechanical performance in fibrous composites.

However, the design variables of composite interface microstructure are not continuous so that the derivative-type optimization method will fail in the case. It is also noted that the uncertainty of initial value limits the capacity of optimization method converging to the global optimum. In addition, the existing mechanical models are imperfect to describe the micromechanical behavior of the composite interface. The mechanical properties of interface layer, residual stress, and stress singularity are the difficulties to constrain the numerical computation [12, 13]. At present, a lot of works are still to seek the appropriate computing optimization methods to solve such problems. It is inevitable and reasonable way for the computation optimization to perfectly combine with

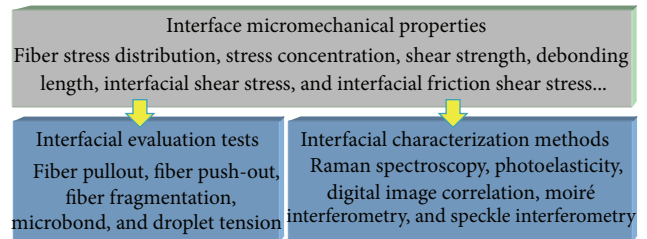


FIGURE 3: Evaluation tests and characterization methods for micromechanical properties of interface.

the interface evaluation tests, fine interface characterization techniques, and interface mechanical models.

### 3. Interface Evaluation and Characterization

**3.1. Interface Evaluation Tests.** The macroscopic damage and failure criteria for fibrous composites do not consider the micromechanical properties of interface, such as fiber stress distribution, stress concentration, shear strength, and frictional shear stress on the debonding interface. In addition, there is still lack of a common understanding about the influence of interfacial microstructural parameters and physicochemical properties on the interface micromechanical properties. Currently, the research on microscale experimental mechanics characterization of the interface failure is not only the most difficult and crucial problem but also the important content of interface mechanical evaluation in fibrous composites, as shown in Figure 3.

The interfacial shear strength is a commonly used parameter to evaluate interfacial bonding quality, fiber/matrix stress transfer efficiency, and the effect of fiber surface modification. The important parameter can be obtained by single fiber micromechanical testing experiments. One kind of these experiments is realized by applying the external load to single fiber, such as fiber pullout test [15], microbond test [21], microdroplet tension test [14, 22], and fiber push-out test [23]. The other is finished by applying the external load to the resin matrix, such as fiber fragmentation test [12, 13] and Broutman test [24].

During the implementation and application of these interface evaluation tests for the characterization of micromechanical properties, it is difficult to ensure the integrity, repeatability, and consistency of the interface evaluation. The experimental results of fiber pullout test, fiber fragmentation test, and fiber push-out test vary widely at the same external conditions. Even using the same test method, the experimental results among different laboratories still have differences [25]. Further studies suggest that this difference comes from the stress singularity at the fiber end [26], so the reevaluation of these test methods and the development of new, more appropriate test methods are concerned [27].

However, the deeper reason is that the differences of many conditions (i.e., interface characteristics) in these interface evaluation tests are neglected, such as interface structure, geometric shape and dimension, and boundary and surface treatment. The testing specimens employed in the

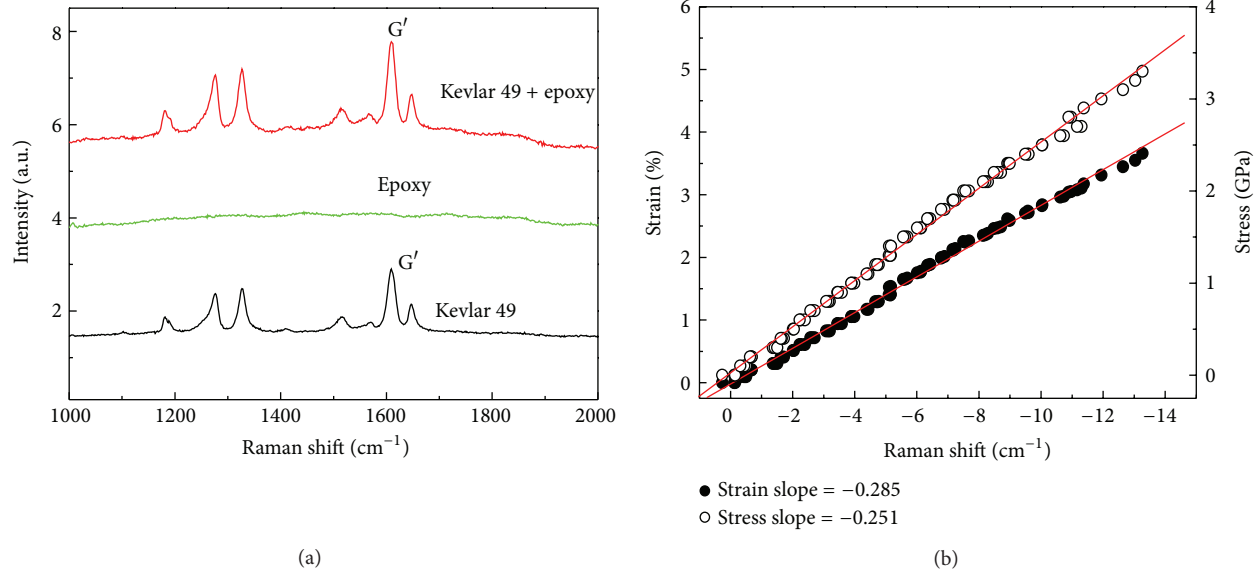


FIGURE 4: Raman spectra of (a) fiber/epoxy droplet specimen compared with pure epoxy and Kevlar 49 fiber [14] and (b) relationships of Raman shift with stress and strain for Kevlar 49 fiber [15].

different interface evaluation methods have different geometric parameters, such as the droplet contact angle and the embedded fiber length in the microdroplets tension test. Even with the same specimen preparation procedure, it is difficult to ensure that all samples have a uniform geometry and dimension size, which affects the repeatability and consistency of the interface micromechanical parameters characterized by the interface evaluation test. The latest research of microdroplet tension test shows that the microdroplet conformations with different contact angles affect the interfacial shear stress distribution and stress transfer efficiency [28]. By optimizing the design of interface geometry to reduce or even eliminate the stress singularity, the mechanical behavior of fibrous composites can be upgraded [29]. Therefore, the further research on the interface geometry and physicochemical properties affecting the interfacial stress transfer behavior will benefit to optimize the interfacial stress distribution and reduce the stress concentrations.

**3.2. Fine Characterization Techniques.** Commonly, the interfacial shear strength obtained by the interface evaluation tests is used as an important characteristic parameter in the interface failure models and is an average value for characterizing the interface bonding properties. It cannot completely describe the details of the interfacial stress transfer and interfacial debonding failure processes. Therefore, more sophisticated real-time experimental data are required to quantitatively and completely characterize the micromechanical behaviors of the fiber/matrix interface [30]. The direct requirement is the use of “partial details” (i.e., stress distribution) of the interface parameters instead of the average. In addition, the respective contributions of the bonding shear stress and frictional shear stress to the interfacial shear failure mechanisms are also concerned in the fiber/matrix debonding procedure. However, most studies are lacking in

the integrity of mechanical description for the procedures of the interfacial stress transfer and interfacial debonding failure. A very important reason is the lack of suitable microscale stress-strain measurement techniques and full-field observation means.

The testing methods having the ability to carry out the microscale fine characterization, including MRS and digital photoelasticity, digital image correlation, and speckle interferometry. These methods are most likely the first application to completely characterize the micromechanical properties of fiber reinforced composites. MRS measurements have unique advantages at the microscales: nondestructive, noncontact, high spatial resolution (1  $\mu\text{m}$ ), and the depth focus [6].

When the fiber is under deformation, it causes the movement and deformation of Raman spectrum [14, 15], as shown in Figure 4(a). Although the epoxy resin has a strong fluorescence effect, the Raman spectrum of fiber/epoxy specimen after fully curing shows a Raman spectrum overlay of fiber and epoxy resin, but this does not affect the identification of the fiber Raman peak. Raman shift has a linear relationship with the strain or stress of aramid fibers [15], as shown in Figure 4(b). Therefore, it is a potential method of microscale experimental mechanics, and it has recently been used to study the interfacial micromechanical behaviors in fibrous composites, such as fiber stress distribution, stress concentration, and interface integrity.

## 4. Interface Mechanics Modeling

The interfacial stress transfer behavior between the fiber and matrix in fibrous composites is a major mechanical problem including several successive stages: the interface intact bonding, interface debonding, interface completely debonding, and fiber pullout. The elastic stress transfer in bonding area and the frictional shear stress transfer in debonded area

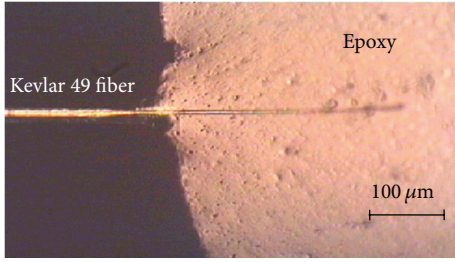


FIGURE 5: Single fiber pullout specimen [15].

have been widely recognized. In the process of interfacial debonding and extension, the interface mechanical parameters of bonding shear stress, debonding friction shear stress, and interface debonding length continuously evolve, and the macropulling force or stress is also changed accordingly. At present, the main interface mechanics problems in fibrous composites discussed are as follows: the elastic stress transfer, partial debonding stress transfer, interface failure criterion and fiber bridging, and so on.

**4.1. Elastic Stress Transfer and Failure.** One end of single fiber embeds in epoxy matrix, as shown in Figure 5, an axis tension load pulls the fiber out from the matrix. Under the assumptions of the stress uniform distribution and homogeneous isotropy, the interfacial shear strength  $\tau_b$  can be calculated by the ratio of maximum pullout load  $F_{max}$  and interface bonding area; namely,

$$\tau_b = \frac{F_{max}}{2\pi r l}, \quad (1)$$

where  $r$  and  $l$  are the fiber radius and the embedded fiber length, respectively.

The stress distribution along the embedded fiber cannot be obtained by the above equation, so it cannot be used to study the stress transfer between the fiber and matrix. Cox's shear-lag model [31] considers the force balance between the fiber axial stress  $\sigma$  and the interfacial shear stress  $\tau$  along the embedded fiber. It satisfies the relationship as

$$\tau = -\frac{r}{2} \left( \frac{d\sigma}{dx} \right). \quad (2)$$

Piggott's model [32] is further used to describe the fiber axial stress along the embedded fiber within the elastic stress transfer, so the fiber elastic stress distribution before the interface debonding is written as

$$\sigma = \sigma_{app} \frac{\sinh [n(L-x)/r]}{\sinh (ns)}, \quad (3)$$

where  $x$  is the distance to fiber entry,  $\sigma_{app}$  is the stress acting on the fiber out of the matrix,  $L$  is the fiber length that the fiber axial stress decays to zero (i.e., the effective length of stress transfer),  $s$  is the fiber aspect ratio ( $L/r$ ), and  $n$  is a constant related with the geometry, material parameters of fiber, and matrix [33].

Figure 6(a) shows the fiber axial stress distribution under different strain levels in fiber pullout test. It can be seen that

the fiber axial stress increased significantly with the applied strain and the constant fiber axial stress out of the matrix ( $x \leq 0$ ) equal to the applied load; that is,  $\sigma = \sigma_{app}$ . Then, the fiber axial stress along the embedded fiber was gradually reduced from the fiber entry ( $x = 0$ ) to the embedded fiber end ( $x = L$ ) in accordance with the theoretical results (solid line) of (3). In the current 1.2% strain level, the debonding phenomenon did not occur at the embedded fiber and the entire embedded fiber was under a certain load, so the intact elastic stress transfer was presented on the fiber/matrix bonding interface.

The interfacial shear stress (ISS) along the embedded fiber is further given from (2) and (3) as

$$\tau = \sigma_{app} \frac{n \cosh [n(L-x)/r]}{2 \sinh (ns)}. \quad (4)$$

As shown in Figure 6(b), the ISS distribution increased with the strain levels. The ISS of fiber out of the matrix was zero and reached the maximum at the fiber entry.

In the fiber pullout experiment, the aspect ratio  $n$  of the embedded fiber is large. The fiber stress and shear stress at the fiber entry ( $x = 0$ ) are given by the combination of (3) and (4) as

$$\sigma_m = \sigma, \quad \tau_m = \frac{n}{2} \sigma. \quad (5)$$

If the applied strain continues, the fiber fracture failure occurs when the fiber stress  $\sigma$  on the free fiber segment is over the fiber stress strength  $\sigma_b$ . Similarly, the interfacial debonding failure occurs when the maximum ISS of  $\tau_m$  at the fiber entry exceeds the shear strength  $\tau_b$ . Then, the strength failure conditions depending on the balance of fiber strength  $\sigma_b$  and interfacial shear strength  $\tau_b$  are written as

$$\begin{aligned} \sigma = \frac{2\tau_m}{n} \geq \sigma_b, & \quad \text{Fiber fracture,} \\ \tau_m = \frac{n\sigma}{2} \geq \tau_b, & \quad \text{Interface debond.} \end{aligned} \quad (6)$$

It can be seen that the fiber/matrix interface is more likely to fail if the fiber strength  $\sigma_b$  increases, and the fiber tends to break if the interface shear strength  $\tau_b$  increases.

**4.2. Frictional Shear Stress Transfer.** When the applied load further increased in the fiber pullout test (Figure 5), the interface debonding failure occurred firstly at the fiber entry and then propagated along the fiber/matrix interface. The fiber axial stress distribution in Figure 7(a) shows that the fiber has debonded from the fiber entry (Point O) to the debonding/bonding transition (Point B), and the interface frictional shear stress existed on the different stages (Figure 7(b)). This is because the debonding segments of OA and AB exhibit different interface microstructures resulting in unequal shear friction effect. The interface frictional shear stress accords with the linear distribution assumption on the debonding segments (the solid lines in Figure 7(a)). After the debonding/bonding transition (Point B), the fiber bonding interface is still intact and the fiber axial stress distribution satisfies with the Piggott's model (Segment BC).

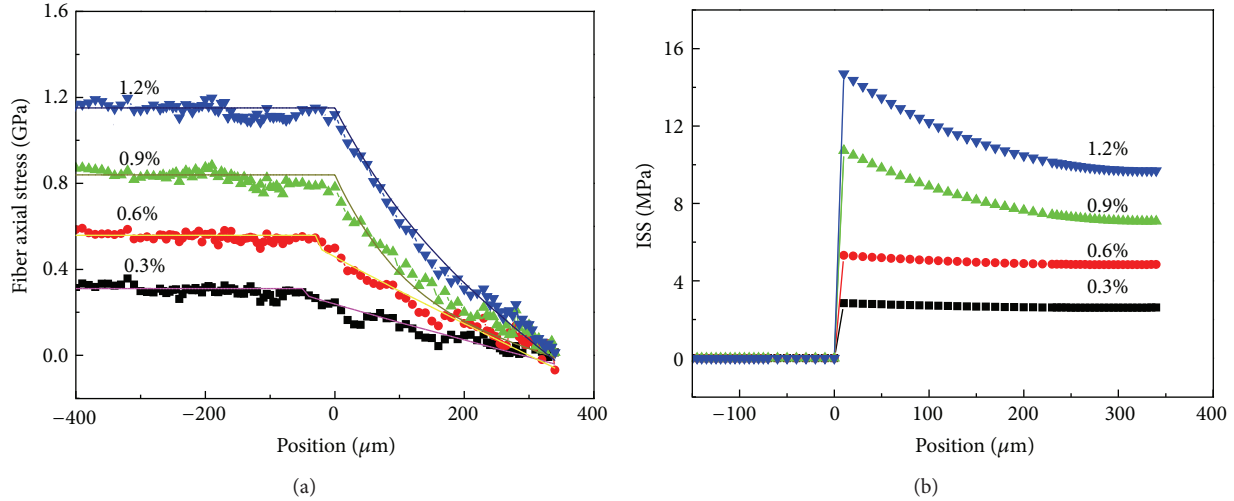


FIGURE 6: (a) Fiber axial stress and (b) shear stress distributions along fiber of pullout specimen under different strain levels [15].

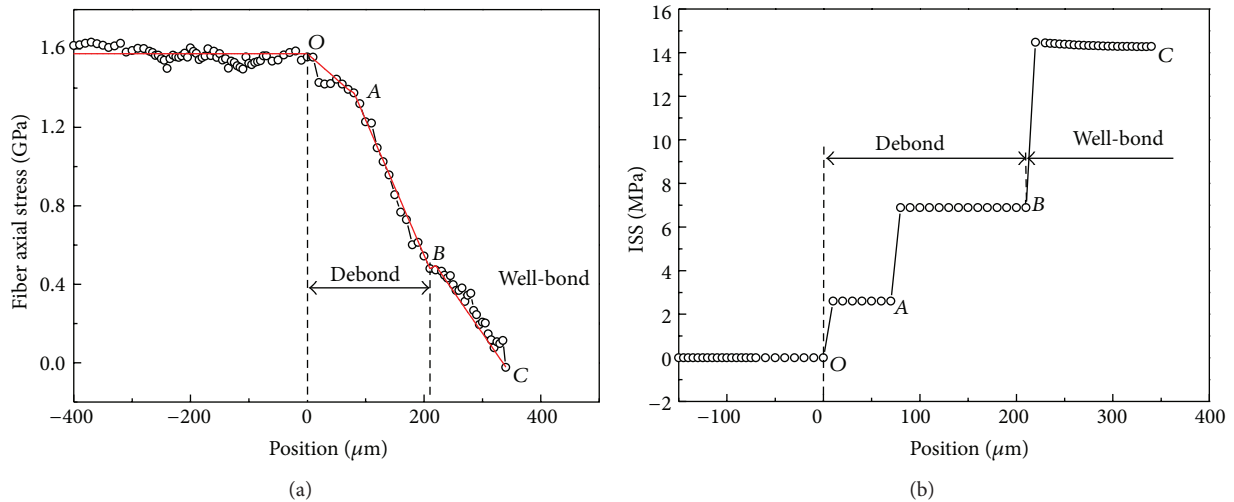


FIGURE 7: (a) Fiber axial stress and (b) shear stress distributions along fiber of pullout specimen under 1.6% strain [15].

Using the simple Cox’s shear-lag model, the frictional stress transfer in the debonding interface can be easily analyzed. Assuming a linear distribution of the interfacial friction stress, a two-stage model of the interfacial friction shown in Figure 7(b) gives the fiber stress distributions on the debonding interface as

$$\begin{aligned} \sigma_{OA} &= \sigma_{app} - 2\bar{\tau}_{OA} \frac{x}{r}, \quad 0 \leq x \leq L_{OA}, \\ \sigma_{AB} &= \sigma_{app} - 2\bar{\tau}_{OA} \frac{L_{OA}}{r} \\ &\quad - 2\bar{\tau}_{AB} \frac{(x - L_{OA})}{r}, \quad L_{OA} < x \leq L_{OB}, \end{aligned} \quad (7)$$

where  $L_{OA}$  is the debonding fiber length on the first stage,  $L_{OB}$  is the total length of the debonding fiber,  $\bar{\tau}_{OA}$  and  $\bar{\tau}_{AB}$ , respectively, correspond to the first and second stages of the interfacial friction shear stress constant, and  $x$  is the distance

to the fiber entry (Point O). Piggott’s model can be used to describe the fiber axial stress at the intact bonding interface (Segment BC in Figure 7). The fiber axial stress equals the fiber stress at the debonding/bonding transition (Point B), which can be obtained by solving (7) under the condition of  $x = L_{OB}$ .

The interface frictional shear stresses on the debonding segments are given by the combination of (2) and (7) as

$$\begin{aligned} \tau_{OA} &= \bar{\tau}_{OA}, \quad 0 \leq x \leq L_{OA}, \\ \tau_{AB} &= \bar{\tau}_{AB}, \quad L_{OA} < x \leq L_{OB}. \end{aligned} \quad (8)$$

It can be seen that the frictional shear stress plays the role of stress transfer on the debonding interface and can be described as the multistage constant distribution in this study.

If the load continues to be applied, the interface debonding failure propagates forward. According to strength failure conditions (6), the fiber breakage failure occurred until the

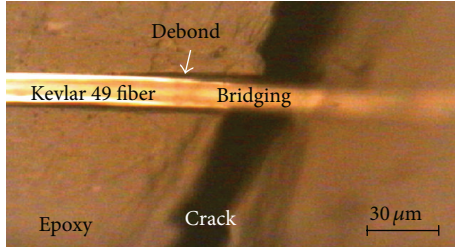


FIGURE 8: Bridging fiber and interfacial debonding during crack opening [16].

maximum fiber stress ( $\sigma = \sigma_{app}$ ) reached the fiber strength  $\sigma_b$ ; otherwise the interfacial debonding failure will continue until the fiber is completely pulled out.

**4.3. Reloading of Bridging Fiber.** As shown in Figure 8, when a matrix crack vertically propagated across an embedded fiber without fiber breakage, the bridging fiber with partial debonding was across both sides of the matrix crack. The formation of bridging fiber can be regarded as two fibers pullout process. The bridging fiber contains three parts: the bonding segment, debonding segment, and bridging segment. The fiber axial stress meets Piggott's model in the bonding segment. It is affected by linear friction shear stress in the debonding segment and remains a constant in the bridging segment. In the following text, the interfacial stress transfer and failure conditions of the bridging fiber are considered to be reloading.

**4.3.1. Slip Transform and Reloading.** For the case of unloading after the formation of bridging fiber, a reverse slip will occur on the debonding segment and the fiber retraction results in residual interfacial friction stress, as shown in Figure 9(a). When the bridging fiber is reloaded, the partial slip on the debonding segment inverses its sliding direction. This will cause the different effects of interface friction force on the debonding segment, as shown in Figures 9(b) and 9(c).

The reverse slip happens on the fiber debonding segment before reloading (Figure 9(a)), generating the interfacial friction in the opposite direction and resulting in compressive residual stress in the debonding segment. When the load is applied again (Figure 9(b)), the partial reverse slip on the debonding segment transforms to the forward slip resulting in the reduction of reverse slip length until all reverse slip completely converses to the forward slip (Figure 9(c)). The interfacial friction in the forward slip region makes the increase of fiber stress; on the contrary, the reverse slip results in the decrease of fiber stress. It is noted that the fiber stress remains constant in the bridging segment.

**4.3.2. Stress Transfer Model.** Raman measurements along the bridging fiber in Figure 8 gave a symmetrical axial stress distribution, as shown in Figure 10. The fiber axial stress is increased with the applied load. The stress platform is close to the bridging segment and the interfacial friction force in the slip segment should be overcome.

During the reloading of bridging fiber, the reverse slip in debonding segment gradually transformed into the forward slip so that the debonding fiber reloaded until the fiber stress eventually reached the maximum in the bridging segment. In fiber bridging segment, the ISS is zero due to the constant fiber stress. Setting a positive constant  $\bar{\tau}$  of the interfacial friction shear stress and the fiber stress  $\sigma_m$  at the bonding/debonding transition point, a stress transfer model for the bridging fiber is shown in Figure 11.

In the fiber debonding segment, the interfacial frictional shear stress (Figures 11(d)–11(f)) is a constant; namely,

$$\tau = \pm \bar{\tau}, \quad (9)$$

where the interfacial frictional shear stress takes a positive sign in the forward slip zone and a negative sign in the reverse slip zone. The fiber stress in the debonding segment meets a linear distribution of the interfacial friction shear stress as

$$\sigma = \sigma_m + 2\bar{\tau} \frac{x_1}{r} - 2\bar{\tau} \frac{x_2}{r}, \quad (10)$$

where  $r$  is the fiber radius,  $x_1$  and  $x_2$  are the forward slip length and the reverse slip length in the debonding segment, respectively.

At initial reloading stage (Figure 11(a)), the fiber stress in the debonding segment is reduced to overcome the reverse interface friction (Figure 11(d)) due to the whole debonding segment belonging to the reverse slip zone. By contrast, the fiber stressing the bridging segment keeps constant due to no interface frictional on the bridging segment.

At middle reloading stage, (Figure 11(b)), the partial reverse slip transforms into the forward slip (Figure 11(e)). The fiber stress in the forward slip zone increases to overcome the positive interface friction so that the partial debonding fiber is reloaded.

At completely reloading stage (Figure 11(c)), the debonding fiber is completely reloaded due to the whole debonding segment belonging to the forward slip zone (Figure 11(f)).

It can be predicted that the debonding interface will continue to extend if the ISS at the bonding/debonding transition point reaches the interfacial shear strength. With the further increase of reloading, the fiber stress in the maximum stress plateau region will reach the fiber tensile strength so that the bridging fiber will fracture. This is the strength criteria for the bridging fiber.

For fibrous composites with stable interface, it can be seen from the above analysis that the physical and chemical nature of the interface determines the interface bonding ability, namely, the interface shear strength. The matrix crack across the fiber will cause interfacial debonding and form the bonding segment, debonding segment, and bridging segment. The fiber stress transfer among these segments has relationship with the interface bonding performance, interface friction, interfacial shear strength, and fiber strength. The balance between them determines whether the bridging fiber is stable or unstable. Once the balance is broken, the bridging fiber cannot exist stably and then transforms into the broken fiber [34]. The strength criteria for the bridging fiber can be used to explain the phenomenon that some of the debonding fibers can form a stable bridge but some of them break.

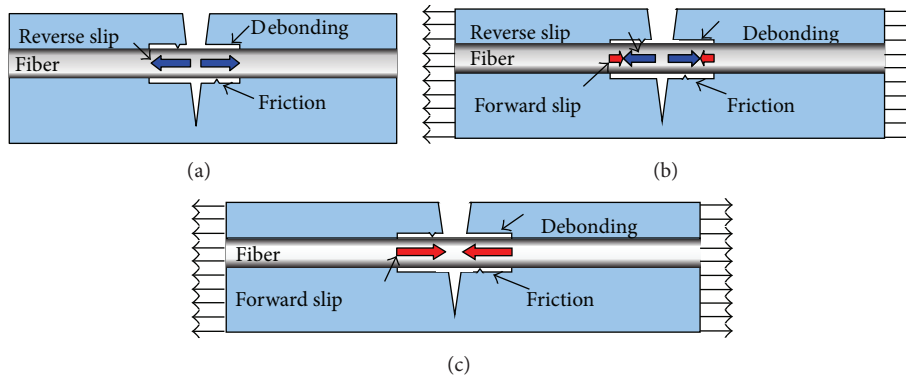


FIGURE 9: Slip transform for bridging fiber after reloading [16].

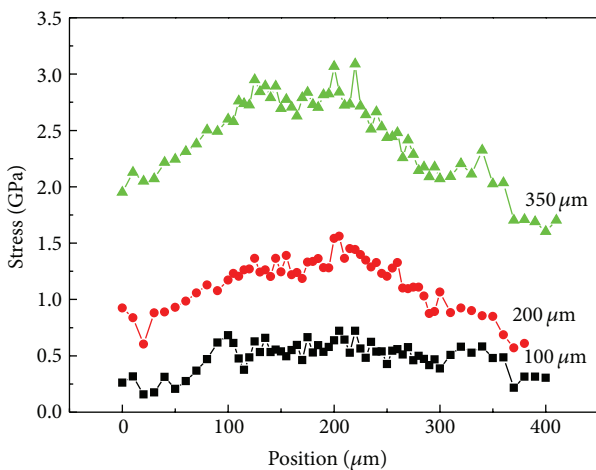


FIGURE 10: Stress distributions on the bridging fiber under different loads [16].

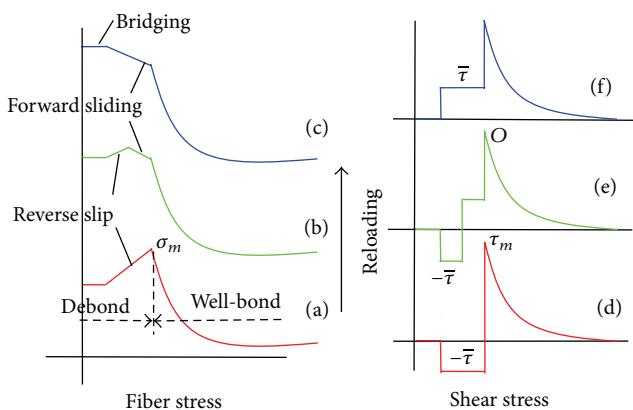


FIGURE 11: Stress transfer model of bridging fiber under reloading.

**5. Remarks**

The interfacial mechanical design problems faced in fibrous composites elaborated from three ways of the material optimization, interface optimization, and computational optimization. The physical, chemical, geometric, and mechanical

properties at microscale have a great impact on the interface behaviors. They are necessary to develop new experimental methods for reasonable evaluation on fiber/matrix interface by fine experimental testing and characterization to improve the interface micromechanical model. Micro-Raman spectroscopy was used to study main mechanical problems in fibrous composites, including the elastic stress transfer and failure criteria of well-bonding fiber, the frictional shear stress transfer behavior of partially debonded fiber, the slip transformation, and stress transfer models of bridging fiber during reloading. These works show that micro-Raman spectroscopy has ability to evaluate the stress transfer behavior of fiber/matrix interface.

**Conflict of Interests**

The authors declare that there is no conflict of interests regarding the publication of this paper.

**Acknowledgments**

This work was supported by National Basic Research Program of China (no. 2014CB046506), National Natural Science Foundation of China (nos. 11172054, 11272232) and Fundamental Research Funds for the Central Universities (no. DUT14LK11).

**References**

- [1] A. Baker, S. Dutton, and D. W. Kelly, *Composite Materials for Aircraft Structures*, American Institute of Aeronautics and Astronautics, Reston, Va, USA, 2 edition, 2004.
- [2] R. F. Gibson, *Principles of Composite Material Mechanics*, CRC Press, Boca Raton, Fla, USA, 3 edition, 2011.
- [3] R. M. Jones, *Mechanics of Composite Materials*, Taylor & Francis, Abingdon, UK, 2 edition, 1998.
- [4] Y. L. Kang, “Experimental analysis for some interfacial mechanics problems,” *Mechanical Engineering*, vol. 21, no. 3, pp. 9–15, 1999 (Chinese).
- [5] B. W. Kim and J. A. Nairn, “Observations of fiber fracture and interfacial debonding phenomena using the fragmentation test in single fiber composites,” *Journal of Composite Materials*, vol. 36, no. 15, pp. 1825–1858, 2002.

- [6] X. G. Yang and Q. L. Wu, *Analysis and Application of Raman Spectroscopy*, National Defense Industry Press, Beijing, China, 2008, (Chinese).
- [7] Y. L. Kang, Y. Qiu, Z. K. Lei, and M. Hu, "An application of Raman spectroscopy on the measurement of residual stress in porous silicon," *Optics and Lasers in Engineering*, vol. 43, no. 8, pp. 847–855, 2005.
- [8] Z. K. Lei, Y. L. Kang, H. Cen, M. Hu, and Y. Qiu, "Residual stress on surface and cross-section of porous silicon studied by micro-Raman spectroscopy," *Chinese Physics Letters*, vol. 22, no. 4, pp. 984–986, 2005.
- [9] Z. K. Lei, Y. L. Kang, H. Cen, and M. Hu, "Variability on Raman shift to stress coefficient of porous silicon," *Chinese Physics Letters*, vol. 23, no. 6, pp. 1623–1626, 2006.
- [10] W. Qiu, Q. Li, Z. K. Lei, Q. H. Qin, W. L. Deng, and Y. L. Kang, "The use of a carbon nanotube sensor for measuring strain by micro-Raman spectroscopy," *Carbon*, vol. 53, pp. 161–168, 2013.
- [11] W. Qiu, Y. L. Kang, Z. K. Lei, Q. H. Qin, Q. Li, and Q. Wang, "Experimental study of the Raman strain rosette based on the carbon nanotube strain sensor," *Journal of Raman Spectroscopy*, vol. 41, no. 10, pp. 1216–1220, 2010.
- [12] M. Nishikawa, T. Okabe, and N. Takeda, "Determination of interface properties from experiments on the fragmentation process in single-fiber composites," *Materials Science and Engineering A*, vol. 480, no. 1–2, pp. 549–557, 2008.
- [13] X. H. Wang, B. M. Zhang, S. Y. Du, Y. F. Wu, and X. Y. Sun, "Numerical simulation of the fiber fragmentation process in single-fiber composites," *Materials and Design*, vol. 31, no. 5, pp. 2464–2470, 2010.
- [14] Z. K. Lei, W. Qiu, Y. L. Kang, G. Liu, and H. Yun, "Stress transfer of single fiber/microdroplet tensile test studied by micro-Raman spectroscopy," *Composites A*, vol. 39, no. 1, pp. 113–118, 2008.
- [15] Z. K. Lei, Q. Wang, and W. Qiu, "Stress transfer of Kevlar 49 fiber pullout test studied by micro Raman spectroscopy," *Applied Spectroscopy*, vol. 67, no. 6, pp. 600–605, 2013.
- [16] Z. K. Lei, Q. Wang, and W. Qiu, "Micromechanics of fiber-crack interaction studied by micro-Raman spectroscopy: bridging fiber," *Optics and Lasers in Engineering*, vol. 51, no. 4, pp. 358–363, 2013.
- [17] S. Zhandarov and E. Mäder, "Characterization of fiber/matrix interface strength: applicability of different tests, approaches and parameters," *Composites Science and Technology*, vol. 65, no. 1, pp. 149–160, 2005.
- [18] L. A. Carlsson, D. F. Adams, and R. B. Pipes, *Experimental Characterization of Advanced Composite Materials*, CRC Press, Boca Raton, Fla, USA, 3 edition, 2002.
- [19] C. Galiotis, A. Paipetis, and C. Mansion, "Unification of fibre/matrix interfacial measurements with Raman microscopy," *Journal of Raman Spectroscopy*, vol. 30, no. 10, pp. 899–912, 1999.
- [20] G. Anagnostopoulos, J. Parthenios, and C. Galiotis, "Thermal stress development in fibrous composites," *Materials Letters*, vol. 62, no. 3, pp. 341–345, 2008.
- [21] R. J. Day and J. V. C. Rodrigez, "Investigation of the micromechanics of the microbond test," *Composites Science and Technology*, vol. 58, no. 6, pp. 907–914, 1998.
- [22] Z. K. Lei, Q. Wang, Y. L. Kang, W. Qiu, and X. M. Pan, "Stress transfer in microdroplet tensile test: PVC coated and uncoated Kevlar-29 single fiber," *Optics and Lasers in Engineering*, vol. 48, no. 11, pp. 1089–1095, 2010.
- [23] G. P. Tandon and N. J. Pagano, "Micromechanical analysis of the fiber push-out and re-push test," *Composites Science and Technology*, vol. 58, no. 11, pp. 1709–1725, 1998.
- [24] R. Sinclair, R. J. Young, and R. D. S. Martin, "Determination of the axial and radial fibre stress distributions for the Broutman test," *Composites Science and Technology*, vol. 64, no. 2, pp. 181–189, 2004.
- [25] M. J. Pitkethly, J. P. Favre, U. Gaur et al., "A round-robin programme on interfacial test methods," *Composites Science and Technology*, vol. 48, no. 1–4, pp. 205–214, 1993.
- [26] B. L. Zheng and X. Ji, "Stress singularity analyses of interface ends in micro-mechanics tests," *Composites Science and Technology*, vol. 62, no. 3, pp. 355–365, 2002.
- [27] X. Ji, Y. Dai, B. L. Zheng, L. Ye, and Y. W. Mai, "Interface end theory and re-evaluation in interfacial strength test methods," *Composite Interfaces*, vol. 10, no. 6, pp. 567–580, 2003.
- [28] H. Cen, Y. L. Kang, Z. K. Lei, Q. H. Qin, and W. Qiu, "Micro-mechanics analysis of Kevlar-29 aramid fiber and epoxy resin microdroplet composite by Micro-Raman spectroscopy," *Composite Structures*, vol. 75, no. 1–4, pp. 532–538, 2006.
- [29] L. R. Xu, H. C. Kuai, and S. Sengupta, "Free-edge stress singularities and edge modifications for fiber pushout experiments," *Journal of Composite Materials*, vol. 39, no. 12, pp. 1103–1125, 2005.
- [30] S. Zhandarov and E. Mäder, "Characterization of fiber/matrix interface strength: applicability of different tests, approaches and parameters," *Composites Science and Technology*, vol. 65, no. 1, pp. 149–160, 2005.
- [31] H. L. Cox, "The elasticity and strength of paper and other fibrous materials," *British Journal of Applied Physics*, vol. 3, no. 3, pp. 72–79, 1952.
- [32] M. R. Piggott, *Load Bearing Composites*, Pergamon Press, Oxford, UK, 1980.
- [33] J. A. Nairn, "On the use of shear-lag methods for analysis of stress transfer in unidirectional composites," *Mechanics of Materials*, vol. 26, no. 2, pp. 63–80, 1997.
- [34] Z. K. Lei, Q. Wang, and W. Qiu, "Micromechanics of fiber-crack interaction studied by micro-Raman spectroscopy: broken fiber," *Optics and Lasers in Engineering*, vol. 51, no. 9, pp. 1085–1091, 2013.

## Research Article

# A Real-Time Optical Tracking and Measurement Processing System for Flying Targets

Pengyu Guo,<sup>1,2</sup> Shaowen Ding,<sup>1,2</sup> Hongliang Zhang,<sup>1,2</sup> and Xiaohu Zhang<sup>1,2</sup>

<sup>1</sup> College of Aerospace Science and Engineering, National University of Defense Technology, Changsha 410073, China

<sup>2</sup> Hunan Provincial Key Laboratory of Image Measurement and Vision Navigation, National University of Defense Technology, Changsha 410073, China

Correspondence should be addressed to Xiaohu Zhang; [zxh1302@hotmail.com](mailto:zxh1302@hotmail.com)

Received 31 October 2013; Accepted 29 December 2013; Published 2 April 2014

Academic Editors: Y. Fu and G. Pedrini

Copyright © 2014 Pengyu Guo et al. This is an open access article distributed under the Creative Commons Attribution License, which permits unrestricted use, distribution, and reproduction in any medium, provided the original work is properly cited.

Optical tracking and measurement for flying targets is unlike the close range photography under a controllable observation environment, which brings extreme conditions like diverse target changes as a result of high maneuver ability and long cruising range. This paper first designed and realized a distributed image interpretation and measurement processing system to achieve resource centralized management, multisite simultaneous interpretation and adaptive estimation algorithm selection; then proposed a real-time interpretation method which contains automatic foreground detection, online target tracking, multiple features location, and human guidance. An experiment is carried out at performance and efficiency evaluation of the method by semisynthetic video. The system can be used in the field of aerospace tests like target analysis including dynamic parameter, transient states, and optical physics characteristics, with security control.

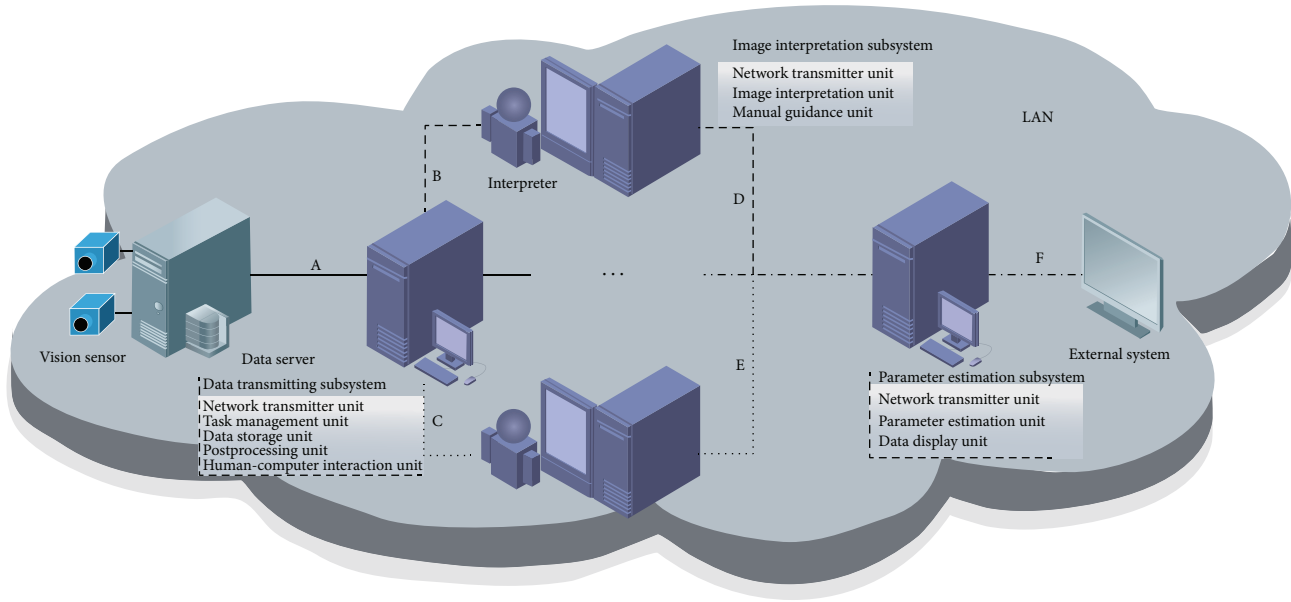
## 1. Introduction

The performance testing of flying targets like aircraft and missile is an important process in their civil or military production. The main testing item is trajectory measurement, including dynamic parameters (such as pose, velocity, and acceleration) and optical physics characteristics analysis (such as infrared radiation, flame spectrum, and luminance brightness). Optical tracking and measurement method is widely adopted in testing process, because optical sensor is passive, of low power consumption, and of noncontact; in addition, optical images are objective and informative. Because of targets' high maneuver ability and large cruising range, the observation environment is extreme, including target changes (such as pose, shape, scale, and motion blur) and circumstance changes (such as illumination and occlusion), but we still need high precision in performance analysis and high efficiency for security control. So an automatic and accurate interpretation method to conquer these extreme conditions is critical in real-time processing and this paper

puts emphasis on the key components including foreground detection, online tracking, and feature location.

There are many worldwide famous video motion analysis systems, like TrackEye [1] from Sweden Image Systems cooperation, Visual Fusion [2] from America MIT, Movias Pro [3] from America NAC, and so forth. They all can provide transient state record, real-time image interpretation, and dynamic parameter estimation for flying targets using high-speed camera. But most of them depend on feature points or markers, whereas we care about the image interpretation for markerless targets with finite prior knowledge on the case that large sensor standoff distance and outdoor environment make a target region with a weak texture in the image.

This paper starts from the demand analysis of the optical tracking and measurement for flying targets. Section 2 designs the architecture of distributed real-time processing system and introduces the compositions in brief. In Section 3 a detailed image interpretation method and a short parameter estimation method are presented. Section 4 realizes the image



A: time stamp, N sensor parameters, N images;  
B and C: time stamp, 1 sensor parameter, 1 image;

D and E: time stamp, N sensor parameters, N image interpretation results;  
F: time stamp, estimated parameters;

FIGURE 1: Architecture of distributed optical tracking and measurement processing system.

interpretation subsystem and validates the performance by the experiment. Section 5 draws the conclusion.

## 2. Architecture

The real-time processing of optical tracking and measurement system has the characteristics of high efficiency, strong parallelism, and rigorous time series. As Figure 1 shows, the system adopts distributed architecture in terms of load balancing to improve efficiency and scalability, which is loosely decomposed into data receiving, image interpretation and parameter estimation three subsystems according to the course of first interpretation and then estimation. In view of the variety of different observation platforms and high computation resource demand of multisite synchronous interpretation, the parallel processing is needed which makes each interpretation subsystem accomplish one site task and the number of observation platforms decides the number of interpretation subsystems. The system communicates by network whose protocol is TCP/IP. Data server provides the data of the system via link A, which distinguishes data from different moments and sensors by time stamp and sensor serial number, and the results of estimation are exported to the external system for analysis and display.

It can provide two kinds of work modes including real-time and post-processing. Data transmitting subsystem is the manager of the whole system, which receives interpretation task data package from data server by link A, splits the package according to the sensor serial number to send each package to the subsystem by link B or C, and records the flying scene grouped by task in the database for postrecurrence and interpretation; image interpretation subsystem picks up the

data package from data transmitting subsystem, extracts the image in the package to realize one site interpretation which can be guided by interpreter when the result is abnormal, and integrates the interpretation result with other information in the package to send it to the estimation subsystem through link D or E. Parameter estimation subsystem decides whether the data is from one site or multisite by time stamp alignment to select one site or multisite measurement manner automatically and send results to the external system for further analysis.

## 3. Real-Time Processing

The difficulty of real-time processing is accuracy and efficiency of the image interpretation, because parameter estimation methods during real-time or post-processing are nearly the same. So in this chapter, we propose a detailed real-time image interpretation method and make a brief introduction about parameter estimation.

**3.1. Image Interpretation.** Image interpretation is an image understanding process, which needs to detect the foreground target, track it online, and locate the feature for parameter estimation during real-time processing. A human guidance policy is essential on account of more false positives and false negatives during long-term flying.

**3.1.1. Foreground Detection.** Automated systems need to use some form of foreground detection mechanisms to identify the target region to be tracked. Foreground detection can be divided into two types including single frame detection and

sequence frames detection according to the number of used frames. Single fame detection is a visual object recognition problem [5] which needs the target prior appearance information from offline training and online update; sequence frames detection is a change detection problem which uses background subtraction like parameter estimation method GMM [6] or nonparameter estimation method VIBE [7] for fixed field of view and adopts a interframe registration such as optical flow [8] to describe motion information followed by a trajectory analysis based on tensor voting [9] or epipolar geometry [10] for varied field of view. Here we propose a simple detection algorithm which combines two-frame motion segmentation with one-single shape recognition.

The motion detector relies on two-frame optical flow filed. Many methods use a pixel-level analysis which is of high computational cost. In view of the scene whose background is nearly a plain region like sky or gobi in flying target tests, we downsample the image with  $G_W \times G_H$  grids which is marked with one pixel in each grid. The pixel  $P$  may be a strong KLT feature point or a central point. If it is a KLT point, a pyramid Lucas-Kanade is used to track it; otherwise a pyramid NCC can be used to match the grid with a template size  $T_W \times T_H$  and a search range  $S_W \times S_H$ . The feature selection is shown in Figure 2(a) with optical flow estimation  $f(u, v, t)$  in Figure 2(b) where white points are KLT feature points, green ones are central points, and red lines are optical flow. The orientation  $\theta \in [0, 2\pi)$  and magnitude  $m$  of  $f$  can be computed in the following:

$$\theta = \tan^{-1} \left( \frac{v}{u} \right), \quad m = \sqrt{u^2 + v^2}, \quad (1)$$

which can be used to count the histogram of optical flow orientation noted as HOOF assigning a weight  $m$  according to the following:

$$h_j = \sum_{i \in P} \sum_{j=1}^{\text{bin}} \left[ \cos \left[ \text{sgn} \left( \frac{\theta_i}{(2 * \pi / \text{bin})} - j \right) \right] \right] * m_i, \quad (2)$$

where  $P$  is the set of sampling pixels,  $\text{sgn}$  is the sign function, and  $\text{bin}$  is the capacity of  $h$ . The normalized  $h$  is in (3). In light of  $h$ , a backprojection is shown in Figure 2(c) without stationary sampling points. Figure 2(d) shows the motion segmentation result with occupy map based on HOOF where the same color means an identical motion region. Because the target may be a small part of the image which provides little motion information to the total optical flow field, we concern the connected region more than occupy value and tend to select larger occupy value when there are multiple connected regions

$$h_j = \frac{h_j}{\sum_{j=1}^{\text{bin}} h_j}. \quad (3)$$

The appearance detector depends on the shape information, because the image intensity is varying along the observation distance, and the shape is more robust feature which is affected by visual angle and acquired easily. In addition, the observation distance is larger than the target dimension, so

a projective transformation can be approximated by an affine warp.

As in Figure 3(a) we render partial 2D aircraft shape models at some step according to the 3D model from Trimble 3D warehouse [11] and the visual angle. The affine-invariant boundary moment [12] in (4) is adopted to represent the shape which can bear small quantity of variable visual angle and noise,

$$\begin{aligned} I_1 &= \frac{(n_{20}n_{02} - n_{11}^2)}{n_{00}^4}, \\ I_2 &= (n_{30}^2n_{03}^2 - 6n_{30}n_{21}n_{12}n_{03} + 4n_{30}n_{12}^3 \\ &\quad + 4n_{21}^3n_{03} - 3n_{21}^2n_{12}^2) \times (n_{00}^{10})^{-1} \\ I_3 &= (n_{20}(n_{21}n_{03} - n_{12}^2) - n_{11}(n_{30}n_{03} - n_{21}n_{12}) \\ &\quad + n_{02}(n_{30}n_{12} - n_{21}^2)) \times (n_{00}^7)^{-1}, \end{aligned} \quad (4)$$

where  $n$  is the normalized boundary central moment. Compute the boundary moment  $I^B(m)$  of the  $m$ th target shape model  $C^B(m)$  offline noted as the set  $(t, v, k, l, p, q, I^B)$ , where  $(t, v)$  is the sample identifier,  $t$  is the target type,  $v$  is the visual angle, the number of contour sampling points  $p$  is  $k$ , the number of predefined interest points  $q$  is  $l$ , and  $I^B$  is the boundary moment descriptor. Calculate the boundary moment descriptor  $I^R(n)$  of the  $n$ th target contour  $C^R(n)$  online like Figure 3(b), and the similarity metric between  $C^B(m)$  and  $C^R(n)$  by a revised chi-square distance  $d(m, n)$  in (5) for the value of  $I^B$  or  $I^R$  may be nonpositive,

$$d(m, n) = \left| \frac{1}{2} \sum_{i=1}^3 \frac{[I_i^B(m) - I_i^R(n)]}{I_i^B(m) + I_i^R(n) + \varepsilon} \right|, \quad (5)$$

where  $\varepsilon$  is a small amount and less  $d$  means more similar. The detection is a nonminimum suppression process and a similarity metric between  $C^R(n)$  and  $C^B(m)$  is shown in Figure 3(c). The association of motion detector and appearance detector is easy, which outputs the biggest intersection as the target region with a bounding box definition.

**3.1.2. Target Tracking.** Tracking must have the function of detection and on-line learning, because flying targets may leave/reenter the field-of-view and gradually change the pose. TLD [13] is a novel framework based on semisupervised learning which decomposes the tracking task into tracking, detection, integration, and learning four components. We improve it from adaption and efficiency for real-time application and propose an AA-TLD [14] as an acronym for adaptive and accelerated tracking-learning-detection.

Figure 4 depicts the workflow of AA-TLD whose solid rectangle is a component, dashed rounded rectangle is a unit, and shaded dashed rounded rectangle is the modified unit. According to the bounding box of the target from foreground detection, initiator builds only the current scale space of the target with a sampling step and trains an initial fern detector

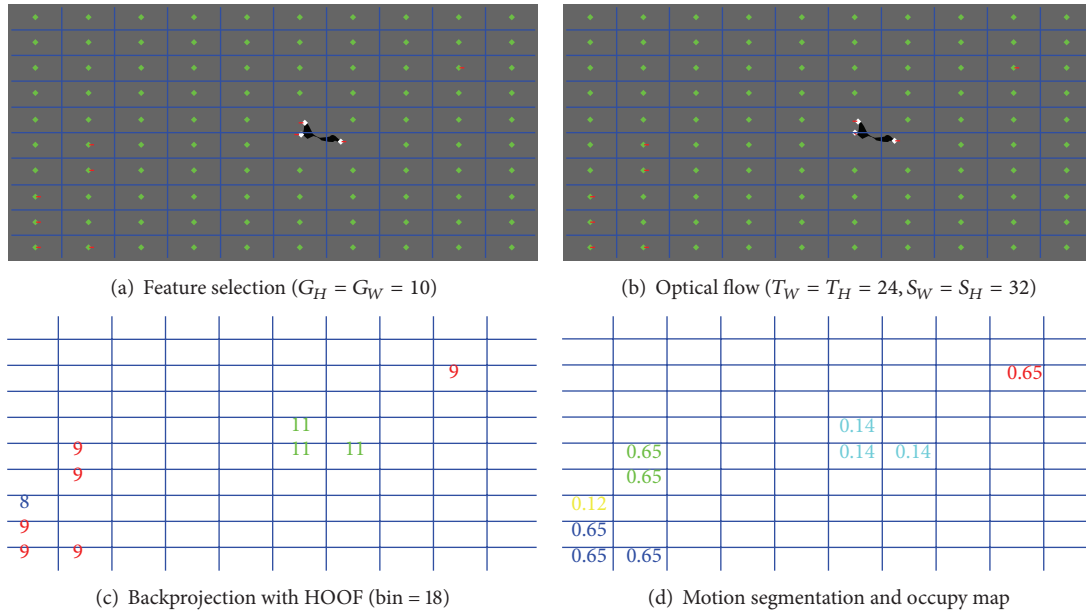
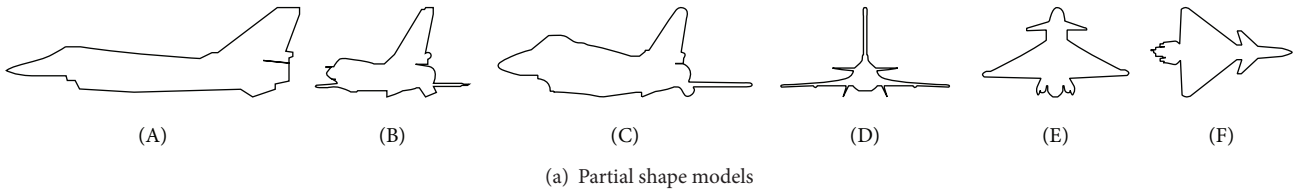


FIGURE 2: Motion detector.



Model	Similarity
A	0.0006
B	0.0128
C	0.0010
D	0.5158
E	0.0052
F	0.0020



(b) Contour detection

(c) Shape similarity

FIGURE 3: Appearance detector.

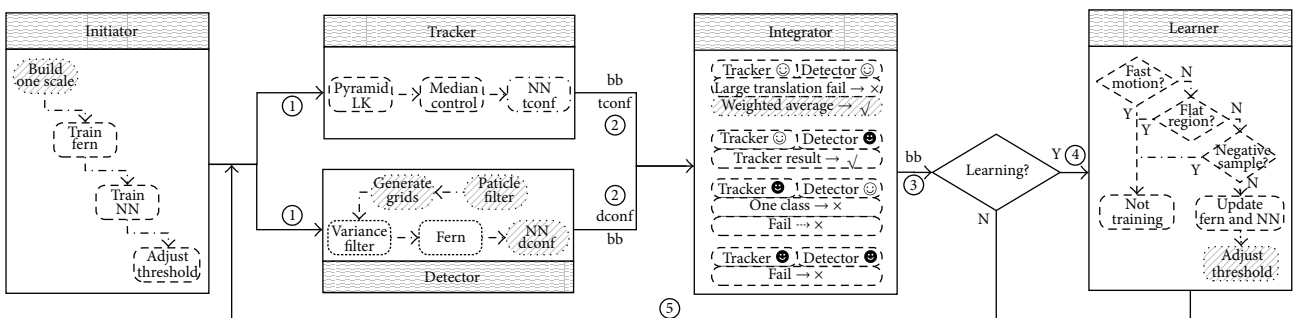


FIGURE 4: Flowchart of AA-TLD for target tracking. The marks white smile face and black smile face separately stand for success and failure symbols. The notations  $\surd$  and  $\times$  are learning flags, which mean learning or not.

and a NN detector according to a handful of samples with a threshold adjustment by cross-validation.

Unlike TLD's sequential execution, AA-TLD parallelizes tracker and detector to enhance the efficiency for independence by OPENMP. The tracker is the same with TLD, which uses median flow based on discrete sampling points in the target region and can be substituted with other easy tracking methods. The detector is realized in the particle filter framework to generate new scale scanning grids online according to the predicted scale and uses the same cascade process but fixes the number of the positive and negative samples which ensures a constant retrieving time by ordering the sample contribution ratio  $c$  as (6), where  $s$  is the positive or negative sample,  $b$  is the potential target grid, and  $S$  is the similarity metric in TLD

$$c(s_i) = \sum_{t=1}^T \sum_{g=1}^G S(b_{tg}, s_i) \quad s_i \in \{p, n\}. \quad (6)$$

TLD associates the results of tracker and detector by weight-average which assigns the weight of tracking result 10, and each detection result 1. Maybe it is not convincing because the results are from different scales but are assessed by normalized correlation coefficient (NCC). AA-TLD adopts a weight computing method considering both NCC and scale size according to [15] as (7), where  $r$  is NCC,  $n$  is the number of pixels, and  $\varepsilon$  is a small quantity

$$\frac{0.5 \ln(1+r) / (1-r+\varepsilon)}{\sqrt{1/(n-3)}}. \quad (7)$$

The learning stage of TLD only puts emphasis on updating the feature library by PN learning but not adjusting the threshold which is also important in decision process. AA-TLD adds a distance metric parameter adjustment component to online update the threshold by cross-validation like initiator. Partial tracking results of Shenzhou IX datasets which are shown in Figures 5 and 6 show the performance contrast details. We can conclude that AA-TLD is faster than TLD but less accurate than TLD at center location which is all right for the emphasis is an initial target region for feature location.

**3.1.3. Feature Location.** The feature can be contour, line, or point which provides image coordinates to parameter estimation. Target tracking provides a bounding box of the target, and locating the feature in the bounding box will bring more accurate results than the total image.

The contour can be detected by a real-time approximate level-set method in [16]. The axis and the edge line are the major line feature in the image. After a state-of-the-art linear-time line segment detector LSD [17], clustering and additional criterion can be used to locate these edge line features. The axis can be extracted using moment of inertia of the target region or the halving line of two edge line segments.

The feature point can be centroid or interest points. The priority of the centroid computing is locating target pixel sets which can be acquired by contour scanning or saliency detection [18]. There are two kinds of interest points. One may

be corners or blob-like points and can be established stereo correspondence by image matching like in [19]; the other can be the projection of the physical points as in [20, 21] with a prior knowledge of the target like 3D or 2D model. Here we propose simple and fast multiple interest physical points locating method based on ICP [22] with 2D shape models in Algorithm 1, which can offer image coordinates to pose estimation based on points.

Some examples of feature location are shown in Figure 7. Different features adapt to different targets and observation conditions.

**3.1.4. Human Guidance.** For correctness and efficiency of the system, when interpretation error occurs, the interpreter instantly provides guidance information which can be a simple seed point or a coarse rectangle region by human-computer interaction. The guidance does not interrupt the continuous running; when the system receives the guidance information, it will seek the bounding box of the target using region growing algorithm based on a guidance point or search it using grab cut [23] based on a guidance rectangle and learn the region feature to update the sample library at the next frame. The update strategy contains adding the feature which puts the positive sample into the library and deleting the feature that removes the similar sample with the guidance region from the library by nearest neighbor (NN) search as shown in Figure 8.

**3.2. Parameter Estimation.** Optical sensor can provide more appearance information like color, texture, and gradient than radar which relies purely on position and motion information [24]. Optical measurement can supply not only dynamic parameter estimation but also optical characteristic analysis.

**3.2.1. Dynamic Parameter Estimation.** Different observation manners and image features need different parameter estimation methods. The conventional observation apparatus for flying target tests is optoelectronic theodolite for long-distance measurement or high-speed camera for close-range measurement.

The measurement based on optoelectronic theodolite [25] can realize one-site localization, because the apparatus outputs the angular altitude, azimuth angle, and slope distance of the target by missing distance interpretation of one point standing for the target. And multisite triangulation will bring higher precision than one-site localization. If there is no slope distance information like high-speed camera observation, one site interpretation with material point hypothesis cannot locate the target, and the triangulation measurement [26] is necessary.

One point interpretation cannot estimate the attitude. But multiple points from single sensor with known correspondence between object points and image points is a classical PNP problem which estimates the pose like [27, 28]. The axis is the common line segment feature for rigid rotation, which can be used to locate with triangulation and estimate the pose in [29, 30]. With 3D model and the contour in the image of the target, model-based pose tracking method can be used to

**Input:** 2D shape model  $C^B$ , real-time contour  $C^R$  with discrete sampling sets expression  $\mathbf{x}_b(x_b, y_b, 1), \mathbf{x}_r(x_r, y_r, 1)$   
**Input:** model interest point sets  $\mathbf{X}_b$   
**Output:** interest point sets  $\mathbf{X}_r$  in the real-time image

(1) // initial registration  
(2) Decide whether  $C^B$  and  $C^R$  are mirrored or not. **if** mirrored, flip them. **end if**  
(3) Compute the initial registration relationship  $H_s(s, \theta, \mathbf{t})$  on the hypothesis of similarity transformation, centroids  $\mathbf{c}(C^B)$  and  $\mathbf{c}(C^R)$ , included angle between main axis with  $x$  axis  $\alpha(C^B)$  and  $\alpha(C^R)$  by moment of inertia, and contour perimeter  $p(C^B)$  and  $p(C^R)$ , so  
scale  $s = p(C^R)/p(C^B)$ ; rotation angle  $\theta = \alpha(C^R)/\alpha(C^B)$ ; translation vector  $[\mathbf{t} \ \mathbf{1}] = \mathbf{x}_r - [sR \ \mathbf{0}^T]^T \mathbf{x}_b$ .  
(4) // iterative optimization  
(5) Iteration frequency  $k := 0$ .  
(6) Change  $\mathbf{x}_b$  to  $\mathbf{x}_b^k$  according to initial registration relationship  $H_s$   
(7) Find the nearest point pairs [4] by  $\text{ass}(i, j) = \text{FANN}(\mathbf{x}_r, \mathbf{x}_b^k)$  where  $i$  and  $j$  are the indexes of the contour sampling points, and size is the function for capacity computing. The distance of the nearest point pairs  $d_k$  is computed by (\*), and the homograph  $H_k$  is estimated with RANSAC.

$$d_k = \sqrt{\sum_{i=1, \text{ass}(i, j)}^{\text{size}(\mathbf{x}_r)} \|\mathbf{x}_r(i) - \mathbf{x}_b^k(j)\|^2} \quad (*)$$

(8) **if**  $k \geq 10$  or  $\Delta d = \|d_k - d_{k-1}\| < \varepsilon$   
(9) Terminate the iteration, optimized  $H$  is as (\*\*),  $\mathbf{X}_r = H\mathbf{X}_b$ .

$$H = \left( \prod_{i=0}^k H_i \right) H_s \quad (**)$$

(10) **else**  $k := k + 1, \mathbf{x}_b^k = H_{k-1}\mathbf{x}_b^{k-1}$ , **goto** (7).  
(11) **end if**

ALGORITHM 1: Multiple interest points location based on 2D contour model.



FIGURE 5: Tracking snapshots of Shenzhou IX. True value, the result of TLD, and the result of AA-TLD are, respectively, marked with blue box, green box, and red box.

estimate the pose, like PWP3D [20]. The trajectory, velocity, and acceleration can be computed with time information.

**3.2.2. Optical Characteristic Analysis.** The analysis of optical physics characteristics about infrared radiation, flame spectrum, and luminance brightness needs the silhouette  $S$  of the target in the image. The histogram of the intensity of the pixels inside  $S$  represents the characteristics, and the histogram  $h$  is defined as follows:

$$h = \left\{ h_k \mid h_k = \frac{N_k}{N} \right\} \quad k = 1, 2, 3, \dots, L, \quad (8)$$

where  $N$  is the number of pixels inside  $S$ ,  $L$  is the intensity bins, and  $N_k$  is the number of pixels which belongs to the  $k$ th intensity bin. The statistical optical characteristics can derive from the mean, variance, coefficient of skewness, coefficient of kurtosis, energy, entropy, and other criteria of

$h$ . Figure 9 illustrates an example of optical characteristic analysis. Figure 9(a) shows an infrared image of Shenzhou X emission marked with the contour, whose histogram is in Figure 9(b) with intensity range from 0 to 255 and 8 intensity bins. Figure 9(c) presents the statistical analysis.

## 4. Experiment

We test our real-time processing system at precision and efficiency based on the image interpretation subsystem, which is developed on VS2008 with VC++ and implemented on an Intel Core i5-3470 3.20 GHz CPU with 3.46 GB RAM/Windows X86-32bit machine. Figure 10 shows the system UI including the menu bar and the windows. The menu bar consists of the human guidance buttons and the configuration button. The windows are the live image, the model image, the curve diagram, and the last five target regions.

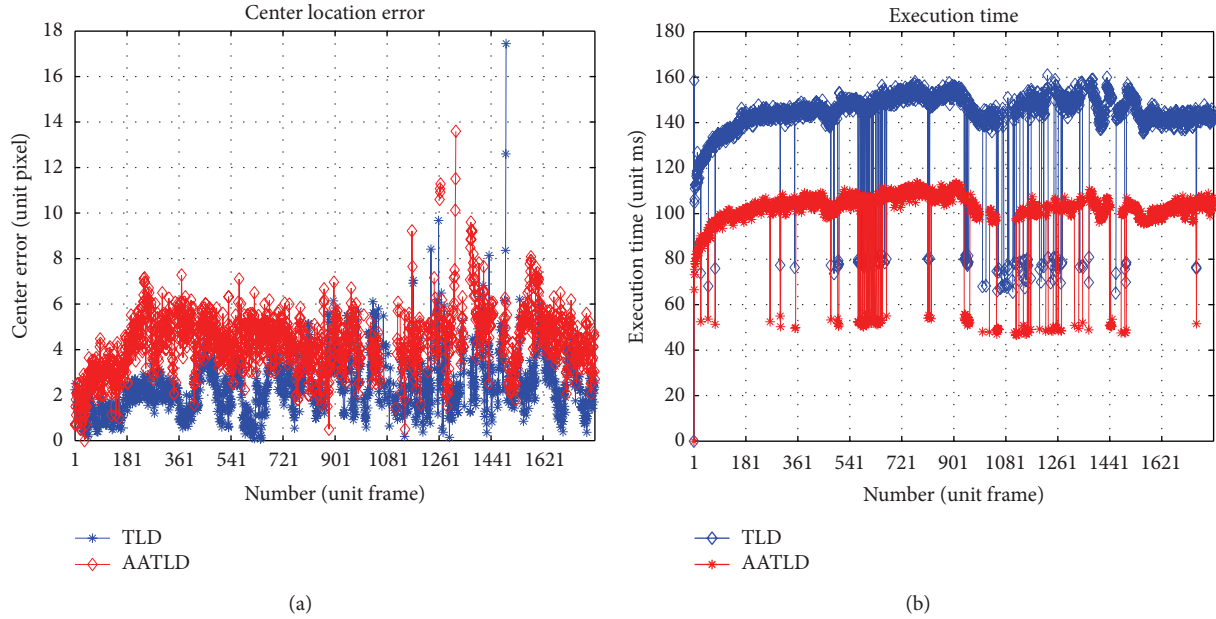


FIGURE 6: Performance contrast plots on center location and execution time of Shenzhou IX.

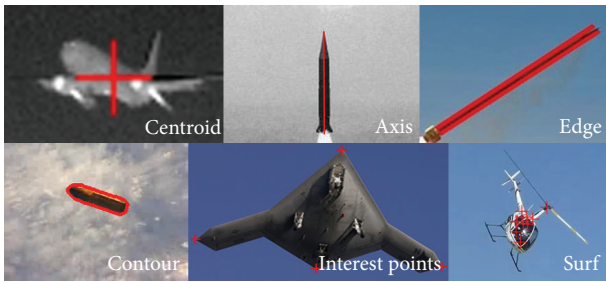


FIGURE 7: Examples of feature location.

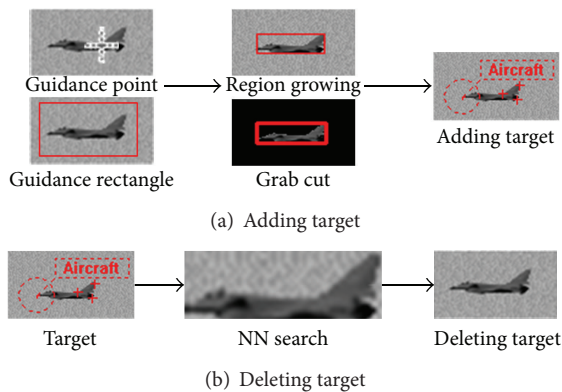


FIGURE 8: Guidance process.

4.1. Performance. Supposing the scene where two following aircrafts (noted as FA-1 and FA-2) are tracking and recording the measured aircraft (MA) during 80 s by a 25 Hz camera

with focal length from 150 mm to 300 mm and pixel size  $6 \mu\text{m}$  shown in Figure 11, we generate 2000 digital gray scale image sequences with resolution of  $720 \times 576$ . Dynamic parameter estimation needs six reference coordinates, which are the world coordinate system  $O_W-X_WY_WZ_W$ , the coordinate system of MA  $O_M-X_MY_MZ_M$ , the camera coordinate system of FA-1  $O_{F1}-X_{F1}Y_{F1}Z_{F1}$  with the image coordinate system  $o-u_1v_1$ , and the camera coordinate system of FA-2  $O_{F2}-X_{F2}Y_{F2}Z_{F2}$  with the image coordinate system  $o-u_2v_2$ . We first locate the four interest points of reference points of MA in the image coordinate then estimate the position and the attitude of MA in  $O_W-X_WY_WZ_W$  with known camera extrinsic parameters and coordinates of reference points.

4.1.1. Image Feature Location Precision. The four predefined interest points of the aircraft model are shown in Figure 12(b) marked with  $P_1$  to  $P_4$ . Figures 12(a) and 12(b) are the foreground detection result signed with bounding box and online interpretation result marked by crosses from two views.

The location precision of multi-interest points is shown in Figure 13. The true value coordinate of the target is  $(x_{ti}^b, y_{ti}^b)$ , and the interpretation coordinate is  $(x_{ti}^r, y_{ti}^r)$ , where  $t$  is the sequence number of frames,  $i$  is the label of the interpretation points,  $M$  is the amount of interpretation frames, and  $N$  is the number of interpretation points. Here  $N$  equals 4, and location standard deviation is (0.3, 0.5) pixel for left view and (0.6, 0.4) pixel for right view on the basis of the following:

$$\delta_x = \sqrt{\frac{\sum_{t=1}^M \sum_{i=1}^N (x_{ti}^b - x_{ti}^r)^2}{MN - 1}} \quad \delta_y = \sqrt{\frac{\sum_{t=1}^M \sum_{i=1}^N (y_{ti}^b - y_{ti}^r)^2}{MN - 1}} \quad (9)$$

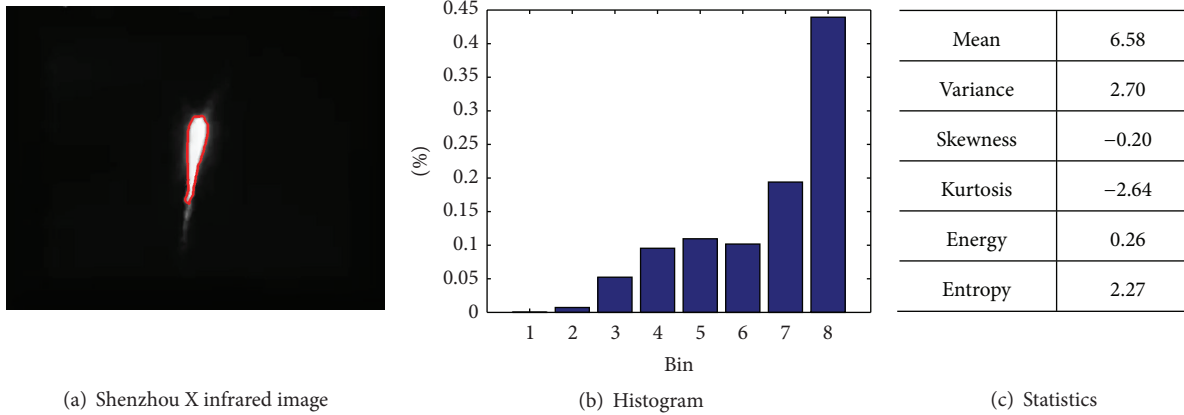


FIGURE 9: Example of optical characteristic analysis.

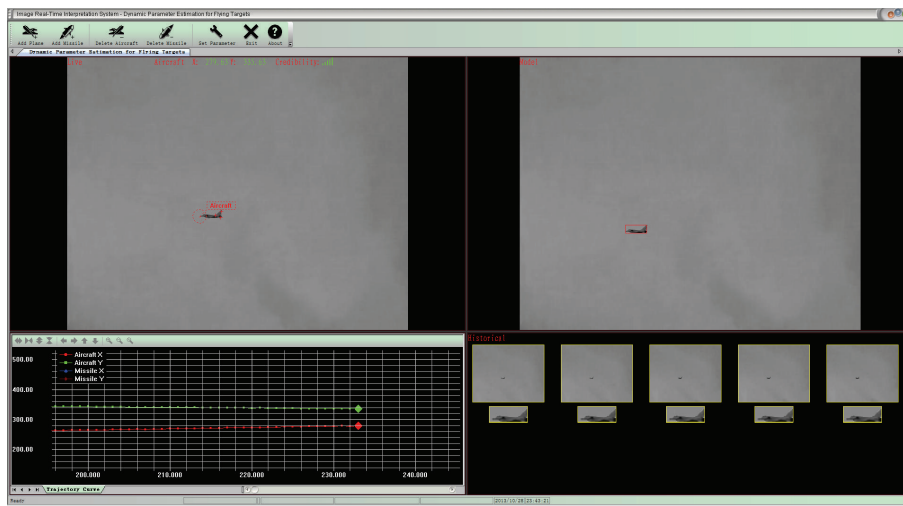


FIGURE 10: Image interpretation subsystem UI.

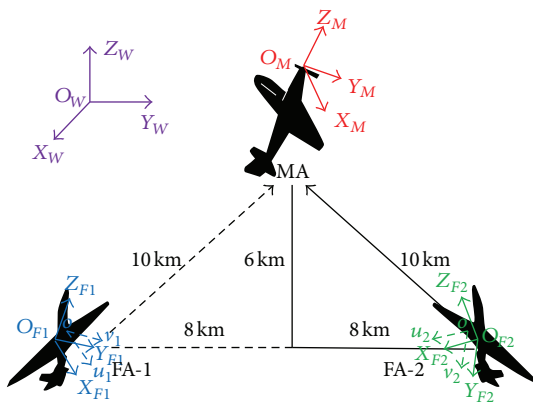


FIGURE 11: Supposed measurement scene.

4.1.2. *Dynamic Parameter Estimation Precision.* The measurement precision about position and attitude is shown

in Figure 14. The position is estimated by two-view triangulation with standard deviation (18.0, 13.6, and 24.1) m, and the attitude is estimated by absolute orientation with standard deviation (1.88, 1.00, and 3.34)° in one experiment, when there are 0.1° system error with 0.05° standard deviation of rotation angle, 10 m system error with 2 m standard deviation of translation about camera extrinsic parameters, and 0.5 m object error. The excellent filter like Kalman can be used to estimate the velocity and the angular velocity with position, attitude, and time information.

4.2. *Efficiency.* Figure 15 shows the execution time of the single frame about 12 ms/frame, and more initialization time is required than online processing. The location of multi-interest points needs an iterative optimization; for real-time, we not only use the frequency limitation, but also build shape samples library with some fixed step to ensure a superior

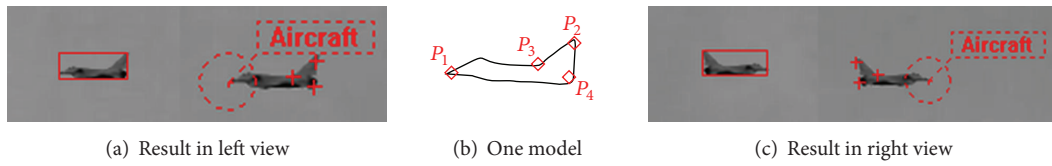


FIGURE 12: Detection and tracking results based on one model.

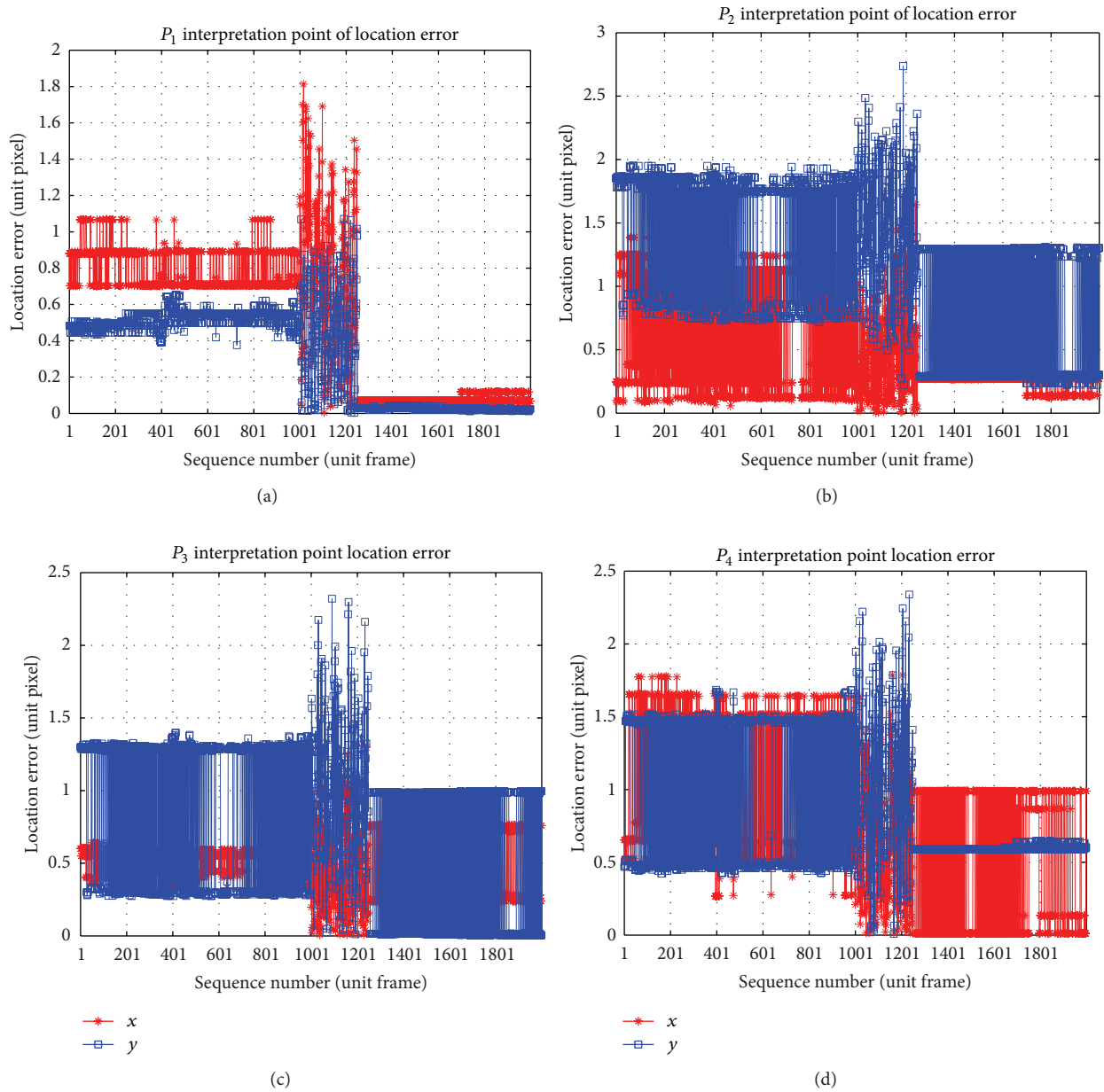


FIGURE 13: Plots of location precision of multiple interest points for left view.

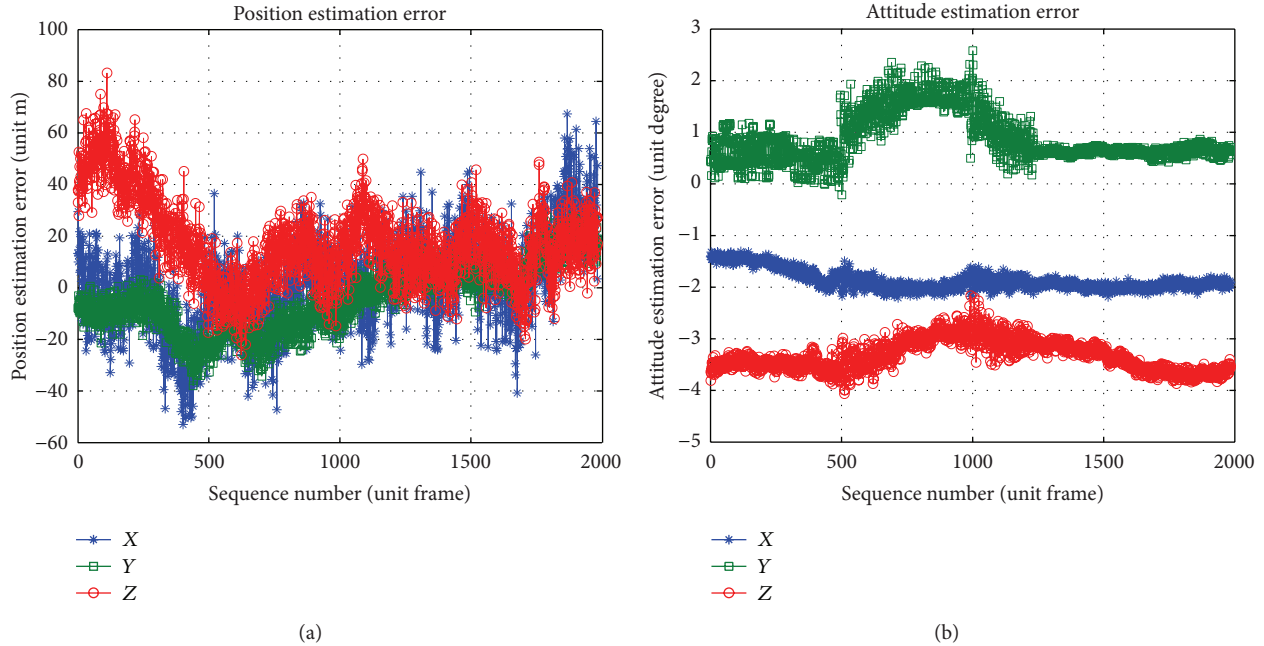


FIGURE 14: Plots of dynamic parameter estimation precision.

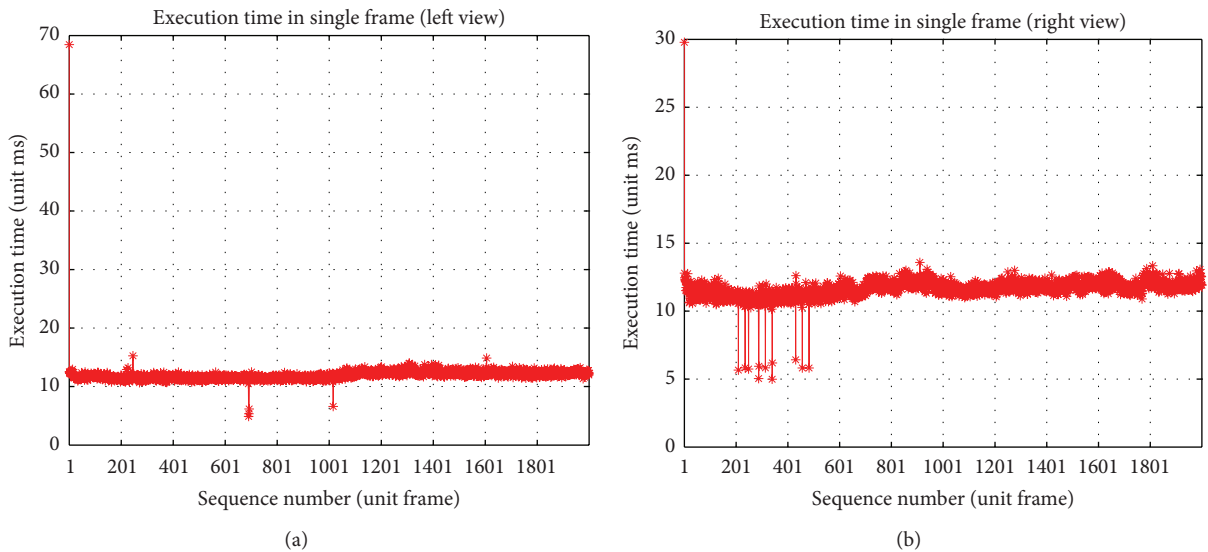


FIGURE 15: Plots of execution time.

initial value. In our experiment, because of the pattern of side direction observation, the number of iteration is less than 2.

### 5. Conclusion

This paper proposes a real-time processing method of optical tracking and measurement system for flying targets with a detailed image interpretation method and a brief parameter estimation review and realizes a distributed real-time image interpretation and parameter estimation

system. The simulated experiments validate the accuracy and the efficiency of the system. The Achilles' heel of the method and the system is not adapting to all the outdoor rigorous observation conditions, like uneven illumination and long-time occlusion, which seriously affect the feature location. Next we will put emphasis on robust feature location algorithms to improve the image interpretation precision and use more sophisticated real experiments for the system optimization. The system can be used to flying targets tests to meet the users' need of real-time interpretation.

## Conflict of Interests

The authors declare that there is no conflict of interests regarding the publication of this paper.

## Acknowledgment

This work was supported by the National Natural Science Foundation of China (Grant nos. 11072263 and 11272347) and the Program for New Century Excellent Talents in University (NCET-12-0140).

## References

- [1] Image Systems, "TrackEye," 2013, <http://www.imagesystems.se/>.
- [2] MIT, "Visual Fusion," 2013, <http://pages.swcp.com/~spsvs/VisualFusion/>.
- [3] NAC, "Movias Pro," 2013, <http://www.nacinc.com/products/Motion-Analysis-Software/>.
- [4] M. Muja and D. G. Lowe, "Fast approximate nearest neighbors with automatic algorithm configuration," in *Proceedings of the International Conference on Computer Vision Theory and Applications (VISAPP '09)*, pp. 331–340, February 2009.
- [5] K. Grauman and B. Leibe, *Visual Object Recognition*, Morgan & Claypool Publishers, 2011.
- [6] Z. Zivkovic, "Improved adaptive Gaussian mixture model for background subtraction," in *Proceedings of the 17th International Conference on Pattern Recognition (ICPR '04)*, vol. 2, pp. 28–31, August 2004.
- [7] O. Barnich and M. van Droogenbroeck, "ViBe: a universal background subtraction algorithm for video sequences," *IEEE Transactions on Image Processing*, vol. 20, no. 6, pp. 1709–1724, 2011.
- [8] D. Q. Sun, S. Roth, and M. J. Black, "Secrets of optical flow estimation and their principles," in *Proceedings of the IEEE Conference on Computer Vision and Pattern Recognition (CVPR '10)*, pp. 2432–2439, San Francisco, Calif, USA, June 2010.
- [9] Q. Yu and G. Medioni, "Motion pattern interpretation and detection for tracking moving vehicles in airborne video," in *Proceedings of the IEEE Conference on Computer Vision and Pattern Recognition (CVPR '09)*, pp. 2671–2678, Miami, Fla, USA, June 2009.
- [10] J. M. Kang, I. Cohen, G. Medioni, and C. Yuan, "Detection of independently moving objects in non-planar scenes via multi-frame monocular epipolar constraint," in *Proceedings of the 12th European Conference on Computer Vision (ECCV '12)*, pp. 860–873, 2012.
- [11] Google, "Trimble 3D warehouse," 2013, <http://sketchup.google.com/3dwarehouse/>.
- [12] J. Flusser and T. Suk, "Pattern recognition by affine moment invariants," *Pattern Recognition*, vol. 26, no. 1, pp. 167–174, 1993.
- [13] Z. Kalal, K. Mikolajczyk, and J. Matas, "Tracking-learning-detection," *IEEE Transactions on Pattern Analysis and Machine Intelligence*, vol. 34, no. 7, pp. 1409–1422, 2011.
- [14] P. Y. Guo, X. Li, S. W. Ding, Z. H. Tian, and X. H. Zhang, "Adaptive and accelerated tracking-learning-detection," in *International Symposium on Photoelectronic Detection and Imaging 2013: Imaging Sensors and Applications*, vol. 8908 of *Proceedings of SPIE*, Beijing, China, June 2013.
- [15] S. Bernstein and R. Bernstein, *Elements of Statistics II: Inferential Statistics*, McGraw-Hill, New York, NY, USA, 1999.
- [16] Y. G. Shi and W. C. Karl, "A real-time algorithm for the approximation of level-set-based curve evolution," *IEEE Transactions on Image Processing*, vol. 17, no. 5, pp. 645–656, 2008.
- [17] R. G. Von Gioi, J. Jakubowicz, J. M. Morel, and G. Randall, "LSD: a fast line segment detector with a false detection control," *IEEE Transactions on Pattern Analysis and Machine Intelligence*, vol. 32, no. 4, pp. 722–732, 2010.
- [18] X. D. Hou and L. Q. Zhang, "Saliency detection: a spectral residual approach," in *Proceedings of the IEEE Conference on Computer Vision and Pattern Recognition (CVPR '07)*, pp. 1–8, Minneapolis, Minn, USA, June 2007.
- [19] H. Bay, A. Ess, T. Tuytelaars, and L. van Gool, "Speeded-up robust features (SURF)," *Computer Vision and Image Understanding*, vol. 110, no. 3, pp. 346–359, 2008.
- [20] V. A. Prisacariu and I. D. Reid, "PWP3D: real-time segmentation and tracking of 3D objects," *International Journal of Computer Vision*, vol. 98, no. 3, pp. 335–354, 2012.
- [21] S. Belongie, J. Malik, and J. Puzicha, "Shape matching and object recognition using shape contexts," *IEEE Transactions on Pattern Analysis and Machine Intelligence*, vol. 24, no. 4, pp. 509–522, 2002.
- [22] P. J. Besl and N. D. McKay, "A method for registration of 3-D shapes," *IEEE Transactions on Pattern Analysis and Machine Intelligence*, vol. 14, no. 2, pp. 239–256, 1992.
- [23] C. Rother, V. Kolmogorov, and A. Blake, "'GrabCut'—interactive foreground extraction using iterated graph cuts," *ACM Transactions on Graphics*, vol. 23, no. 3, pp. 309–314, 2004.
- [24] K. Cannos, "A review of visual tracking," Tech. Rep., York University, 2008.
- [25] L. S. Liu, *Post-Flight Data Processing of Trajectory Measurement*, National Defense Industry Press, 2000.
- [26] R. Hartley and A. Zisserman, *Multiple View Geometry in Computer Vision*, Cambridge University Press, New York, NY, USA, 2003.
- [27] C. P. Lu, G. D. Hager, and E. Mjolsness, "Fast and globally convergent pose estimation from video images," *IEEE Transactions on Pattern Analysis and Machine Intelligence*, vol. 22, no. 6, pp. 610–622, 2000.
- [28] V. Lepetit, F. Moreno-Noguer, and P. Fua, "EPnP: an accurate O(n) solution to the PnP problem," *International Journal of Computer Vision*, vol. 81, no. 2, pp. 155–166, 2009.
- [29] Q. F. Yu, X. Y. Sun, and G. J. Chen, "A new method of measure the pitching and yaw of the axes symmetry object through the optical image," *Journal of National University of Defense Technology*, vol. 22, no. 2, pp. 15–19, 2000.
- [30] K. P. Wang, X. H. Zhang, L. C. Li, and X. C. Liu, "A new method for measurement of rolling angle by optical image," *Journal of Projectiles, Rockets, Missiles and Guidance*, vol. 29, no. 1, 2009.

## Research Article

# Nanoscale Strain Fields Research of Boundaries between B2 Matrix and G.P. Zone in Ni-Ti Alloy Thin Films

Shilei Zhao and Chunwang Zhao

College of Science, Inner Mongolia University of Technology, Hohhot 010051, China

Correspondence should be addressed to Chunwang Zhao; [cwzhao@aliyun.com](mailto:cwzhao@aliyun.com)

Received 9 November 2013; Accepted 19 February 2014; Published 24 March 2014

Academic Editors: Y. Fu, X. Li, and G. Pedrini

Copyright © 2014 S. Zhao and C. Zhao. This is an open access article distributed under the Creative Commons Attribution License, which permits unrestricted use, distribution, and reproduction in any medium, provided the original work is properly cited.

Ti-47at.%Ni alloy films were prepared by magnetron sputtering followed by 460°C for 40 minutes heat-treatment. The strain fields between B2 phase matrix and G.P. zone were mapped by a combination of high-resolution transmission electron microscopy and geometric phase analysis method. It was found that there is a compressive strain region parallel to the longitudinal axis of G.P. zone with 2 nm in width, -2.2% in average strain at the boundaries between B2 phase and G.P. zone.

## 1. Introduction

Shape memory alloy (SMA) with shape memory effect and superelasticity has had an increasing interest for researchers of mechanics of materials in recent decades. With the deepening of theoretical research, the applications of SMA have also made considerable progress including machinery, electronics, chemicals, aerospace, energy, and medical care and many other fields. SMA has a unique solid phase transformation characteristic that is thermoelastic martensitic transformation. The high temperature phase of SMA is austenite, while the low temperature phase of SMA is martensite [1]. The actual SMA is usually in a polycrystalline status, and the grain size and the microstructure are closely related to the thermal treatment history, which often results in a multiphase coexistence in the grain interior of SMA. Thus, there are a lot of grain boundaries and phase boundaries in SMA, which have a critical influence on the mechanical properties of the shape memory material [2].

So far, it has been found that there are AuCd, CuZn, TiNi, and a variety of alloy systems possessing the shape memory effect, wherein the NiTi-based alloys have excellent shape memory effect, biocompatibility, and other characteristics, which have become the most widely used alloy systems. Among Ni-Ti binary alloys are the most representative memory alloy materials. The high temperature austenitic parent phase of Ni-Ti binary alloy is B2 cubic structure, while

the low temperature martensite phase is B19' monoclinic structure [3]. The martensite transformation from high temperature phase to low temperature phase can have two paths. One is 1-stage B2-B19' transformation, and the other is 2-stage B2-R-B19' transformation. The occurrence of 1-stage transformation or 2-stage transformation depends on the composition and thermodynamic processing history of Ni-Ti binary alloy. Ni-rich Ni-Ti binary alloy usually forms Ni<sub>4</sub>Ti<sub>3</sub> precipitates after aging treatment, which has an important impact on the phase transformation. Kim et al. studied the phase transformation before and after heat-treatment in a Ti-50.9at.%Ni alloy. It was found that Ni-rich alloy only occurred 1-stage transformation after solution treatment, while the alloy occurred multi-stages transformation after aging treatment at 473 K. The microstructural analysis showed that the Ni<sub>4</sub>Ti<sub>3</sub> precipitates appeared during aging treatment, which plays a key role in the phase transformation process. It is because the lattice mismatch strain exists at the boundaries between B2 matrix and Ni<sub>4</sub>Ti<sub>3</sub> precipitates which results in the R-phase transformation occurrence prior to the martensitic transformation [4]. But for the Ti-rich Ni-Ti binary alloy, the heat-treatment can form two kinds of different precipitates, which are plate-like Guinier-Preston (G.P.) zones and granular Ti<sub>2</sub>Ni. Although they do not affect obviously phase transformation of Ni-Ti binary alloy, the presence of lattice mismatch strain at the boundaries between these precipitates and the matrix will affect the

overall mechanical properties of the Ni-Ti binary alloy [5]. So, measurement of the lattice mismatch strain at the boundaries between these precipitates and the matrix is very important. However, the strain is usually only in the region of boundaries with several nanometers width, which is very difficult to measure and analyze. So far, there is still no report in the literature about the strain field measurement of boundaries between matrix and G.P. zone in Ni-Ti binary alloy.

With the development of electron microscopy, transmission electron microscope (TEM) has been becoming a powerful tool for observing the microstructure and measuring the microscopic deformation fields [6]. A number of high-precision transmission electron microscopy-based experimental mechanics methods have been proposed, such as the geometric phase analysis [7], which has been applied to dislocations [8], nanoparticles [9], and other strain field research. It provides an effective measurement method for the strain field of grain boundaries or phase boundaries in Ni-Ti alloy. In this paper, the microstructure of boundaries between matrix and G.P. zone in Ti-rich Ni-Ti alloy was observed by using transmission electron microscopy. The high-resolution transmission electron microscopy (HRTEM) image was taken for the boundaries followed by strain fields mapping of the boundaries using the geometric phase analysis method.

## 2. Materials and Methods

### 2.1. Preparation of Ni-Ti Alloy Thin Films and Heat-Treatment.

Ni-Ti binary alloy films were prepared by the vacuum magnetron sputtering, using two elemental targets of Ti-50 at.%Ni and Ti. The substrate was silicon wafer coated with about 100 nm thick silicon nitride film. The base vacuum is  $4.7 \times 10^{-5}$  Pa. The thickness of as-deposited films is about 1.3  $\mu\text{m}$ . The composition was determined to be Ti-47at.%Ni by an energy dispersive spectrometry equipped in a scanning electron microscope. Because the as-deposited films were amorphous, the films were carried out a crystallization heat treatment. The substrate with the films was put into a vacuum tube furnace and then heated at 460°C for 40 minutes followed by cooling to room temperature with a fan.

**2.2. Transmission Electron Microscopy.** The films were peeled off the substrate and glued on a 3 mm diameter TEM copper ring with an epoxy. Ar ion milling was applied for the sample at a very small angle until perforation. Then microstructure was observed with a JEM-2010 TEM at 200 kV. The TEM images were recorded with a GATAN 1k  $\times$  1k CCD and processed by using DigitalMicrograph software. Strain fields were mapped by using the GPA Phase software. The simulation image of electron diffraction of Ni-Ti B2 phase was calculated by using the JEMS software.

## 3. Results and Discussion

Figure 1 depicts the TEM bright field image of Ni-Ti alloy thin films. It can be seen that the Ni-Ti alloy is in polycrystalline status, and the grain size is larger with an average diameter

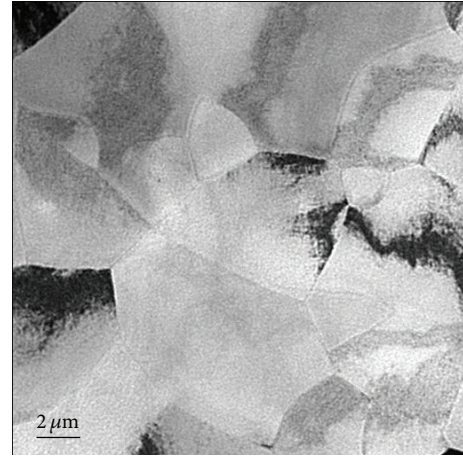


FIGURE 1: TEM bright field image of Ni-Ti alloy thin films.

of 3.5  $\mu\text{m}$ . Because of the interaction between grains during growth process, the grain boundaries are in irregular shape and the contrast of the image is not uniform. It is believed that there is a certain distortion or microscopic strain in the grain interior or boundaries.

For analyzing the microstructure of the alloy in more detail, a grain interior region was observed carefully and its TEM bright field image is depicted in Figure 2(a). It is seen that there is a plate-shaped precipitate in the middle region of the image. The length of the precipitate is about 110 nm, while the maximum width is about 9 nm. The electron diffraction pattern of the observed area (Figure 2(a)) is depicted in Figure 2(b). It shows that observed area is approximate in single crystal except those arrowed spots. After comparing with the stimulation image of electron diffraction pattern of NiTi<sub>B2</sub> in [001] zone axis (Figure 2(c)), the matrix in Figure 2(a) can be determined to be Ni-Ti B2 phase. Those additional diffraction spots marked by arrows do not belong to the NiTi<sub>B2</sub> diffraction pattern, which indicates they are not from the matrix. Comparing with Figure 1(b) in reference [5], it is found that the positions of these additional diffraction spots are very near in agreement with the so-called G.P. zone diffraction pattern. But in the current work, these diffraction spots deviate  $\langle 110 \rangle_{B2}$  direction for 5°. This can be explained as follows: since the as-deposited Ti-rich Ni-Ti binary alloy films are amorphous, the heat-treatment is necessary for crystallization. When the atomic fraction of Ti is large, G.P. zones are formed first, and then crystallization occurs. Thus G.P. zone and B2 matrix have no certain orientation relationship [2]. So, the precipitate in Figure 2(a) can be determined to be a G.P. zone, and the matrix is Ni-Ti B2 phase.

Figure 3(a) depicts the HRTEM image of boundaries between B2 phase and G.P. zone (boxed area in Figure 2(a)). The inset is the corresponding fast Fourier transformation image of the HRTEM image, which is the same as Figure 2(b). Taking the  $x$ -axis parallel to  $[1\bar{1}0]_{B2}$  and the  $y$ -axis parallel to  $[110]_{B2}$ , then the strain field can be calculated from the HRTEM image (Figure 3(a)). The full-field normal strains  $\epsilon_{xx}$  and  $\epsilon_{yy}$  were mapped, respectively, in Figures 3(b) and 3(c)

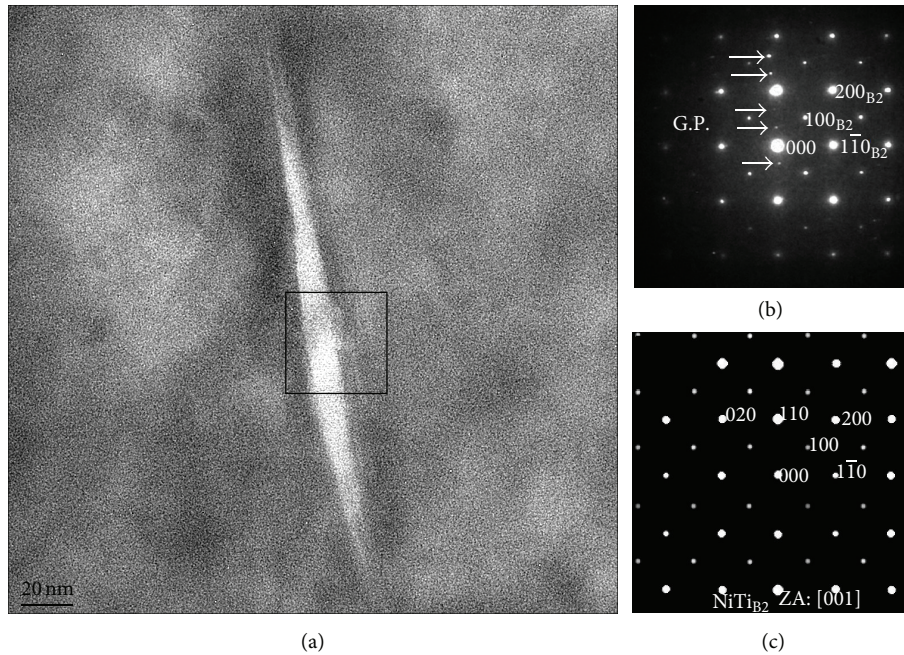


FIGURE 2: TEM bright field image and electron diffraction image of B2 phase and GP zone in Ni-Ti alloy thin films: (a) TEM bright field image; (b) electron diffraction image of (a); (c) simulated diffraction image of  $\text{NiTi}_{\text{B}_2}$  in [001] zone axis.

by using geometric phase analysis method [7]. A reference (boxed area in Figure 3(c)) which is far from the boundaries was selected for the strain field calculation. The different colors in strain field maps represent the different strain values, and the relationship between the colors and the strain values can be identified with the color marker shown in the bottom right area of Figures 3(b) and 3(c). Two diffraction spots of  $110_{\text{B}_2}$  and  $[\bar{1}\bar{1}0]_{\text{B}_2}$  were used for strain field calculation. So, we can only obtain and analyze the strain of boundaries in B2 matrix side. There are a lot of strain concentrated areas in the B2 matrix, which indicate dislocation existence [9]. Meanwhile, strain concentrated areas in the G.P. zone indicate nothing, because only the strains of the B2 matrix that have been calculated.

G.P. zones are Ti-rich regions [2, 5]. The first formation of G.P. zones makes the Ni-rich for surrounding area of G.P. zone, which results in a Ni-rich B2 phase microstructure in a very small area around the G.P. zones during the crystallization process of Ni-Ti alloy films. So, comparing with the normal B2 lattice, the lattice will inevitably shrink in this small area in B2 matrix around the G.P. areas, because Ti atoms are larger than Ni atoms by 19% [2]. As a result, we can get a compressive strain in the small area around the G.P. zone. The experimental measurement result actually has confirmed this deduction. According to Figure 3(b), we can find a small area with a width of 2 nm, average strain of  $-2.2\%$  in the B2 matrix besides the boundaries between B2 matrix and G.P. zone. But in Figure 3(c), the strain field is uniform and the strain values are close to 0, which indicates that there is no deformation in  $y$  direction. As mentioned previously, there is no strictly crystallographic orientation relationship

between B2 phase and G.P. zone in current Ni-Ti alloy. But the electron diffraction pattern (Figure 2(b)) and HRTEM image (Figure 3(a)) show that the crystal planes which are normal to the  $y$  direction in G.P. zone are nearly parallel to the  $110_{\text{B}_2}$  crystal planes, which results in an approximate semicoherent relationship for B2 phase and G.P. zone in  $y$  direction. So there is no deformation or strain which can be detected in  $y$  direction because of the microscopic interactions of these planes. But there is no crystallographic orientation relationship for B2 phase and G.P. zone in  $x$  direction, which results in a Ni-rich lattice contraction exhibiting compressive strain.

#### 4. Conclusions

In this work, Ni-Ti binary alloy films were prepared by magnetron sputtering followed by heat-treatment for crystallization. The microstructure of the alloy films was observed using a transmission electron microscope. It was found that the films were in polycrystalline status with large grains of  $3.5\ \mu\text{m}$  in average diameter. Meanwhile, precipitate exists in the grain interior. According to the analysis for electron diffraction pattern and HRTEM image, the matrix was determined to be  $\text{NiTi}_{\text{B}_2}$  phase, while the precipitate is G.P. zone. The strain fields of boundaries between B2 phase and G.P. zone were mapped by using geometric phase analysis method. It was found that there is a compressive strain region parallel to the longitudinal axis of G.P. zone with 2nm in width,  $-2.2\%$  in average strain at the boundaries between B2 phase and G.P. zone.

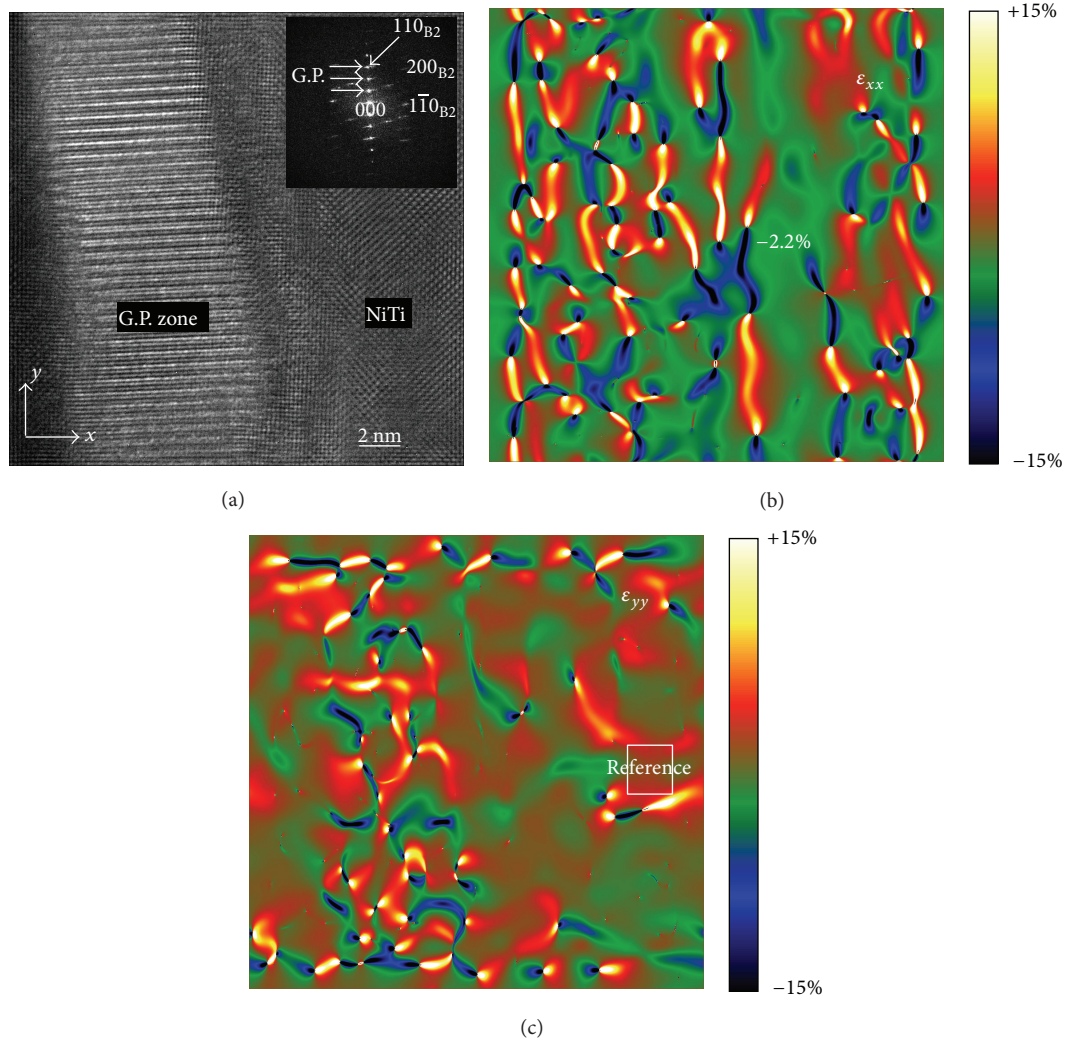


FIGURE 3: HRTEM image and strain maps of boundaries between B2 phase and GP zone in Ni-Ti alloy thin films (a) HRTEM image; (b)  $\epsilon_{xx}$  strain map; (c)  $\epsilon_{yy}$  strain map.

## Conflict of Interests

The authors declare that there is no conflict of interests regarding the publication of this paper.

## Acknowledgments

This work was supported by the National Natural Science Foundation of China (Grant no. 51261017), the Specialized Research Fund for the Doctoral Program of Higher Education (Grant no. 20101514110002), and the Program for New Century Excellent Talents in University (Grant no. NCET-10-0909).

## References

- [1] K. Otsuka and C. M. Wayman, *Shape Memory Materials*, Cambridge University Press, Cambridge, UK, 1998.
- [2] K. Otsuka and X. Ren, "Physical metallurgy of Ti-Ni-based shape memory alloys," *Progress in Materials Science*, vol. 50, no. 5, pp. 511-678, 2005.
- [3] X. Huang, G. J. Ackland, and K. M. Rabe, "Crystal structures and shape-memory behaviour of NiTi," *Nature Materials*, vol. 2, no. 5, pp. 307-311, 2003.
- [4] J. I. Kim, Y. Liu, and S. Miyazaki, "Ageing-induced two-stage R-phase transformation in Ti-50.9at.%Ni," *Acta Materialia*, vol. 52, no. 2, pp. 487-499, 2004.
- [5] S. Kajiwara, "Strengthening of Ti-Ni shape-memory films by coherent subnanometric plate precipitates," *Philosophical Magazine Letters*, vol. 74, no. 3, pp. 137-144, 1996.
- [6] S. Kret, P. Ruterana, A. Rosenauer, and D. Gerthsen, "Extracting quantitative information from high-resolution electron microscopy," *Physica Status Solidi B*, vol. 227, no. 1, pp. 247-295, 2001.
- [7] M. J. Hytch, J. L. Putaux, and J. M. Pénisson, "Measurement of the displacement field of dislocations to  $0.03\text{\AA}$  by electron microscopy," *Nature*, vol. 423, no. 6937, pp. 270-273, 2003.

- [8] C. W. Zhao, Y. M. Xing, C. E. Zhou, and P. C. Bai, "Experimental examination of displacement and strain fields in an edge dislocation core," *Acta Materialia*, vol. 56, no. 11, pp. 2570–2575, 2008.
- [9] C. L. Johnson, E. Snoeck, M. Ezcurdia et al., "Effects of elastic anisotropy on strain distributions in decahedral gold nanoparticles," *Nature Materials*, vol. 7, no. 2, pp. 120–124, 2008.

## Research Article

# 3D Online Submicron Scale Observation of Mixed Metal Powder's Microstructure Evolution in High Temperature and Microwave Compound Fields

Dan Kang,<sup>1</sup> Feng Xu,<sup>1</sup> Xiao-fang Hu,<sup>1</sup> Bo Dong,<sup>1</sup> Yu Xiao,<sup>1</sup> and Ti-qiao Xiao<sup>2</sup>

<sup>1</sup> CAS Key Laboratory of Mechanical Behavior and Design of Materials, University of Science and Technology of China, Hefei 230026, China

<sup>2</sup> Shanghai Institute of Applied Physics, Chinese Academy of Sciences, Shanghai 201204, China

Correspondence should be addressed to Feng Xu; xufeng3@ustc.edu.cn

Received 31 October 2013; Accepted 2 January 2014; Published 11 March 2014

Academic Editors: Y. Fu and G. Pedrini

Copyright © 2014 Dan Kang et al. This is an open access article distributed under the Creative Commons Attribution License, which permits unrestricted use, distribution, and reproduction in any medium, provided the original work is properly cited.

In order to study the influence on the mechanical properties caused by microstructure evolution of metal powder in extreme environment, 3D real-time observation of the microstructure evolution of Al-Ti mixed powder in high temperature and microwave compound fields was realized by using synchrotron radiation computerized topography (SR-CT) technique; the spatial resolution was enhanced to  $0.37 \mu\text{m}/\text{pixel}$  through the designed equipment and the introduction of excellent reconstruction method for the first time. The process of microstructure evolution during sintering was clearly distinguished from 2D and 3D reconstructed images. Typical sintering parameters such as sintering neck size, porosity, and particle size of the sample were presented for quantitative analysis of the influence on the mechanical properties and the sintering kinetics during microwave sintering. The neck size-time curve was obtained and the neck growth exponent was 7.3, which indicated that surface diffusion was the main diffusion mechanism; the reason was the eddy current loss induced by the external microwave fields providing an additional driving force for mass diffusion on the particle surface. From the reconstructed images and the curve of porosity and average particle size versus temperature, it was believed that the presence of liquid phase aluminum accelerated the densification and particle growth.

## 1. Introduction

A lot of the metals and alloys with excellent properties are prepared by powder metallurgy at high temperature [1, 2]. Microwave technology [3, 4] can not only provide high-temperature environment rapidly and uniformly but also make the materials have excellent mechanical properties (e.g., higher strength, hardness, ductility, and toughness) because of the combined effects of high temperature and electromagnetic fields. Since the first full sintering of powdered-metal [5] in 1999, microwave sintering has caused widespread concern and has become a new approach to prepare the high-performance metals and alloys. The properties of metals and alloys are greatly influenced by microstructures; consequently, high spatial resolution observations of the metal powder's microstructure evolution in high temperature and microwave compound fields are indispensable. The methods

of observation, such as TEM and SEM, have been used for high spatial resolution online experiments in extreme environments (e.g., high temperature, high radiation, high pressure, etc.), but only the information of surface or two-dimensional (2D) section can be obtained. For the morphology, distribution, and scale of microstructures in three dimensions (3D) that control the properties, in summary, 3D online high spatial resolution characterization is more real and effective.

Synchrotron radiation X-ray computed tomography (SR-CT) technique is such a powerful imaging tool developed in recent years [6, 7]. It has been used in physical, chemical, and biological researches for its ability to image structure in 3D with high spatial resolution at macroscopic to submicroscopic scales; it is nondestructive and can realize the observation of microstructure evolution under extreme conditions in a real-time way [8, 9]. Currently, few scholars

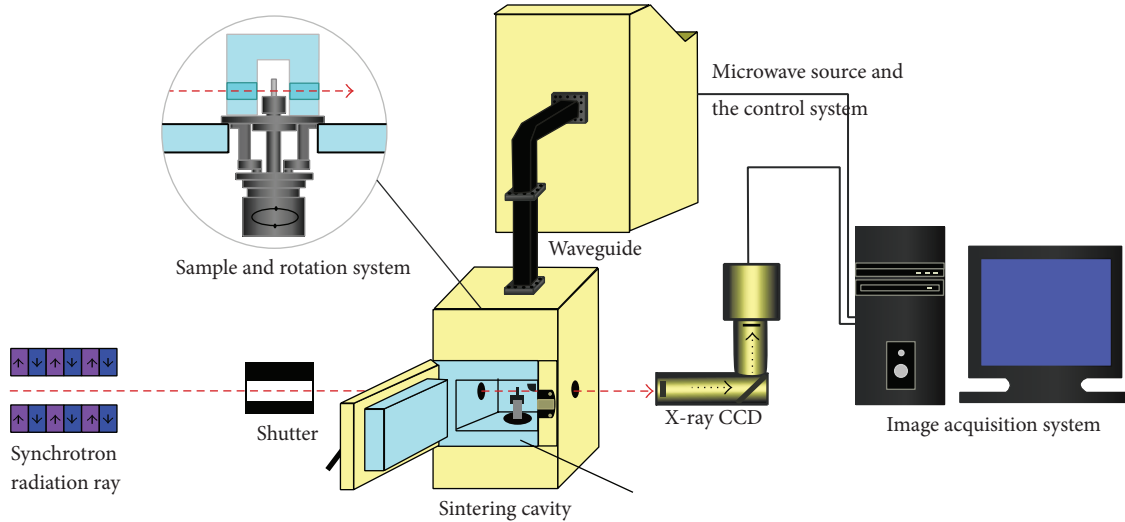


FIGURE 1: The schematic diagram of the SR-CT experiment system of microwave sintering.

have carried out the in situ investigation of microwave sintering by the SR-CT technique. In our research group, in situ studies on the microwave sintering of metals have been carried out for the first time. However, due to the limitation of experimental apparatus and methods, it is difficult to increase the resolution yet it is essential.

In this paper, 3D microstructure characterization of Ti-Al metal powder mixture in high temperature and microwave compound fields was studied in situ, and the spatial resolution was firstly increased to  $0.37 \mu\text{m}/\text{pixel}$ . Phase recovery method was used to get high-contrast qualitative microtomography, and microstructure evolution during sintering was clearly distinguished from 2D and 3D reconstructed images, such as sintering neck size, porosity, and particle size of the sample. The size of the sintering neck in each cross section image was calculated by using watershed algorithm, and typical sintering parameters during sintering were presented for quantitative analysis of the influence on the mechanical properties and the sintering kinetics during microwave sintering.

## 2. Experiment

**2.1. Brief Introduction of SR-CT Technique and Microwave Equipment.** The SR-CT technique is a testing method by which the specimen passed through by synchrotron radiation. X-ray is placed on a rotation device and the projection images of the specimen are received by an X-ray charge-coupled device (CCD). One projection image is collected each time when the specimen turns for an angle. After obtaining a set of projection data, reconstruction algorithm is used to obtain the internal microstructure of the sectional images. The 3D images of the microstructure can be obtained from a series of sectional images.

**2.2. Experimental Procedure.** In the experiment, Al and Ti were selected because they were more commonly used in high-performance metals and alloys. The elemental Al and

TABLE 1: Relationship between size of view field and resolution.

Number	Size of view field/mm	Resolution/ $\mu\text{m}$
1	0.38	0.19
2	0.74	0.37
3	1.40	0.74
4	3.7	1.85
5	7.4	3.7
6	11	5.9

Ti powders were 300~600 mesh and mixed in the ball mill with alcohol for 10 hours to prepare 87Al-13Ti (wt.%) and then dried in a vacuum oven. The mixed alloy powder was filled into a quartz tube with an inner diameter of  $260 \mu\text{m}$ . The microwave sintering experiment was carried out on the BL13W1 beamline at Shanghai Synchrotron Radiation Facility (SSRF, China); the energy of the beam ranged from 8 to 72 KeV. Considering the X-ray absorption coefficient of Al and Ti, an X-ray with 26 KeV was applied.

A set of unique equipment specifically for the 3D imaging of samples using synchrotron of X-ray had been designed (Figure 1); the power of the microwave facility could be regulated continuously from 0 to 3 KW; online observation at very high temperature (above  $1500^\circ\text{C}$ ) could be achieved. The system was capable of maintaining 3D tomograms at high spatial resolution to image structural details at high spatial resolution scale.

Due to the sampling capacity limit of CCD target surface, size of the view field would decrease with the improvement of the resolution; therefore, precise positioning of the sample was critical to achieve high resolution SR-CT experiment. The relationship between field of view size and resolution is shown in Table 1.

In order to carry out high resolution experiments, we developed a special multidimensional high-precision translation and rotation equipment; the design is shown in

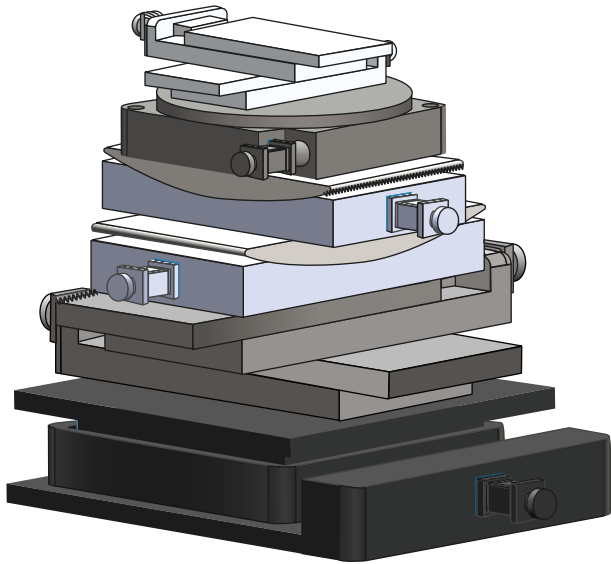


FIGURE 2: Structure of multidimensional high-precision translation and rotation equipment.

Figure 2. This device can adjust the sample to ensure it is rotating in the field of view, and it is independent from the cavity; the disturbance caused by the vibration of the cavity is eliminated. In order to guarantee the quality of projections, a loop control system of image acquisition and storage was designed to prevent exposure and image acquisition when the turntable was rotating. Based on this system, we have achieved the SR-CT experiment with resolution of  $0.37 \mu\text{m}/\text{pixel}$  successfully.

### 3. Results and Discussion

When there is a certain distance between CCD and the sample, phenomenon of absorption and phase shift occur simultaneously, the information received by CCD includes both absorption and phase information, and the phase contrast image cannot directly reflect the phase and structural information of the sample. X-ray propagation-based phase contrast CT (PPCT) method [10, 11] was used to get high-contrast qualitative microtomography (especially the microtomography of weakly absorbing samples), that is, edge enhancement. The microstructure boundaries become clear, as shown in Figure 3. This method is extremely useful for high-resolution experiments.

The exposure time would be longer and more projectors would be required in high resolution SR-CT experiment, which led to significant changes in microstructure in the same group of projections, and because the intensity of X-ray decreased with time, the background intensity of projections would be inconsistent. Therefore, in order to increase data acquisition speed, the number of projections would be reduced. Using the inverse projection method could acquire high-quality reconstructed images with fewer projections. By using this method, a series of cross-sectional images at different sintering times was produced, from which 3D images

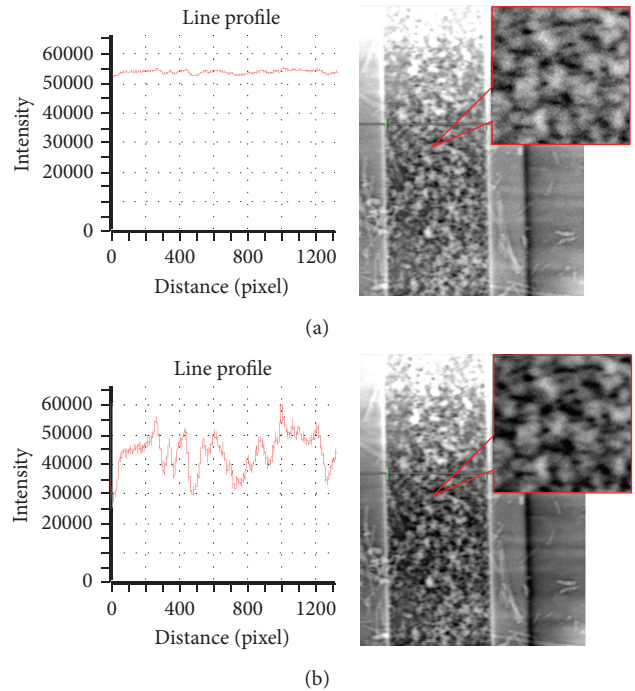


FIGURE 3: The intensity of projection image. (a) Original projection image. (b) Projection image after phase.

were obtained by applying a 3D rendering algorithm. The 3D reconstructed images of the same microstructure at different sintering times are shown in Figure 4. Various conventional sintering phenomena can be observed clearly from the figure, such as the sintering necks form and grow; the interconnected pores become isolated and smaller, with the annexation of small particles; the particle size becomes larger; the sample appears to be dense. It is apparent that the combined effect of electromagnetic and high temperature field led the sintering phenomena to be more rapid and intense, especially the particle surfaces smoothing quickly, which may be caused by the “nonthermal effect” of microwave fields such as the increase of eddy current [12] on the particles’ surface and the interfacial polarization between the grain surface and the pore.

Sintering necks which initiate and grow during sintering connect loose powders to form a solid metal material. The tensile strength of the metals can be significantly improved by improving the sintering neck structure. Neck growth is a basic phenomenon of sintering, and it plays an important role in determining the main diffusion mechanism and calculating the diffusion coefficient of the material [13]. Therefore, in order to research the kinetics mechanism of sintering neck growth, the watershed algorithm was used to extract the neck size; areas with different gray represent different particles; the detailed processing procedure is available elsewhere.

The dynamics of stable neck growth as summarized by Kuczynski is shown in the formula below [14]:

$$\left(\frac{x}{a}\right)^n = \frac{F(T)}{a^m}t, \tag{1}$$

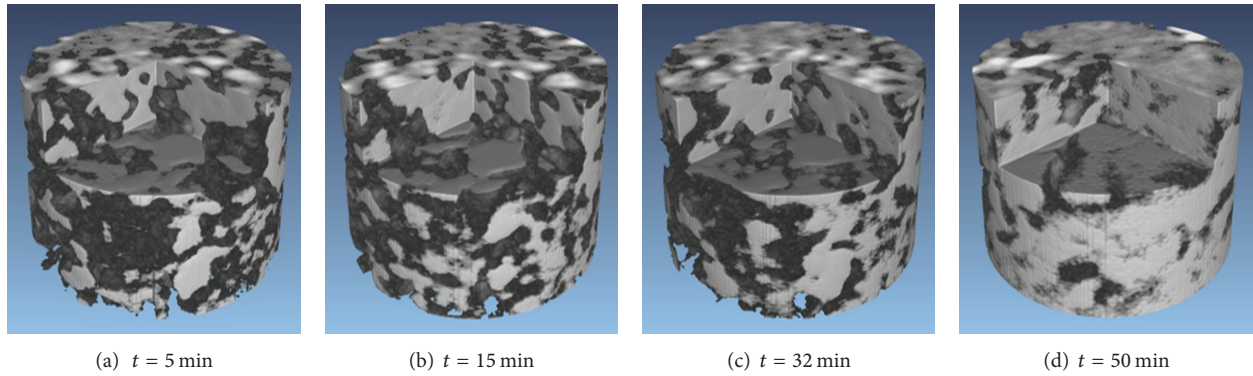


FIGURE 4: 3D images of the microstructure at different sintering times.

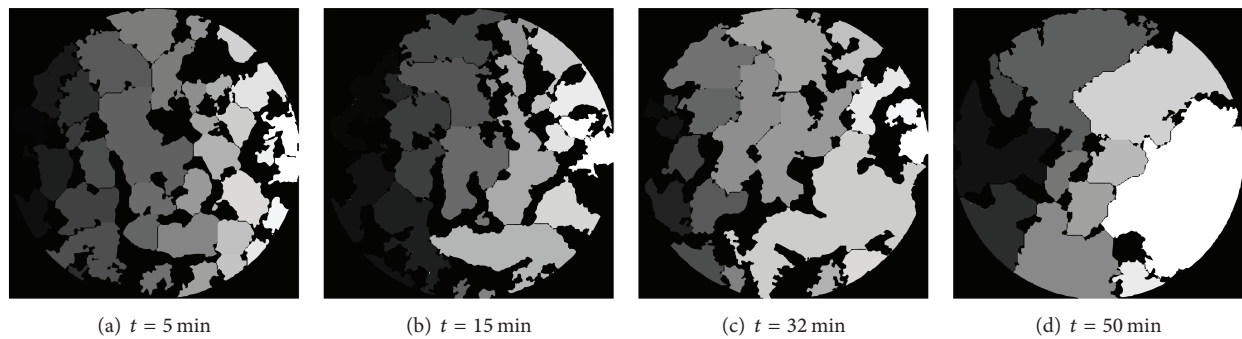


FIGURE 5: Microstructure of the same cross section using the watershed algorithm.

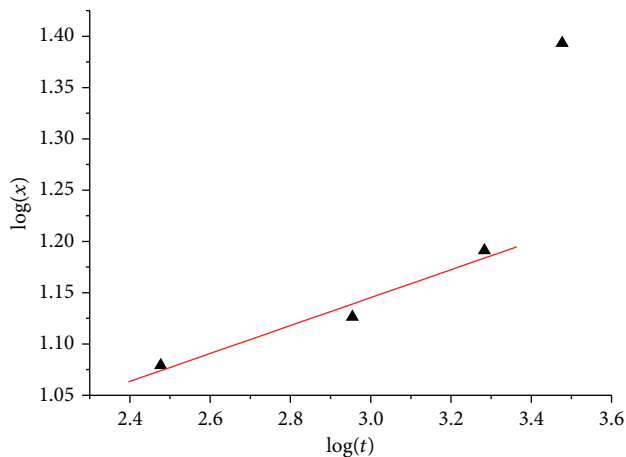


FIGURE 6: Double logarithm curve of mean neck size versus time.

where  $x$  and  $a$  represent sintering neck and particle size, respectively,  $t$  is the sintering time, and different  $n$  represents different main diffusion mechanisms. The fourth state is not taken into account because of the presence of liquid aluminum. From Figure 6, it can be seen that there is a linear relationship between  $\log(x)$  and  $\log(t)$ , and the slope is 0.1361; the value of inverse slope equals 7.3, indicating that surface diffusion was the dominant diffusion mechanism, which was caused by conductance characteristic of metals. Al and Ti are electrical conductors; the eddy current loss induced

by the external microwave fields constitutes the main loss mechanism. This eddy current is along the particle surface layer with the thickness about  $1\ \mu\text{m}$  and will probably provide an additional driving force for mass diffusion on the particle surface. Therefore, on the Al and Ti particle surface, the mass transformation process was promoted preferentially.

Pores of a material reduce its mechanical properties, such as compressive strength, modulus, shear strength, and flexural strength [15]. With the movement of grain boundaries which is caused by the chemical potential difference at high-negative-curvature neck surfaces and grain boundaries, pores become fewer and neighboring particles become close to each other, with the disappearance of small particles, the number of particles is reduced, and the size is gradually increased (Figures 5 and 7). The temperature was measured by thermal infrared imager; the model was Thermo Tracer TH5104 (temperature range  $-10^\circ\text{C}\sim 1500^\circ\text{C}$ , accuracy  $\pm 1.0\%$ ). As shown in Figure 7, the temperature increases to  $1381.1^\circ\text{C}$ , which is higher than the melting point of Al. It can be inferred that liquid aluminum was wetting on the surface of titanium and produced a capillary force. Densification process was accelerated by the force; it can be found in the rapid growth of particles in Figures 4(d), 5(d), and 7.

#### 4. Conclusion

Based on the SR-CT technique, microstructure evolution of Ti-Al metal powder mixture was observed, and through the design of equipment and the introduction of excellent

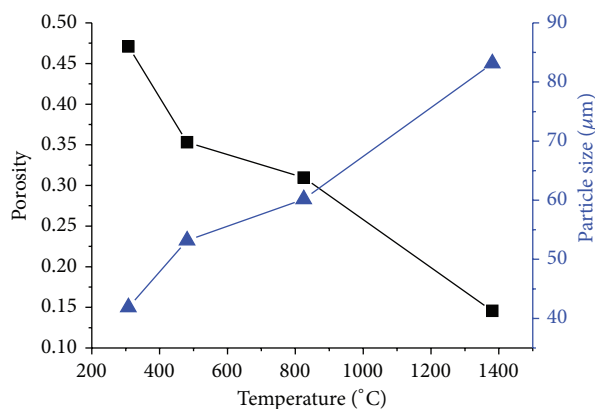


FIGURE 7: Mean particle size and porosity at different temperature.

reconstruction method, the spatial resolution was firstly increased to  $0.37 \mu\text{m}/\text{pixel}$  during microwave sintering, which demonstrated that high-resolution experiments under electromagnetic and high temperature compound fields were feasible. The reconstructed 3D images provided good understanding of various sintering phenomena. Parameters that typically influenced the mechanical properties such as neck size, porosity, and average particle size were analyzed. The neck size-time curve was obtained and the neck growth exponent was 7.3, which indicated that surface diffusion was the main diffusion mechanism, and the reason was the eddy current loss induced by the external microwave fields providing an additional driving force for mass diffusion on the particle surface. From the reconstructed images and the curve of average particle size versus temperature, it was believed that the presence of liquid phase aluminum accelerated the particle growth and densification. In this exploratory study, only a small part of the data acquired by SR-CT was used for quantitative statistical analysis. The 3D reconstructed images represent the complete evolution of microstructure in high temperature and microwave compound fields, such as the smoothness and relative positions of particles, the volume shrinkage of the powder system, and collapse caused by thermal stress; all of these parameters are vital and need to be studied, and they contain the kinetic and thermodynamic information which directly determine the performance of the materials. The challenge is to decouple the information and find the key influence parameters used to calculation model, which makes the study on the sintering more thorough.

### Conflict of Interests

The authors declare that there is no conflict of interests regarding the publication of this paper.

### Acknowledgments

This paper was supported by the National Nature Science Foundation of China under Contract nos. 11272305, 11172290, and 10902108 and the National Basic Research Program of China (973 Program, Grant no. 2012CB937504). The authors

greatly acknowledge Jian Fang and Wen-chao Liu at USTC and Hong-lan Xie, Biao Deng, and Rong-chang Chen at SSRF for their valuable contribution to this work.

### References

- [1] Y. Kawamura, K. Hayashi, A. Inoue, and T. Masumoto, "Rapidly solidified powder metallurgy Mg97Zn1Y2 alloys with excellent tensile yield strength above 600 MPa," *Materials Transactions*, vol. 42, no. 7, pp. 1172–1176, 2001.
- [2] E. O. Ezugwu and Z. M. Wang, "Titanium alloys and their machinability—a review," *Journal of Materials Processing Technology*, vol. 68, no. 3, pp. 262–274, 1997.
- [3] J. Yan, Y. Shen, F. Li, and T. Li, "Synthesis and photocatalytic properties of  $\text{ZnWO}_4$  nanocrystals via a fast microwave-assisted method," *The Scientific World Journal*, vol. 2013, Article ID 458106, 8 pages, 2013.
- [4] S. Bodhak, S. Bose, and A. Bandyopadhyay, "Densification study and mechanical properties of microwave-sintered mullite and mullite-zirconia composites," *Journal of the American Ceramic Society*, vol. 94, no. 1, pp. 32–41, 2011.
- [5] R. Roy, D. Agrawal, J. Cheng, and S. Gedeonshvili, "Full sintering of powdered-metal bodies in a microwave field," *Nature*, vol. 399, no. 6737, pp. 668–670, 1999.
- [6] F. Beckmann, R. Grupp, A. Haibel et al., "In-situ synchrotron X-ray microtomography studies of microstructure and damage evolution in engineering materials," *Advanced Engineering Materials*, vol. 9, no. 11, pp. 939–950, 2007.
- [7] X. D. Li, X. F. Hu, Y. Hu, and Y. Kan, "Synchrotron radiation tomography for reconstruction of layer structures and internal defects of composite materials," *Chinese Journal of Lasers B*, vol. 8, no. 6, pp. 503–508, 1999.
- [8] A. Vagnon, O. Lame, D. Bouvard, M. Di Michiel, D. Bellet, and G. Kapelski, "Deformation of steel powder compacts during sintering: correlation between macroscopic measurement and in situ microtomography analysis," *Acta Materialia*, vol. 54, no. 2, pp. 513–522, 2006.
- [9] F. Xu, Y. C. Li, X. F. Hu, Y. Niu, J. Zhao, and Z. Zhang, "In situ investigation of metal's microwave sintering," *Materials Letters*, vol. 67, no. 1, pp. 162–164, 2012.
- [10] R. C. Chen, H. L. Xie, L. Rigon, R. Longo, E. Castelli, and T. Q. Xiao, "Phase retrieval in quantitative x-ray microtomography with a single sample-to-detector distance," *Optics Letters*, vol. 36, no. 9, pp. 1719–1721, 2011.
- [11] R. C. Chen, D. Dreossi, L. Mancini et al., "PITRE: software for phase-sensitive X-ray image processing and tomography reconstruction," *Journal of Synchrotron Radiation*, vol. 19, part 5, pp. 836–845, 2012.
- [12] J. Ma, J. F. Diehl, E. J. Johnson et al., "Systematic study of microwave absorption, heating, and microstructure evolution of porous copper powder metal compacts," *Journal of Applied Physics*, vol. 101, no. 7, Article ID 074906, 2007.
- [13] D. L. Johnson, "New method of obtaining volume, grain-boundary, and surface diffusion coefficients from sintering data," *Journal of Applied Physics*, vol. 40, no. 1, pp. 192–200, 1969.
- [14] G. C. Kuczynski, "Self-diffusion in sintering of metallic particles," *Metallurgical and Materials Transactions*, vol. 185, no. 2, pp. 169–178, 1949.
- [15] L. Olmos, C. L. Martin, and D. Bouvard, "Sintering of mixtures of powders: experiments and modelling," *Powder Technology*, vol. 190, no. 1-2, pp. 134–140, 2009.

## Research Article

# In Situ Investigation of the 3D Mechanical Microstructure at Nanoscale: Nano-CT Imaging Method of Local Small Region in Large Scale Sample

Bo Dong,<sup>1</sup> Feng Xu,<sup>1</sup> Xiao-fang Hu,<sup>1</sup> Hong-yan Qu,<sup>1</sup> Dan Kang,<sup>1</sup> and Ti-qiao Xiao<sup>2</sup>

<sup>1</sup> CAS Key Laboratory of Mechanical Behavior and Design of Materials, University of Science and Technology of China, Hefei 230026, China

<sup>2</sup> Shanghai Institute of Applied Physics, Chinese Academy of Sciences, Shanghai 201204, China

Correspondence should be addressed to Feng Xu; xufeng3@ustc.edu.cn

Received 31 October 2013; Accepted 31 December 2013; Published 27 February 2014

Academic Editors: Y. Fu and G. Pedrini

Copyright © 2014 Bo Dong et al. This is an open access article distributed under the Creative Commons Attribution License, which permits unrestricted use, distribution, and reproduction in any medium, provided the original work is properly cited.

To investigate the local micro-/nanoscale region in a large scale sample, an image reconstruction method for nanometer computed tomography (nano-CT) was proposed in this paper. In the algorithm, wavelets were used to localize the filtered-backprojection (FBP) algorithm because of its space-frequency localization property. After the implementation of the algorithm, two simulation local reconstruction experiments were performed to confirm its effectiveness. Three evaluation criteria were used in the experiments to judge the quality of the reconstructed images. The experimental results showed that the algorithm proposed in this paper performed best because (1) the quality of its results had improved 20%–30% compared to the results of FBP and 10%–30% compared to the results of another wavelet algorithm; (2) the new algorithm was stable under different circumstances. Besides, an actual reconstruction experiment was performed using real projection data that had been collected in a CT experiment. Two-dimensional (2D) and three-dimensional (3D) images of the sample were reconstructed. The microstructure of the sample could be clearly observed in the reconstructed images. Since much attention has been directed towards the nano-CT technique to investigate the microstructure of materials, this new wavelet-based local tomography algorithm could be considered as a meaningful effort.

## 1. Introduction

With the rapid development of material science, advanced experiment and investigation technique have been developed and used to investigate the micro-/nanoscale morphology and mechanical properties of samples. It is well known that the mechanical properties are determined by the material itself and its internal microstructure. It has been found that the mechanical properties of materials changed greatly as their internal structure varies from macroscale to micro-/nanoscale. So it is very important to find the technique that is capable of investigating the micro-/nanoscale structure and mechanical properties. The major investigation techniques included electron microscope and ultrasonic inspection. But considering that the structure to be investigated was extremely tiny and the sample was sometimes placed in external field (including stress, heat and electric), those

techniques could not complete the investigation under these circumstances. But the CT technique was a good choice because of its nondestructive and noncontacted characteristics. More importantly, 2D and 3D images of the internal microstructure of materials could be obtained by CT and the images could achieve micro-/nanoscale spatial resolution. Taking the nano-CT device in Beijing Synchrotron Radiation Facility as an example, its spatial resolution has reached 30 nm/pixel.

However, the number of pixels is limited by the size of the X-ray acquisition lens. If the spatial resolution was improved, the view field decreased. Once again taking the nano-CT device as an example, there were 1024 pixels along the horizontal direction. So the transverse size of the view field was about 30  $\mu\text{m}$ . If the size of a sample exceeded that number, the sample could not be correctly reconstructed using conventional image reconstruction algorithm (i.e.,

the FBP). On the other hand, fabricating tiny samples was usually a challenge and the samples may be too small to represent the real structure of the material. Thus, how to complete exact tomography under the condition of relative large sample and small view field has become a problem that needs urgent solution. The problem could also be described as local reconstruction in which only the projections of a small local region were acquired and used. The corresponding image method was referred to as local reconstruction algorithm. During the past years, several different local reconstruction algorithms have been proposed by Smith [1–3], Katsevich [4, 5], Noo and Pan [6, 7], and so forth.

Wavelets have received much attention in the past few years. As wavelets are designed to have many good characteristics, it is possible to apply wavelet theory to image reconstruction field. The research on that aspect has been developed rapidly. Some local tomography algorithms have been proposed in recent years [8–12].

In this paper, a new wavelet-based reconstruction algorithm was proposed and implemented. At first, the reason why the FBP could not complete local reconstruction was discussed. Then a new local reconstruction algorithm based on wavelet was proposed and implemented. The key to this algorithm is that many wavelets have the space-frequency localization property. The difference between this new method and another wavelet reconstruction algorithm was also discussed. Next, simulation experiments were performed to test the algorithm. The results of the new algorithm were presented in this paper, together with the results of other algorithms. Besides, the new algorithm was applied to an actual CT experiment and the reconstructed images of local area were also presented.

## 2. Algorithm and Implementation

The most commonly used image reconstruction algorithm is the FBP. However, it is not competent to reconstruct a local region with only local projection data. The reason is that the ideal ramp filtering function in the algorithm is truncated by a spectral window in frequency domain and the windowed ramp filter is unbounded in space domain. So the key point of local reconstruction is to find a window function which ensures that the windowed ramp filter is bounded both in frequency and space domain. A possible alternative is the wavelet due to its time-frequency localization property. So the wavelet-based local reconstruction algorithm was proposed. More details about it will be given below.

At the beginning, the terminology and definitions required in the subsequent discussions will be briefly introduced. In this paper, the following notations are used. The  $n$  dimensional Euclidean space is denoted by  $R^n$ . The Fourier transform in  $R^n$  is defined by  $\hat{f}(\vec{\omega}) = \int_{R^n} f(\vec{x}) e^{i2\pi\vec{\omega}\cdot\vec{x}} d\vec{x} = F[f]$ . The inverse Fourier transform is defined by  $f(\vec{x}) = \int_{R^n} \hat{f}(\vec{\omega}) e^{-i2\pi\vec{x}\cdot\vec{\omega}} d\vec{\omega} = F^{-1}[\hat{f}]$ . The convolution of two measurable square-integral functions  $f(x)$  and  $g(x)$  is denoted by  $f(x) * g(x)$ , with identical notation for discrete convolution.

*2.1. The Nonlocality of FBP Coming from the Window Function.* The goal of CT is to reconstruct an image from a set of its line-integral projections. In the 2D case, the projection of  $f(x, y)$  at an angle  $\theta$  is as follows:

$$R_\theta f(s) = \int \int_{-\infty}^{\infty} f(x, y) \delta(s - x \cos \theta - y \sin \theta) dx dy. \quad (1)$$

Equation (1) is known as the Radon transform of  $f(x, y)$ .

Conversely, function  $f$  could be reconstructed from the projection data  $R_\theta f(s)$  by

$$f(x, y) = \int_0^\pi \int_{-\infty}^{\infty} (R_\theta \hat{f})(\omega) e^{j2\pi\omega(x \cos \theta + y \sin \theta)} |\omega| d\omega d\theta. \quad (2)$$

The above formula can be implemented in two steps: the filtering step and the backprojection step.

The filtering step can be written as

$$\widehat{Q}_\theta(\omega) = R_\theta \hat{f}(\omega) |\omega|. \quad (3)$$

The above formula indicates that the Radon transform data is filtered by  $|\omega|$ . This filter is referred to as the ideal ramp filter.

And the backprojection step is

$$f(x, y) = \int_0^\pi Q_\theta(x \cos \theta + y \sin \theta) d\theta. \quad (4)$$

Because the ideal ramp filter  $|\omega|$  is not bounded in frequency domain, it is expedient in practice to multiply this operator by a spectral window  $W(\omega)$  as

$$\widehat{Q}_\theta(\omega) = R_\theta \hat{f}(\omega) |\omega| W(\omega). \quad (5)$$

The above operation can be converted to space domain as

$$\begin{aligned} Q_\theta(s) &= F^{-1} [R_\theta \hat{f}(\omega) |\omega|] * F^{-1} [W(\omega)] \\ &= H\partial R_\theta f(s) * F^{-1} [W(\omega)], \end{aligned} \quad (6)$$

where  $H$  is the Hilbert transform and  $\partial$  is ordinary differentiation.

Generally, the Hamming window is chosen to be  $W(\omega)$ . In this case, the windowed ramp filter  $|\omega|W(\omega)$  is bounded in frequency domain, but it is not bounded in space domain (see Figure 1). As a consequence, in order to calculate the convolution in (6) at a point, not only those projections near that point, but also those far away from that point are required. It means that the inverse Radon transform based on (2) cannot be accomplished locally. This property is known as the nonlocality of the FBP algorithm.

Considering the equivalent relation that  $F^{-1}[|\omega|W(\omega)] = H\partial F^{-1}[W(\omega)]$ , the spreading of the support of the windowed ramp filter in space domain will not occur if the Hilbert transform of a window function is compactly supported. It has been noted that if a function has numbers of vanishing moments, then its Hilbert transform will decay very rapidly at infinity [11, 12]. If a compactly supported function has this property, then the essential support of its Hilbert transform should not be large. This property is fundamental to the wavelet local reconstruction algorithm, which will be discussed below.

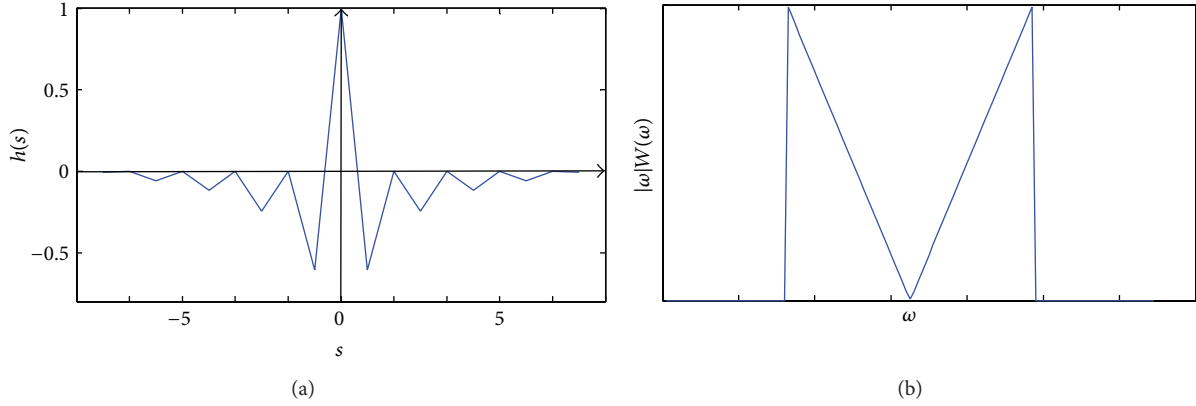


FIGURE 1: The truncated ramp filter by Hamming window. (a) Space domain. (b) Frequency domain.

**2.2. Localization of FBP by Using Wavelet as the Window Function.** For the reasons outlined above, the functions which are compactly supported and have several vanishing moments are wanted. This second condition will ensure that the functions remain compactly supported after the differential and Hilbert transform process and will ensure that a reconstruction from local data can be accomplished. Wavelets are generally designed with many vanishing moments. So they can be used as the window function in local reconstruction algorithm. In this section, a wavelet-based reconstruction algorithm is presented. The key point of the algorithm is that each projection is filtered by four different wavelet filters, respectively. The filtering formula comes from (6) but the window function is replaced by the Radon transform of 2D wavelet functions:

$$\begin{aligned}
 Q_{\theta}^A(s) &= H\partial R_{\theta}f * R_{\theta}(\Phi(x, y)), \\
 Q_{\theta}^{D_1}(s) &= H\partial R_{\theta}f * R_{\theta}(\Psi_1(x, y)), \\
 Q_{\theta}^{D_2}(s) &= H\partial R_{\theta}f * R_{\theta}(\Psi_2(x, y)), \\
 Q_{\theta}^{D_3}(s) &= H\partial R_{\theta}f * R_{\theta}(\Psi_3(x, y)).
 \end{aligned}
 \tag{7}$$

In (7), the four 2D wavelet functions  $\Phi(x, y)$ ,  $\Psi_1(x, y)$ ,  $\Psi_2(x, y)$ , and  $\Psi_3(x, y)$  are composed by the 1D orthogonal wavelet basis  $\Psi(x)$  and scaling function  $\Phi(x)$ :

$$\begin{aligned}
 \Phi(x, y) &= \Phi(x)\Phi(y), \\
 \Psi_1(x, y) &= \Phi(x)\Psi(y), \\
 \Psi_2(x, y) &= \Psi(x)\Phi(y), \\
 \Psi_3(x, y) &= \Psi(x)\Psi(y).
 \end{aligned}
 \tag{8}$$

Many kinds of wavelet have been designed by researchers so far. For example, Daubechies, Coiflets, Symlets are commonly used in signal and image processing. Most kinds of wavelet come from a corresponding unique function called the scaling function (see Figure 2). The scaling function has some similar properties with wavelet. It is compactly supported and has high order vanishing moments.

As wavelet and scaling functions are both compactly supported and have many vanishing moments, the functions  $H\partial R_{\theta}g(x, y)$  for each  $\theta$  will decay rapidly outside the support interval, where  $g(x, y)$  stands for the four functions denoted in (8). Therefore the filtering in (7) can be accomplished locally. In order to calculate the filtered projection at a point, only a few projections near that point are required. This is the reason why this wavelet-based reconstruction algorithm can complete local tomography.

Besides, the filtering process in (7) can reduce aliasing and high-frequency noise. To explain this it is better to switch (7) into the frequency domain form:

$$\widehat{Q}_{\theta}(\omega) = R_{\theta}\widehat{f}(\omega) |\omega| \widehat{g}(\omega \cos \theta, \omega \sin \theta), \tag{9}$$

where  $g$  is one of the four functions denoted in (8).

It is obvious that the filter at a certain angle is the multiplication of the ideal ramp filter and the slice of the Fourier transform of the 2D wavelet at the same angle:

$$\begin{aligned}
 H_{\theta}^A &= |\omega| \widehat{\Phi}(\omega \cos \theta, \omega \sin \theta) = |\omega| \widehat{\Phi}(\omega \cos \theta) \widehat{\Phi}(\omega \sin \theta), \\
 H_{\theta}^{D_1} &= |\omega| \widehat{\Psi}_1(\omega \cos \theta, \omega \sin \theta) = |\omega| \widehat{\Phi}(\omega \cos \theta) \widehat{\Psi}(\omega \sin \theta), \\
 H_{\theta}^{D_2} &= |\omega| \widehat{\Psi}_2(\omega \cos \theta, \omega \sin \theta) = |\omega| \widehat{\Psi}(\omega \cos \theta) \widehat{\Phi}(\omega \sin \theta), \\
 H_{\theta}^{D_3} &= |\omega| \widehat{\Psi}_3(\omega \cos \theta, \omega \sin \theta) = |\omega| \widehat{\Psi}(\omega \cos \theta) \widehat{\Psi}(\omega \sin \theta).
 \end{aligned}
 \tag{10}$$

These angle-dependent filters are simplified into  $|\omega|\widehat{\Phi}(\omega)$  and  $|\omega|\widehat{\Psi}(\omega)$  at special angles like  $\theta = 0$  or  $\theta = (\pi/2)$ . The simplified form can be referred to as the ramped scaling function and the ramped wavelet function. Figure 3 shows the spectrogram of them. It can be seen that the amplitude of the ramped scaling function and the ramped wavelet function at high frequency is lower than that of the ideal ramp filter. Thus aliasing and high-frequency noise can be reduced after filtering.

**2.3. Implementation and Comparison with Other Wavelet Algorithm.** In the following, the new wavelet-based reconstruction algorithm is summarized in four steps.

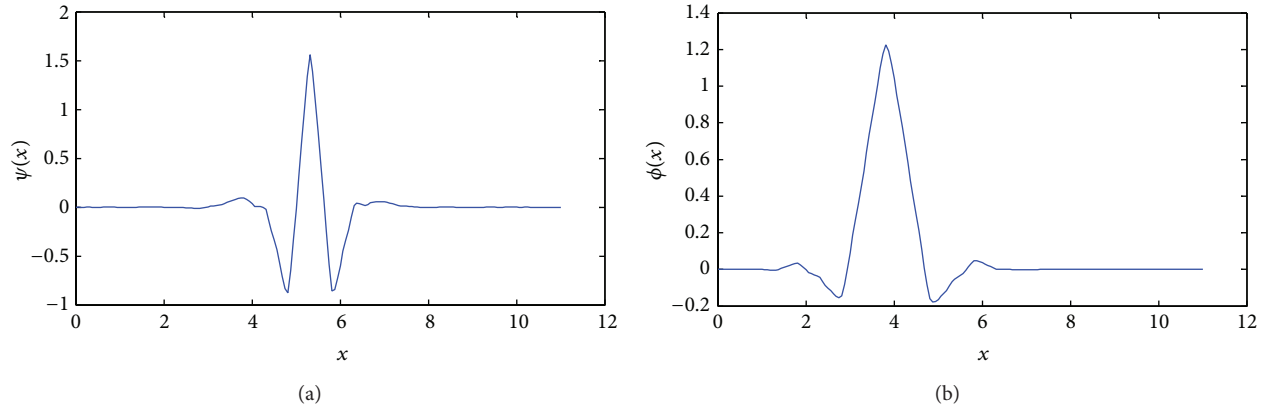


FIGURE 2: An example of wavelets. (a) Coiflets. (b) Scaling function of Coiflets.

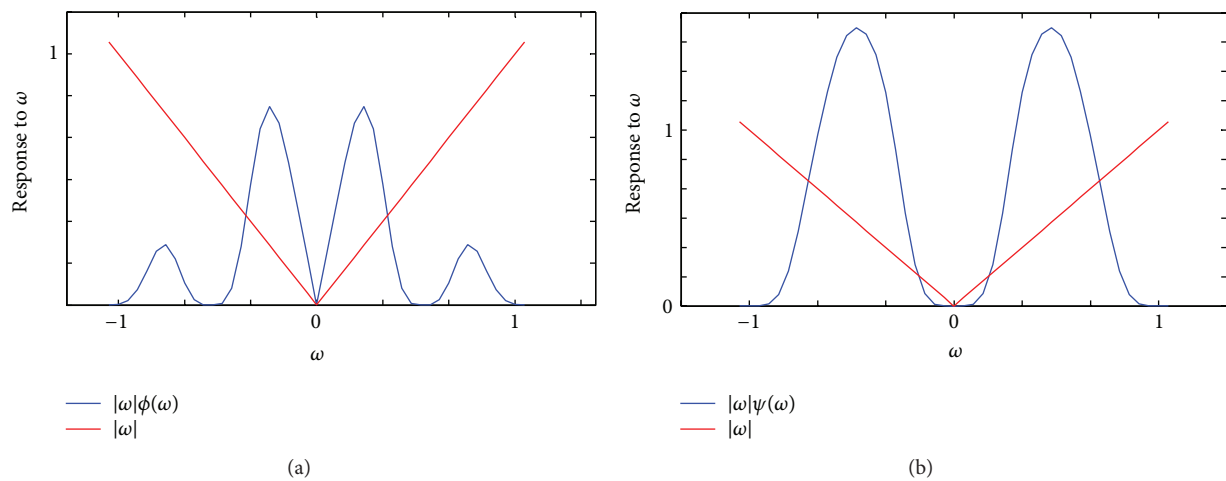


FIGURE 3: Spectrogram of (a) ramped scaling function and (b) ramped wavelet function. In comparison, the ideal ramp filter was also curved in red line.

- (I) For each projection data at angle  $\theta$ , calculate its differentiation and Hilbert transform.
- (II) The results that have been obtained in step (I) are filtered as the formulas in (7).
- (III) Filtered projections are back projected using (4) and the results are, respectively, the approximation coefficient, the horizontal detail coefficient, the vertical detail coefficient, and the diagonal detail coefficient.
- (IV) The four coefficients are composed into the reconstruction image by 2D inverse wavelet transform.

However, it's worth mentioning that another wavelet algorithm has been proposed in [13]. The main difference is that in [13] the differential operator and the Hilbert operator are conducted to the 2D wavelet function, instead of the projection data. So the filtering step can be written as

$$Q_{\theta}(s) = R_{\theta}f * H\partial R_{\theta}g(x, y). \quad (11)$$

It can be derived that (7) and (11) are equivalent under continuous situation. But they give different results in practice because actual local projection data are truncated and

sampled discretely. Thus the local projection can be considered as a compactly supported function. But generally it does not have vanishing moment. According to (7), after the differentiation and Hilbert transform, the original compactly supported projection will no longer be compactly supported. And after the convolution with the wavelet function, the result is still not bounded (see Figures 4(a), 4(b), and 4(c)). On the other hand, according to (11), after the differentiation and Hilbert transform the wavelet function is still compactly supported. And after the convolution with the truncated projection, the support of the result is almost the same to the projection (see Figure 4(d)). Therefore the two filtering methods provide different filtered projections (see Figure 4(e)). This difference will further lead to a different reconstructed image.

### 3. Experiments and Results

In this section, two different phantom images were introduced to the local reconstruction experiment. The reconstruction algorithms included FBP and wavelet

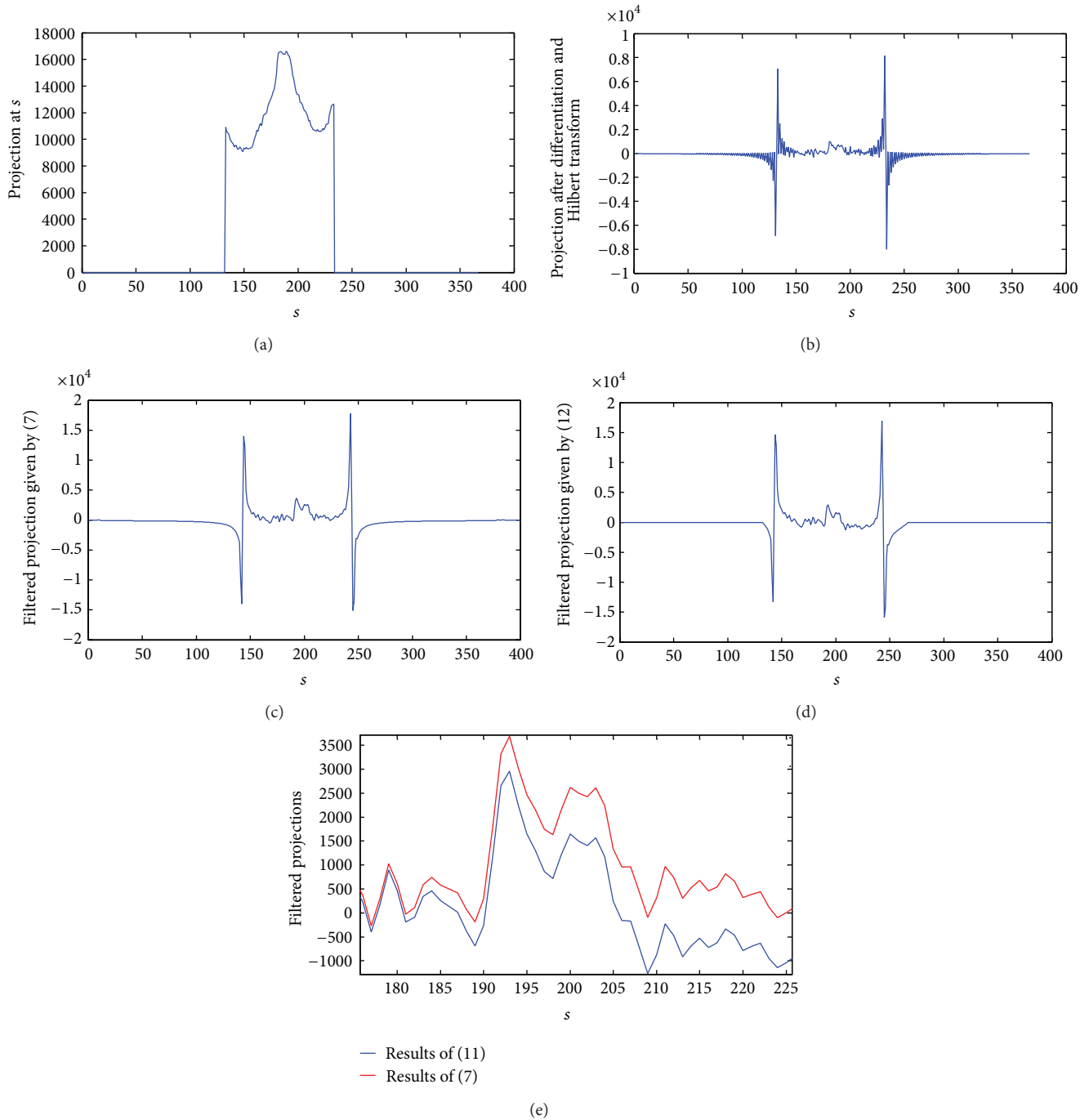


FIGURE 4: The projection of the Shepp-Logan head phantom at  $\theta = 0$  was truncated and filtered by different methods. The original length of the projection is 367, but only 100 of them were preserved and the rest were set to zero. In this figure, the horizontal axis represented the index of projection line, the vertical axis represented the projection value before and after filtering. (a) Truncated projection at  $\theta = 0$ . (b) Projection after differentiation and Hilbert transform. (c) Filtered projection given by (7). (d) Filtered projection given by (11). (e) Comparison of the filtered projections. Only a part of projections was shown in this figure.

reconstruction algorithm proposed in this paper and in [13]. To evaluate the reconstructed images, three evaluation criteria were used. The experimental results have shown that the filtered-backprojection method is not suitable for local reconstruction; the two wavelet reconstruction algorithms

can complete the mission, but the one proposed in this paper performed better than the other one.

3.1. Phantom Images and Criteria. The model images used in the experiment were the stacked particles phantom and

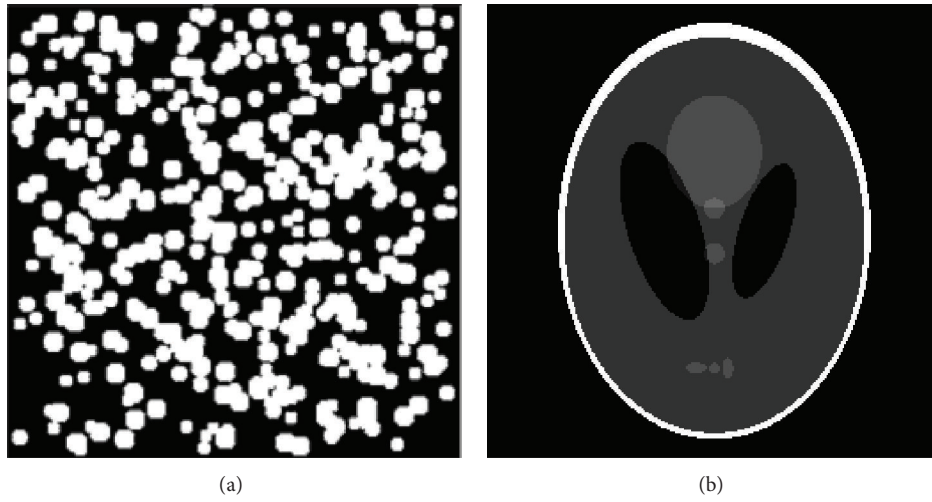


FIGURE 5: Two phantom images. (a) Stacked particles phantom. (b) Shepp-Logan head phantom.

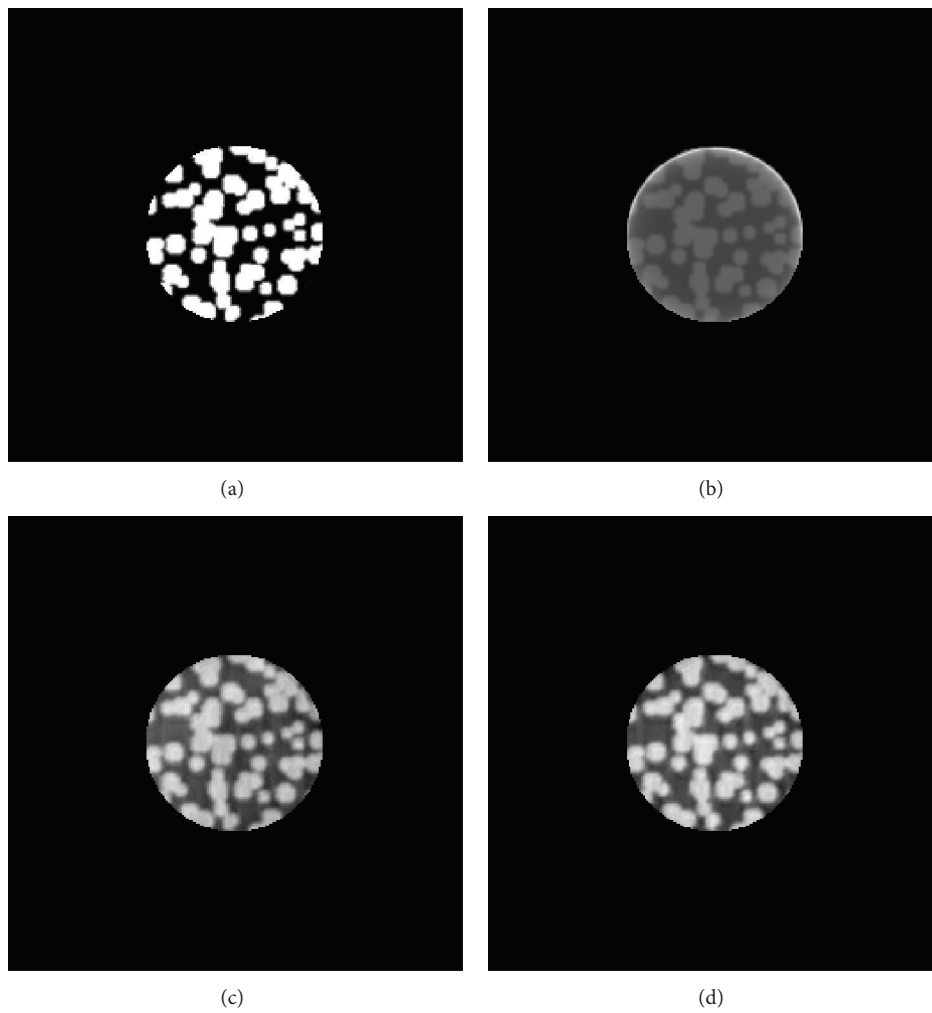


FIGURE 6: Reconstructed images of the local area in stacked particles phantom. (a) Local area in the phantom. (b) Local reconstruction using FBP. (c) Using wavelet method in [13]. (d) Using new wavelet method in this paper.

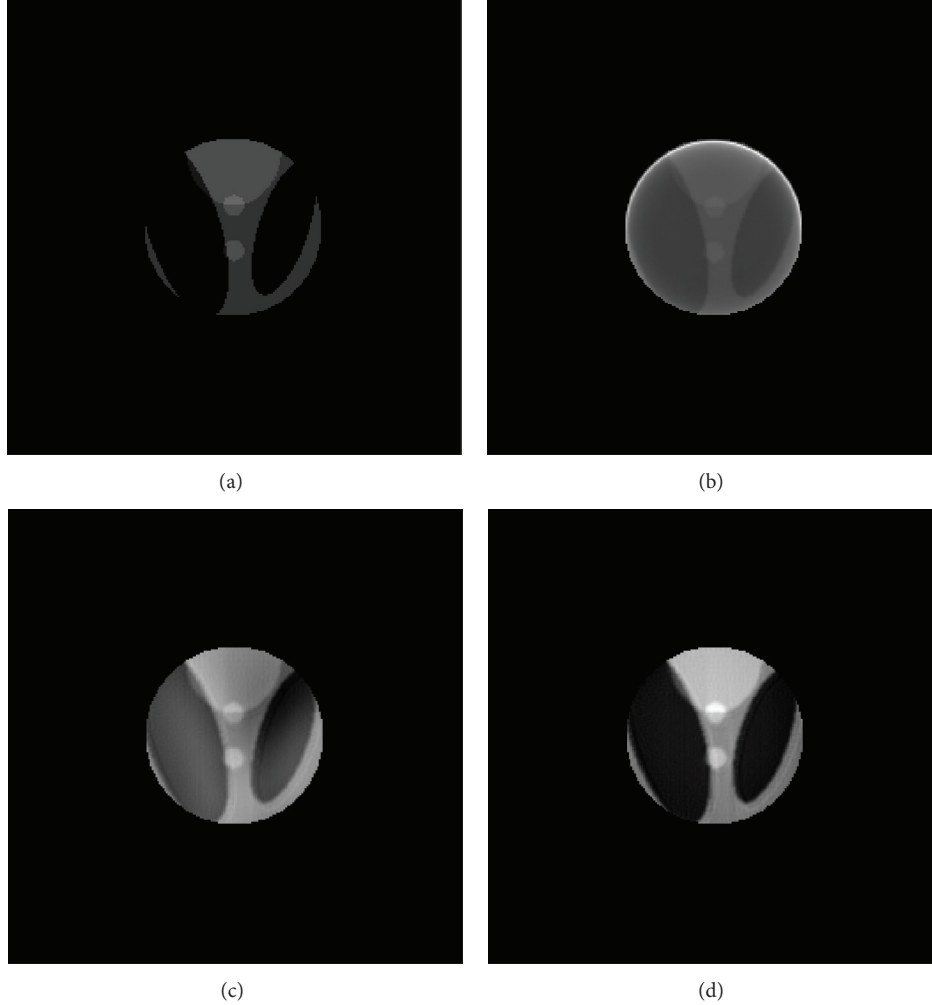


FIGURE 7: Reconstructed images of the local area in Shepp-Logan head phantom. (a) Local area in the phantom. (b) Local reconstruction using FBP. (c) Using wavelet method in [13]. (d) Using new wavelet method in this paper.

the Shepp-Logan head phantom (see Figure 5). The size of the two images was 256 by 256 pixels and the local area was a disk of 50 pixels in the center of the image. The stacked particles phantom could be considered to contain more high-frequency components because they were composed of a large number of irregularly stacked particle elements whose radius is about 5 pixels. And this image included only two colors: black and white. The Shepp-Logan head phantom was composed of several ellipse elements with different areas and grayscales. In general it could be considered to contain relatively more low-frequency components.

In the following were three criteria to objectively evaluate the differences between original and reconstructed images.

(1) Normalized mean square criterion  $d$ :

$$d = \left[ \frac{\sum_{u=1}^N \sum_{v=1}^N (T(u, v) - R(u, v))^2}{\sum_{u=1}^N \sum_{v=1}^N (T(u, v) - \bar{T})^2} \right]^{1/2}, \quad (12)$$

where  $T(u, v)$  and  $R(u, v)$  denoted the grayscale of pixels in phantom and reconstructed images.  $\bar{T}$  denoted the mean

value of the phantom image.  $d = 0$  represented exact reconstruction of the phantom. Larger  $d$  indicated greater error. Besides,  $d$  was more sensitive to large errors caused by individual pixels.

(2) Normalized average absolute distance criterion  $r$ :

$$r = \frac{\sum_{u=1}^N \sum_{v=1}^N |T(u, v) - R(u, v)|}{\sum_{u=1}^N \sum_{v=1}^N |T(u, v)|}, \quad (13)$$

$r = 0$  meant that the reconstructed image was same to the phantom. And like the previous criterion, larger  $r$  indicated greater error. But  $r$  was more sensitive to small errors caused by most pixels.

(3) Standardized covariance criterion  $c$ :

$$c = \left| \frac{\sum_{u=1}^N \sum_{v=1}^N (T(u, v) - \bar{T})(R(u, v) - \bar{R})}{\sqrt{\sum_{u=1}^N \sum_{v=1}^N (T(u, v) - \bar{T})^2 \sum_{u=1}^N \sum_{v=1}^N (R(u, v) - \bar{R})^2}} \right|, \quad (14)$$

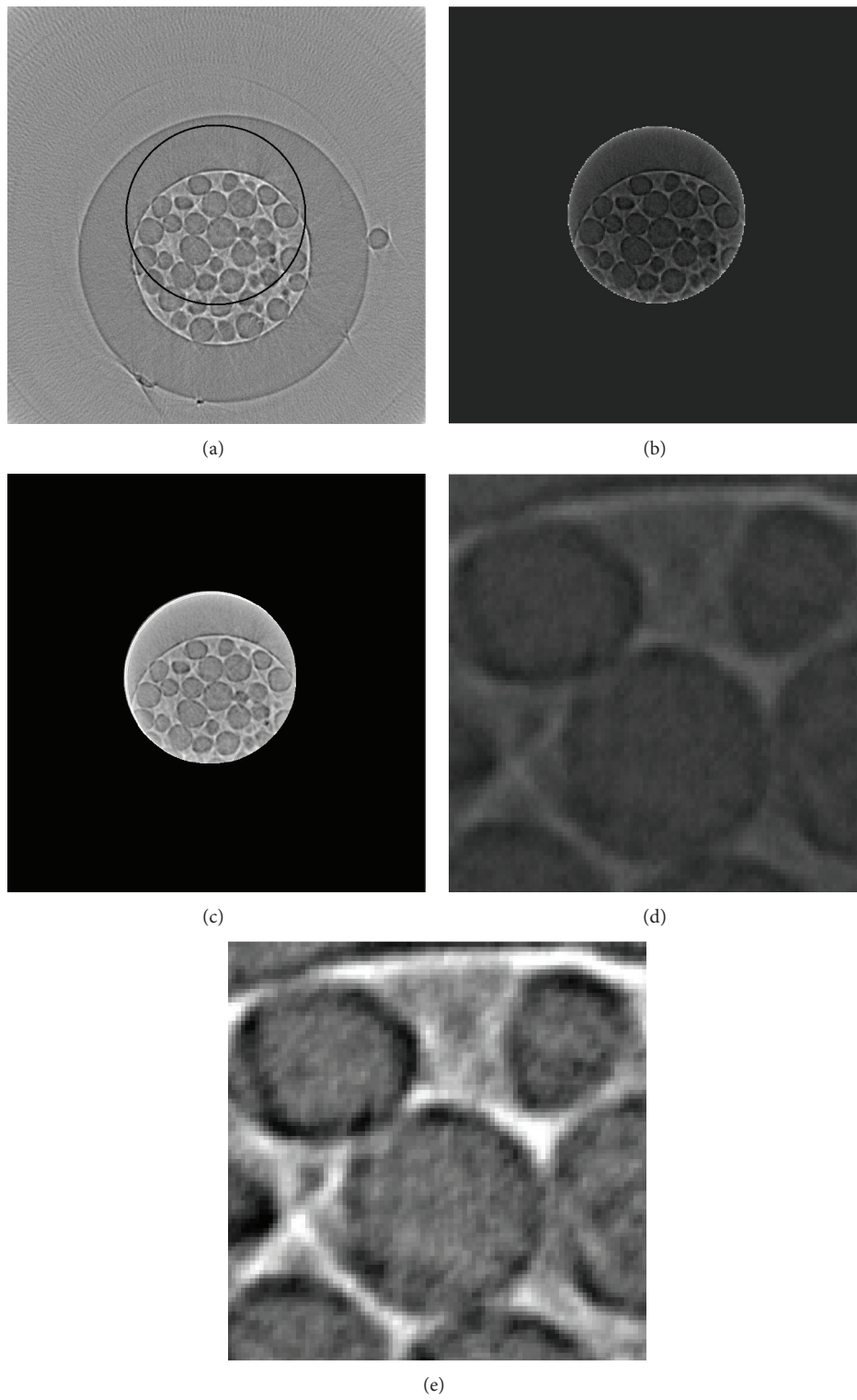


FIGURE 8: (a) Reconstruction by FBP using global data. (b) Reconstruction by FBP using local data. (c) Reconstruction by the new algorithm using local data. (d) and (e) were the amplifications of (b) and (c), respectively.

TABLE 1: Criteria values for the local reconstruction of the stacked particles phantom.

Algorithm	$d$	Relative change of $d$	$r$	Relative change of $r$	$c$	Relative change of $c$
FBP	0.6446	—	0.7782	—	0.7896	—
Method in [13]	0.4347	↑ 32.56%	0.5295	↑ 31.96%	0.9047	↑ 14.58%
Method in this paper	0.3918	↑ 39.22%	0.4749	↑ 38.97%	0.9222	↑ 16.79%

TABLE 2: Criteria values for the local reconstruction of the Shepp-Logan head phantom.

Algorithm	$d$	Relative change of $d$	$r$	Relative change of $r$	$c$	Relative change of $c$
FBP	1.8632	—	2.6380	—	0.7095	—
Method in [13]	1.7999	↑ 3.40%	2.5667	↑ 2.70%	0.8116	↑ 14.4%
Method in this paper	1.5042	↑ 19.27%	1.8156	↑ 31.18%	0.9796	↑ 38.07%

$c = 0$  indicated that the reconstructed image and the phantom image was completely irrelevant. As the degree of correlation between the two images became higher, the value of  $c$  became closer to 1.

**3.2. Results and Discussion.** The reconstructed images of the local area in stacked particles phantom were shown in Figure 6 and Table 1. And Figure 7 and Table 2 showed the reconstructed images of the Shepp-Logan head phantom. As a supplement, the relative changes of the parameters compared with the results of FBP were also calculated and listed in the tables.

From the figures and tables, the following could be found.

(1) Among the three algorithms, the FBP did not perform well in local reconstruction. The boundaries in reconstructed images were indistinct and the grayscale of the majority pixels was greatly distorted. The standardized covariance values were less than 0.9 for both phantoms. The algorithms based on wavelets could complete local reconstruction with higher quality than FBP. But in the images reconstructed by the method in [13], there existed a visible difference in grayscale among the pixels inside an element (see Figure 7(c)). At last the new wavelet algorithm performed best generally. Not only the boundaries were clearly reconstructed, but also the average grayscale of each element is close to the origin image.

(2) For the wavelet method in [13], the criteria values changed greatly according to different phantom images. As for the new wavelet method, the relative change of  $d$  and  $r$  did not vary much (between 20% and 30%) under different phantom images and values of  $c$  maintained greater than 0.9. It indicated that this algorithm was more stable and suitable for a wide range of situations.

(3) The criteria values of the reconstructed particle phantom were better than those of the head phantom. This may be caused by the different complexity of the phantom images. Though the particle phantom involved large number of particle elements, they were generally in the same size. And there were only two gray levels in the image. So the complexity of the particle phantom could be considered to be relatively low. On the contrary, in the head phantom, the size of the ellipse varies from small to large and there were six gray levels in this phantom. So the head phantom is more

complex than the particle phantom and it is more difficult to reconstruct it.

**3.3. Local Reconstruction Using Real Experimental Data.** In previous section, the effectiveness of this new wavelet method was validated by two phantom images. In this section the method was applied to practical data collected in a CT experiment. Figure 8(a) showed a slice of the sample reconstructed by FBP. The projections had been collected at 180 angles over 180 degrees. And the length of each projection was 1207 pixels. Using the new wavelet algorithm, a local centered region of radius 150 pixels had been reconstructed. So only 25% of the projections were used in the reconstruction (see Figure 8(c)). The reconstructed local region was as good as what could be obtained using the FBP and global data. For comparison, the local region was reconstructed using the FBP and local data and the result was shown in Figure 8(b). The amplifications of the images reconstructed by the new method and FBP were, respectively, shown in Figures 8(d) and 8(e). It could be seen that the image was brighter and the boundaries of particles are clearer in Figure 8(e). This fact indicated that the wavelet method had advantages over the FBP when reconstructing local region.

## 4. Conclusion

Based on the properties of wavelet, a local reconstruction algorithm has been proposed and implemented. It has been observed that for some wavelet bases with many vanishing moments, the scaling and wavelet functions have essentially the same support after differentiation and Hilbert transform. According to this fact, a local reconstruction scheme has been developed to reconstruct a local region of a cross-section of a sample with essentially local data. Some experiments have been performed and the results confirmed the effectiveness of this new algorithm. Because this algorithm is able to reconstruct local small region in a large sample that exceeds the view field, it may contribute to make more kinds of materials appropriate for CT investigation whose spatial resolution can achieve micro-/nanoscale. However, there are still some unsolved problems. For example, when using different wavelet functions, the results of the algorithm were

different. But how to select a suitable wavelet function for a certain situation is still no solution.

### Conflict of Interests

The authors declare that there is no conflict of interests regarding the publication of this paper.

### Acknowledgments

This paper was supported by the National Nature Science Foundation of China under Contract Nos. 11272305, 11172290, 10902108, the National Basic Research Program of China (973 Program, Grant No. 2012CB937504). The authors greatly acknowledge Jian Fang, Yu Xiao and Wen-chao Liu at USTC and Hong-lan Xie, Biao Deng and Ya-nan Fu at SSRF for their valuable contribution to this work.

### References

- [1] K. T. Smith and F. Keinert, "Mathematical foundations of computed tomography," *Applied Optics*, vol. 24, no. 23, pp. 3950–3957, 1985.
- [2] A. Faridani, E. Ritman, and K. T. Smith, "Local tomography," *SIAM Journal on Applied Mathematics*, vol. 52, no. 2, pp. 459–484, 1992.
- [3] A. Faridani, D. V. Finch, E. L. Ritman, and K. T. Smith, "Local tomography II," *SIAM Journal on Applied Mathematics*, vol. 57, no. 4, pp. 1095–1127, 1997.
- [4] A. I. Katsevich, "Local reconstructions in exponential tomography," *Journal of Mathematical Analysis and Applications*, vol. 199, no. 2, pp. 425–444, 1996.
- [5] A. I. Katsevich and A. G. Ramm, "Pseudolocal tomography," *SIAM Journal on Applied Mathematics*, vol. 56, no. 1, pp. 167–191, 1996.
- [6] F. Noo, R. Clackdoyle, and J. D. Pack, "A two-step Hilbert transform method for 2D image reconstruction," *Physics in Medicine and Biology*, vol. 49, no. 17, pp. 3903–3923, 2004.
- [7] X. Pan, D. Xia, Y. Zou, and L. Yu, "A unified analysis of FBP-based algorithms in helical cone-beam and circular cone- and fan-beam scans," *Physics in Medicine and Biology*, vol. 49, no. 18, pp. 4349–4369, 2004.
- [8] M. Holschneider, "Inverse Radon transforms through inverse wavelet transforms," *Inverse Problems*, vol. 7, no. 6, article 008, pp. 853–861, 1991.
- [9] G. Kaiser and R. F. Streater, "Windowed Radon transforms," in *Wavelets: a Tutorial in Theory and Applications*, C. K. Chui, Ed., pp. 199–441, Academic Press, New York, NY, USA, 1992.
- [10] D. Walnut, "Application of Gabor and wavelet expansions to the radon transform," in *Probabilistic and Stochastic Methods in Analysis, with Applications*, J. S. Byrnes, J. L. Byrnes, K. A. Hargreaves, and K. Berry, Eds., pp. 187–205, Kluwer Academic Publishers, Boston, Mass, USA, 1992.
- [11] C. Berenstein and D. Walnut, "Local inversion of the Radon transform in even dimensions using wavelets," in *75 Years of Radon Transform*, S. Gindikin and P. Michor, Eds., pp. 38–58, International Press, Cambridge, Mass, USA, 1994.
- [12] T. Olson and J. Destefano, "Wavelet localization of the Radon transform," *IEEE Transactions on Signal Processing*, vol. 42, no. 8, pp. 2055–2067, 1994.
- [13] F. Rashid-Farrokhi, K. J. R. Liu, C. A. Berenstein, and D. Walnut, "Wavelet-based multiresolution local tomography," *IEEE Transactions on Image Processing*, vol. 6, no. 10, pp. 1412–1430, 1997.

## Research Article

# Automatic Three-Dimensional Measurement of Large-Scale Structure Based on Vision Metrology

Zhaokun Zhu,<sup>1,2</sup> Banglei Guan,<sup>1,2</sup> Xiaohu Zhang,<sup>1,2</sup> Daokui Li,<sup>1</sup> and Qifeng Yu<sup>1,2</sup>

<sup>1</sup> College of Aerospace Science and Engineering, National University of Defense Technology, Changsha 410073, China

<sup>2</sup> Hunan Provincial Key Laboratory of Image Measurement and Vision Navigation, National University of Defense Technology, Changsha 410073, China

Correspondence should be addressed to Zhaokun Zhu; warrior.zzk@gmail.com

Received 8 November 2013; Accepted 31 December 2013; Published 17 February 2014

Academic Editors: Y. Fu and G. Pedrini

Copyright © 2014 Zhaokun Zhu et al. This is an open access article distributed under the Creative Commons Attribution License, which permits unrestricted use, distribution, and reproduction in any medium, provided the original work is properly cited.

All relevant key techniques involved in photogrammetric vision metrology for fully automatic 3D measurement of large-scale structure are studied. A new kind of coded target consisting of circular retroreflective discs is designed, and corresponding detection and recognition algorithms based on blob detection and clustering are presented. Then a three-stage strategy starting with view clustering is proposed to achieve automatic network orientation. As for matching of noncoded targets, the concept of matching path is proposed, and matches for each noncoded target are found by determination of the optimal matching path, based on a novel voting strategy, among all possible ones. Experiments on a fixed keel of airship have been conducted to verify the effectiveness and measuring accuracy of the proposed methods.

## 1. Introduction

As science and technology develop, more and more large-scale structures come into our lives, such as bridges, tunnels, airplanes, airships, wind turbine blades, and antennas. To ensure safety and prevent potential accidents and disasters, it is necessary to conduct mechanical testing and dimensional quality monitoring for these large-scale structures, which require automatic three-dimensional measurement with high metric precision.

Deformation measurement of large-scale structures constitutes a 3D coordinate measuring problem involving large measurement ranges and high measuring accuracy. Compared to other measuring means such as strain gauge method [1, 2], surveying method [3, 4], and GPS method [5–7], photogrammetry displays a number of advantages [8]. For example, this image-based technology facilitates high-precision noncontact measurement, and it can handle very large arrays of 3D feature points simultaneously, thus making it suitable for time-constrained deformation measurement of large-scale structures.

Nonexpert user oriented vision metrology systems are well established in industrial metrology [9–13], though

application of photogrammetric measuring systems warrants further research and development to make the technology optimally qualified for deformation monitoring of large-scale structures.

Usually, in order to facilitate image measurement, retroreflective targets and highly controlled illumination conditions are employed in vision metrology, and together with the usage of coded target system [14–17], full automation of 3D measurement can be achieved. Recent developments in computer vision put emphasis upon 3D reconstruction of scene structure without the artificial targeting and controlled lighting conditions, which involves extraction of natural feature, feature description, dense matching [18–20], and so forth. These are the developing trends of photogrammetric vision metrology as well, but compared to photogrammetric vision metrology, without targeting, controlled lighting, and coded targets, so far these developments are still far from being fully automated for accurate 3D measurement of large-scale structure.

In this paper, we focus on photogrammetric vision metrology for fully automatic 3D measurement of large-scale structure; all relevant key techniques involved are studied, such as coded target, network orientation, and matching

of noncoded target. All will be described in the following sections detailedly.

## 2. Preliminaries

**2.1. Pinhole Imaging Model.** The image point is denoted by a homogeneous 3-vector  $\mathbf{x}$ , and the world point is denoted by a homogeneous 4-vector  $\mathbf{X}$ ; then the Pinhole Imaging Model can be simply expressed by

$$a\mathbf{x} = K [R | \mathbf{t}] \mathbf{X}, \quad (1)$$

where the scalar  $a$  is an arbitrary scale factor.  $K$  is a  $3 \times 3$  upper triangular calibration matrix, holding the intrinsic parameters.  $R$  is a  $3 \times 3$  rotation matrix and  $\mathbf{t}$  is a 3-vector representing the translation vector;  $R$  and  $\mathbf{t}$  together denote the rigid body transformation between the view and the world coordinate system. The  $3 \times 4$  matrix  $P = K[R | \mathbf{t}]$  is the projection matrix.

**2.2. Epipolar Geometry.** As shown in Figure 1, a spatial point  $P$  is projected to  $\mathbf{x}$  and  $\mathbf{x}'$ , respectively, on view  $S$  and  $S'$ , obviously,  $P$ ,  $\mathbf{x}$ ,  $\mathbf{x}'$ , and two optical centers  $C$  and  $C'$  are in the same spatial plane  $\pi$ , this is the well-known coplanarity or epipolar constraint, which is encoded in the  $3 \times 3$  fundamental matrix  $F$  [21]:

$$\mathbf{x}'^T F \mathbf{x} = 0. \quad (2)$$

It can be deduced more intuitively in this way that  $\mathbf{x}$  and  $\mathbf{x}'$  are located on the epipolar lines  $\mathbf{l} = F^T \mathbf{x}'$  and  $\mathbf{l}' = F \mathbf{x}$ , respectively, which means  $\mathbf{l}^T \mathbf{x} = 0$  and  $\mathbf{l}'^T \mathbf{x}' = 0$ , respectively; both can be rewritten as (2).

The relative pose between view  $S$  and  $S'$  is  $[R | \mathbf{t}]$ , slightly different from what is stated in 2.1; the coordinate system of view  $S$ , which is  $C$ -XYZ, is now the world coordinate system. Let  $[\mathbf{t}]_{\times}$  denote the skew symmetric matrix:

$$[\mathbf{t}]_{\times} = \begin{bmatrix} 0 & -t_z & t_y \\ t_z & 0 & -t_x \\ -t_y & t_x & 0 \end{bmatrix}, \quad (3)$$

then the fundamental matrix  $F$  is

$$F = K'^T [\mathbf{t}]_{\times} R K^{-1}, \quad (4)$$

where  $K$  and  $K'$  are the calibration matrices of view  $S$  and  $S'$ , respectively.

The fundamental matrix  $F$  can be considered without knowledge of the calibration matrices [21], once  $K$  and  $K'$  are known, which means view  $S$  and  $S'$  are calibrated; image points can be normalized

$$\hat{\mathbf{x}} = K^{-1} \mathbf{x}, \quad \hat{\mathbf{x}}' = K'^{-1} \mathbf{x}', \quad (5)$$

where  $\hat{\mathbf{x}}$  and  $\hat{\mathbf{x}}'$  are the normalized image points of  $\mathbf{x}$  and  $\mathbf{x}'$ , respectively; then the epipolar constraint (2) can be simplified to

$$\hat{\mathbf{x}}'^T E \hat{\mathbf{x}} = 0, \quad (6)$$

where  $E$  is the  $3 \times 3$  essential matrix:

$$E = [\mathbf{t}]_{\times} R. \quad (7)$$

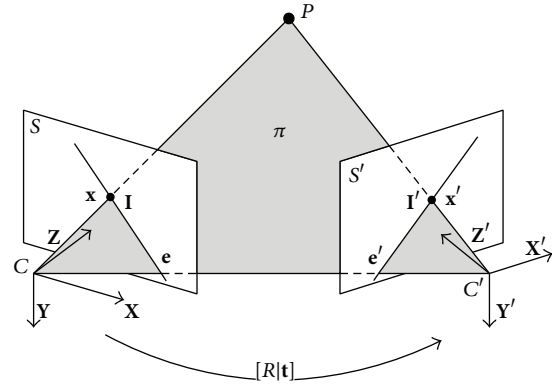


FIGURE 1: Epipolar geometry.

**2.3. Relative Orientation.** The mission of relative orientation is to determine the relative pose  $[R | \mathbf{t}]$  between two views, as shown in (7); essential matrix  $E$  contains information about  $R$  and  $\mathbf{t}$ , so almost every existing relative orientation method, such as the 5-point method [21] and 7- [22] and 8-point methods [22], is based on recovering essential matrix first and then recovering  $R$  and  $\mathbf{t}$  from it. For simplicity and robustness, the 8-point relative orientation method is adopted in this paper [22].

The projection matrices of  $S$  and  $S'$  are  $K[I | 0]$  and  $K'[R | \mathbf{t}]$ , respectively; once  $R$  and  $\mathbf{t}$  are recovered, the scene structure can be reconstructed in the coordinate system of  $S$  by spatial intersection. Preferably, bundle adjustment [23, 24] follows on when relative pose and scene structure are recovered linearly, by which optimal results can be obtained in the least squares sense. Actually, bundle adjustment serves as the last step in almost all motion and structure estimation problems [23].

## 3. Technical Route

Automatic deformation measurement of large-scale structure in this paper is carried out mainly in the following three steps:

- (i) automatic detection of targets, including coded and noncoded ones;
- (ii) automatic network orientation using coded targets;
- (iii) automatic matching of noncoded targets based on epipolar constraint.

Each step can be further broken down into several detailed substeps; the complete measuring scheme is shown in Figure 2. Key techniques involved are presented in detail in the following sections.

## 4. Design of Coded Target

Coded targets are essential to automation of the whole measuring procedure; they provide point correspondences automatically [25] and ensure reliable results in succeeding network orientation once there is a sufficient number of pairs of homologous points between two images to facilitate relative orientation [25].

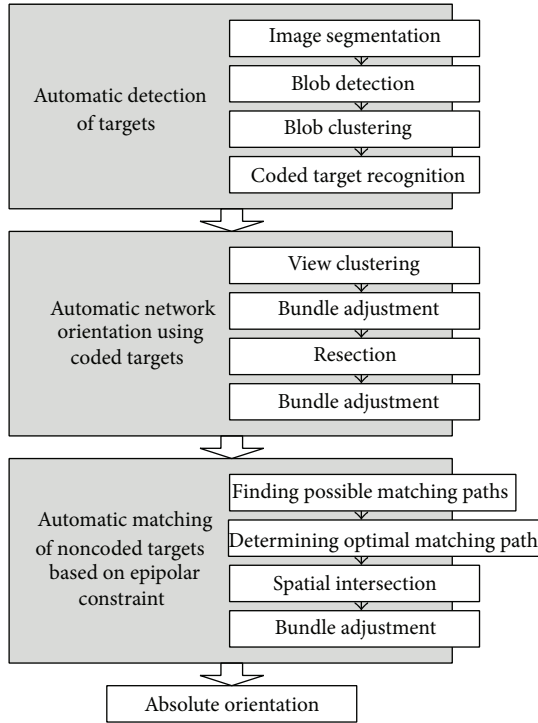


FIGURE 2: Measuring scheme.

Coded target is an automatically detected and recognized pattern of geometric features within the image [14–17]; a qualified coded target is supposed to have sufficient coding capacity and be projective invariant to a certain degree, its corresponding detection algorithm is supposed to be simple, efficient, and robust; moreover, due to measuring accuracy concern, its image points should be able to be measured with high precision.

The coded target designed in this paper is shown in Figure 3; it consists of several circular retroreflective points, which are arranged according to a certain coding pattern. One reason why circular retroreflective points are adopted is that compared with other geometric features a circular retroreflective point is always imaged as a bright blob under illumination; it is more robust against image degrading processes (e.g., defocusing or changing of the imaging distance and angle) [14]. The other reason is that noncoded target adopted in this paper consists of single circular retroreflective point, like points in coded target; it is also imaged as a bright blob under illumination; thus, identical blob detection algorithm can be applied to coded and noncoded targets at the same time in preliminary stage of detection, avoiding developing different algorithms, respectively.

Out of consideration for detection efficiency, if color images are applied, preferably, the circular retroreflective points in color can be used, just as shown in Figure 3; color information will greatly facilitate the image segmentation, which is essential to detection efficiency.

**4.1. Coding Principle.** There are two kinds of circular points in the designed coded target; one is reference points; there

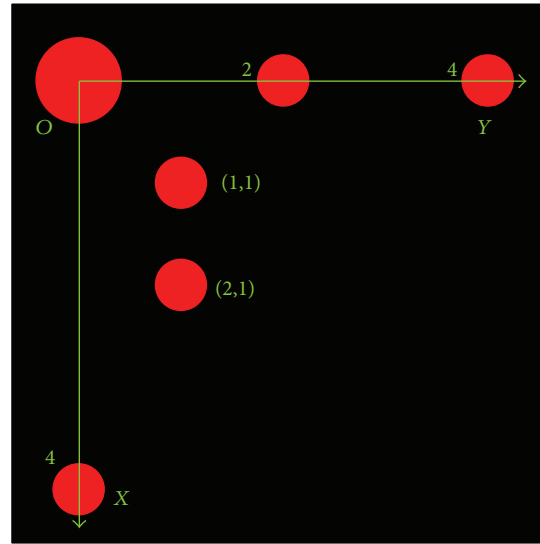


FIGURE 3: Design of coded target.

are 4 of them in total, and they together establish the two-dimensional target coordinate system  $O\text{-}XY$ , as shown in Figure 3; the biggest among them represents the origin  $O$  two of the rest represent two different points on  $Y$ -axis, whose coordinates are  $(0, 2)$  and  $(0, 4)$ , respectively, and the last one represents the point on  $X$ -axis with coordinates  $(4, 0)$ .

The other kind is coding points; they are located in positions with positive integer coordinates  $(i, j)$ , and each one of them represents one binary bit  $k$ ; the presence and absence of it represent the status 1 and 0 of this binary bit, respectively. If there are  $m$  coding points at most per column, in other words, the  $X$  coordinate  $i$  is not more than  $m$ , then the relationship between the binary bit  $k$  and the coordinates  $(i, j)$  is given by

$$k = (j - 1) \times m + i. \tag{8}$$

Given that the capacity of coding points per row is  $n$ , the total amount of binary bits encoded by the designed coded target is  $m \times n$ ; then the overall coding capacity is  $2^{m \times n}$ , which means  $2^{m \times n}$  instances of coded target with different coding information can be derived, for  $m$  and  $n$  are chosen arbitrarily; thus, theoretically, there is no upper limit to the coding capacity of the designed coded target.

Take the coded target shown in Figure 3, for example; given that  $m$  and  $n$  are both 3, then it represents a binary code with  $9 = 3 \times 3$  binary bits; thus, its coding capacity is 512. There are two coding points in it, with coordinates  $(1, 1)$  and  $(2, 1)$ , respectively; according to (8), they represent the 1st and 2nd binary bits, respectively; the absence of coding points in other 7 positions with positive integer coordinates means the statuses of other 7 binary bits are 0; thus, the encoded binary code is 000000011, and the corresponding decimal code is  $2^0 + 2^1 = 3$ .

### 5. Detection of Coded and Noncoded Target

Detection of coded and noncoded targets in this paper is carried out mainly in the following four steps:

- (i) image segmentation simply based on gray information and, preferably, color information, if applicable;
- (ii) blob detection based on (Normalized Laplacian of Gaussian) NLoG;
- (iii) blob clustering based on image distance between two points; the clusters containing only single blob are determined to be noncoded targets, whereas the clusters containing the required amount of blobs are treated as potential coded targets in succeeding recognition process;
- (iv) coded target recognition based on geometric characteristics and coding principle of the designed coded target; potential coded targets cannot be diagnosed until all constraints are met in this recognition process.

5.1. *Blob Detection.* The blob detector adopted in this paper is the well-known scale invariant (Normalized Laplacian of Gaussian) NLoG, which is given as follows:

$$NLoG(x, y; \sigma) = \frac{x^2 + y^2 - 2\sigma^2}{2\pi\sigma^4} \exp\left(-\frac{x^2 + y^2}{2\sigma^2}\right), \quad (9)$$

where  $\sigma$  is the scale parameter; and the detection of blobs with multiple scales is to detect scale-space maxima/minima, which are points that are simultaneously local maxima/minima with respect to both space and scale [26, 27].

5.2. *Blob Clustering.* As stated before, a coded target is imaged as a group of blobs, whereas a noncoded one is imaged as one single blob, which means the blobs within a coded target distributes much denser than blobs of multiple noncoded targets do; this will not change as long as the distribution density of multiple noncoded targets in space does not exceed the one of points within a coded target, and the depths of noncoded targets, relative to camera, do not vary too much from the one of a coded target. Thus, simple blob clustering based on image distance between two points can be conducted to distinguish between coded and noncoded targets.

The blob clustering process is demonstrated in Figure 4. The group of blobs surrounded by the big green circle is a coded target, and the rest blobs are all noncoded ones. The white circle surrounding each blob with radius  $r$  denotes the adjacent area of each blob; if a blob is within this adjacent area of another blob, then these two blobs are adjacent to each other and can be clustered into the same cluster. As you can see, there are no other blobs within the adjacent area of each noncoded target, so the cluster of each noncoded target contains only its own blob.

Let us check out step by step how clustering works out for coded target; if it starts at blob  $a$  first, blob  $b$  will be added into cluster next, for it is within the adjacent area of blob  $a$ ,

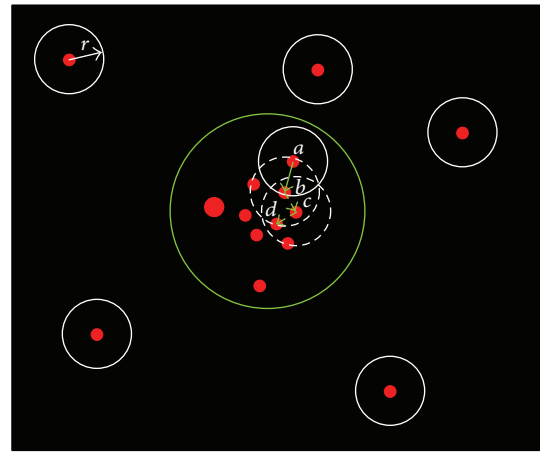


FIGURE 4: Blob clustering process.

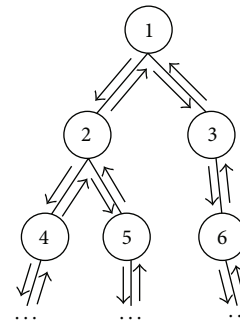


FIGURE 5: Recursive routine.

and then come blobs  $c$  and  $d$ ; clustering will keep going until no more adjacent blobs are found.

This blob clustering process, like the view clustering process which is going to be described in the succeeding section, is a standard recursive process; they both can be implemented by the recursive routine shown in Figure 5.

After clustering, clusters containing only single blob are determined to be noncoded targets directly, and clusters containing reasonable amount of blobs are determined to be potential coded targets, since a true coded target contains at least 4 reference points and limited amount of coding points. If a cluster contains unreasonable amount of blobs, blobs within it will be sentenced to be noncoded targets as well.

5.3. *Coded Target Recognition.* As stated before, coded target recognition is based on geometric characteristics and coding principle of the designed coded target; potential coded targets coming from blob clustering cannot be diagnosed until all constraints are met in this recognition process. Coded target recognition is carried out mainly in the following two steps:

- (i) recognition of reference points;
- (ii) decoding.

5.3.1. *Recognition of Reference Points.* The first thing to do is to determine which blob is the origin  $O$  of the target coordinate system. As shown in Figure 6, the origin  $O$  is much bigger than any of the other blobs, so it can be located simply

by finding the blob with the biggest size. Naturally, radius can be considered; it is a measure of blob size, and it is readily acquired in blob detection stage, but radius alone cannot ensure clear distinction between the origin  $O$  and other blobs, since the radius difference between two blobs may be smaller than the scale resolution in blob detection, which is the scale step between two NLoG templates; thus, more robust method is needed. In this paper, the grayscale sum of pixels within blob radius, in other words, the grayscale weighted area, is used to make a clear distinction of the origin  $O$  from other blobs; the blob with the biggest grayscale weighted area is determined to be the origin  $O$ .

The rest three reference points,  $x$ ,  $y_1$ , and  $y_2$ , have their own geometric characteristics; the angle between segments  $Oy_1$  and  $Ox$  equals the angle between  $Oy_2$  and  $Ox$ , which is both  $\alpha_0$  as shown in Figure 6; besides, these two angles are bigger than angle  $\alpha_i$  formed by any other two blobs toward origin  $O$ ; based on these,  $x$ ,  $y_1$ , and  $y_2$  are determined in this paper by finding angle  $\alpha_0$ .

5.3.2. *Decoding.* Technically, the relationship between the image coordinates of a coding point, which is  $(x, y)$ , and its target coordinates  $(i, j)$  is a projective transformation; however, 4 pairs of correspondences between image and target generated by 4 reference points are unable to solve this projective transformation, since there are 3 reference points which are collinear, which are  $O$ ,  $y_1$ , and  $y_2$ , respectively. Fortunately, when target depth, relative to camera, is far greater than target size, as is usually the case in practice, the relationship between  $(x, y)$  and  $(i, j)$  approximates to an affine transformation  $H_a$ :

$$\begin{pmatrix} j \\ i \\ 1 \end{pmatrix} = \begin{pmatrix} a_1 & a_2 & a_3 \\ a_4 & a_5 & a_6 \\ 0 & 0 & 1 \end{pmatrix} \begin{pmatrix} x \\ y \\ 1 \end{pmatrix}. \quad (10)$$

At least 3 pairs of correspondences, generated by 3 non-collinear points, are adequate to solve  $H_a$ ; thus, the recognized 4 reference points in Section 5.3.1 can be used to solve  $H_a$ .

Once  $H_a$  is recovered, the target coordinates  $(i, j)$  of each coding point can be computed according to (9), and corresponding binary bit  $k$  of each coding point can be further acquired according to (8); then the binary and decimal code is finally decoded.

## 6. Automatic Network Orientation

The mission of automatic network orientation is to automatically determine the relative pose between each view and certain reference frame, which is usually the coordinate system of the first view, and reconstruct all coded targets at the same time. A three-stage automatic network orientation strategy is proposed in this paper:

- (i) view clustering based on relative orientation with the help of coded targets and reconstruction of coded targets at the same time;
- (ii) connecting those view clusters which contain multiple views using absolute orientation;

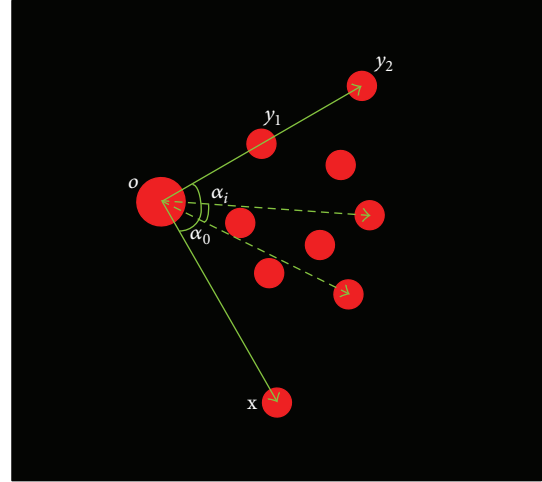


FIGURE 6: Recognition of reference points.

- (iii) conducting resections for isolate views, which cannot be clustered with other views, using coded targets reconstructed in view clustering.

6.1. *View Clustering.* As stated in [28], many researches on structure and motion recovery have been based on some certain image ordering, usually in chronological order if image set is sequential; this image ordering allows small baseline matching algorithms to be used between consecutive frames of the sequence and avoids wide baseline situations, in which matching is difficult; thus, all images can be successfully sewed together into tracks image by image.

In our case, the usage of coded targets greatly alleviates our concerns with matching; it can provide reliable point correspondences between views, even in wide baseline situations for coded target itself is robust to large perspective distortions, as stated in Sections 4 and 5. Yet this ordering remains advantageous to our case, since the small baseline conditions it brings mean bigger overlapping area between footprints of consecutive views, in other words, more point correspondences available for relative orientation. But sometimes this ordering is not guaranteed in our case, in which way relative orientation between views may fail for overlapping area between footprints of these views is not big enough to provide adequate correspondences; in order to cope with this situation and automate the network orientation process, view clustering is carried out.

Unlike view clustering in [28], in which feature matching is involved, view clustering in our case is much simpler due to the usage of coded targets; whether two views can be clustered into one group or not simply depends on whether the relative orientation between these two views succeeds or fails.

As stated in Section 5.2, like the blob clustering, view clustering process is also implemented by the recursive routine shown in Figure 5.

The whole network orientation process is demonstrated in Figure 7 by images of a steel structure, as shown; there are 9

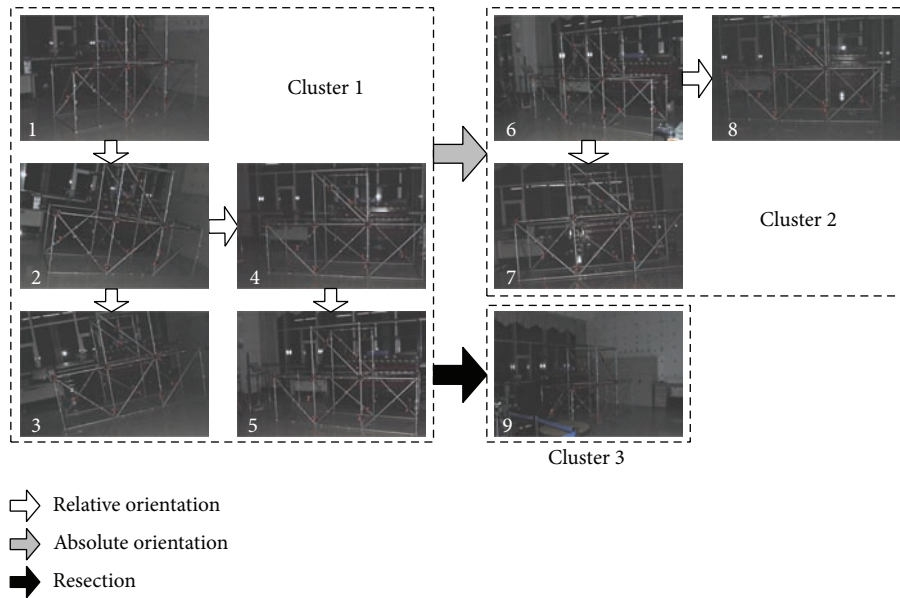


FIGURE 7: Network orientation process.

views in total, and three clusters emerge after view clustering. The first five are clustered together to be cluster 1, view 6 to view 8 form the cluster 2, and view 9 is left alone to be cluster 3.

If at least three homologous coded targets are reconstructed both in cluster 1 and cluster 2, then cluster 2 can be connected to cluster 1 using absolute orientation.

As for view 9, it is an isolate view for it observes only five coded targets, which is insufficient to carry out relative orientation between it and any other views, but connection can still be built between it and cluster 1 by resection, as long as there are adequate observed coded targets, which have already been reconstructed in cluster 1, the minimum amount required for resection can be at least 4 under certain circumstances.

Be aware that bundle adjustment is recommended as the last step in all three stages of network orientation.

## 7. Matching of Noncoded Target

Unlike coded target, noncoded target cannot provide its matches over multiple views by itself; besides, feature descriptor based methods [18–20] are not suitable for matching of noncoded targets in our case, where the illumination is highly controlled to ensure that all targets can be readily detected; for the same reason, images in our case are usually textureless, which makes feature descriptor not applicable.

Given that all views that can be oriented have already been automatically oriented in network orientation, noncoded targets can be matched over views based on epipolar constraints, introduced in Section 2.2, and this is also how it is done in this paper but in a subtler way. The concept of matching paths is proposed, and matching of noncoded targets in this paper is carried out mainly in two steps:

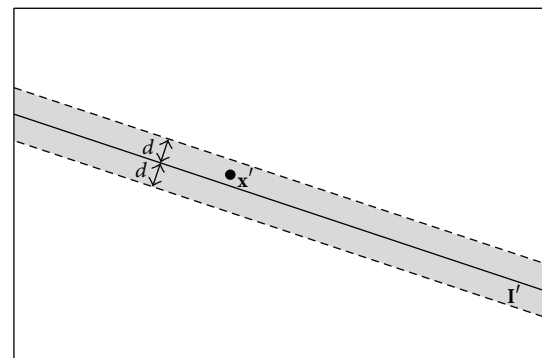


FIGURE 8: Determining potential match based on epipolar constraint.

- (i) finding all possible matching paths through multiple views for each noncoded target;
- (ii) determining the optimal matching path for each noncoded target by a novel voting strategy.

**7.1. Finding Possible Matching Paths.** As stated in Section 2.2 and shown in Figure 1, given the fundamental matrix  $F$ , the match in view  $S'$ , which is  $x'$ , for a given  $x$  in view  $S$ , is theoretically located on the epipolar line  $l' = Fx$ , which means  $l'^T x' = 0$ , and this is what our matching strategy is based on. But when the estimate for  $F$  and the measurements of  $x$  and  $x'$  are not error free, as is the case in practice,  $x'$  will not be exactly on  $l'$  anymore but close to it; in other words,  $l'^T x' \neq 0$ ; thus, in practice once the image distance between  $x'$  and  $l'$  is smaller than certain threshold  $d$ , as shown in Figure 8,  $x'$  will be determined to be a potential match for  $x$ .

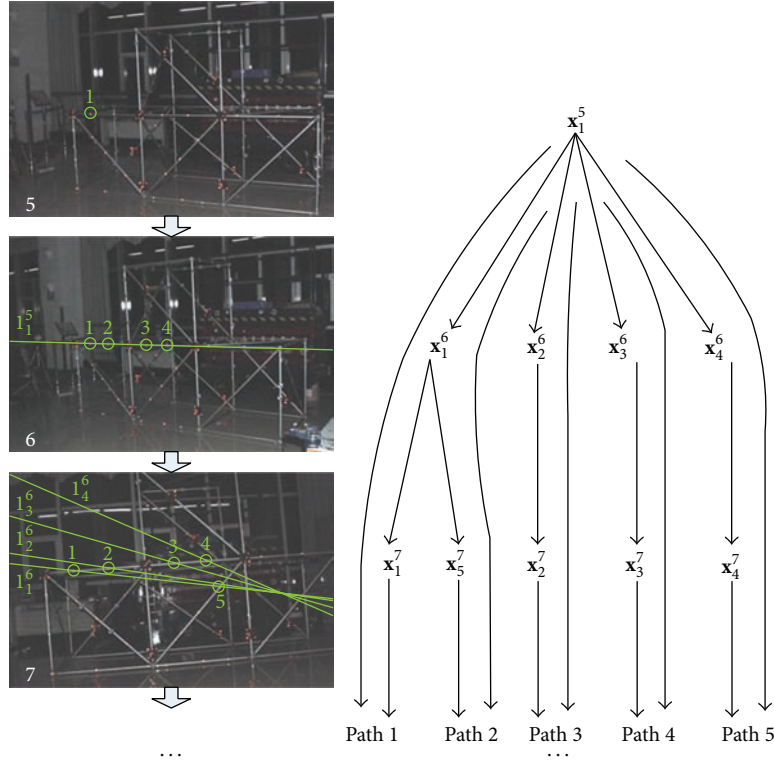


FIGURE 9: Finding possible matching paths.

Sometimes, besides  $P$  there will be other spatial points in the plane  $\pi$  as well, as shown in Figure 1; this will bring ambiguity to finding match for  $\mathbf{x}$ , since projections of these points on view  $S'$  are also on  $I'$ . In such cases, when we try to determine which image point on  $S'$  is the match for  $\mathbf{x}$  based on criterion shown in Figure 8, we will be expected to find multiple candidates rather than one, just as shown in Figure 9; four potential matches in view 6 for point 1 in view 5 are found.

Obviously, if there is a third view with optical center out of the plane  $\pi$ , this ambiguity will be eliminated. But in order to reduce complexity and increase the automaticity and robustness, we do not explicitly attempt to find this third view during matching in this paper; instead, a simpler and subtler way is adopted. We first maintain the ambiguity and find all possible matching paths through multiple views for a given point, then determine the optimal path based on a novel voting strategy, eliminating the ambiguity, and finally find the real match.

A matching path is defined as follows:

$$\text{path}(\mathbf{x}_{j_1}^{i_1}, \mathbf{x}_{j_2}^{i_2}, \dots, \mathbf{x}_{j_k}^{i_k}, \dots, \mathbf{x}_{j_w}^{i_w}), \quad (11)$$

$$1 \leq k \leq w, \quad 1 \leq i_k \leq m, \quad 1 \leq j_k \leq n(i_k),$$

where  $\mathbf{x}_{j_k}^{i_k}$  denotes the  $k$ th matching image point in the matching path,  $i_k$  is the view number of this point, or in which view it is measured,  $j_k$  is its point number among all observations in view  $i_k$ ,  $w$  is the total amount of points contained in the path,  $m$  denotes the total amount of views,

and  $n(i_k)$  represents the total amount of observations in view  $i_k$ .

The process of finding possible matching paths for a given image point is demonstrated in Figure 9 still by images of a steel structure. As shown, the point 1 in view 5, which is  $\mathbf{x}_1^5$ , finds four matches in view 6, resulting in four separate paths; then we continue to find matches in view 7 for those four points. Since the point 1 in view 6, which is  $\mathbf{x}_1^6$ , can find two different matches in view 7, a previous path now splits into two, resulting in five separate paths in total, which are

$$\begin{aligned} &\text{path 1}(\mathbf{x}_1^5, \mathbf{x}_1^6, \mathbf{x}_1^7) \\ &\text{path 2}(\mathbf{x}_1^5, \mathbf{x}_1^6, \mathbf{x}_5^7) \\ &\text{path 3}(\mathbf{x}_1^5, \mathbf{x}_2^6, \mathbf{x}_2^7) \\ &\text{path 4}(\mathbf{x}_1^5, \mathbf{x}_3^6, \mathbf{x}_3^7) \\ &\text{path 5}(\mathbf{x}_1^5, \mathbf{x}_4^6, \mathbf{x}_4^7). \end{aligned} \quad (12)$$

Given that  $F_b^a$  is the fundamental matrix between view  $a$  and view  $b$ , then the epipolar line  $I_j^a$  in view  $b$ , as shown in Figure 9, is

$$I_j^a = F_b^a \mathbf{x}_j^a, \quad (13)$$

where  $\mathbf{x}_j^a$  is the point  $j$  in view  $a$ . In short,  $I_j^a$  is an epipolar line induced by  $\mathbf{x}_j^a$ .

As the process described above continues, the amount of matching paths will be expected to increase, but if the amount of paths remains one eventually, image points contained in the only matching path will naturally be determined to be matched or the voting strategy, which is described in the next section, will step in.

**7.2. Determining Optimal Matching Path.** The novel voting strategy proposed in this paper is still based on epipolar constraint; if image points contained in a matching path are really matched, epipolar constraint should be met between all N-choose-2 points; thus, we can determine whether a path is the real one simply by checking if all the N-choose-2 cases in it meet the epipolar constraint. However, due to error, probably not all the cases are qualified, so in practice it is reasonable to choose the path with most qualified cases instead of all qualified cases as the optimal matching path, which contains points really matched.

The vote that a matching path can get is given by

$$\text{vote} = \sum_{k_1=1}^w \sum_{k_2=1}^w \text{check}(\mathbf{x}_{j_{k_1}}^{i_{k_1}}, \mathbf{x}_{j_{k_2}}^{i_{k_2}}), \quad k_2 \neq k_1, \quad (14)$$

where  $\mathbf{x}_{j_{k_1}}^{i_{k_1}}$  and  $\mathbf{x}_{j_{k_2}}^{i_{k_2}}$  are, respectively, the  $k_1$ th and  $k_2$ th points in the path, and the function check is given as follows:

$$\text{check}(\mathbf{x}_{j_{k_1}}^{i_{k_1}}, \mathbf{x}_{j_{k_2}}^{i_{k_2}}) = \begin{cases} 1 & \text{if } \text{dist}(\mathbf{x}_{j_{k_1}}^{i_{k_1}}, F_{i_{k_1}}^{i_{k_2}} \mathbf{x}_{j_{k_2}}^{i_{k_2}}) < d \\ 0 & \text{else,} \end{cases} \quad (15)$$

where  $\text{dist}(\mathbf{x}_{j_{k_1}}^{i_{k_1}}, F_{i_{k_1}}^{i_{k_2}} \mathbf{x}_{j_{k_2}}^{i_{k_2}})$  is the distance between point  $\mathbf{x}_{j_{k_1}}^{i_{k_1}}$  and the epipolar line  $F_{i_{k_1}}^{i_{k_2}} \mathbf{x}_{j_{k_2}}^{i_{k_2}}$  and  $d$  is some certain distance threshold, as explained in Section 7.1. In short, the function check means that if the  $k_1$ th point is close enough to the epipolar line in view  $i_{k_1}$  induced by the  $k_2$ th point, the path gets one vote.

Apparently, each N-choose-2 case has two votes to give, which is  $\text{check}(\mathbf{x}_{j_{k_1}}^{i_{k_1}}, \mathbf{x}_{j_{k_2}}^{i_{k_2}})$  and  $\text{check}(\mathbf{x}_{j_{k_2}}^{i_{k_2}}, \mathbf{x}_{j_{k_1}}^{i_{k_1}})$ , respectively, so if all N-choose-2 cases in a path meet the epipolar constraint, this path will get a unanimous vote, which is  $w(w-1)$ .

Taking the three images shown in Figure 9 as an example again and using the voting strategy described above, path 1 gets the most votes, which is 6, whereas all other paths get only 4 votes, so path 1 is chosen to be the optimal matching path up to this point, just as what it really is; thus, the points contained in path 1 are determined to be matched.

## 8. Experimental Results

The main types of airship are nonrigid blimps, semirigid airship, and rigid airship. Unlike the nonrigid blimps, semirigid airship usually has a fixed keel besides internal pressure, which runs the length of the ship along the bottom of the hull, as shown in Figure 10, and provides greater structural strength to maintain its shape and structural integrity.

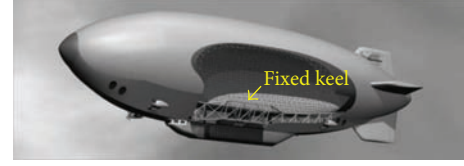


FIGURE 10: Semirigid airship.



FIGURE 11: Designed keel structure.



FIGURE 12: Designed keel structure in field.

A designed keel structure in a practical semi-airship is shown in Figures 11 and 12.

In order to ensure safety and prevent potential structural failure in extreme conditions like storm, it is necessary to conduct mechanical testing and high-precision dimensional quality monitoring for this designed keel structure before the airship is put into use.

The proposed methods in this paper have been applied to this mechanical testing, and results are shown in the following figures. The reference frame is established by the three points on the chessboard shown in Figure 14, with origin located on the top left corner of the chessboard. Red noncoded targets are attached to the main axis of the keel node by node, with the positional changes of these noncoded targets reflecting the deformations of the keel under different loads and internal pressures. Red coded targets are scattered evenly in the scene to facilitate network orientation; examples of detection of coded targets are given in Figure 13, and as you can see, detection of coded targets is quite robust to large perspective distortions.

There are 18 images which are taken under one working condition; some of these images are shown in Figure 14, and the recovered camera motion and scene structure are shown in Figure 15.

In order to verify the measuring accuracy, vertical deformations of one node under different load and internal pressure conditions are measured by total station besides our automatic vision metrology as true values, and the deviations of our measurement results from the true values are given in Table 1. As you can see, measuring errors under all working conditions are within 1 mm, which is considerably good.

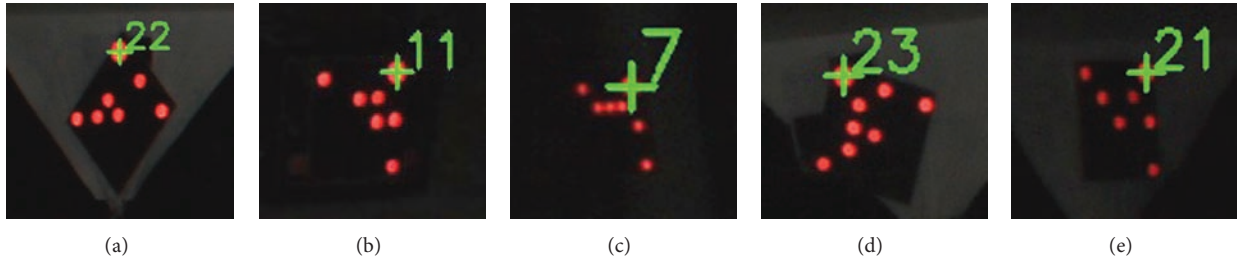


FIGURE 13: Detection of coded targets.

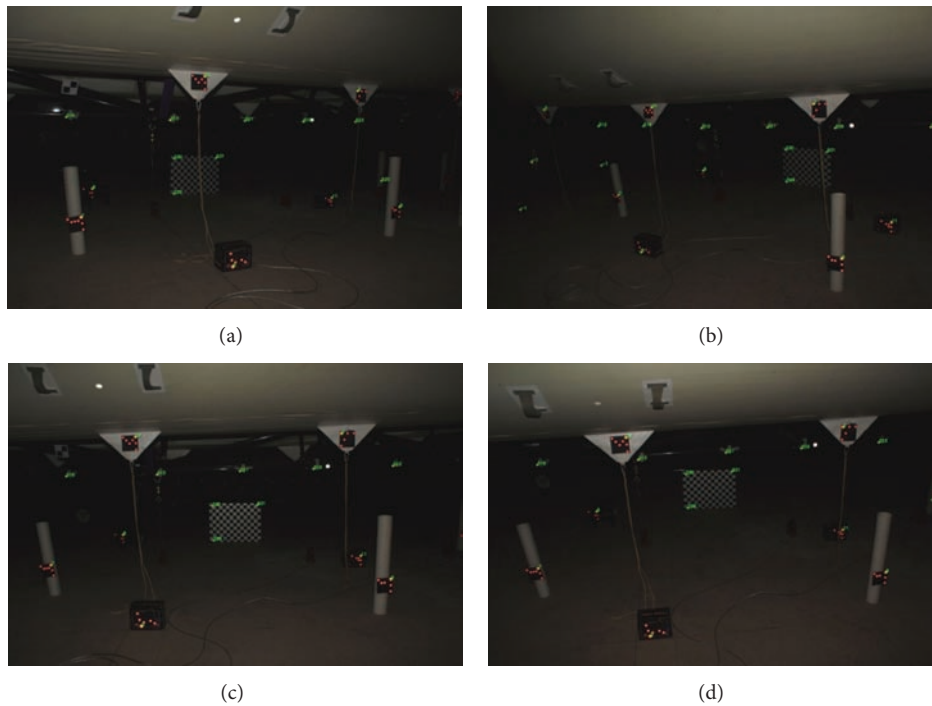


FIGURE 14: Images of scene structure.

TABLE 1: Measurement deviations.

Working conditions	1 kN/500 Pa	1 kN/700 Pa	2 kN/500 Pa	2 kN/700 Pa	3 kN/500 Pa	3 kN/700 Pa
Total station	21.78 mm	21.62 mm	46.05 mm	42.69 mm	66.42 mm	61.83 mm
Ours	22.07 mm	21.90 mm	46.61 mm	43.27 mm	67.22 mm	62.52 mm
Error	0.29 mm	0.28 mm	0.56 mm	0.58 mm	0.80 mm	0.69 mm

### 9. Summary and Conclusions

In this paper, all relevant key techniques involved in photogrammetric vision metrology for fully automatic 3D measurement of large-scale structure are studied. A new kind of coded target consisting of circular retroreflective discs is designed, and corresponding detection and recognition algorithms based on blob detection and clustering are presented. Then a three-stage strategy starting with view clustering is proposed to achieve automatic network orientation. As for matching of noncoded targets, the concept of matching path is proposed, and matches for each noncoded target are found

by determination of the optimal matching path, based on a novel voting strategy, among all possible ones. Experiments on a fixed keel of airship have been conducted to verify the effectiveness and measuring accuracy of the proposed methods.

Future work will mainly focus on developing new blob clustering method that is more adaptive to coded targets in different depths, and improved method that is less sensitive to starting point should be developed for finding all possible matching paths, since, in current way, different starting points may lead to different amount of points within the optimal paths with some matched points missed.

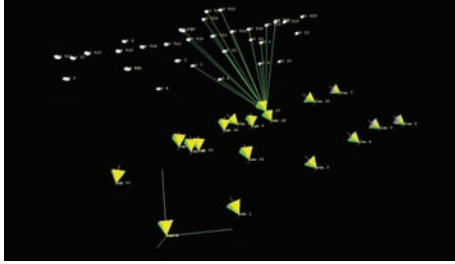


FIGURE 15: Recovery of camera motion and scene structure.

## Conflict of Interests

The authors declare that there is no conflict of interests regarding the publication of this paper.

## References

- [1] A. L. Window and G. S. Holister, *Strain Gauge Technology*, Applied Science, 1982.
- [2] M. Bertrand, J. Meunier, M. Doucet, and G. Ferland, "Ultrasonic biochemical strain gauge based on speckle tracking," in *Proceedings of the IEEE Ultrasonics Symposium*, pp. 859–863, IEEE, October 1989.
- [3] W. F. Caspary and J. M. Rüeger, *Concepts of Network and Deformation Analysis*, University of New South Wales, 1987.
- [4] K. L. Feigl, D. C. Agnew, Y. Bock et al., "Space geodetic measurement of crustal deformation in central and southern California, 1984–1992," *Journal of Geophysical Research*, vol. 98, no. 12, pp. 21677–21712, 1993.
- [5] K. M. Larson and D. C. Agnew, "Application of the global position system to crustal deformation measurement 1. Precision and accuracy," *Journal of Geophysical Research*, vol. 96, no. 10, pp. 16547–16565, 1991.
- [6] Q. Wang, P.-Z. Zhang, J. T. Freymueller et al., "Present-day crustal deformation in China constrained by global positioning system measurements," *Science*, vol. 294, no. 5542, pp. 574–577, 2001.
- [7] J. W. Lovse, W. F. Teskey, G. Lachapelle, and M. E. Cannon, "Dynamic deformation monitoring of tall structure using GPS technology," *Journal of Surveying Engineering*, vol. 121, no. 1, pp. 35–40, 1995.
- [8] T. Luhmann, S. Robson, S. Kyle, and I. Harley, *Close Range Photogrammetry: Principles, Methods and Applications*, Whittles, 2006.
- [9] C. S. Fraser and S. Cronk, "A hybrid measurement approach for close-range photogrammetry," *Journal of Photogrammetry and Remote Sensing*, vol. 64, no. 3, pp. 328–333, 2009.
- [10] G. Ganci and H. Handley, "Automation in videogrammetry," *International Archives of Photogrammetry and Remote Sensing*, vol. 32, pp. 53–58, 1998.
- [11] C. Fraser, S. Cronk, and H. Hanley, *Close-Range Photogrammetry in Traffic Incident Management*, 2008.
- [12] C. Fraser, "Automated vision metrology: a mature technology for industrial inspection and engineering surveys," *Australian Surveyor*, vol. 46, no. 1, pp. 5–11, 2001.
- [13] C. S. Fraser, D. Brizzi, and A. Hira, *Vision-Based, Multi-Epoch Deformation Monitoring of the Atrium of Federation Square*, 2003.
- [14] S. J. Ahn, W. Rauh, and S. I. Kim, "Circular coded target for automation of optical 3D-measurement and camera calibration," *International Journal of Pattern Recognition and Artificial Intelligence*, vol. 15, no. 6, pp. 905–919, 2001.
- [15] S. J. Ahn and M. Schultes, "A new circular coded target for the automation of photogrammetric 3D-surface measurements," in *Optical 3-D Measurement Techniques IV*, A. Gruen and H. Kahmen, Eds., pp. 225–234, Herbert Wichmann, 1997.
- [16] F. Gaspard, S. Naudet, E. Noirfalise, and P. Sayd, "Coded target and photogrammetry method using such targets," Google Patents, 2008.
- [17] A. K. Vladimir and S. Alexander, *Non-Contact 3D Model Reconstruction Using Coded Target*, 1998.
- [18] D. G. Lowe, "Distinctive image features from scale-invariant keypoints," *International Journal of Computer Vision*, vol. 60, no. 2, pp. 91–110, 2004.
- [19] H. Bay, A. Ess, T. Tuytelaars, and L. van Gool, "Speeded-Up Robust Features (SURF)," *Computer Vision and Image Understanding*, vol. 110, no. 3, pp. 346–359, 2008.
- [20] E. Tola, V. Lepetit, and P. Fua, "DAISY: an efficient dense descriptor applied to wide-baseline stereo," *IEEE Transactions on Pattern Analysis and Machine Intelligence*, vol. 32, no. 5, pp. 815–830, 2010.
- [21] D. Nistér, "An efficient solution to the five-point relative pose problem," *IEEE Transactions on Pattern Analysis and Machine Intelligence*, vol. 26, no. 6, pp. 756–770, 2004.
- [22] R. Hartley and A. Zisserman, *Multiple View Geometry in Computer Vision*, vol. 2, Cambridge University Press, 2003.
- [23] M. I. A. Lourakis and A. A. Argyros, "SBA: a software package for generic sparse bundle adjustment," *ACM Transactions on Mathematical Software*, vol. 36, no. 1, article 2, 2009.
- [24] B. Triggs, P. F. McLauchlan, R. I. Hartley, and A. W. Fitzgibbon, "Bundle adjustment—a modern synthesis," in *Vision Algorithms: Theory and Practice*, B. Triggs, A. Zisserman, and R. Szeliski, Eds., vol. 1883 of *Lecture Notes in Computer Science*, pp. 298–372, Springer, 2000.
- [25] C. S. Fraser, "Network orientation models for image-based 3D measurement," *International Archives of Photogrammetry and Remote Sensing & Spatial Information Science*, vol. 36, no. 5, p. 9, 2005.
- [26] T. Lindeberg, "Scale-space theory: a basic tool for analyzing structures at different scales," *Journal of Applied Statistics*, vol. 21, 1-2, pp. 225–270, 1994.
- [27] T. Lindeberg, "Feature detection with automatic scale selection," *International Journal of Computer Vision*, vol. 30, no. 2, pp. 79–116, 1998.
- [28] F. Schaffalitzky and A. Zisserman, "Multi-view matching for unordered image sets, or 'How do I organize my holiday snaps?'," in *Computer Vision—ECCV 2002*, A. Heyden, G. Sparr, M. Nielsen, and P. Johansen, Eds., vol. 2350 of *Lecture Notes in Computer Science*, pp. 414–431, Springer, 2002.

## Research Article

# Formation of Three-Way Scanning Electron Microscope Moiré on Micro/Nanostructures

Qinghua Wang,<sup>1</sup> Satoshi Kishimoto,<sup>2</sup> and Hiroshi Tsuda<sup>1</sup>

<sup>1</sup> *Research Institute of Instrumentation Frontier, National Institute of Advanced Industrial Science and Technology, 1-1-1 Umezono, Tsukuba, Ibaraki 305-8568, Japan*

<sup>2</sup> *Hybrid Materials Unit, National Institute for Materials Science, 1-2-1 Sengen, Tsukuba, Ibaraki 305-0047, Japan*

Correspondence should be addressed to Satoshi Kishimoto; [kishimoto.satoshi@nims.go.jp](mailto:kishimoto.satoshi@nims.go.jp)

Received 31 October 2013; Accepted 29 December 2013; Published 11 February 2014

Academic Editors: Y. Fu and G. Pedrini

Copyright © 2014 Qinghua Wang et al. This is an open access article distributed under the Creative Commons Attribution License, which permits unrestricted use, distribution, and reproduction in any medium, provided the original work is properly cited.

Three-way scanning electron microscope (SEM) moiré was first generated using a designed three-way electron beam (EB) in an SEM. The spot-type three-way SEM moiré comes from the interference between the three-way EB and the specimen grating in which the periodic cells are arranged in a triangular manner. The deformation and the structure information of the specimen grating in three directions can be simultaneously obtained from the three-way SEM moiré. The design considerations of the three-way EB were discussed. As an illustration, the three-way SEM moiré spots produced on a silicon slide were presented. The proposed three-way SEM moiré method is expected to characterize micro/nanostructures in triangular or hexagonal arrangements in three directions at the same time.

## 1. Introduction

Among various micro/nano optical measurement techniques, the moiré method [1] has been developed into a mature deformation measurement technique due to its noncontact and full-field properties. In the middle of 1980s, moiré interferometry [2, 3] was proposed and gradually improved to study the mechanical behaviors of materials. With the development of high-resolution microscopes, the micro/nano moiré methods have got fast development and wide applications. The scanning lines of microscopes instead of actual gratings can be regarded as reference gratings, and the implements of high-resolution microscope moiré methods are fairly simple. Since the electron beam (EB) moiré or scanning electronic microscope (SEM) moiré method was firstly put forward [4, 5], this method has been widely used for micro/nanodeformation measurement and the further stress analysis [6–9].

Furthermore, many other high-resolution microscope moiré methods have been proposed and developed, such as the focused ion beam (FIB) moiré method [10], the atomic force microscope (AFM) moiré method [11], the scanning tunneling microscope (STM) moiré method [12],

the transmission electron microscope (TEM) moiré method [13], and the laser scanning confocal microscope (LSCM) moiré method [14]. In addition, the digital micro/nano moiré method using a digital grating as the reference grating has also been applied to measure micro/nanodeformation [15, 16]. Besides deformation measurement, micro/nanostructure characterization can also be realized from micro/nano moiré fringes, such as the LSCM moiré fringes [17], the SEM moiré fringes [18], the secondary moiré fringes [19], and the three-way digital moiré fringes [20, 21].

Each moiré method has its own advantages and disadvantages. Considering that numerous micro/nanostructures are arranged in triangular manners, we first generate three-way SEM moiré fringes in this study to analyze the deformation as well as the structure information in three directions at the same time.

## 2. Formation and Measurement Principles of Three-Way SEM Moiré

**2.1. Formation Principle of One-Way SEM Moiré.** In the traditional SEM moiré method, SEM moiré fringes come from the interference between the scanning lines of a SEM

and the specimen grating, as shown in Figure 1. The specimen grating (also called model grid) can be found from the natural periodic structure of the sample or be fabricated on the sample surface by various methods such as photolithography. The scanning lines of the SEM which have almost the same pitch (spacing) as that of the specimen grating can be used as the reference grating (also called master grid). If there is a mismatch or misalignment between the SEM scanning lines and the specimen grating, the difference in the amount of emitted secondary electrons per primary electron will produce the SEM moiré fringes which consists of periodically distributed bright and dark parts [22]. Because the scanning lines are in the same direction, the formed moiré fringes are one-way SEM moiré fringes. Using the traditional SEM moiré fringes, the deformation and the structure information of a sample in the direction perpendicular to the scanning lines can be analyzed.

**2.2. Formation Principle of Three-Way SEM Moiré.** When the specimen grating is a three-way grating; that is, the periodic structure on the sample surface is arranged in a triangular manner, we can design an EB pattern containing three groups of scanning lines in three directions. If the specimen grating is hole-type such as a nanoporous structure; that is, the periodic dots or cells are holes, the SEM image of the specimen grating will be similar to the schematic diagram in Figure 2(a) in which the periodic dots are black due to less secondary electrons. In this case we will design an EB pattern as illustrated in Figure 2(b), in which the periodic white dots represent the exposed EB and the black lines express the unexposed EB. The interference between the specimen grating in Figure 2(a) and the EB in Figure 2(b) will generate the three-way electron moiré as shown in Figure 2(c).

For the pillar-type specimen grating such as a nanoparticle structure; that is, the periodic dots are pillars, the SEM image of the specimen grating will be similar to Figure 3(a) in which the periodic dots are white owing to more secondary electrons. Then, we will design an EB pattern presented in Figure 3(b), in which the periodic black dots stand for the unexposed EB and the white lines denote the exposed EB. When the EB in Figure 3(b) is superimposed on the specimen grating in Figure 3(a), the spot-type three-way SEM moiré will emerge as shown in Figure 3(c).

Figure 3(b) looks like the inverted gray scale image of Figure 2(b). If we use Figure 3(b) to interference with Figure 2(a), or use Figure 2(b) to interfere with Figure 3(a), we can get hexagonal moiré fringes [20] which look like the inverted gray scale pattern of Figures 2(c) or 3(c). As the spot-type moiré is more distinct than the hexagonal moiré, we choose to form the spot-type moiré in Figures 2(c) and 3(c) as the three-way SEM moiré.

The difference between the spot shapes of the three-way SEM moiré in Figures 2(c) and 3(c) suggests the different deformation of the specimen grating relative to the three-way EB. If the deformation of the specimen grating relative to the EB can be expressed by uniform rotation and uniform expansion or shrink, the SEM moiré spots will be in a circular type as seen from Figure 2(c). If the deformation of the specimen grating relative to the EB is not uniform in three

directions, the SEM moiré spots will be close to an elliptical shape as displayed in Figure 3(c).

### 2.3. Measurement Principle of Three-Way SEM Moiré Method.

Figure 4 shows the relationship between the three-way SEM moiré and the traditional one-way SEM moiré. If we divide the three-way EBs into three one-way EBs, we can find three groups of one-way SEM moiré fringes which are, respectively, generated from the interferences between the three one-way EBs and the specimen grating. From Figure 4, the three-way SEM moiré spots result from the interferences among the three groups of one-way SEM moiré fringes.

Let  $D_1$ ,  $D_2$ , and  $D_3$  represent the distances between each two spot centers of three adjacent SEM moiré spots, respectively, and  $d_1$ ,  $d_2$ , and  $d_3$  mean the fringe spacings of three groups of one-way SEM moiré fringes, respectively. The quantitative relationship between  $D_1$ ,  $D_2$ ,  $D_3$  and  $d_1$ ,  $d_2$ ,  $d_3$  can be obtained based on the geometric relationship of a triangle labelled in Figure 4.  $D_1$ ,  $D_2$ , and  $D_3$  are the three side lengths and  $d_1$ ,  $d_2$ , and  $d_3$  signify the three altitudes of the triangle. The variables of  $d_1$ ,  $d_2$ ,  $d_3$  can be calculated by

$$d_i = \frac{\sqrt{(D_1 + D_2 + D_3)(D_1 + D_2 - D_3)(D_2 + D_3 - D_1)(D_3 + D_1 - D_2)}}{2D_i} \quad (i = 1, 2, 3). \quad (1)$$

As a consequence, after  $D_1$ ,  $D_2$ , and  $D_3$  are measured from the three-way SEM moiré image, we can easily use the traditional SEM moiré method to get the deformation and the structure information of the specimen grating which are related to  $d_1$ ,  $d_2$ , and  $d_3$ . The calculation formula of the deformation of the specimen grating relative to the EB in the traditional SEM moiré method can be found in [22, equation (1)]. The calculation formulas of the pitch and the orientation angle of the specimen grating in three directions can be seen in [20, equation (2)].

An obvious advantage of the three-way SEM moiré method is that the deformation and the structure information of the micro/nanospecimen grating in three directions can be simultaneously obtained. Using the three-way EB to replace the three-way digital grating [20] as the reference grating is expected to reach a wider view field.

## 3. Design of the Three-Way EB

In the implementation process of the three-way SEM moiré method, design of an EB pattern is a crucial step. There are three aspects that need to be considered.

- (1) It is better to use the EB pattern in Figure 2(b) for a hole-type specimen grating and in Figure 3(b) for a pillar-type specimen grating. We can introduce Figure 2(b) into a SEM, and if we choose "Reverse" in the process of scanning, the used EB pattern is almost the same as Figure 3(b).

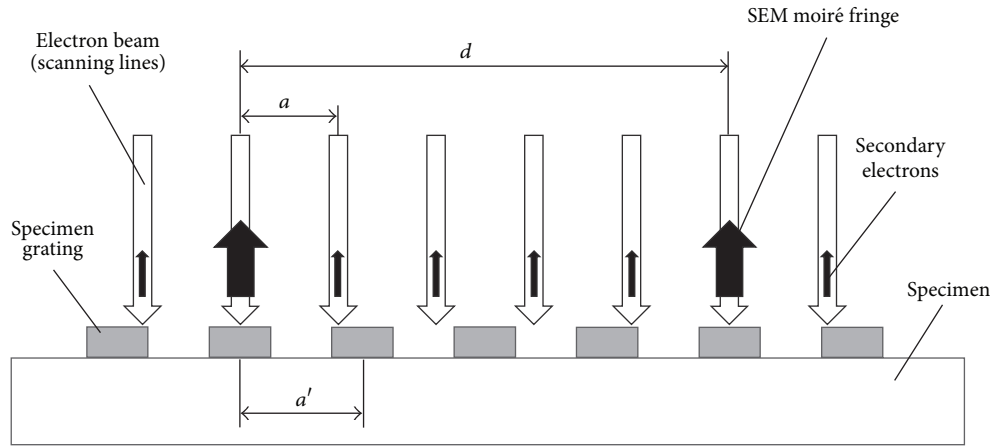


FIGURE 1: Formation principle of one-way SEM moiré fringes.

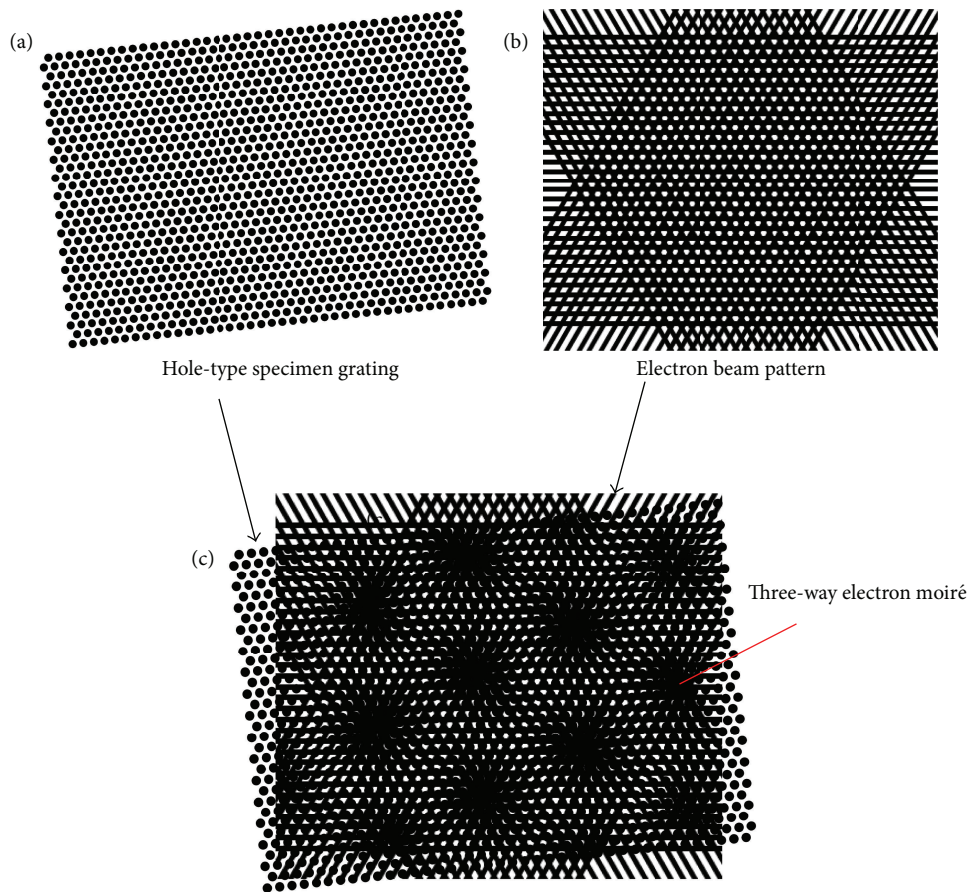


FIGURE 2: Formation principle of three-way SEM moiré for a hole-type specimen grating. In (b), the white part means the exposed EB and the black part expresses the unexposed EB.

(2) Due to the exposure lag of the EB in the scanning process, the real exposed region is smaller than the designed exposed region if there are both exposed and unexposed regions in an EB pattern. Consequently, it is recommended that the exposed sizes of the oblique one-way lines ( $l_{exp2}$  and  $l_{exp3}$  in Figure 5) should be equal to or greater than that of the horizontal one-way

line ( $l_{exp1}$  in Figure 5) of the designed three-way EB pattern. Usually,  $l_{exp2} = l_{exp3}$  is 1~1.2 times  $l_{exp1}$ . To facilitate calculation, the pitch ( $a_i$ ), that is, the sum of the exposed size ( $l_{exp_i}$ ) and the unexposed size ( $l_{unexp_i}$ ) of each one-way EB line, is better to be set to be equal, where  $i = 1, 2, 3$ . So we can use one symbol  $a$  ( $a = a_i$ ) to express the pitch of the three-way EB. Besides, the

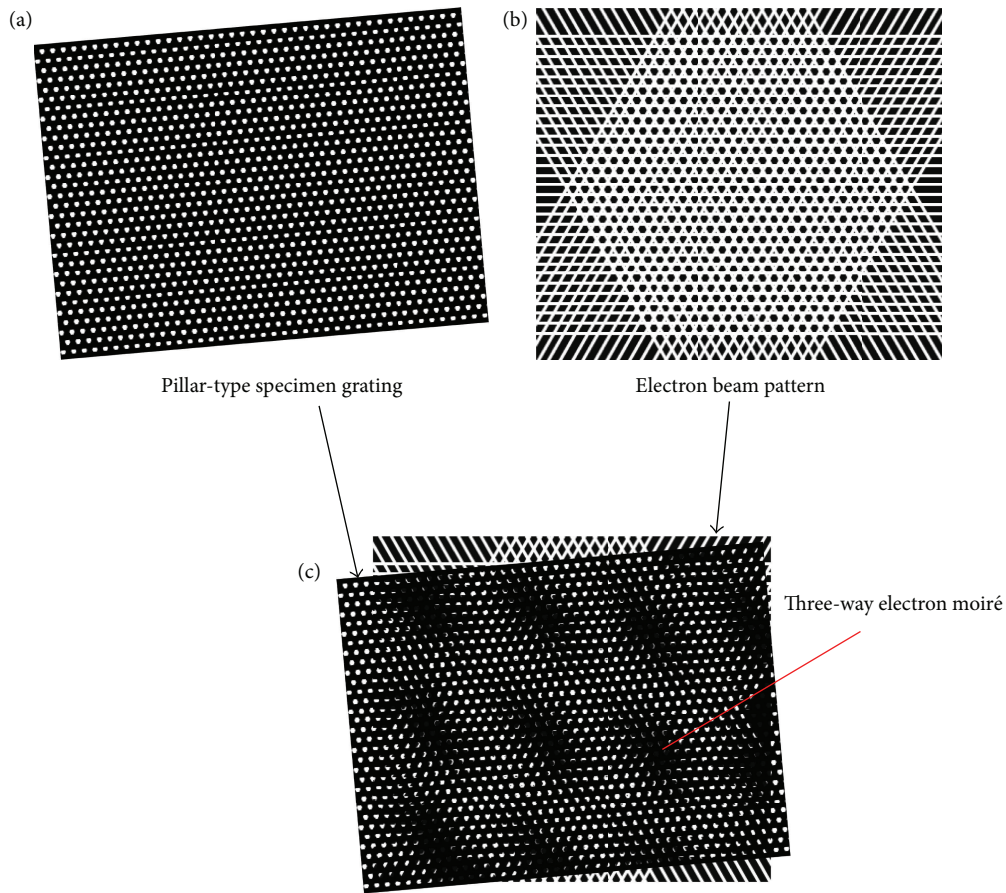


FIGURE 3: Formation principle of three-way SEM moiré for a pillar-type specimen grating. In (b), the white part denotes the exposed EB and the black part represents the unexposed EB.

included angles between each two one-way lines of the three-way EB is usually set to be  $60^\circ$  (Figure 5) for easy calculation.

- (3) To form three-way SEM moiré, the pitch ( $a$ ) of the three-way EB should be close to the specimen grating pitch. Usually,  $a$  is 0.8~1.2 times the pitches ( $a_i'$ ) of the specimen grating in three directions, where  $i = 1, 2, 3$ . Then, we will discuss how to control the EB pitch when using the SPG-724 pattern generator in an SEM. In this pattern generator, only a square region can be exposed. The pixel number ( $N$ ) and the length ( $L$ ) of this square region under the SEM magnification of 200x can be chosen from some options. The options include  $N = 1000, 2000, 4000, 5000,$  and  $10000$  pixels and  $L = 50, 100, 200,$  and  $500 \mu\text{m}$ . If we choose different values of  $N, L$  and different SEM magnifications, the EB sizes will be different. The variation of the EB size in nanometer per pixel along with the SEM magnification under different combinations of  $N$  and  $L$  is plotted in Figure 6. The EB pitch can be calculated by

$$a = n * sp, \quad (2)$$

where  $n$  is the pixel number of the EB pitch and  $sp$  represents the EB size in nanometer per pixel which can be determined from Figure 6.

#### 4. Observation of Three-Way SEM Moiré

In this section, we will show the observed three-way SEM moiré taking a hole-type specimen grating (grid) as an example. The specimen grating in which the holes are arranged in a triangular manner was produced by the EB lithography (EBL) method [5]. The used SEM (SX-40A) is equipped with a pattern generator (SPG-724).

The procedure for fabricating the grid includes four steps. First, a silicon slide was covered with an electron-sensitive layer (EB resist, EBR9) by a spin coater. Then, an EB pattern was designed according to the desired grating shape and size. Next, the silicon slide was placed on the specimen stage in the SEM and the EB pattern was introduced for the EB exposure. Finally, the silicon slide with the EB resist was developed and then immediately rinsed. When the exposed EB resist was removed, the three-way grating pattern with a pitch of about  $2.05 \mu\text{m}$  emerged on the specimen. Figure 7 exhibits the specimen grating image recorded by a Lasertec scanning laser microscope (ILM15). It should be noted that although we can design an EB pattern in which the unexposed areas

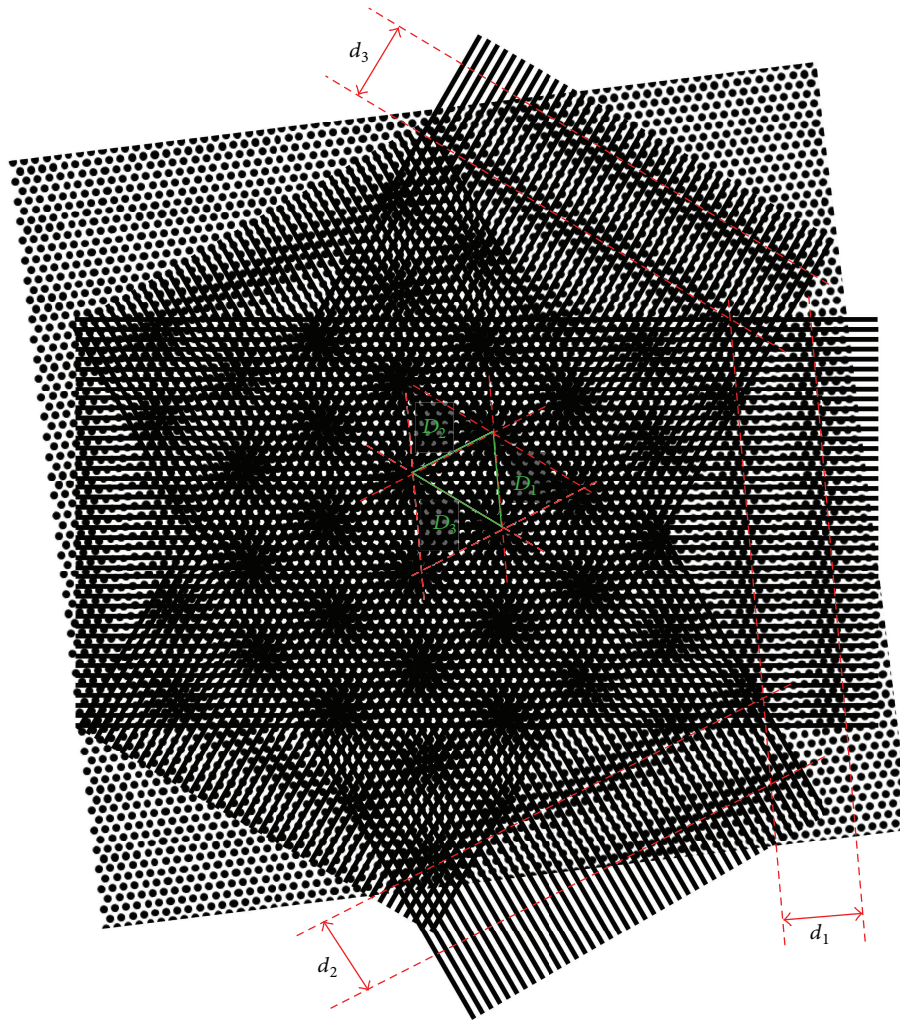


FIGURE 4: Relationship between three-way SEM moiré and one-way SEM moiré.

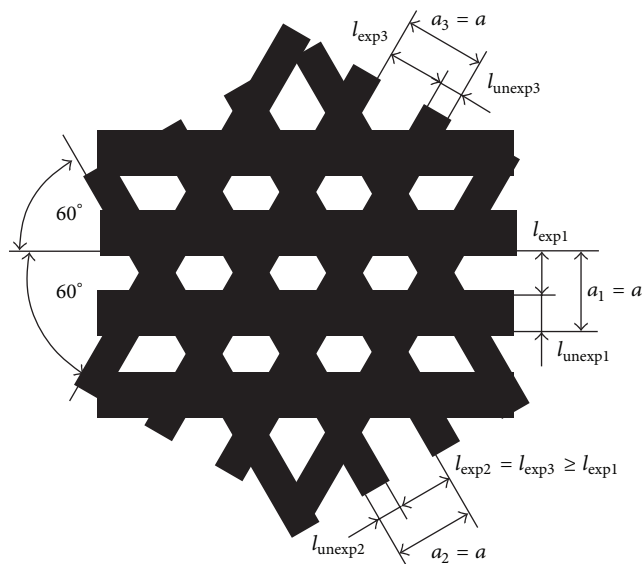


FIGURE 5: Size design of the three-way EB pattern.

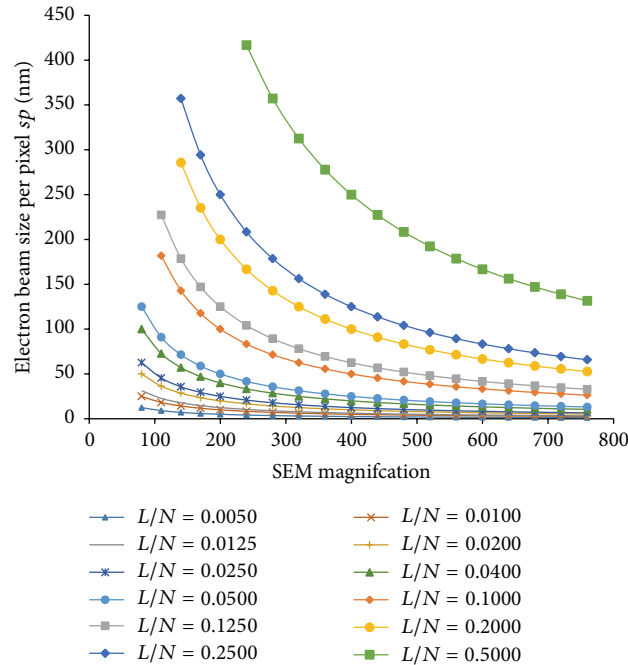


FIGURE 6: Variation of the EB size per pixel ( $sp$ ) along with the SEM magnification.



FIGURE 7: The hole-type three-way grating on silicon fabricated by the EBL method.

are distributed in arbitrary shapes and regions, the EB scans row by row in the horizontal direction. The reason why one direction is more distinct than the other two directions is that the distinct direction is in the horizontal direction during the EBL process.

Before generating three-way SEM moiré on this silicon slide, we should determine the used EB pattern. For this hole-type specimen grating, we adopted the EB pattern similar to Figure 2(b). Since the specimen grating pitch is about  $2.05 \mu\text{m}$ , the designed EB pitch should be in the range of  $1.64\text{--}2.46 \mu\text{m}$  (0.8–1.2 times). Next, suitable options should be chosen to realize an applicable EB pitch in the SEM and the pattern generator which were the same as in the EBL process. The pixel number of the EB pitch was set to be  $n = 50$ , with the exposed pixels of 20 and the unexposed pixels of 30. The pixel number and the length of a square in the pattern generator were chosen to be  $N = 5000$  pixels, an  $L = 500 \mu\text{m}$  from the existing options. When scanning, the magnification of the

SEM was chosen as 500x. From Figure 6, it is found that the EB size per pixel is  $sp = 40 \text{ nm}$  in the case of  $L/N = 0.1$ . Therefore, the EB pitch can be calculated using (2); that is,  $a = 2 \mu\text{m}$ .

When the designed EB pattern is used to scan on the specimen grating on the silicon slide, the “Spot scan” mode in the SPG-724 pattern generator should be adopted. The exposure dose and the electric current are better to be small. In this experiment, the exposure dose was  $1 \mu\text{C}/\text{cm}^2$  and the electric current was 70 pA measured by a digital electrometer (8252, ADCMT). When the EB patterns are at an appropriate position, three-way SEM moiré will appear (Figure 8(a)). But the three-way SEM moiré is not distinct in Figure 8(a). In this case we can rotate the EB slightly until distinct three-way SEM moiré emerges. Figures 8(b) and 8(c) show the three-way SEM moiré patterns when the EB used in Figure 8(a) is clockwise rotated by  $1^\circ$  and  $2^\circ$ , respectively. Both the three-way SEM moiré patterns in Figures 8(a) and 8(b) are clear,

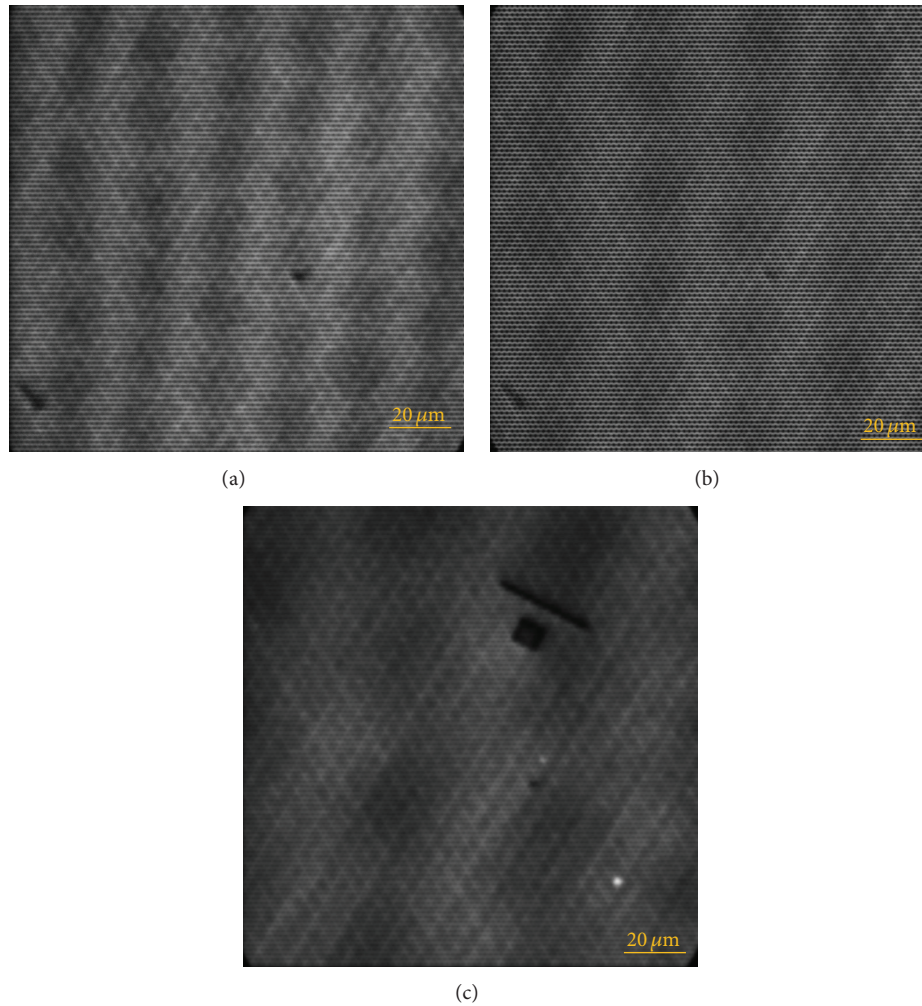


FIGURE 8: The three-way SEM moiré patterns on silicon. (a) The moiré spots are not distinct, (b) when the EB pattern is clockwise rotated by  $1^\circ$ , and (c) when the EB pattern is clockwise rotated by  $2^\circ$ .

and can be used to characterize the specimen grating on silicon in three directions at the same time, based on the measurement principle of the three-way SEM moiré method mentioned in Section 2.3.

## 5. Conclusions

The three-way SEM moiré method was proposed for deformation and structure analysis of periodic structures in triangular or hexagonal arrangements. The three-way SEM moiré is derived from the interference between the three-way EB and the specimen grating. It can also be regarded as the result of the interference among the three groups of one-way SEM moiré fringes. The measurement principle for the deformation and the structure pitch as well as the orientation from the three-way SEM moiré pattern was presented. Three key points of design about the three-way EB were pointed out. The operation sequence and the matters needing attention in the forming process of the

three-way SEM moiré were demonstrated taking a hole-type specimen grating on silicon as the example. The three-way SEM moiré method is able to simultaneously characterize micro/nanostructures in three directions. This method is promising in determining the domain boundary or grain boundary of micro/nanostructures from the difference of moiré spots in different domains or grains in a large view field.

## Conflict of Interests

The authors declare that there is no conflict of interests regarding the publication of this paper.

## References

- [1] R. Weller and B. M. Shepherd, "Displacement measurement by mechanical interferometry," *Proceedings of Society for Experimental Stress Analysis*, vol. 6, no. 1, pp. 35–38, 1948.

- [2] D. Post, B. Han, and P. Ifju, *High Sensitivity Moiré*, Springer, Berlin, Germany, 1994.
- [3] F.-L. Dai, J. McKelvie, and D. Post, "An interpretation of Moiré interferometry from wavefront interference theory," *Optics and Lasers in Engineering*, vol. 12, no. 2-3, pp. 101-118, 1990.
- [4] J. W. Dally and D. T. Read, "Electron beam Moiré," *Experimental Mechanics*, vol. 33, no. 4, pp. 270-277, 1993.
- [5] S. Kishimoto, M. Egashira, and N. Shinya, "Microcreep deformation measurements by a Moiré method using electron beam lithography and electron beam scan," *Optical Engineering*, vol. 32, no. 3, pp. 522-526, 1993.
- [6] Y. M. Xing, S. Kishimoto, and Y. R. Zhao, "An electron Moiré method for a common SEM," *Acta Mechanica Sinica*, vol. 22, no. 6, pp. 595-602, 2006.
- [7] S. Kishimoto, Q. Wang, H. Xie, and Y. Zhao, "Study of the surface structure of butterfly wings using the scanning electron microscopic Moiré method," *Applied Optics*, vol. 46, no. 28, pp. 7026-7034, 2007.
- [8] Y. J. Li, H. M. Xie, M. J. Tang, J. G. Zhu, Q. Luo, and C. Z. Gu Gu, "The study on microscopic mechanical property of polycrystalline with SEM Moiré method," *Optics and Lasers in Engineering*, vol. 50, no. 12, pp. 1757-1764, 2012.
- [9] Y. Tanaka, K. Naito, S. Kishimoto, and Y. Kagawa, "Development of a pattern to measure multiscale deformation and strain distribution via in situ FE-SEM observations," *Nanotechnology*, vol. 22, no. 11, Article ID 115704, 2011.
- [10] H. Xie, B. Li, R. Geer, B. Xu, and J. Castracane, "Focused ion beam Moiré method," *Optics and Lasers in Engineering*, vol. 40, no. 3, pp. 163-177, 2003.
- [11] J.-H. Park and S.-B. Lee, "High resolution AFM Moiré technique for the detection of defects in nano structure," in *Proceedings of the International Conference on Electronic Materials and Packaging (EMAP '07)*, November 2007.
- [12] H. M. Guo, H. W. Liu, Y. L. Wang et al., "Nanometre moire fringes in scanning tunnelling microscopy of surface lattices," *Nanotechnology*, vol. 15, no. 8, pp. 991-995, 2004.
- [13] D. Su and Y. Zhu, "Scanning moiré fringe imaging by scanning transmission electron microscopy," *Ultramicroscopy*, vol. 110, no. 3, pp. 229-233, 2010.
- [14] B. Pan, H. Xie, S. Kishimoto, and Y. Xing, "Experimental study of Moiré method in laser scanning confocal microscopy," *Review of Scientific Instruments*, vol. 77, no. 4, Article ID 043101, 2006.
- [15] C.-M. Liu, L.-W. Chen, and C.-C. Wang, "Nanoscale displacement measurement by a digital nano Moiré method with wavelet transformation," *Nanotechnology*, vol. 17, no. 17, article 4359, 2006.
- [16] Z. Liu, X. Lou, and J. Gao, "Deformation analysis of MEMS structures by modified digital Moiré methods," *Optics and Lasers in Engineering*, vol. 48, no. 11, pp. 1067-1075, 2010.
- [17] H. Xie, Q. Wang, S. Kishimoto, and F. Dai, "Characterization of planar periodic structure using inverse laser scanning confocal microscopy Moiré method and its application in the structure of butterfly wing," *Journal of Applied Physics*, vol. 101, no. 10, Article ID 103511, 2007.
- [18] S. Kishimoto and Y. Yamauchi, "The exploration of domain sizes and orientation directions in ordered assembled nanoparticles with electron Moiré fringes," *Physical Chemistry Chemical Physics*, vol. 11, no. 27, pp. 5554-5557, 2009.
- [19] Q. H. Wang, S. Kishimoto, X. F. Jiang, and Y. Yamauchi, "Formation of secondary Moiré patterns for characterization of nanoporous alumina structures in multiple domains with different orientations," *Nanoscale*, vol. 5, no. 6, pp. 2285-2289, 2013.
- [20] Q. Wang, S. Kishimoto, and Y. Yamauchi, "Three-directional structural characterization of hexagonal packed nanoparticles by hexagonal digital Moiré method," *Optics Letters*, vol. 37, no. 4, pp. 548-550, 2012.
- [21] Q. H. Wang, S. Kishimoto, and Y. Yamauchi, "Structural analysis of a micro hexagonal mesh using a three-way grating by hexagonal digital Moiré method," *Journal of the Japanese Society for Experimental Mechanics*, vol. 13, pp. s143-s147, 2013.
- [22] S. Kishimoto, "Electron Moiré method," *Theoretical and Applied Mechanics Letters*, vol. 2, no. 1, article 011001, 2012.

## Research Article

# Strain Sensor of Carbon Nanotubes in Microscale: From Model to Metrology

Wei Qiu, Shi-Lei Li, Wei-lin Deng, Di Gao, and Yi-Lan Kang

*Tianjin Key Laboratory of Modern Engineering Mechanics, Department of Mechanics, Tianjin University, Tianjin 300072, China*

Correspondence should be addressed to Wei Qiu; [qiuwei@tju.edu.cn](mailto:qiuwei@tju.edu.cn) and Yi-Lan Kang; [tju\\_ylkang@tju.edu.cn](mailto:tju_ylkang@tju.edu.cn)

Received 30 October 2013; Accepted 25 December 2013; Published 10 February 2014

Academic Editors: Y. Fu and G. Pedrini

Copyright © 2014 Wei Qiu et al. This is an open access article distributed under the Creative Commons Attribution License, which permits unrestricted use, distribution, and reproduction in any medium, provided the original work is properly cited.

A strain sensor composed of carbon nanotubes with Raman spectroscopy can achieve measurement of the three in-plane strain components in microscale. Based on previous work on the mathematic model of carbon nanotube strain sensors, this paper presents a detailed study on the optimization, diversification, and standardization of a CNT strain sensor from the viewpoint of metrology. A new miniaccessory for polarization control is designed, and two different preparing methods for CNT films as sensing media are introduced to provide diversified choices for applications. Then, the standard procedure of creating CNT strain sensors is proposed. Application experiments confirmed the effectiveness of the above improvement, which is helpful in developing this method for convenient metrology.

## 1. Introduction

The requirement of mechanical measurement is increasing with the rapid development of micro-nanoscience and technology [1]. Owing to its peculiarities, such as non-destructiveness, convenience, and high-resolution, micro-Raman spectroscopy has been widely applied to on-line in situ measurement of residual stress in microstructure caused by the processing [2, 3] and to real-time mechanical investigation of graphene, carbon nanotubes, and other low-dimensional materials under force loading [4–7].

Mechanical measurement based on Raman spectroscopy has a kernel limitation, for it is only applicable to “Raman-active” materials. This could be overcome by using “Raman-active” materials as sensors or sensing media. Carbon nanotubes (CNT) may become robust sensors in mechanical measurement by Raman because of their excellent mechanical and spectral properties [8, 9]. The Raman-strain sensitivity of CNTs was investigated by Cronin et al. [10] using atomic force probe to apply axial strain on single-walled carbon nanotube and recording the Raman peak position change with strain. Zhao and Wagner et al. [11–15] introduced the idea of a CNT strain sensor by Raman. Qiu et al. [16] presented a mathematical model for the measurement of all

the in-plane strain components (normal strain,  $\epsilon_X$ ,  $\epsilon_Y$ , and shear strain,  $\gamma_{XY}$ ) by utilizing polarized Raman and evaluating the quantitative contributions of carbon nanotubes in all directions to the entire spectrum. By using this model and Raman strain rosette technology that is proposed, the three in-plane strain components can be achieved in microscale by measuring the Raman information of CNTs randomly distributed on the measured sample with three specified polarization directions [17, 18].

The interface between CNTs and the matrix (bonding or attaching CNTs on the sample surface) behaves as a primary influence on the sensing properties, such as measuring range, sensitivity, and stability, of the CNT strain sensor. It is not only the materials but also the methods of preparing CNTs or their composite films that influence sensing properties on samples. The experiments by Schadler et al. [19] proved that multiwalled carbon nanotubes (MWNTs) were not suitable for strain sensing due to the low interface load transfer efficiency. Ma et al. [20] studied the behavior of load transfer in functionalized single-walled carbon nanotube (SWNT)/epoxy nanocomposites and showed that some functionalized groups may effectively improve the interface efficiency. Ma and Larsen [21] presented a comparative study on dispersion and interfacial properties of three

different modified single-walled carbon nanotubes and three different polymer (PC, PVDF, and Epoxy) composites using Hansen solubility parameters and found that the association of the  $-\text{COOH}$  functionalized SWNT and epoxy had the highest interface load transfer efficiency. In addition to the sensing media, it has been proved that the method control of polarization direction in the Raman system also affects the precision of a CNT strain sensor [22].

Therefore, the equipment, materials, and procedure of this method should be optimized to improve the sensing properties and then diversified and standardized for convenience and efficiency. This work presents a detailed study on the optimization, diversification, and standardization of CNT strain sensors by Raman to promote development from a model to convenient metrology.

## 2. Mathematic Model of CNT Strain Sensor

The CNT strain sensor in microscale requires CNTs deforming together with the measured object and uses polarized micro-Raman spectroscopy to detect the strain information of the CNTs. For each individual CNT, its Raman G' peak (namely, Raman shift) changes coincident with the in-plane strain with small deformation,

$$\Delta\omega(\theta) = \Psi_{\text{Sensor}} \cdot (\varepsilon_X \cos^2\theta + \varepsilon_Y \sin^2\theta - \gamma_{XY} \cos\theta \sin\theta), \quad (1)$$

where  $\theta$  is the axial direction of the carbon nanotubes,  $\Delta\omega$  is the Raman shift increment after deformation,  $\Psi_{\text{Sensor}}$  is the strain-Raman shift coefficient of the CNT sensor,  $\varepsilon_X$ ,  $\varepsilon_Y$  and  $\gamma_{XY}$  are the normal strain components in the X, and Y-directions and the shear strain component of the in-plane strain, respectively.

For real measurement, it is more practical to use a CNT film, which contains a large number of randomly oriented carbon nanotubes, as the strain sensor rather than single CNTs. The film can be adhered to the surface of the measured object. In Raman measurement, the sampling point contains hundreds or thousands of carbon nanotubes in different directions. The spectrum information obtained by the microscopic Raman system is essentially the sum of all scattering information of CNTs within the sampling point.

Because the G' peak of CNTs is a Gauss (or Lorenz) shape, the properties of normal (or Cauchy) distribution are applied to the peak position of overall spectrum as follows [18]:

$$\Delta\Omega^{(\varphi)} = \frac{\int_{-\pi/2}^{\pi/2} \Delta\omega(\theta) \cdot R(\theta - \varphi) \cdot \rho(\theta) d\theta}{\int_{-\pi/2}^{\pi/2} R(\theta - \varphi) \cdot \rho(\theta) d\theta}. \quad (2)$$

The variable  $\Delta\Omega^{(\varphi)}$  represents the Raman shift increment after deformation when the polarization angle of the incident light is  $\varphi$ .  $R$  is a function of the CNTs polarized Raman antenna effect, and  $\rho(\theta)$  is the CNT plane distribution function. For the CNT film whose direction is randomly distributed,  $\rho(\theta)$  is a constant. By substituting the detail function form of  $\Delta\omega$  and  $R$  in (3), the analytical relationship between the polarized Raman results and the in-plane strain components of the measured object was achieved, whose final form lies in the

polarization configuration and control method of the Raman system. For instance, keeping the incident and scattering polarization direction parallel,  $R(\theta - \varphi) = \cos^4(\theta - \varphi)$ , the relationship equation (2) becomes (3) [18],

$$\Delta\Omega^{(\varphi)} = \frac{1}{6} \Psi_{\text{Sensor}} \cdot \begin{bmatrix} 3 + 2 \cos 2\varphi \\ 3 - 2 \cos 2\varphi \\ -2 \sin 2\varphi \end{bmatrix}^T \cdot \begin{bmatrix} \varepsilon_X \\ \varepsilon_Y \\ \gamma_{XY} \end{bmatrix}. \quad (3)$$

According to the above equation, the Raman shift increment at any polarization angle can be expressed by a linear combination of the in-plane strain components with different weights, either of which is a trigonometric function of polarization angle. Given three different polarization angles, such as  $0^\circ$ ,  $45^\circ$ , and  $90^\circ$ , a simultaneous equation can be set up and the strain components solved,

$$\begin{aligned} \varepsilon_X &= \frac{1}{4\Psi_{\text{Sensor}}} \cdot (5\Delta\Omega^{(0)} - \Delta\Omega^{(90)}), \\ \varepsilon_Y &= \frac{1}{4\Psi_{\text{Sensor}}} \cdot (5\Delta\Omega^{(90)} - \Delta\Omega^{(0)}), \\ \gamma_{XY} &= \frac{3}{2\Psi_{\text{Sensor}}} \cdot (\Delta\Omega^{(0)} + \Delta\Omega^{(90)} - 2\Delta\Omega^{(45)}). \end{aligned} \quad (4)$$

## 3. Equipment, Material and Procedure of Metrology

**3.1. Measurement System and Control Method.** Strain measurement using a CNT sensor requires a research level cofocus micro-Raman spectrometer, such as the InVia series by Renishaw, LabRam HR series by Horiba JY, or Alpha series by Witec. In the Raman system, a He-Ne laser is preferred because the Raman spectra of metal SWNTs show outstanding antenna effects when excited by a 632.8 nm laser [23]. Moreover, according to (2), the detailed relationship between Raman shift and strain components depends on the polarization configuration and control method of the Raman system. Hence, the polarization of the Raman system should be controllable.

The control method of the current micro-Raman system requires special improvement for strain measurement using the CNT sensor. It has been shown that the dual coordination configuration, which regulates the incident and scattered polarization directions continuously and parallel permanently, is most suitable for a CNT strain sensor [22]. This configuration was traditionally realized by using a polarizer in the incident path and an analyzer in the scattering path. The incident polarizer is usually placed at the open space of the laser export, while the analyzer can be located inside the spectrometer and generally needs to be customized and processed by the user. Moreover, control of scattering polarization requires the user to repeatedly open the box of the spectrometer to regulate the analyzer.

The dual coordination configuration can also be achieved by a more practicable method as follows. A half-wave plate, whose frequency is similar to that of the Raman laser, replaces the polarized plate inside the  $180^\circ$  (or  $360^\circ$ ) continuous polarizer, a standard accessory of the microscope in the

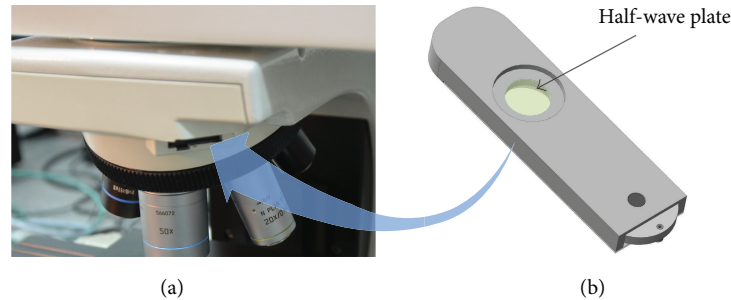


FIGURE 1: (a) 45° slot for the  $\lambda$ -plate of the microscope in the Raman system, (b) miniaturization-designed 180° continuous polarizer.

Raman system. The transformed continuous polarizer is inserted in the open slot of the microscope when applying the CNT strain sensor. Meanwhile, the orthogonal analyzer, also a standard accessory of the Raman system, is used and adjusted to the parallel polarization direction.

The above method has some exceptions, especially for Raman systems that lack open slots in the microscopes, use a UV laser, or lack dual-scan accessories, or other reasons. Even then, there is an alternative to the traditional method. As Figure 1 shows, the microscope in the Raman system always has a small 45° slot for a  $\lambda$ -plate, through which a miniature-designed 180° continuous polarizer (shown in Figure 1(b)) can be inserted into the public path of the incident and scattered light inside the microscope.

**3.2. Preparing the Sensing Media.** Single-walled carbon nanotubes (SWNTs) functionalized by a  $-\text{COOH}$  group (TIMES-NANO Ltd.) were optimized as the “sensor” material. This is because the Raman spectra of SWNTs show an outstanding antenna effect [23], and the  $-\text{COOH}$  group improves the interface between the nanotubes and the polymer matrix [21]. Meanwhile, E51 epoxy resin, with low viscosity and room temperature curing, was selected as a polymer matrix, adhering the SWNTs onto the surface of the measured object.

Two methods are presented to prepare the CNT film onto the surface of the measured object, named the “ultrasonic blending method” and “coating-transfer method,” respectively. For the former one, 1 wt% SWNTs were mixed and dispersed into a liquid epoxy for 24 h using ultrasound in 60°C and then mixed with the curing agent (25 wt%) in 80°C. The mixture was dropped onto the surface of the measured object and then covered with a quartz glass plate coated by a release agent. The glass plate was pressed slowly, loaded by weight to extrude the CNT/epoxy mixture to a thin film, and then peeled from the sample carefully after curing the epoxy at 60°C for 5 h and at room temperature for 24 h.

The “coating-transfer method” was composed of two steps. For the first step, the SWNTs were dispersed in deionized water using ultrasound, then the liquid mixture film was coated on a polyethylene terephthalate (PET) plate by using a single roller-coating machine. When the water was completely volatilized, a pure CNT film was achieved. Next, the film was transferred onto the measured object by coating an epoxy film on the sample surface. The CNT film side of the PET plane was pressed on the surface slowly, then weights

were loaded on the plane until the resin was totally cured, and the PET plane was peeled from the sample carefully.

**3.3. Sensing Properties and Calibrations.** For the study of the properties of CNT films as strain sensors, free-standing CNT film samples were prepared by using the above two methods and replacing the measured objects as quartz glass plates coated by release agents. After peeling the films from the glass plates, the films were cut to  $50 \times 3 \text{ mm}^2$  strips. The strip samples were tagged as Film-I for those made by the ultrasonic blending method and as Film-II for those made by the coating-transfer method.

The basic mechanical properties of the films were measured by utilizing an Instron 3343 testing machine (Figure 2). The loading rate was 0.05 mm/min. The typical stress-strain curves of the films under uniaxial stretching are shown in Figure 3. According to the experiment results, the mechanical properties of the Film-I and Film-II were almost similar. In detail, Young’s modulus of Film-I and Film-II were 3.49 GPa and 4.13 GPa, tensile strengths were 77.96 MPa and 84.73 MPa, and the elongations were 2.66% and 2.56%, respectively.

The Raman-mechanical characteristics, namely, sensing properties, were achieved through calibration tests as follows. A Renishaw InVia Reflex Raman spectroscope with a He-Ne laser source (632.8 nm, 2 mW) was utilized, and the incident beam was focused on the CNT film surface of each sample in a backscattering geometry through a 50x objective lens (N.A. = 0.8), forming a sample spot of approximately  $2 \mu\text{m}$  in diameter. Each CNT film strip was uniaxially stretched step-by-step using a minitensile machine specially designed for the micro-Raman system. Before loading, 21 random points on the surface of each specimen were detected by the Raman system. At every point, Raman data with nine different polarization directions, from 0° to 90°, were achieved. Under each loading step, the Raman spectra around the  $G'$  band ( $2450$  to  $2800 \text{ cm}^{-1}$ ) of the same sampling spot in 0°, 45°, and 90° polarization directions, were recorded. The  $G'$  peak of the spectra near  $2650 \text{ cm}^{-1}$  is fitted by using a Gauss or Lorenz function. Because the characteristic peaks of epoxy resin do not exist within the scope of  $2450\text{--}2850 \text{ cm}^{-1}$ , the Raman shift of the  $G'$  peak is caused by deformation of carbon nanotubes.

Figures 4(a) and 4(b) give the Raman shift data of each film without loading. In Figure 4(a), the Raman shifts

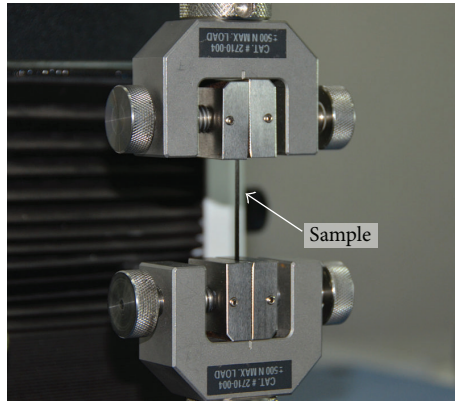


FIGURE 2: Sample under uniaxial tension.

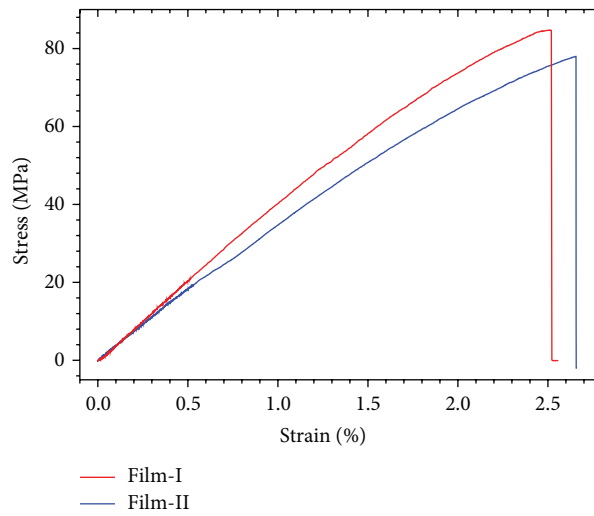


FIGURE 3: The typical stress-strain curves of the films under uniaxial tension.

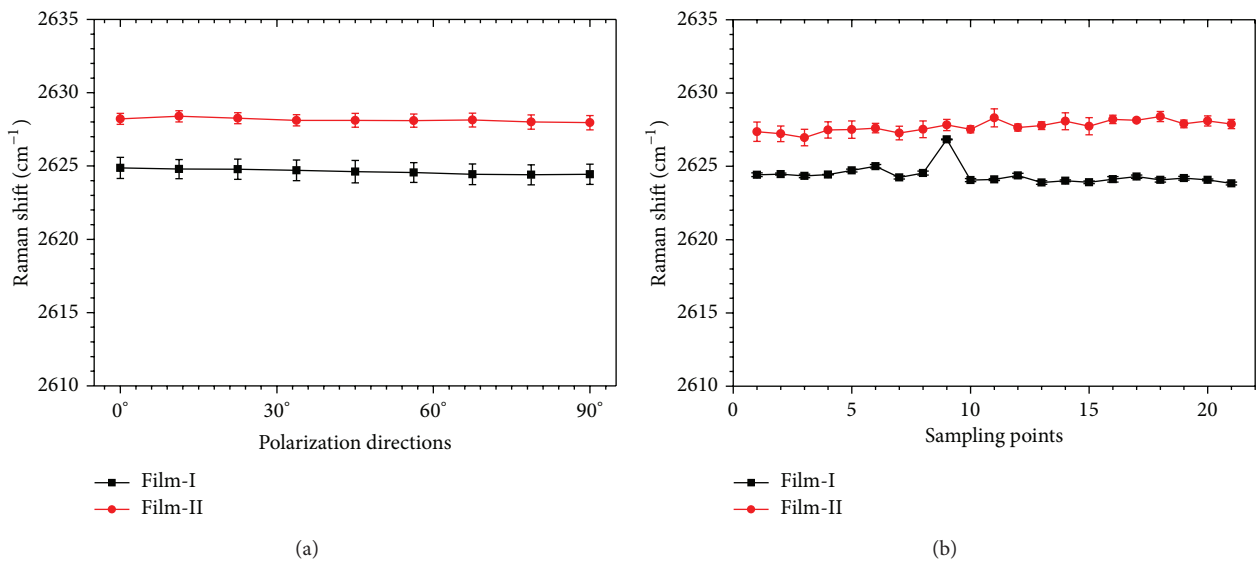


FIGURE 4: (a) Raman shifts (average of 21 points) at nine different polarization directions without loading. (b) Raman shifts (average of nine polarization directions) of 21 different points without loading.

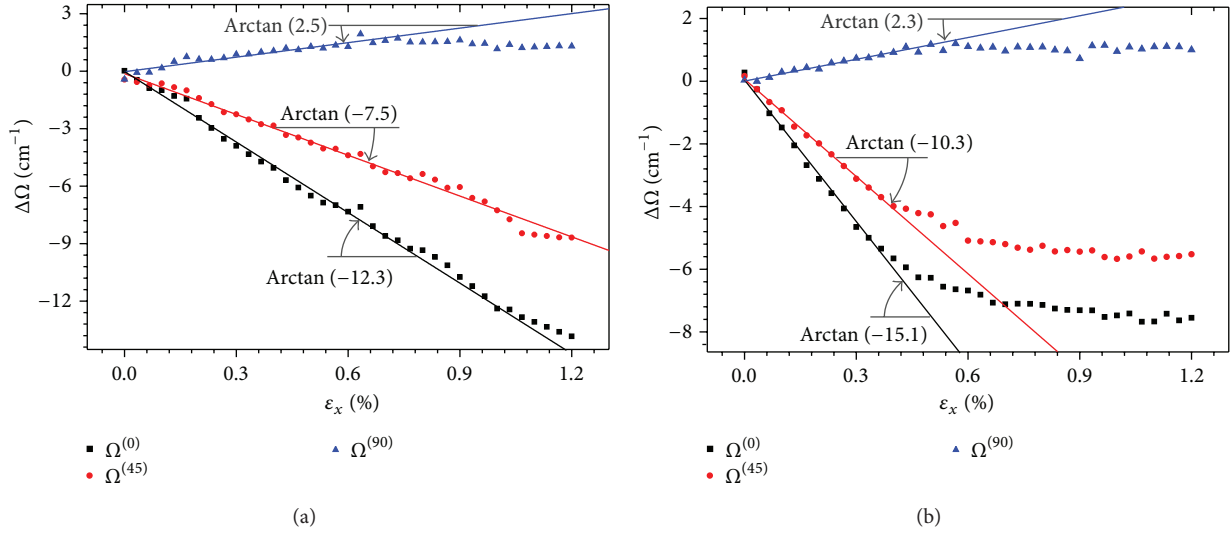


FIGURE 5: The results of the calibration experiments on (a) Film-I and (b) Film-II.

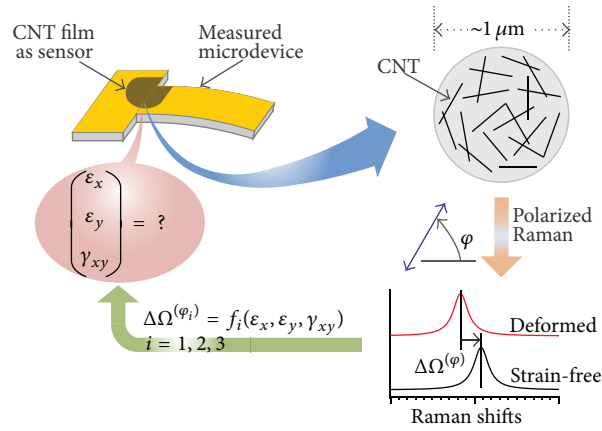


FIGURE 6: The standard procedure of strain measurements using the CNT strain sensor.

(average of 21 points) in nine different polarization directions are almost similar. In Figure 4(b), the Raman shifts (average of nine polarization directions) of 21 different points are also accordant. All these results show that the CNTs disperse uniformly inside both Film-I and Film-II.

Figure 5(a) gives the results of the calibration experiment on Film-I, which show that the Raman shift change of polarization directions  $0^\circ$ ,  $45^\circ$ , and  $90^\circ$  ( $\Delta\Omega^{(0)}$ ,  $\Delta\Omega^{(45)}$ , and  $\Delta\Omega^{(90)}$ ) maintains satisfactory linearity in 1.0% strain extent. When  $\epsilon_x$  exceeds this extent, the Raman shift change becomes nonlinear. Hence, the segment inside this strain extent represents the measuring range of Film-I as strain sensor. Similarly, Figure 5(b) gives the results of the calibration experiment of Film-II, showing the measuring range of 0.4%.

The data in the linear segments were fitted (shown in Figure 5). Meanwhile, (5) was concluded by using the partial derivative of the first equation of (4),

$$\Psi_{\text{Sensor}} = \frac{1}{4} \cdot \left( 5 \frac{\partial \Delta\Omega^{(0)}}{\partial \epsilon_x} - \frac{\partial \Delta\Omega^{(90)}}{\partial \epsilon_x} \right). \quad (5)$$

The fitted data in Figure 5 were substituted into (5), achieving the strain-Raman shift coefficients of each CNT film as a strain sensor. For the CNT film made by the ultrasonic blending method,  $\Psi_{\text{Sensor}} = -1600 \text{ cm}^{-1}$ . Similarly, for the film made by the coating-transfer method,  $\Psi_{\text{Sensor}} = -1945 \text{ cm}^{-1}$ .

There are obvious differences of the sensing properties (listed in Table 1) between two CNT films, which are mainly caused by the interfacial strength and rigidity between the carbon nanotubes and epoxy matrix. The CNT/epoxy interfaces in Film-I have higher average strength, showing a relative large measuring range. The interface in Film-II behaves more rigidly, corresponding to a bigger sensitivity. Such differences provide diversified choices for application.

**3.4. Standard Procedure.** As shown in Figure 6, the standard procedure of strain measurements using a CNT strain sensor is as follows. A CNT film is prepared on the surface of the measured microdevice. The sample is put into the microscope of the cofocus micro-Raman spectrometer,

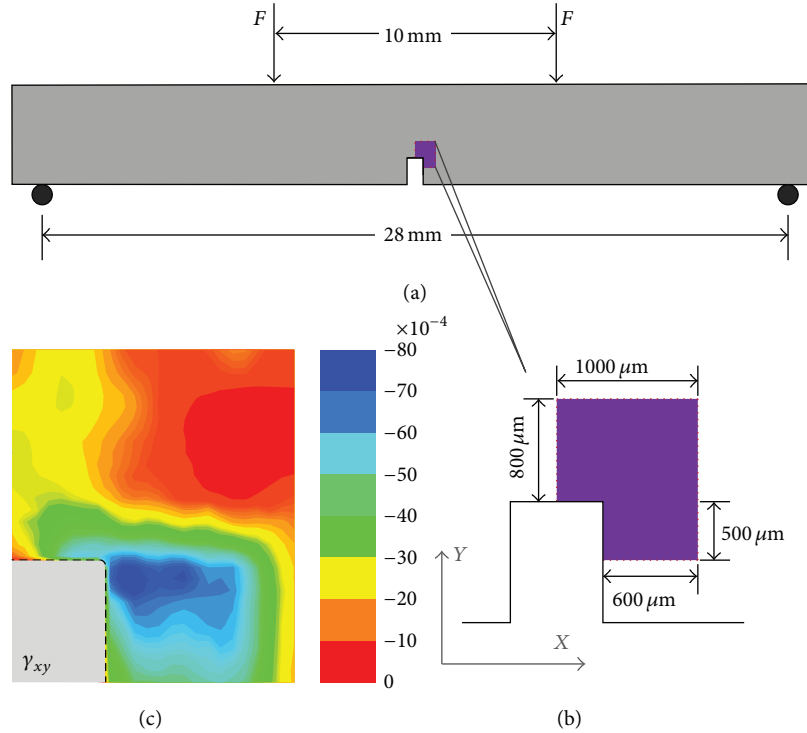


FIGURE 7: The experiment on the fiber-reinforced bar under four-point bend loading. (a) The geometrical shape, dimensions, and loading type, (b) Raman mapping region, (c) the distribution of  $\gamma_{xy}$  near the vicinity of the slot tip achieved by the CNT strain sensor.

TABLE 1: Strain-sensing properties of CNT films prepared by different methods.

CNT films	$\frac{\partial \Delta \Omega^{(0)}}{\partial \varepsilon_U}$ ( $\text{cm}^{-1}/\% \varepsilon$ )	$\frac{\partial \Delta \Omega^{(45)}}{\partial \varepsilon_U}$ ( $\text{cm}^{-1}/\% \varepsilon$ )	$\frac{\partial \Delta \Omega^{(90)}}{\partial \varepsilon_U}$ ( $\text{cm}^{-1}/\% \varepsilon$ )	$\Psi_{\text{Sensor}}$ ( $\text{cm}^{-1}/\varepsilon$ )	Range ( $\varepsilon$ )
Film-I	-12.3	-71	2.5	-1600	1.0%
Film-II	-15.1	-10.3	2.3	-1945	0.4%

whose polarization is controlled with the dual coordination configuration by using the transformed continuous polarizer. The laser is focused on the CNT film using a high magnification lens with a sampling spot of 1 to 2  $\mu\text{m}$ , where there exist thousands of randomly oriented CNT individuals. The Raman spectra of every sampling spot with different polarization angles, such as  $0^\circ$ ,  $45^\circ$ , and  $90^\circ$ , are detected before and after deformation. The G' peak of the spectra near  $2650 \text{ cm}^{-1}$  are fitted by using a Gauss or Lorentz function. The Raman shift increments are substituted into (4); hence, all the strain components of the sampling spot are obtained. Through Raman mapping, the distribution field of each strain component may be achieved.

#### 4. Applications and Discussions

To prove the metrology advantage of the CNT sensor, a series of applications were performed on the samples. Figure 7 shows four-point bend experiments on a fiber-reinforced epoxy bar (Figure 7(a)) whose dimensions are  $32 \times 6 \times 2 \text{ mm}^3$ . The epoxy is DGEBA-based epoxy resin (E51), with Young's module of 3.5 GPa and a Poisson ratio of 0.3. The unidirectional carbon fiber (Toray M40JB-12k) is parallel

to the length direction (namely,  $x$ -direction). The interface strength of resin and fiber is approximately 50–100 MPa. A slot, approximately 0.8 mm wide and 2 mm tall, normal to the  $x$ -direction, was prepared at the middle of one longitudinal side of the bar. Then, a CNT film that was 30  $\mu\text{m}$  thick was prepared on the epoxy bar surface. The sample was four-point bend loaded to a 300  $\mu\text{m}$  maximum deflection. An area next to the rectangle tip of the slot (shown in Figure 7(b)) was scanned with a 50  $\mu\text{m}$  step length by using the Raman spectroscope (Renishaw InVia Reflex, 632.8 nm laser, 50x lens) and applying the CNT strain sensor at each spot.

The experimental result of shear strain distribution is given in Figure 7(c), which shows that nonuniform deformation exists near the vicinity of the slot tip. Particularly, the shear zone is parallel to the fiber direction, neither the slope direction nor the  $45^\circ$  direction, which shows the specific mechanical behavior of unidirectional fiber-reinforced materials. Quantitatively, the maximum of the shear strain is approximately  $8 \times 10^{-3}$ ; thus, the shear stress reaches 10.8 Mpa, where  $\tau = E\gamma/2(1 + \mu) = 3.5 \times 8/2(1 + 0.3) = 10.8 \text{ MPa}$ .

Figure 8 shows the experimental result of strain distribution near the tip of a mode I crack by using the CNT strain sensor. The sample was a CNT/epoxy composite made

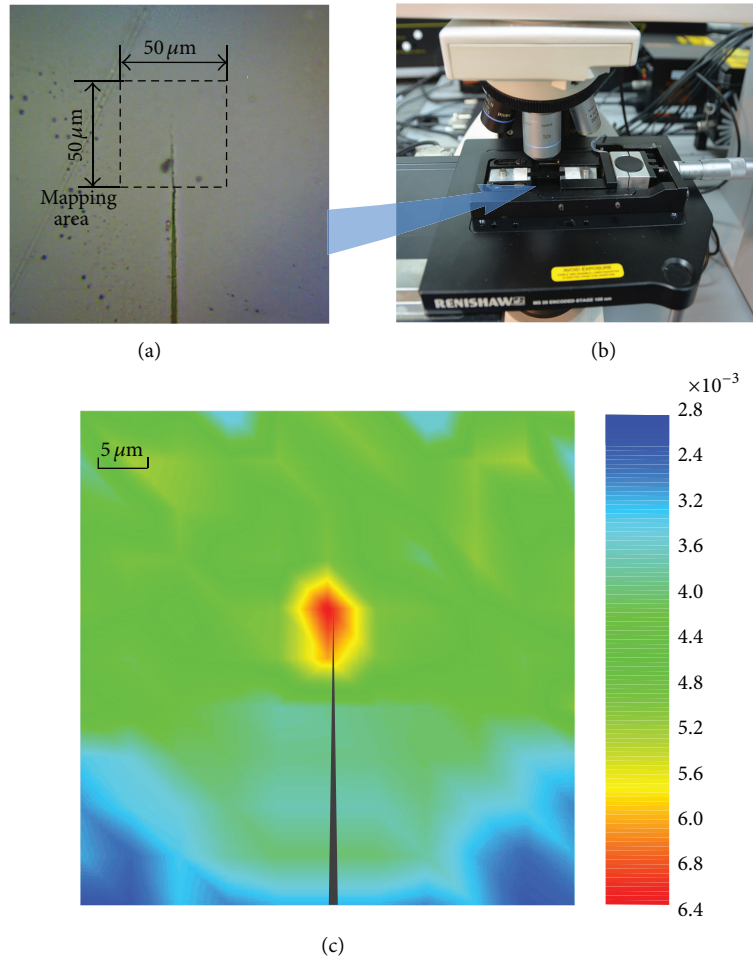


FIGURE 8: The experiment on the mode I crack. (a) Experimental system, (b) the image of the sample and Raman mapping region, (c) the distribution of  $\varepsilon_x$  around the crack tip.

by ultrasonic blending method (Film-I), whose dimensions were  $50 \times 3 \times 0.05 \text{ mm}^3$ . A transverse crack (Figure 8(a)), approximately 0.5 mm in length, was cut normal to the longitudinal direction of the sample by using a razor blade. The strip sample was uniaxially loaded to 0.3% tensile mean strain. The vicinity around the crack tip,  $50 \times 50 \mu\text{m}^2$ , was scanned with the Raman spectroscopy (Renishaw InVia Reflex, 632.8 nm laser, 50x lens, shown in Figure 8(b)) in  $5 \mu\text{m}$  steps. Figure 8(c) gives the distribution of normal strain in the  $x$ -direction (via the tensile direction). It shows that  $\varepsilon_x$  behaves as a serious concentration in front of the crack tip and even in the whole measured area.

Figure 9 shows the experimental result of the residual strain field around a Vickers microindentation. The sample was a CNT/epoxy composite made by ultrasonic blending method (Film-I), whose thickness was also approximately  $50 \mu\text{m}$ . The sample was pressed by a Vickers microindenter gradually, until the force reached 0.5 N. After leaving the microindenter, the vicinity inside and outside the indentation, as shown in Figure 9(a), was scanned by the Renishaw InVia Reflex Raman spectroscopy with a 632.8 nm laser and a 50x lens. Figure 9(b) gives the distribution of the sum of the in-plane principal strain ( $= \varepsilon_x + \varepsilon_y$ ), which demonstrates that

there are distinct residual compressive strains at the middle of the indentation and residual tensile strains at the edge of the indentation.

## 5. Conclusions

In this paper, the strain sensor composed of carbon nanotubes in microscale was studied, and several improvements were achieved. The applicable micro-Raman systems and the control modes of polarizations were discussed, and a new miniaccessory for polarization control was designed. Then, two different preparing methods of CNT films as sensing media were presented. Calibration experiments showed that both preparing methods had high stabilities. The differences of sensing properties between the two methods provide diversified choices for application. Also, a standard procedure of measurement using the CNT strain sensor is proposed. Through several application experiments (such as vicinity round a notch area, mode I crack tip, and Vickers indentation), the effectiveness of the improvements was proved, promoting the strain sensor of carbon nanotubes from a model to very convenient metrology.

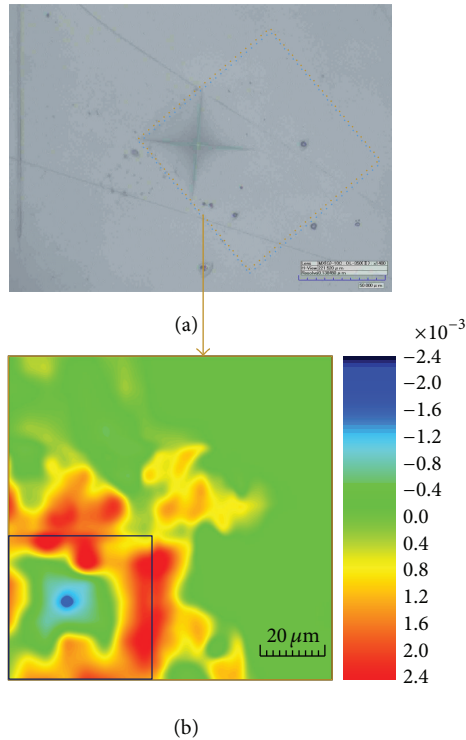


FIGURE 9: The experiment on the Vickers microindentation. (a) The image of the sample and Raman mapping region, (b) the distribution of residual in-plane principal strain ( $\epsilon_x + \epsilon_y$ ).

## Conflict of Interests

The authors declare that there is no conflict of interests regarding the publication of this paper.

## Acknowledgments

This work is financially supported by the National Basic Research Program of China (no. 2012CB937500), the National Natural Science Foundation of China (Grant nos. 11227202, 11272232, and 11002097), and the Program for New Century Excellent Talents in University (Grant no. NCET-13).

## References

- [1] X. Li, H. Xie, Y. Kang, and X. Wu, "A brief review and prospect of experimental solid mechanics in China," *Acta Mechanica Sinica*, vol. 23, no. 6, pp. 498–548, 2010.
- [2] W. Qiu, Y.-L. Kang, Q. Li, Z.-K. Lei, and Q.-H. Qin, "Experimental analysis for the effect of dynamic capillarity on stress transformation in porous silicon," *Applied Physics Letters*, vol. 92, no. 4, Article ID 041906, 2008.
- [3] Q. Li, W. Qiu, H. Tan, J. Guo, and Y. Kang, "Micro-Raman spectroscopy stress measurement method for porous silicon film," *Optics and Lasers in Engineering*, vol. 48, no. 11, pp. 1119–1125, 2010.
- [4] Z. K. Lei, R. X. Bai, W. Qiu et al., "Optical evaluation of the buckling behavior of stiffened composite laminates," *Composites A*, vol. 43, no. 11, pp. 1850–1859, 2012.
- [5] W. L. Deng, W. Qiu, Q. Li et al., "Multi-scale experiments and interfacial mechanical modeling of carbon nanotube fiber," *Experimental Mechanics*, 2013.
- [6] R. J. Young, L. Gong, I. A. Kinloch, I. Riaz, R. Jalil, and K. S. Novoselov, "Strain mapping in a graphene monolayer nanocomposite," *ACS Nano*, vol. 5, no. 4, pp. 3079–3084, 2011.
- [7] Z. K. Lei, W. Quan, and Q. Wei, "Micromechanics of fiber-crack interaction studied by micro-Raman spectroscopy: bridging fiber," *Optics and Lasers in Engineering*, vol. 51, no. 4, pp. 358–363, 2013.
- [8] H. Dai, "Carbon nanotubes: synthesis, integration, and properties," *Accounts of Chemical Research*, vol. 35, no. 12, pp. 1035–1044, 2002.
- [9] M. Terrones, "Science and technology of the twenty-first century: synthesis, properties, and applications of carbon nanotubes," *Annual Review of Materials Research*, vol. 33, no. 1, pp. 419–501, 2003.
- [10] S. B. Cronin, A. K. Swan, M. S. Ünlü, B. B. Goldberg, M. S. Dresselhaus, and M. Tinkham, "Resonant Raman spectroscopy of individual metallic and semiconducting single-wall carbon nanotubes under uniaxial strain," *Physical Review B*, vol. 72, no. 3, Article ID 035425, 2005.
- [11] J. R. Wood, Q. Zhao, M. D. Frogley et al., "Carbon nanotubes: from molecular to macroscopic sensors," *Physical Review B*, vol. 62, no. 11, pp. 7571–7575, 2000.
- [12] A. H. Barber, Q. Zhao, H. D. Wagner, and C. A. Baillie, "Characterization of E-glass-polypropylene interfaces using carbon nanotubes as strain sensors," *Composites Science and Technology*, vol. 64, no. 13-14, pp. 1915–1919, 2004.
- [13] Q. Zhao, M. D. Frogley, and H. D. Wagner, "Direction-sensitive strain-mapping with carbon nanotube sensors," *Composites Science and Technology*, vol. 62, no. 1, pp. 147–150, 2002.
- [14] M. D. Frogley, Q. Zhao, H. D. Wagner et al., "Polarized resonance Raman spectroscopy of single-wall carbon nanotubes within a polymer under strain," *Physical Review B*, vol. 65, no. 11, Article ID 113413, 2002.
- [15] Q. Zhao, M. D. Frogley, H. D. Wagner et al., "Direction-sensitive stress measurements with carbon nanotube sensors," *Polymers for Advanced Technologies*, vol. 13, no. 10–12, pp. 759–764, 2002.
- [16] W. Qiu, Y. L. Kang, Q. Li et al., "A new theoretical model of carbon nanotube strain sensor," *Applied Physics Letters*, vol. 92, no. 4, Article ID 041906, 2008.
- [17] W. Qiu, Y.-L. Kang, Z.-K. Lei, Q.-H. Qin, Q. Li, and Q. Wang, "Experimental study of the Raman strain rosette based on the carbon nanotube strain sensor," *Journal of Raman Spectroscopy*, vol. 41, no. 10, pp. 1216–1220, 2010.
- [18] W. Qiu, Y. L. Kang, Z. K. Lei et al., "The use of a carbon nanotube sensor for measuring strain by micro-Raman spectroscopy," *Carbon*, vol. 53, pp. 161–168, 2013.
- [19] L. S. Schadler, S. C. Giannaris, and P. M. Ajayan, "Load transfer in carbon nanotube epoxy composites," *Applied Physics Letters*, vol. 73, no. 26, pp. 3842–3844, 1998.
- [20] P. C. Ma, Q. B. Zheng, E. Mäder et al., "Behavior of load transfer in functionalized carbon nanotube/epoxy nanocomposites," *Polymer*, vol. 53, no. 26, pp. 6081–6088, 2012.
- [21] J. Ma and R. M. Larsen, "Comparative study on dispersion and interfacial properties of single walled carbon nanotube/polymer composites using Hansen solubility parameters," *ACS Applied Materials & Interfaces*, vol. 5, no. 4, pp. 1287–1293, 2013.
- [22] S. L. Li, W. Qiu, Y. L. Kang et al., "Study on the CNT Sensor for strain measurement and its control method of Raman

polarization,” *Spectroscopy and Spectral Analysis*, vol. 33, no. 5, pp. 1244–1248, 2013.

- [23] M. A. Pimenta, A. Marucci, S. A. Emedocles et al., “Raman modes of metallic carbon nanotubes,” *Physical Review B*, vol. 58, no. 24, pp. 16016–16019, 1998.

## Research Article

# Fiber Optic Projection-Imaging System for Shape Measurement in Confined Space

Lujie Chen,<sup>1</sup> Viswanath Bavigadda,<sup>1</sup> Theodoros Kofidis,<sup>2</sup> and Robert D. Howe<sup>3</sup>

<sup>1</sup> *Engineering Product Design, Singapore University of Technology and Design, Singapore 138682*

<sup>2</sup> *Yong Loo Lin School of Medicine, National University of Singapore, Singapore 119228*

<sup>3</sup> *School of Engineering and Applied Sciences, Harvard University, Cambridge, MA 02138, USA*

Correspondence should be addressed to Lujie Chen; [iiuufgitt@gmail.com](mailto:iuufigtt@gmail.com)

Received 24 September 2013; Accepted 30 December 2013; Published 10 February 2014

Academic Editors: Y. Fu and G. Pedrini

Copyright © 2014 Lujie Chen et al. This is an open access article distributed under the Creative Commons Attribution License, which permits unrestricted use, distribution, and reproduction in any medium, provided the original work is properly cited.

A fiber-based projection-imaging system is proposed for shape measurement in confined space. Owing to the flexibility of imaging fibers, the system can be used in special scenarios that are difficult for conventional experimental setups. Three experiments: open space, closed space, and underwater are designed to demonstrate the strength and weakness of the system. It is shown that when proper alignment is possible, relatively high accuracy can be achieved; the error is less than 2% of the overall height of a specimen. In situations where alignment is difficult, significantly increased error is observed. The error is in the form of gross-scale geometrical distortion; for example, flat surface is reconstructed with curvature. In addition, the imaging fibers may introduce fine-scale noise into phase measurement, which has to be suppressed by smoothing filters. Based on results and analysis, it is found that although a fiber-based system has its unique strength, existing calibration and processing methods for fringe patterns have to be modified to overcome its drawbacks so as to accommodate wider applications.

## 1. Introduction

Substantial research and development efforts have gone into enhancing the accuracy, functionality, and implementation of various optical techniques based on the principle of holography, interferometry, morié, structured light projection, stereo vision, and photometry. Optical systems for three-dimensional (3D) shape measurement have found wide range of applications. They encompass metrological evaluation in macro-, meso-, and microscales.

Existing approaches, commercial systems, and well-known experimental setups have standardized the solution to many different measurement tasks in diverse scenarios. At macroscale, stereo vision and photometric methods are commonly used to reconstruct 3D shape of objects whose dimensions are above one cubic meter [1]. At mesoscale, desktop-sized objects can be conveniently measured on an optical table in a lab environment. Depending on the objective of evaluation (shape or displacement), a technique may be chosen that best suits the problem under consideration. Holography [2] and interferometry [3] are suited for

displacement measurement; morié [4] and structured light projection [5] are suited for shape measurement. There are certainly variations, for example, white light interferometry for shape measurement [6]. Some method, such as digital image correlation [7], can even achieve both in one go. At microscale, precise optical alignment of a system becomes increasingly important. Most implementations of optical techniques are based on a microscope to take advantage of its well designed lens relay [8].

While the main stream of optical system development assumes that specimen can be put at a designated position, this is not possible in *in-situ* measurement; thus developers have been motivated to incorporate optical techniques in special devices, such as endoscopes and fiber scopes. Over the years, holograms were produced out of fiber optic systems [9–11]; morié fringe patterns were generated through single-mode fibers, with potential use in medical diagnosis [12]; fringe projection was achieved by transmitting the image of a grating through fibers to make measurement on microobjects [13]. Data-processing methods: phase-shifting and Fourier

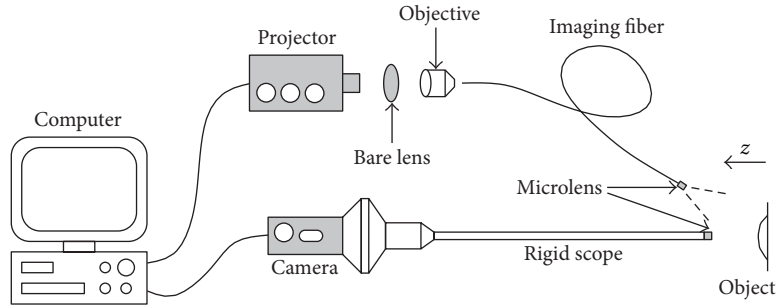


FIGURE 1: System diagram.

transform were applied to fringe patterns obtained by an endoscope or a fiber scope, just as in free-space scenarios [14–16]. Photometric approaches were also adapted to these devices [17, 18].

Several trends along the development of endoscopic shape measurement have been observed. First, more digital components are integrated in a system; for example, gratings were replaced by digital mirror devices (DMD) or spatial light modulation (SLM) units [8, 19]. Second, special projection patterns were applied to retrieve 3D information [20–22]. Third, the applications were more specific and the solutions were more customized [23–25]. Last but not least, low-cost, off-the-shelf digital projectors were demonstrated to be a feasible projection unit [26, 27]. They provide similar level of flexibility to the expensive DMD or SLM devices in generating projection patterns.

However, as an off-the-shelf digital projector has its own built-in optics, not optimized for microscopic applications, severe optical distortion is likely to occur. In this paper, we describe a fiber optic projection-imaging system for shape measurement; compare the measurement results of a MEMS component in three scenarios: free space, confined space and underwater; discuss the pros and cons of the system; and suggest tentative approaches to enhance the performance of the low-cost digital-projector-based fiberscope as a high-precision measurement tool.

## 2. Principle

Constructing a structured light projection system based on fiber optics is straight forward in principle, as illustrated in Figure 1. The major difference from a nonfiber version lies in the use of imaging fiber bundles for directing the light, either in projection or in imaging, or both. Note that, despite its name, the imaging fiber works equally well for transmitting the projected light as for collecting light to pass to a camera. Depending on requirement, flexible or rigid imaging fibers may be incorporated. On the market, there are commercial rigid scopes that work with various types of cameras; hence, the real challenge in optical alignment is to couple the light from the projector to the imaging fiber.

Two components: a bare lens and an objective lens, as indicated in Figure 1, are necessary for light coupling. Usually, an off-the-shelf digital projector has a big divergence angle.

The bare lens is used to reduce the size of the projected optical cone so that a large portion of the projection area can enter the objective lens. Without the bare lens, most pixels of the projector will be wasted and the subsequent resolution will be low. Rule of thumb for choosing a suitable bare lens is to get at least as many pixels as the resolution of the imaging fiber into the objective lens. At the distal end of the fiber, a microlens is often attached to increase the numerical aperture (NA) of the imaging fiber. Consequently, a fairly complicated lens relay is in between the projector chip and the pattern projected on an object. The relay consists of the projector's built-in lens, the bare lens, the objective lens, and the microlens. Misalignment of the optical center of these lenses will cause distortion. Same applies to the imaging optical path.

The following procedures are applied to system calibration. They have been proven to be valid and accurate for nonfiber based fringe projection systems [28, 29]. A pinhole model is assumed on both the projection and the camera optics.

To calibrate the camera optics, a chessboard pattern is imaged at two positions along the  $z$  direction (Figure 1), with a known shift in between. The actual size of the squares on the chessboard is known too; hence, the 3D coordinate of all corners of the pattern is known. The origin of the world coordinate may be chosen arbitrarily. For instance, the origin may be the first chessboard corner on the far  $z$  direction position. The corresponding corner points on the images can be extracted at subpixel accuracy. Then, a matrix that represents the mapping between the image (2D) and the world (3D) points is calculated based on numerical methods described in [1]:

$$(x_i, y_i, 1)^T = M \cdot (x_w, y_w, z_w, 1)^T, \quad (1)$$

where  $M$  is the camera matrix,  $T$  denotes matrix transpose,  $x_i$  and  $y_i$  are coordinates of an imaged corner point,  $x_w$ ,  $y_w$ , and  $z_w$  are coordinates of the corresponding world point.  $M$  is used later to retrieve 3D coordinates of an object surface.

To calibrate the projection optics, the matrix of the lens relay is not calculated but the phase-to-height relationship is inferred from phase maps at two positions along  $z$  direction [28, 29]. As shown in Figure 2, planes 1 and 2 are two reference planes with a pure  $z$  direction shift. “Object” indicates an object surface in between the reference planes. At  $(x_1, z_1)$ ,  $(x_2, z_2)$  and  $(x_o, z_o)$ , the fringe patterns should have identical phase values, which can be found by phase mapping [30].

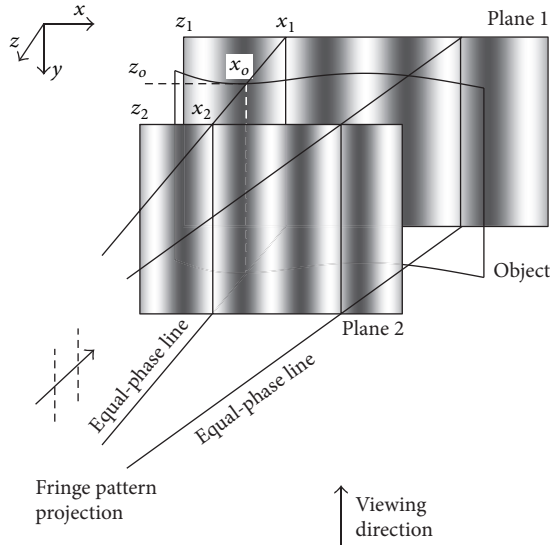


FIGURE 2: Calibration of phase-to-height relationship.

On each equal-phase line, three  $x$  coordinates,  $x_1$ ,  $x_2$ , and  $x_o$ , should be mapped to subpixel accuracy; hence, the unknown object surface height  $z_o$  can be calculated by

$$z_o = \frac{x_o - x_1}{x_2 - x_1} z_2, \quad (2)$$

assuming  $z_1 = 0$ . Note that (2) is theoretically valid even if an object surface point is beyond the reference planes.

After phase-to-height conversion, an object point obtains a 3D coordinate of mixed units. The  $x$  and  $y$  coordinates of the point are in the image coordinate, with a unit of pixel.  $z$  is a world coordinate, with a unit of an actual distance, such as millimeter. To obtain  $x$  and  $y$  in the world coordinate, (1) should be used again. Since  $M$  is known after calibration of the camera optics, there are only two unknowns  $x_w$  and  $y_w$ . The matrix representation contains three equations, two of which are linearly independent; hence,  $x_w$  and  $y_w$  can be solved. This completes the measurement process and the resultant object surface is in the 3D world coordinate.

The calibration is a relatively time-consuming procedure and is expected to be performed only when the system geometrical configuration is modified.

### 3. Experiment

Three experiments were conducted on a MEMS component shown in Figure 3. They represent different *in-situ* scenarios: open space, closed space and underwater. 3D measurement in closed space, and underwater is challenging, where a fiber-based projection-imaging system finds its special application.

Figure 4 shows the experimental setup of the closed-space scenario; the specimen was enclosed in a ping pong ball. The imaging optical path consisted of a CCD camera (Allied Vision Technology, Manta G-504B mono) and a rigid fiber scope. The projection path consisted of a miniprojector, a bare lens (attached to and behind the 3D stage), an objective

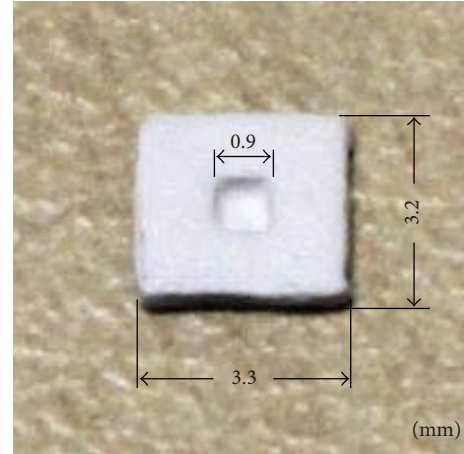


FIGURE 3: A MEMS component with a thickness of 0.55 mm. The surface was treated with diffusive paint.

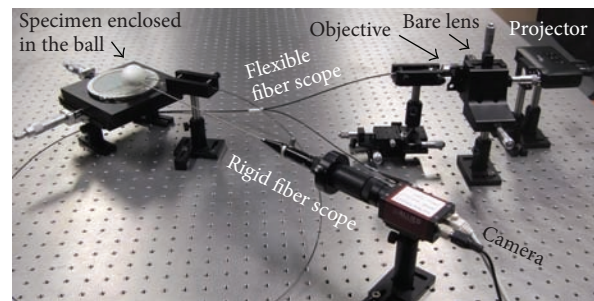


FIGURE 4: Experimental setup of the closed-space scenario.

lens and a flexible fiber scope (Fujikura FIGH-15-600N). Both the rigid and the flexible fiber scopes had an integrated microlens, with a divergent angle of around 100 degrees. The experimental setup of the other two scenarios was similar.

The flexible fiber bundle (Fujikura FIGH-15-600N) has 15,000 pixels with a working distance of 5 mm. It has an outer diameter of 1.3 mm. Specification of the rigid fiber scope is not on record unfortunately but based on our tests, it has 10,000 to 15,000 pixels with a working distance of 4 mm. It has an outer diameter of 2 mm. An adjustable lens at the camera end of the scope is quite useful in getting relatively good focus; hence, defocus is not present as a big challenge. Like any fringe projection system based on triangulation, projection shadow will cause trouble in data processing. However, due to confined space, the angle between the two fiber scopes is small: 5–10 degrees; there is little projection shadow caused by the object surface variation.

Figure 5 shows a typical fringe pattern projected on a reference plane. Relatively large radial distortion can be seen by an observer in Figure 5(a); nevertheless, the pattern recorded by the CCD camera, Figure 5(b), exhibits less radial distortion because (1) it was the central portion of the projected area and (2) the imaging optics had radial distortion too, which happened to cancel out that of the projection optics. In all experiments, the  $z$  direction shift of the reference plane was introduced through a mechanical micrometer.

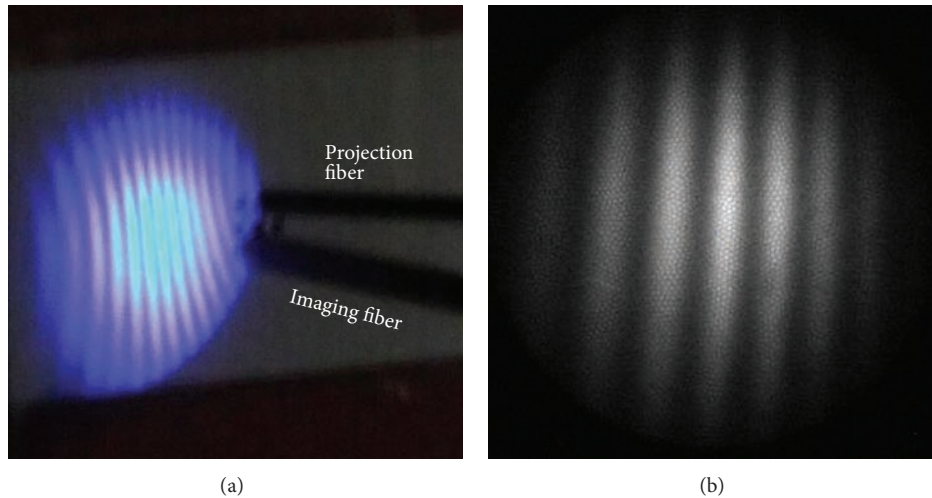


FIGURE 5: A fringe pattern projected on a reference plane, as seen (a) by an observer and (b) by the camera attached to the rigid fiber scope.

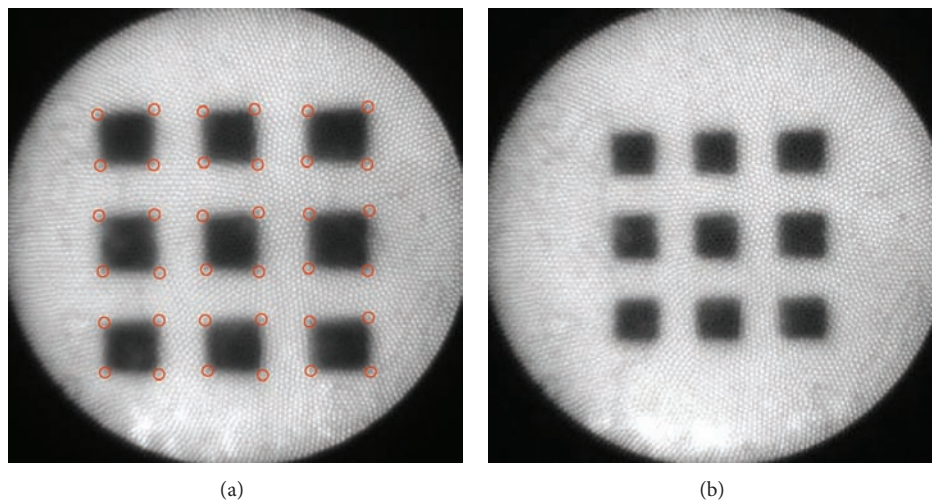


FIGURE 6: A chessboard pattern for camera calibration, recorded at (a) near and (b) far  $z$  positions. Red circles in (a) indicate the automatically detected corner points.

Figure 6 shows the chessboard pattern for camera calibration, recorded at two  $z$  positions. They were on the same positions as where the reference fringe patterns were captured.

In the open-space experiment, Figure 7(a), the specimen was aligned perpendicular to the viewing direction, ideal for 3D measurement. Figure 7(b) shows a typical fringe pattern obtained. Result of this experiment is an indication of the best-scenario case achievable by the system, since there is no constraint in space.

In the closed-space experiment, the specimen was attached to the inner surface of a ping pong. Several holes were created on the ping pong to provide access for the fibers, as shown in Figure 8(a). Figure 8(b) shows a typical fringe pattern obtained, in which one can see lots of individual fiber ends of the imaging fiber bundle. If they are in focus as in this picture, it implies that the imaging optics is in focus as well. In the closed-space scenario, alignment of the specimen with the projection or imaging optics is difficult. The subsequent side-effect will be discussed in Section 4.

The third experiment was aimed at testing the system for underwater measurement. There were two major challenges: first, the working space was confined and, second, projection or imaging through both air and water is in general not feasible because of refraction at the air-water interface. A fiber-based system is a good candidate for such *in-situ* measurement tasks. As shown in Figure 9(a), the fibers were dipped in the water. The fringes around the fibers, as seen by an observer, were indeed distorted due to refraction; however, those seen by the camera (Figure 9(b)) were not because the reflected light was collected by the imaging fiber in the water without passing through the air-water interface.

#### 4. Results and Discussion

Figure 10 shows the surface profile of the MEMS component obtained in the open-space experiment; (a) is the height map visualized in 2D, where  $x$  and  $y$  are in pixel unit and

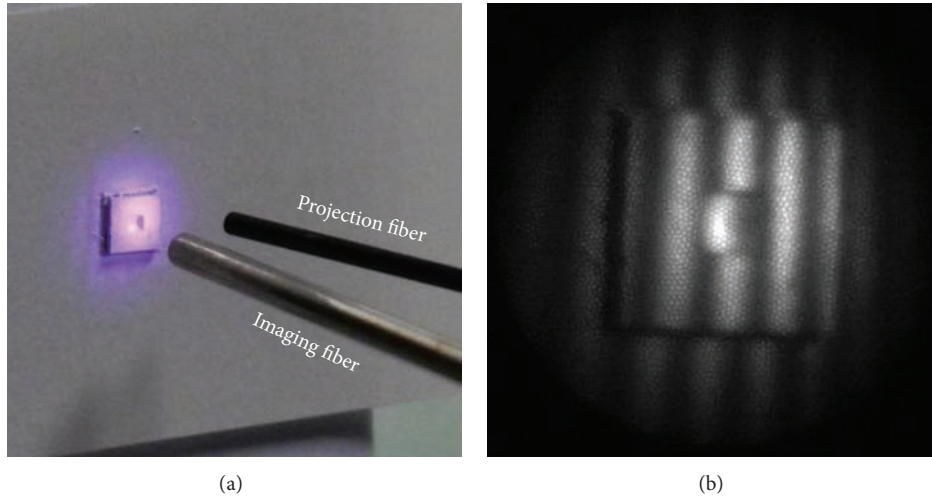


FIGURE 7: Open-space scenario. (a) Closeup of the fiber distal end. (b) A fringe pattern recorded by the camera.

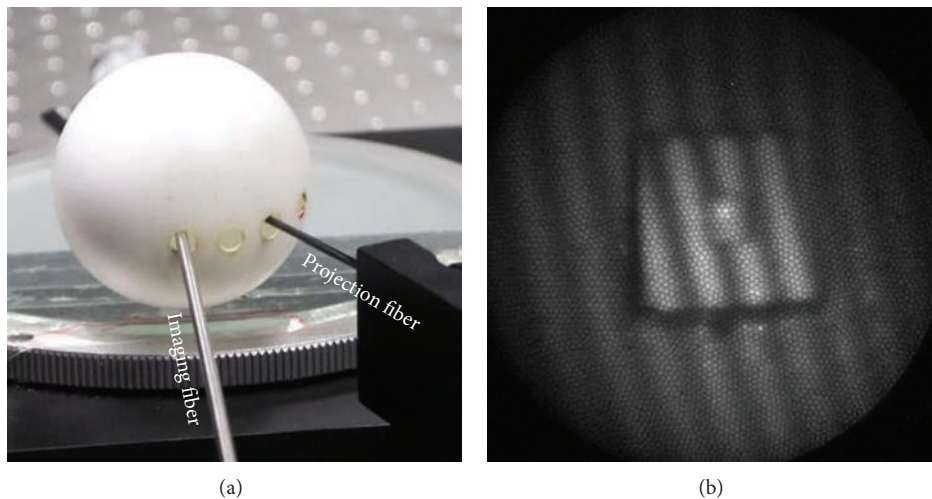


FIGURE 8: Closed-space scenario. (a) Several holes were created on the surface of the ping pong to provide access for the fibers. (b) A fringe pattern recorded by the camera. Zooming in the picture, one can see the image of lots of individual fiber ends.

the intensity indicates the height in millimeter; in (b), all coordinates are converted to the actual distance based on (1), as described in Section 2. The right-top and right-bottom corners of Figure 10(a) contain invalid phase mapping data due to limited field of view in the reference and the object phase maps. They are masked in white. The immediate phase mapping results are very noisy; hence, 3-by-3 median followed by mean filtering is applied to suppress the noise. The images shown are results after smoothing. The noise is mostly caused by void regions in a fiber bundle: this issue will be further discussed in the underwater experiment.

The specimen has a thickness of 0.55 mm, measured by a calliper. The value is used as a reference to evaluate the overall measurement accuracy. In Figure 10(a), the regions enclosed by red dashed lines are the front surface of the specimen and that enclosed by the cyan dashed lines are the base plane. The average height difference between these two regions is 0.56 mm, obtained by the optical method, which is in good

agreement with that obtained by the calliper. The depth of the central dip is not known. Based on the optical measurement, it is around 0.46 mm from the front surface. Visual inspection from different viewing angles suggests that there is no obvious measurement error.

Figure 11 shows in 2D and 3D, respectively, the surface profile of the specimen obtained in the closed-space experiment. As can be seen, the surface is tilted, indicating that the specimen was not perpendicular to the imaging fiber, nor to the reference plane, during the experiment. This is not surprising, since the MEMS component was enclosed in a ping pong (Figure 8(a)) and alignment was difficult. Such imperfect alignment is typical in closed-space scenarios, where accessibility is limited. The results reveal a problem of distortion: the flat front surface and the base plane become curved.

The curvature is more obvious with the gross tilt removed by fitting a plane to the front surface and then subtracting

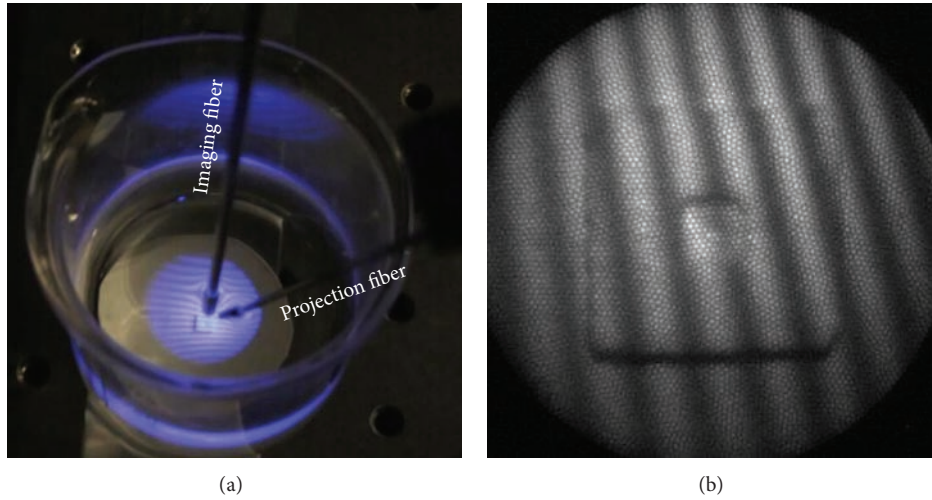


FIGURE 9: Underwater scenario. Both fibers were dipped in the water. A fringe pattern as seen (a) by an observer and (b) by the camera attached to the rigid fiber scope.

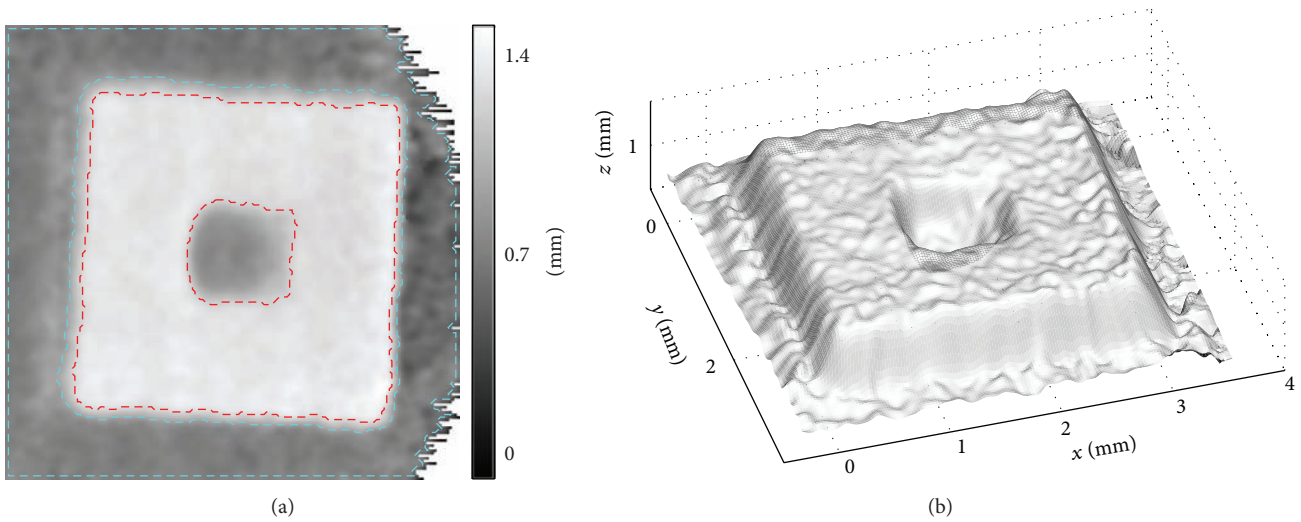


FIGURE 10: Open-space experiment. (a) Surface height map in 2D and (b) surface profile in 3D of the MEMS component.

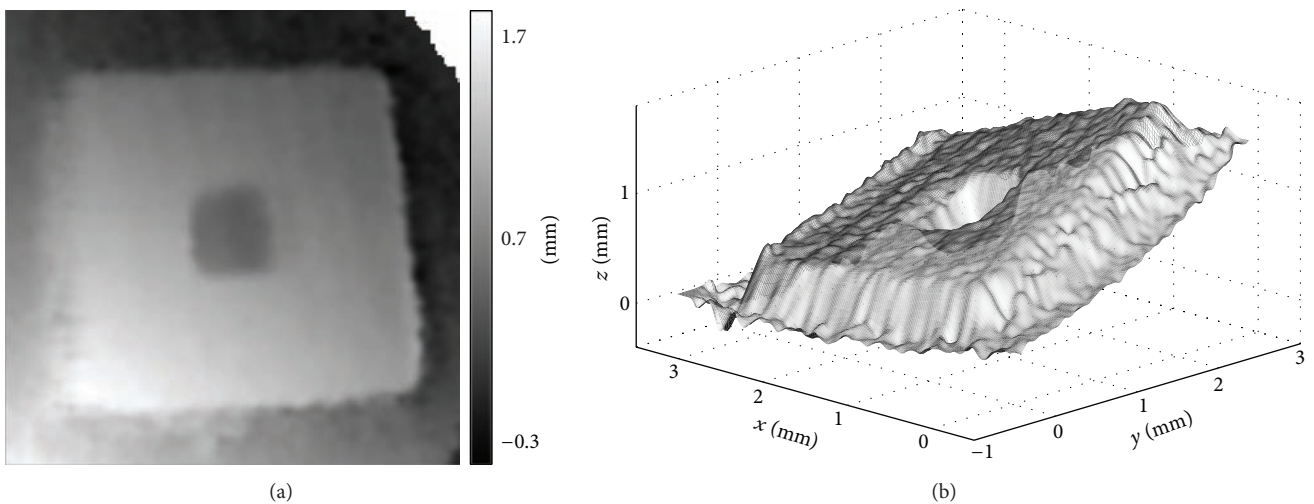


FIGURE 11: Closed-space experiment. (a) Surface height map in 2D and (b) surface profile in 3D of the MEMS component.

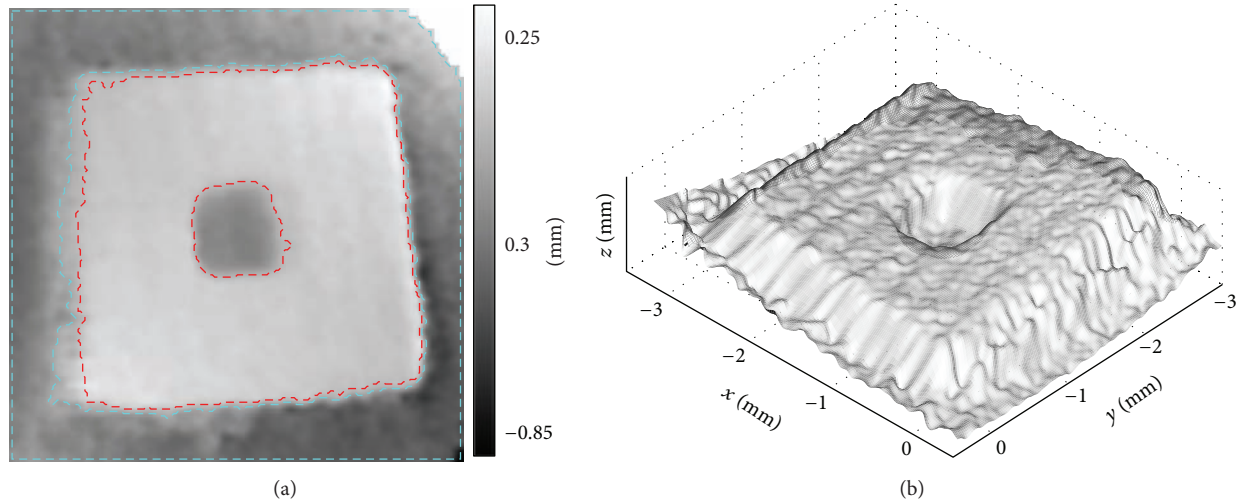


FIGURE 12: The gross tilt is removed from Figure 11.

the plane from the profile. The resultant 2D and 3D surface height distributions are shown in Figure 12. The distortion is most likely caused by the lens relay of the projection and imaging optics, which deviates from the pinhole model assumed in camera calibration and phase mapping. The deviation is small in the plane of the reference but is quite significant out of plane. Consequently, the results of the first experiment are relatively accurate but those of the second are poor. The average height difference of the front surface and the base plane, indicated in Figure 12(a), is 0.44 mm. Though it only differs from the result of the calliper by 20%, the deviation is quite severe because the surface is not even flat.

Figure 13 shows the unfiltered results of the underwater experiment. In the 2D surface height map in Figure 13(a), strong speckle noise is observed. A region indicated by a white square is magnified in Figure 13(b), where the density and frequency of the noise are clearly visualized. As mentioned earlier, the noise is due to void regions of an imaging fiber. They are the spaces in between many individual fibers, as shown in the fringe contrast map in Figure 13(c). Bright spots in the contrast map are image of the individual fibers. They change their intensity according to the projection pattern, thereby gaining high contrast. The space in between individual fibers has lower contrast because no light passes through. Its intensity varies weakly, owing to the defocused light from the surrounding fibers. Phase errors are inevitable in these regions and have caused the significant amount of noise.

Another artifact in Figure 13(a) is the bright crescent region at the central dip. The root cause is quite unexpected; it is part of the image of the projector's bulb. In this experiment, constrained by the size of the vessel (see Figure 9(a)), the angle between the projection and imaging fibers is small; subsequently, the image of the bulb, produced by and beneath the water, is in the field of view. Without carefully arranging the two fibers, one may easily end up with a big bright spot (the image of the bulb) in the recorded images. We specifically put the imaging fiber closer to the specimen than

the projection fiber so that the former blocked the spot light from the bulb. However, a residual edge of the spot light remains in the recorded fringe patterns; it has produced a low contrast region in Figure 13(c) and an erroneous phase distribution in the wrapped phase map; see Figure 13(d).

The surface height map after smoothing exhibits improved uniformity but the artefact in the central region persists, as shown in Figure 14. The average height difference between the front surface and the base plane, indicated in Figure 14(a), is 0.65 mm. The relatively large deviation from 0.55 mm, obtained by the calliper, may be attributed to two factors. First, the angle between projection and imaging is small, leading to low sensitivity in height measurement. Second, the specimen was stuck to the base plane by double-faced tape, which might become less sticky in the water and the space between the two surfaces expanded slightly. Similar to the first experiment, the specimen was aligned perpendicular to the imaging fiber; hence, no curved distortion is present in the results.

Based on the three experiments, the unique feature of the fiber optic projection-imaging system is well demonstrated. However, it is also found that in using calibration and processing methods designed for conventional systems, noticeable error may be produced in scenarios where proper alignment is difficult. Furthermore, if the optics is in focus, which is considered necessary in common practice, an imaging fiber bundle will produce relatively strong fine-scale noise. The noise reduces the phase measurement accuracy and resolution but, to some extent, can be suppressed by smoothing filters.

## 5. Conclusion and Future Work

A fiber-based projection and imaging system is constructed for shape measurement. The experiments and results have demonstrated its strength and weakness. It is suitable for confined space applications and is able to reconstruct fairly accurate surface profile under proper alignment. When

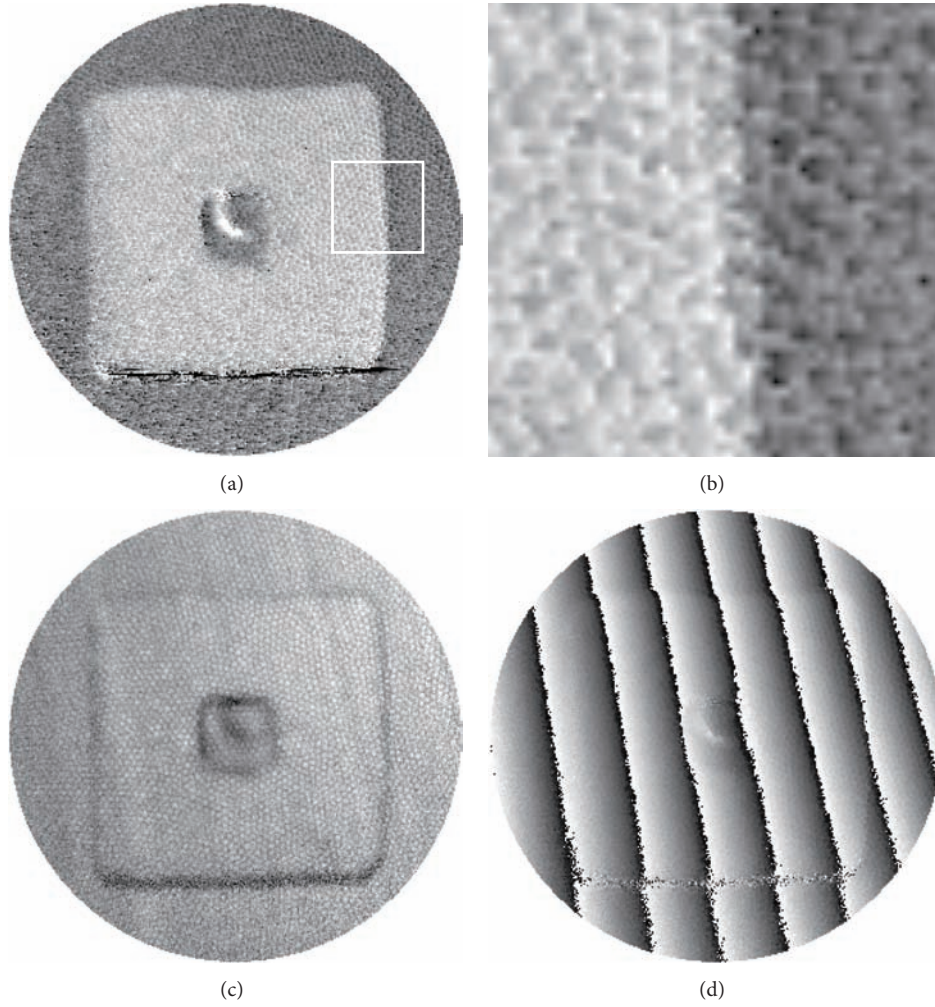


FIGURE 13: Underwater experiment. (a) Unfiltered height map. (b) Magnified white square region in (a). (c) Fringe contrast map. (d) Wrapped phase map.

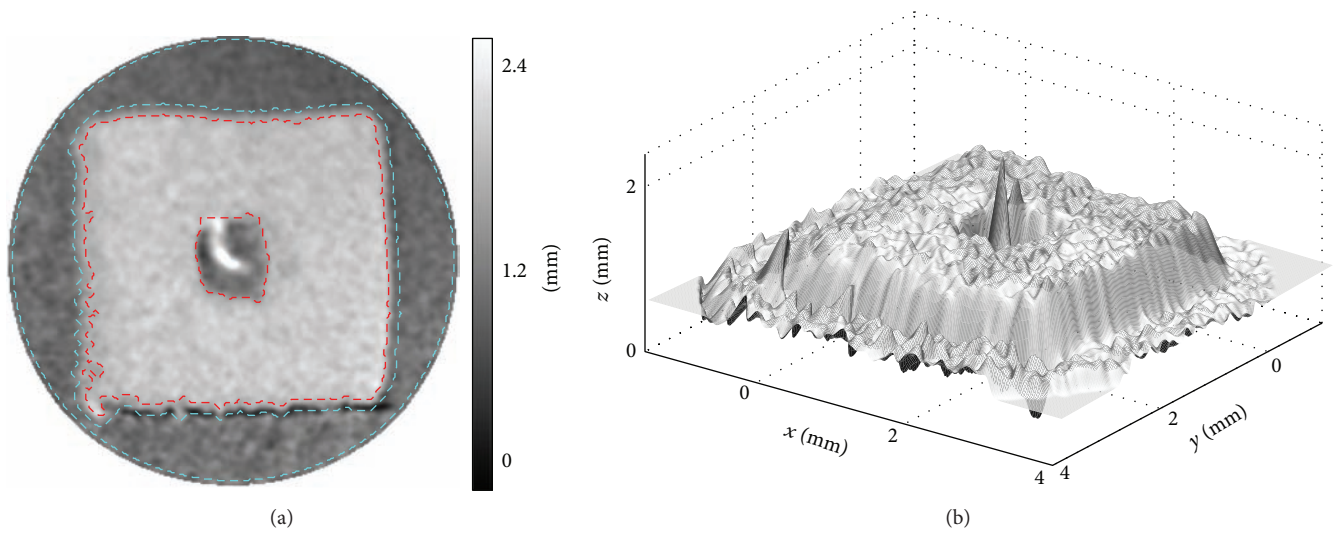


FIGURE 14: Underwater experiment. (a) Surface height map in 2D and (b) surface profile in 3D of the MEMS component.

alignment is different, the system is able to retrieve the gross shape but is subject to noticeable distortion. Future work could focus on computational and instrumental approaches to mitigate the distortion. In the computational approach, a scaling factor can be incorporated in a modified camera model to take account of the second-order scale change with respect to different depth in  $z$  direction. (The first-order change is considered in the pinhole model.) In the instrumental approach, special couplers can be designed to tightly mount the projector, the bare lens, the objective lens, and the fiber bundle for projection. Such an integrated and fixed projection unit would require a once-only calibration, achieving the same level of compactness as an endoscope available on the market. A combination of the computational and instrumental approaches could reach a new generation of measurement devices, applicable to more complex objects. They can accommodate new applications difficult to embark previously and still maintain high measurement accuracy and flexibility of fringe projection.

### Conflict of Interests

The authors declare that there is no conflict of interests regarding the publication of this paper.

### Acknowledgments

The authors thank Dr. Paul Kumar Upputuri of National University of Singapore for providing the MEMS component. This work was supported by the International Design Center (IDC) Grant nos. IDD31200102, IDG31200109, and SUTD SREP11013.

### References

- [1] R. Hartley and A. Zisserman, Eds., *Multiple View Geometry in Computer Vision*, Cambridge University Press, 2000.
- [2] T. Kreis, Ed., *Handbook of Holographic Interferometry*, Wiley-VCH, 2005.
- [3] J. W. Goodman, Ed., *Speckle Phenomena in Optics: Theory and Applications*, Roberts and Company Publishers, 2007.
- [4] K. Patorski, Ed., *Handbook of the Moiré Fringe Technique*, Elsevier, 1993.
- [5] J. Geng, "Structured-light 3d surface imaging: a tutorial," *Advances in Optics and Photonics*, vol. 3, pp. 128–160, 2011.
- [6] J. C. Wyant, "White light interferometry," in *Holography: A Tribute to Yuri Denisyuk and Emmet Leith*, vol. 4737 of *Proceedings of the SPIE*, pp. 98–107, Orlando, Fla, USA, April 2002.
- [7] M. A. Sutton, J. J. Orteu, and H. W. Schreier, Eds., *Image Correlation for Shape, Motion and Deformation Measurements: Basic Concepts, Theory and Applications*, Springer, 2009.
- [8] C. Zhang, P. S. Huang, and F.-P. Chiang, "Microscopic phase-shifting profilometry based on digital micromirror device technology," *Applied Optics*, vol. 41, no. 28, pp. 5896–5904, 2002.
- [9] M. Yonemura, T. Nishisaka, and H. Machida, "Endoscopic hologram interferometry using fiber optics," *Applied Optics*, vol. 20, no. 9, pp. 1664–1667, 1981.
- [10] S. Schedin, G. Pedrini, H. J. Tiziani, and F. M. Santoyo, "All-fibre pulsed digital holography," *Optics Communications*, vol. 165, no. 4, pp. 183–188, 1999.
- [11] E. Kolenovic, W. Osten, R. Klattenhoff, S. Lai, C. Von Kopylow, and W. Jüptner, "Miniaturized digital holography sensor for distal three-dimensional endoscopy," *Applied Optics*, vol. 42, no. 25, pp. 5167–5172, 2003.
- [12] L. Wosinski and R. Schumann, "Endoscopic moiré metrology," in *Interferometry '94: Interferometric Fiber Sensing*, vol. 2341 of *Proceedings of the SPIE*, pp. 249–252, May 1994.
- [13] S. H. Wang, C. J. Tay, C. G. Quan, and H. M. Shang, "Optical fiber fringe projector for micro-component," *Optik*, vol. 111, no. 9, pp. 419–422, 2000.
- [14] C. R. Mercer and G. Beheim, "Fiber optic phase stepping system for interferometry," *Applied Optics*, vol. 30, no. 7, pp. 729–734, 1991.
- [15] I. Merta, L. R. Jaroszewicz, and S. Świłło, "Simple method of the 3-D shape measurement by system of fibre-optic fringe projection," in *Optical Fibers: Applications*, vol. 5952 of *Proceedings of the SPIE*, pp. 1–10, Warsaw, Poland, September 2005.
- [16] F. Zhang, F. Duan, C. Lv, X. Duan, E. Bo, and F. Feng, "Fiber-optic project-fringe interferometry with sinusoidal phase modulating system," *Optical Engineering*, vol. 52, no. 6, Article ID 065601, 2013.
- [17] K. Kaneda, T. Ohashi, T. Tsumanuma, and K. Sanada, "Ultrathin fiberscope for stereoscopic vision," in *Holography, Interferometry, and Optical Pattern Recognition in Biomedicine III*, vol. 1893 of *Proceedings of the SPIE*, pp. 233–242, Los Angeles, Calif, USA, January 1993.
- [18] A. G. Albertazzi Jr., A. C. Hofmann, A. V. Fantin, and J. M. C. Santos, "Photogrammetric endoscope for measurement of inner cylindrical surfaces using fringe projection," *Applied Optics*, vol. 47, no. 21, pp. 3868–3876, 2008.
- [19] C. H. Wong, N. G. Chen, and C. J. R. Sheppard, "Study on potential of structured illumination microscopy utilizing digital micromirror device for endoscopy purpose," in *Proceedings of the International Symposium on Biophotonics, Nanophotonics and Metamaterials, Metamaterials*, pp. 218–221, Hangzhou, China, October 2006.
- [20] G. Zhang, J. He, and X. Li, "3D vision inspection for internal surface based on circle structured light," *Sensors and Actuators A*, vol. 122, no. 1, pp. 68–75, 2005.
- [21] N. T. Clancy, D. Stoyanov, L. Maier-Hein, A. Groch, G. Yang, and D. S. Elson, "Spectrally encoded fiber-based structured lighting probe for intraoperative 3d imaging," *Optics Express*, vol. 2, no. 11, pp. 3119–3128, 2011.
- [22] C. Schmalz, F. Forster, A. Schick, and E. Angelopoulou, "An endoscopic 3D scanner based on structured light," *Medical Image Analysis*, 2012.
- [23] C. Ohrt, M. Kästner, and E. Reithmeier, "Endoscopic geometry inspection by modular fiberoptic sensors with increased depth of focus," in *Optical Measurement Systems for Industrial Inspection VII*, vol. 8082 of *Proceedings of the SPIE*, 2011.
- [24] C. Ohrt, M. Kästner, and E. Reithmeier, "High resolution measurements of filigree, inner geometries with endoscopic micro fringe projection," in *Optical Measurement Systems for Industrial Inspection VIII*, vol. 8788 of *Proceedings of the SPIE*, May 2013.
- [25] H. Cui, N. Dai, W. Liao, and X. Sheng, "Intraoral 3d optical measurement system for tooth restoration," *Optik*, vol. 124, no. 9, pp. 1142–1147, 2013.

- [26] T. Pfeifer and S. Driessen, "3D image acquisition by fibre-based fringe projection," in *Proceedings of the 8th International Symposium on Laser Metrology*, pp. 589–595, Merida, Mexico, February 2005.
- [27] K.-C. Fan, R. Li, H.-M. Song, and K.-M. Yeh, "Fiber image techniques in digital stereomicroscopy," in *Proceedings of the IEEE International Conference on Mechatronics (ICM '05)*, pp. 295–300, Taipei City, Taiwan, July 2005.
- [28] R. Ishiyama, T. Okatani, and K. Deguchi, "Precise 3-D measurement using uncalibrated pattern projection," in *Proceedings of the 14th IEEE International Conference on Image Processing (ICIP '07)*, pp. I225–I228, San Antonio, Tex, USA, September 2007.
- [29] M. Dai, L. Chen, F. Yang, and X. He, "Calibration of revolution axis for 360 deg surface measurement," *Applied Optics*, vol. 52, no. 22, pp. 5440–5448, 2013.
- [30] V. Srinivasan, H. C. Liu, and M. Halioua, "Automated phase-measuring profilometry: a phase mapping approach," *Applied Optics*, vol. 24, no. 2, pp. 185–188, 1985.